Designing, Building, and Calibrating a Lithium Fluoride with Zinc Sulfide Neutron Multiplicity Counter

By

Christian C. Cowles

Dissertation

submitted in partial fulfillment

of the requirements for the degree of

Doctor of Philosophy

in Nuclear Science and Engineering

from Idaho State University

December 2016

Committee Approval

To the Graduate Faculty:

The members of the committee appointed to examine the dissertation of CHRISTIAN COWLES find it satisfactory and recommend that it be accepted.

_____

George Imel

Major Advisor

_____

Sean Stave

Committee Member

_____

Chad Pope

Committee Member

_____

Jason Harris

Committee Member

_____

Dan Dale

Graduate Faculty Representative

Acknowledgments

Funding for this work has been provided by the U.S. National Nuclear Security Administration's (NNSA) Office of Nonproliferation and the Next Generation Safeguards Initiative (NGSI). Battelle operates PNNL for the U.S. Department of Energy under contract DE-AC05-76RLO 1830.

The Alternative Multiplicity Counter project and the Neutron Detection without Helium-3 project, which both contributed to this research, were completed with substantial contributions from Phoenix Baldez, Richard (Spencer) Behling, Bruce Bernacki, Mary Bliss, James Ely, Micah Folsom, Richard (Dick) Kouzes, Vladislav Kukharev, Azaree Lintereur, Sean Robinson, Edward Siciliano, Martyn Swinhoe, Sean Stave, Lynn Wood, Mitchell Woodring, and Zheming Wang.

Contents

List of Figures

List of Tables

Acronyms and Abbreviations

BF_3	Boron trifluoride
ε	Neutron detection efficiency
ENMC	Epithermal neutron multiplicity counter
FoM	Figure-of-Merit, $FoM = \frac{\varepsilon^2}{\tau}$
HDPE	High density polyethylene
LANL	Los Alamos National Laboratory
LiF/ZnS	Lithium fluoride zinc sulfide fixed in a hydrogenous binder
LiNMC	Lithium fluoride and zinc sulfide-based neutron multiplicity counter
MCNP	Monte-Carlo N-Particle software, version 2.70 [1]
PMMA	Poly-methyl methacrylate
PMT	Photomultiplier tube
PNNL	Pacific Northwest National Laboratory
PSD	Pulse shape discrimination
PVT	Polyvinyl-toluene
τ	Neutron die-away time
VCF	Validation correction factor
WSP	Wavelength shifting plastic

Use Authorization

In presenting this dissertation in partial fulfillment of the requirements for an advanced degree at Idaho State University, I agree that the Library shall make it freely available for inspection. I further state that permission to download and/or print my dissertation for scholarly purposes may be granted by the Dean of the Graduate School, Dean of my academic division, or by the University Librarian. It is understood that any copying or publication of this dissertation for financial gain shall not be allowed without my written permission.

Signature _____

Date _____

Abstract

Past ^{3}He shortages have led to investigations into ^{3}He-free technologies for neutron detection applications that have often been accommodated by ^{3}He-based technologies. The goal of the Alternative Multiplicity Counter Project was to investigate ^{3}He-free technologies for neutron multiplicity counting for safeguards applications. Of the technologies investigated, lithium fluoride with silver-activated zinc sulfide scintillator (LiF/ZnS) was identified as the most promising material for developing ^{3}He-free neutron multiplicity counters. This project has successfully designed, built, and tested a lithium fluoride with zinc sulfide-based neutron multiplicity counter with a high neutron detection efficiency, short neutron die-away time, and low gamma-ray sensitivity. LiNMC design and construction involved optimizing scintillator and moderator materials, photomultiplier tube (PMT) size, number, shape and location, detector dimensions, optical reflector materials, and gamma-ray discrimination methods. By the end of the project, the LiNMC's basic components have been brought together and validated, achieving technological readiness level four, and providing strong evidence that LiF/ZnS-based neutron detection is viable technology for development into a high performance ^{3}He-free neutron detector.

Preliminary calibration with ^{252}Cf showed that the LiNMC was able to achieve a 39% neutron detection efficiency and a 13.2 μs neutron die-away time, resulting in FoM of 120. Preliminary calibration with ^{137}Cs and ^{60}Co showed that the LINMC was able to achieve a gamma-ray detection efficiency as low as 1.5×10^{-3}**.** Increases in neutron detection efficiency, reductions in neutron die-away time, and reductions in gamma-ray sensitivity are anticipated to be achievable with further development

1 Introduction

The goals of this project were to design, build, and calibrate a lithium fluoride and zinc sulfide (LiF/ZnS) -based neutron multiplicity counter (LiNMC) with the intent of determining the feasibility of using a LiNMC system as an alternative to helium-3 based systems for neutron multiplicity counting. My work on this project included 1) validating simulation results, 2) developing LiNMC designs, 3) building a functional LiNMC prototype, 4) calibrating the prototype for plutonium assay, 5) developing gamma-ray rejection methods, and 6) determining the effects of gamma-ray misidentification on neutron multiplicity counting. This project was motivated by a need to identify feasible replacements for ^{3}He-based neutron detectors due to the depletion of ^{3}He reserves and forecasted limited production [2, 3], and to provide rapid neutron multiplicity counter capabilities for various plutonium samples [4].

Neutron multiplicity counters are used to non-destructively quantify fissile materials in samples by counting time-correlated neutrons. This technique exploits the fact that fission neutrons are emitted essentially simultaneously. Delayed neutrons are generally ignored. The rate of multiple neutrons detected within a short time window can be used to obtain signatures for particular nuclear materials. These measurements can be made in the presence of background neutrons and (α, n) reactions because these neutrons are non-correlated, or random, in their arrival times [5].

The LiNMC was compared to the Epithermal Neutron Multiplicity Counter (ENMC), in simulations, due to the high capabilities of the ENMC, making it one of the most challenging systems to match. A viable alternative to the ENMC should also be a

viable alternative to less stringent ^{3}He-based systems, including coincidence counters [6]. Preliminary calibration with ^{252}Cf indicates that the LiNMC will take 67% longer to perform assays than the ENMC. Although the LiNMC's current assay time is inferior to the ENMC, it remains superior to most neutron multiplicity and coincidence counters.

The characteristic time required for a neutron to leave the system, through capture or escape, is the system's die-away time (τ). Minimizing τ minimizes the time gate required to adequately count the burst of neutrons released from a fission event and minimizes the number of non-fission neutrons that may be detected within that time gate and misidentified as fission neutrons. Detector systems with short τ values may be required to accurately assay samples with high uncorrelated neutron rates in a timely manner, such as salt residues from some pyrochemical processes, in-process nuclear materials, nuclear waste, and treaty verification materials [4, 7]. Although an extremely small τ (≤ 4 μs) is desirable, and could be used for a fast neutron multiplicity counter, reducing τ to such low values tends to come at the cost of reducing neutron detection efficiency (ε) to cripplingly low values and problems. Fast neutron multicity counters may also suffer from neutron cross-talk if detections are based on neutron scatter instead of neutron capture; therefore, no fast neutron multiplicity counters have reached full development at the time this was written [5, 8, 9].

Previous research has investigated three potential neutron multiplicity counter technologies as alternatives to the ENMC. A collaborative effort between Pacific Northwest National Laboratory (PNNL) and Los Alamos National Laboratory (LANL) investigated boron trifluoride (BF_3) proportional tubes, boron-lined proportional tubes, and lithium fluoride with zinc sulfide scintillators (LiF/ZnS). Of these investigated technologies, a LiF/ZnS-based system showed the greatest promise for development into a

full-scale neutron multiplicity counter, and therefore became the subject of this research [6, 10]. A more complete description of the precursor research to this project can be found in Section 2.4.

The LiNMC was built using 12 neutron detector stacks surrounding a sample chamber. Each of these stacks was composed of alternating layers of LiF/ZnS and wavelength shifting plastic (WSP) sandwiched together with ET Enterprise 9821KB07 PMTs on both ends. Neutrons from a sample capture in the lithium-6, producing an energetic triton and an alpha particle. These particles travel through the ^{6}LiF/ZnS mixture causing the ZnS to scintillate [3]. Scintillation light propagates to WSP, where it is isotropically re-emitted and propagates to photomultiplier tubes (PMTs) where it is converted to an electronic signal for a data acquisition system [11]. Although gamma rays can also produce scintillation light, this light tends to be much dimmer than the light from neutron captures; therefore, events are only counted as neutrons if signals are detected from PMTs on both ends of a stack.

The LiNMC was designed and built in interactive steps between MCNP modeling and experimentation measurements. Models of the ENMC were compared to models of lithium, boron-lined, and boron trifluoride-based neutron multiplicity counter models. These models indicated that a lithium-based design showed the greatest promise for neutron multiplicity counter development, based on its high neutron capture efficiency (ε) and low neutron die-away time (τ). This was followed by small-scale experimentation to validate the modeling [6]. The total neutron capture efficiency of the LiNMC design was calculated by comparing the number of neutrons captured by ^{6}Li atoms in the LiF/ZnS sheets to the total number of generated neutrons. Neutron die-away times were calculated

by tracking the time for neutrons to exit the system (through capture or escape), and then fitting an exponential decay function to the neutron exit times and taking the decay constant as the neutron die-away time. The modeled neutron capture rates were expected to overestimate measured detection count rates since the MCNP models did not account for the homogeneous distribution of the LiF/ZnS mixture, alpha and triton transport and capture, or scintillation light transport [6]. Therefore, a validation correction factor (VCF) was used to account for the difference between the modeled and measured systems. Following validation, models were updated to simulate full-sized detector stacks, which were again validated through experimental measurement. The differences between these single stack simulations and measurements were used to identify ways to improve ε and τ by eliminating light guides, using larger off-center PMTs, and replacing the Teflon overwrap with Enhanced Spectral Reflector overwrap. These modifications were incorporated into full-scale models, which guided measurements to determine the optimal detector stack locations.

There were several challenges with the LiF/ZnS material used in the LiNMC system development. First, MCNP simulation could not adequately account for triton and alpha particle energy deposition in the ZnS scintillator, scintillation light generation, or scintillation light propagation and remittance in the stacks, and scintillation light detection in the PMTs. The steps from neutron capture in ^{6}Li to signal detection have loss mechanisms including: failure of alpha and triton particles to excite ZnS; photon loss from self-absorption, scattering, and re-emission; and signals failing to be detected if they do not surpass a minimum charge collection threshold for either of the two PMTs. A correction for the loss of signal from neutron capture to the electronic signal reaching the data

acquisition system was accounted for using a VCF. The VCF is a parameter determined by dividing the measured neutron counting efficiency by the simulated neutron capture efficiency. The VCF from the demonstration system was used to develop a more accurate estimate of the neutron counting efficiency of the full-scale LiNMC system [6].

Another challenge associated with using LiF/ZnS as a neutron detector material is that the silver-activated zinc sulfide (ZnS:Ag) is sensitive to gamma rays, and produces scintillation light. However, the electronic signals arising from gamma-ray energy deposited in the ZnS:Ag have a shorter decay time than (heavy) charged particles, and therefore can be identified using pulse-shape analysis. Once gamma rays are identified, their information can be removed from the data set, adding an additional analysis step compared to ^{3}He or boron-based systems, where gamma-ray discrimination can be accomplished with a simple threshold on pulse height cut.

Removing gamma-ray signals from the data stream is important since a shift register uses the numbers of time stamps within predefined time windows to determine timing characteristics about the data stream. These timing characteristics can then be used to determine characteristics about the radiation source that produces the data stream, such as fissile mass, neutron multiplication (*M*), and the ratio of (α, n) neutron to fission neutrons (*Alpha*) [5]. If gamma rays are detected but are not removed from the time stamp list, they will be treated like neutron events by the shift register, potentially resulting in erroneous measurements of sample characteristics. The ideal neutron multiplicity counter has minimal gamma-ray sensitivity to negate measurement errors associated with misidentifying gamma rays as neutrons.

Several methods exist to reduce the number of gamma rays that are misidentified as neutrons, including demanding coincidence between two PMTs, pulse shape analysis, and shielding. Since the energy deposited in LiF from gamma rays is closely correlated with gamma-ray energy and a ^{6}Li(n, α) reaction has a Q-value of 4.78 MeV, neutrons tend to produce much brighter signals in the LiF/ZnS than gamma rays [3]. Therefore, the number of counted gamma-ray signals can be significantly reduced by demanding coincidence between two PMTs located on opposite ends of a detector stack, with minimal neutron signal losses. Coincidence windows were set for each channel pair based on relative channel performance, and were typically 200 – 600 ns long. Neutron pulses also tend to have a peak followed by a tail as long as a few microseconds, whereas gamma-ray pulses tend to have a single peak and little if any tail. Pulse shapes can therefore be analyzed to discriminate against gamma-ray-like pulses, further reducing counted gamma-ray events. The sample chamber can be lined with gamma-ray attenuating materials to reduce gamma rays without significantly reducing detected neutrons. Gamma-ray-like signals can also be generated by electronic noise, which can be reduced by using shielded power and signal cables, a power-smoothing power supply, ferrite chokes, separating signal and power cables from each other, grounding all cables to a single point, and other electronic noise reduction techniques. A more complete description of gamma-ray discrimination techniques can be found in Chapter 4.

Signals from the PMTs are converted into digital signals with an analog-to-digital converter (ADC) and then passed to a field-programmable gate array (FPGA), where triggering and filters are applied. Filtered signals are then passed from the FPGA across a peripheral component interconnect express (PCIe) bus and converted into ROOT files for

analysis. The events in the ROOT files are analyzed, including using coincidence between PMTs and pulse shape analysis to discriminate against gamma-ray-like events. The time stamps of the remaining events are then passed to a virtual shift register to analyze the time correlation between events. These timing characteristics are then used to determine sample properties such as fissile mass, *M* and *alpha* (ratio of (α, n) neutron to fission neutrons).

The most important detector properties for determining timing characteristics are ε and τ, which can be used to obtain a Figure-of-Merit (*FoM*) to generally compare the performance of different neutron multiplicity counter systems. The *FoM* is defined as ε^2/τ. Although ε and τ do depend on the vertical position and neutron energy of the sample, they are generally assumed to be constant. A single Cf-252 source at the center of the detector is usually used to determine ε and τ [6]. A more complete description of total neutron count efficiency, die-away time and Figure-of-Merit can be found in Section 2.1.

2 Literature Review / Background

This project incorporated results and concepts from previous projects. The most relevant project results related to LiNMC development are summarized below.

2.1 Multiplicity Counting and Shift Registers

Multiplicity counting is a method of gaining quantitative information about the characteristics of samples from the neutrons emitted by samples. This information can be used to determine the effective ^{240}Pu mass of samples, which is ^{240}Pu-effective mass is defined as the mass of ^{240}Pu that would give the same double coincidence response as that obtained from all even isotopes of the samples:

$^{240}Pu_{eff} = 2.52\times{}^{238}Pu + {}^{240}Pu + 1.68\times{}^{242}Pu$ [5].

Neutron detection can be affected by several parameters that may be known, unknown, or partially known. These sample parameters are listed roughly in order of practical importance:

1. spontaneous fission rate,
2. induced fission, or sample self-multiplication,
3. the (α, n) reaction rate in the sample,
4. the energy spectrum of the (α, n) neutrons,
5. spatial variation of the neutron multiplicity,
6. spatial variation in the neutron detection efficiency,
7. energy spectrum effects on detection efficiency,
8. neutron capture in the sample, and
9. the neutron die-away time in the detector.

There are N measured parameters for N unknown parameters. The singles, doubles, triples, (etc.) rates (multiplicity rates) provided by a multiplicity counter are typically used to solve for the listed parameters in the order presented above. The remaining parameters require assumptions or prior measurements and are generally assumed to be uniform across all samples. Therefore, the more parameters and the higher the multiplicity a detector can reliably measure, the fewer assumptions or prior measurements are required to assay samples [5].

A shift register analyzes a stream of time stamps from a detector to determine multiplicity events recorded in the data stream, which can then be used as parameters to determine characteristics of the sample. A trigger event opens a time window which counts all subsequent events for a duration that is proportional to the neutron die-away time of the detector system. After the time gate has closed, the system waits a long time (such as a millisecond) relative to the neutron die-away time to allow all prompt neutrons associated with a fission event to leave the system. Another time gate is then opened for the same duration as the first time gate and all events in that second time gate are counted. The number of events from the second time gate are subtracted from the number of events from the first time gate as a means of background subtraction. After performing this operation many times, statistics can be built up of the average numbers of multiples above background. The relative and absolute rates of these event rates can be used to determine certain qualities about the sample assayed [5].

If correlated events from fissions are present, then the correlated neutrons produce an exponential decay distribution with time, where the time constant is the die-away time of the detector. Although multiple exponential decays may be present from different

neutron removal mechanisms, a single exponential decay is generally considered to be a reasonable approximation. The time distribution is given by

Equation 2.1 $N(t) = A + Re^{\frac{-t}{\tau}}$

where *N(t)* is the neutron population at time *t*, *A* is the accidental or random rate, *R* is the real or correlated rate, and τ is the mean neutron die-away time. If only random, uncorrelated events are detected, the event distribution will be, on average, constant with time [5]. This relationship between a constant background of uncorrelated events and the exponential decay of correlated events is illustrated in Figure 2.1.

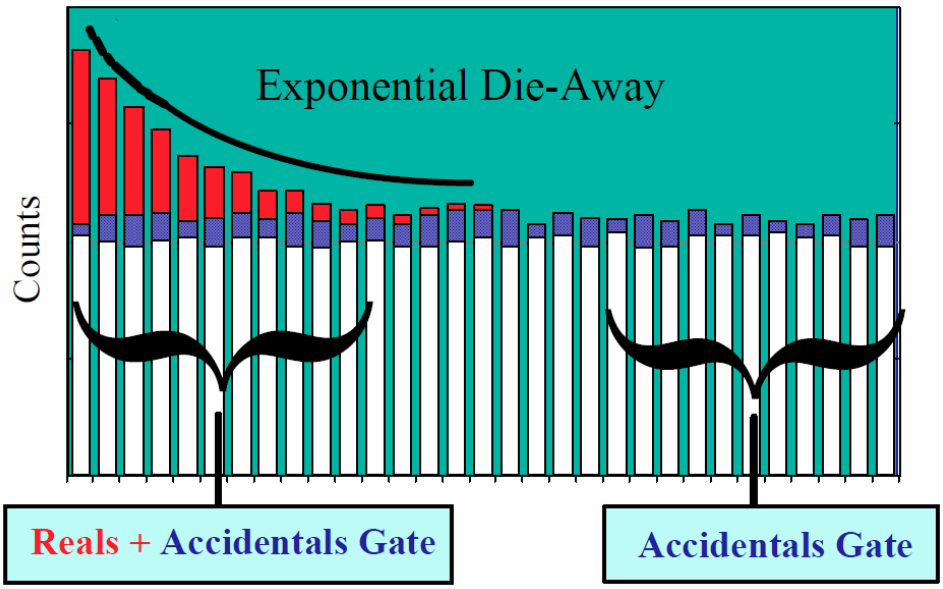

Figure 2.1 Histogram of detected neutrons in a pulse stream. A measured distribution with exponential die-away is above the histogram, and the (Reals + Accidentals) and (Accidentals) coincidence gates are below the histogram (figure from [5]).

These accidental and real events, which are indistinguishable from each other on an event-by-event basis, can be read into a shift register. Historically, shift registers have been built as integrated circuits, although a digital shift register, also known as a virtual

shift register, was selected for this project. When the shift resister detects an event, it opens a time gate *G* that records subsequent real *R* and accidental *A* events (*R*+*A*). Once *G* ends, the shift register delays for time *D*, counting for a sufficiently long period of time for neutrons associated with a fission event to exit the system or be captured. Once *D* has passed, a second time gate, identical to *G*, opens to count only accidental events *A*. Coincidence counting does not begin until a short time *P* (the predelay) after the first event, to prevent counting events multiple times and mitigate dead time traditionally associated with ^{3}He tubes. ^{3}He coincidence counters typically have predelays of 3 to 6 μs, time gates of 32 to 64 μs, and delays of 1 to 4 ms. Note that multiple gates and delays can be active simultaneously [12].

Although delayed neutrons from fission events are time-correlated with prompt neutrons, the effects of delayed neutrons are considered insignificant over the time scales of the shift register, which measures events on a scale of tens of microseconds. Prompt neutrons are emitted within ~10^{-14} seconds of fissions, while delayed neutrons may not begin being emitted until ~0.1 seconds after fission, long beyond the time scales of a shift register. Delayed neutrons, which account for ~0.2% of emitted neutrons from ^{239}Pu, usually produce an insignificant increase in the uncorrelated signal rate compared to neutrons from (α, n) reactions.

If two events appear within the same time gate *G*, then one coincidence will be recorded. If three or more events appear within the same time gate, then n(n-1)/2 coincidences will be recorded, where n is the number of events within the time gate. These coincidence events may have originated from fission events (*R*) or random background events (*A*). Therefore, the shift register counts *R*+*A* events for *G* followed by *D* and then

collects *A* for *G*. Ideally *R* could be determined by subtracting *A* from *R*+*A*, but systems can be limited by several factors: (a) pulse pileup and electronics dead time can perturb the counted event distribution after a trigger; therefore, a predelay time *P* is allied after each counted event, wherein no other events can be counted; (b) due to the fact that the distribution of real events extends beyond the gate interval *G*, some real events will not be counted in *R*+*A*; (c) some real events may even appear in the delayed gate. Taking these limitations into account, the true shift register real event rate can be determined by the following equation:

Equation 2.2 $$R = \frac{(R+A)-(A)}{e^{-P/\tau}\,(1-e^{-G/\tau})(1-e^{-(D+G)/\tau})}\,e^{-GT}$$

where *R* is the real event rate, (*R*+*A*) is the event rate from the first time gate, (*A*) is the event rate from the second time gate, *P* is the predelay, *G* is the gate time, *D* is the delay between gates, and τ is the neutron die-away time [12].

Within counting statistics, the number of accidental events in *A* from the second time gate is the same number of accidental events in *R*+*A* from the first time gate. Therefore, the difference between the events from the first time gate and the events from the second time gate is the real coincident events *R*. The multiplicity distributions are determined by analyzing the 0's, 1's, 2's, 3's, etc. of the *R*+*A* and *A* events. The first step of this analysis is to record the number of times that each multiplicity occurs within each time gate. For example, if seven events are in the *R*+*A* time gate, then "1" is added to the *R*+*A* counter that tallies events. The same tally procedure occurs for the *A* time gate. A correlated pulse stream has more high-multiplicity events in the *R*+*A* distribution and more low-multiplicity events in the *A* distribution. The sum of all multiplicities in the *A* distribution is the total number of events, or singles *S*. The doubles *D* is the sum of all the

events times the mean of the *R+A* distribution minus the mean of the *A* distribution. The triples *T* and higher involve a more complex relationship between the *R+A* and *A* distributions. The singles, doubles, and triples are actually the first, second, third factorial moments of events, as given by

Equation 2.3 $D = S(f_1 - b_1)$

Equation 2.4 $T = S(f_2 - b_2 - 2b_1(f_1 - b_1))/2$

where *S* is the singles rate, *D* is the doubles rate, *T* is the triples rate, f_1 and f_2 are the first and second multiplicity distributions of *R+A*, and b_1 and b_2 are the first and second multiplicity distributions of *A* [5].

Singles, doubles, and triples can be expressed analytically in terms of variables of interest, as seen in Equation 2.5,

Equation **2.6**, and Equation 2.7. These equations were derived by Bohnel [13] and Cifarelli and Hage [14] based on point geometry sample and reasonable assumptions.

Equation 2.5 $S = F\varepsilon M\nu_{s1}(1 + \alpha)$

Equation 2.6 $D = \frac{1}{2}F\varepsilon^2 f_d M^2(\nu_{s2} + \frac{M-1}{\nu_{i1}-1}\nu_{s1}(1 + \alpha)\nu_{i2})$

Equation 2.7 $T = \frac{1}{6}F\varepsilon^3 f_t M^3(\nu_{s3} + \frac{M-1}{\nu_{i1}-1}(3\nu_{s2}\nu_{i2} + \nu_{s1}(1 + \alpha)\nu_{i3}) + (\frac{M-1}{\nu_{i1}-1})^2\nu_{s1}(1 + \alpha)\nu_{i2}^2)$

where F = spontaneous fission rate,

ε = neutron detection efficiency,

M = neutron multiplication,

α = the (α, n) to spontaneous fission neutron ratio,

f_d = the doubles gate fraction,

f_t = the triples gate fraction,

ν_{s1}, ν_{s2}, ν_{s3} = factorial moments of the spontaneous fission neutron distribution,

ν_{i1}, ν_{i2}, ν_{i3} = factorial moments of the induced fission neutron distribution [5].

Fission neutron factorial moments are unique to each isotope, but since the scope of this project is limited to plutonium assay, only ^{240}Pu spontaneous fission and ^{239}Pu thermally-induced fission neutron factorial moments are presented in Table 2.1.

Table 2.1 Plutonium-240 spontaneous fission and plutonium-239 induced fission neutron factorial moments [5, 15].

Factorial moment	Value*
ν_{s1}	2.154
ν_{s2}	3.789
ν_{s3}	5.211
ν_{i1}	2.879
ν_{i2}	6.773
ν_{i3}	12.630

*Published values will vary depending on the nuclear data selected for computation and typically do not report uncertainties.

The doubles gate fraction f_d and triples gate fraction f_t are the fraction of the detected doubles and triples that are actually counted inside the time gate G of the shift register, which must be known to gain useful information about samples from the doubles and triples rates. For a neutron detector with a single characteristic die-away time τ, f_d is given by

Equation 2.8 $$f_d = e^{-P/\tau}(1 - e^{-G/\tau})$$

where τ is the detector die-away time, G is the shift register time gate, and P is the shift register predelay. The triples gate fraction is then given by $f_t = f_d^2$. In practice, f_d and f_t are often determined experimentally since the die-away curve of real detectors is not exactly a single exponential [5].

A shift register can calculate the singles, doubles, and triples rates through accidentals counting, Equation 2.3, and Equation 2.4 which can be related to unknown sample parameters with Equation 2.5 through Equation 2.7. Detector efficiency ε is usually assumed to be known from careful calibrations with a californium reference source.

Equation **2.6** through Equation 2.8 can then be solved for fissile mass, α, and M. The scope of this project involves neutron multiplicity counting for plutonium mass assay, therefore only $^{240}Pu_{eff}$ mass will be considered at this time. M can be determined by solving the following equation:

Equation 2.9 $$a + bM + cM^2 + M^3 = 0$$

where the coefficients a, b, and c are functions of S, D, and T as follows:

Equation 2.10 $$a = \frac{-6T\nu_{s2}(\nu_{i1}-1)}{\varepsilon^2 f_d S(\nu_{s2}\nu_{i3}-\nu_{s3}\nu_{i2})},$$

Equation 2.11 $$b = \frac{2D(\nu_{s3}(\nu_{i1}-1)-3\nu_{s2}\nu_{i2})}{\varepsilon f_t S(\nu_{s2}\nu_{i3}-\nu_{s3}\nu_{i2})},$$

Equation 2.12 $$c = \frac{6D\nu_{s2}\nu_{i2}}{\varepsilon f_t S(\nu_{s2}\nu_{i3}-\nu_{s3}\nu_{i2})} - 1\,.$$

Once M is determined, the sample fission rate F can be calculated as follows:

Equation 2.13 $$F = \left(\frac{2D}{\varepsilon f_d} - \frac{M(M-1)\nu_{i2}S}{\nu_{i1}-1}\right)\Big/(\varepsilon M^2 \nu_{s2})\,.$$

The second term in Equation 2.13 accounts for the sample's self-fission-neutron-interrogation, which must be considered to obtain the correct spontaneous fission rate. Once F is determined, the sample's ^{240}Pu effective mass m_{240} can be calculated as follows:

Equation 2.14 $$m_{240} = \frac{F}{(473.5\ fissions/s{-}g)}\,.$$

If the sample's isotopic composition is known, then the total Pu mass can be calculated as follows:

Equation 2.15 $$Pu = m_{240}/(2.52f_{238} + f_{240} + 1.68f_{242})\,,$$

where f_{238}, f_{240}, and f_{242} are the fractions of plutonium isotopes present in the sample, which are usually obtained through mass spectroscopy or gamma-ray spectroscopy. *F* can also be used to calculate α as follows:

Equation 2.16 $$\alpha = \frac{S}{F\varepsilon\nu_{s1}M} - 1$$ [5].

Neutron detection efficiency ε can vary for low fission density samples, such as waste drums. This is because materials in the waste containers can significantly affect the neutron energy spectrum emitted from the containers. In these situations, if *M* can be considered equal to 1, then ε can be calculated instead. *S*, *D*, and *T* are first determined from neutron multiplicity counter measurements and shift register analysis to obtain α as follows:

Equation 2.17 $$\alpha = \frac{3ST f_d^2 \nu_{s2}^2}{2D^2 f_t \nu_{s1}\nu_{s3}} - 1\,.$$

Once α is determined, *F* can be calculated as follows:

Equation 2.18 $$F = \frac{S^2 f_d \nu_{s2}}{2D\nu_{s1}^2(1+\alpha)^2}\,,$$

and neutron detection efficiency ε can be calculated as follows:

Equation 2.19 $$\varepsilon = \frac{S}{F\nu_{s1}(1+\alpha)}$$ [15].

Equations to determine other combinations of sample characteristics based on three sample parameters have been derived by Cifarelli and Hage [14].

2.2 Pulse Shape Discrimination

Pulse shape discrimination (PSD), as described and used in Chapter 4, was first used in 1959 to distinguish between electron and proton signals from gamma rays and neutrons, respectively, interacting in organic scintillators such as anthracene, stilbene, and quaterphenyl crystals. It was observed that a two-dimensional plot of the peak pulse energy against the integrated energy of pulses produced a clear separation between gamma-ray induced pulses and neutron induced pulses, very similarly to PSD Method 3 discussed in Chapter 4. Comparing the peak pulse energy to the integrated energy produced a one-dimensional plot with clearly separated gamma-ray induced pulses to neutron induced pulses. These pulses tended to group into Gaussian distributions that could be defined by the distance between the mean of each group divided by the full width-at-half-maximum for the groups [16].

This method of dividing the pulse peak energy by the integrated energy to produce a charge ratio that clearly separates gamma-ray pulses from neutron pulses in a material has remained in use up to the writing of this document, such as displayed in Figure 2.2. Once a charge ratio is developed, a double Gaussian function can be fit to the data set and a figure-of-merit (γFoM) calculated by the difference between the means (or centroids) of the two Gaussian functions divided by the sum of the full-width-at-half-maximum of the Gaussian functions [17].

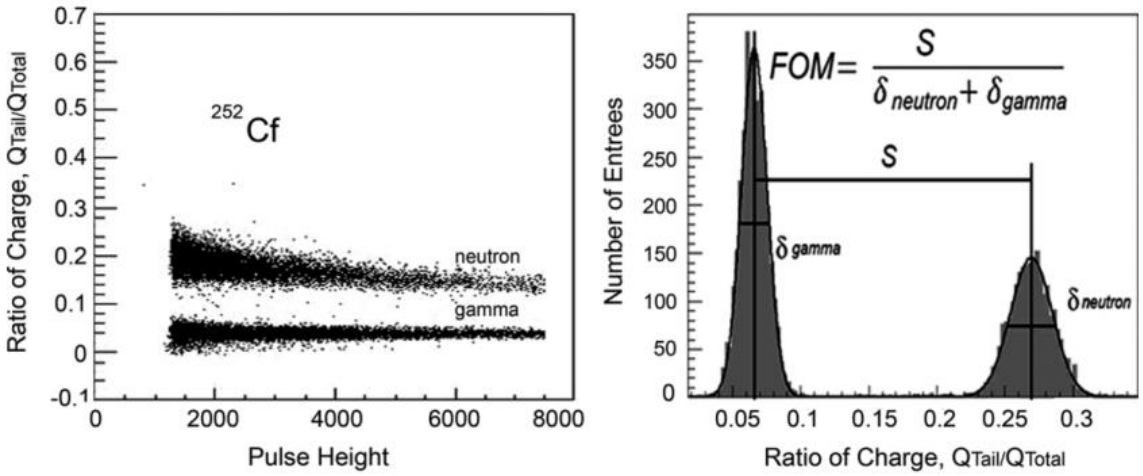

Figure 2.2 (Left) Typical PSD pattern of a stilbene crystal obtained by digitized separation of neutron and gamma-ray pulses. (Right) PSD profiles of an experimental data set used for calculation of the PSD figure-of-merit (γFoM) (figure from [17]).

PSD based on measuring the decay time of pulses has also been used previously with LiF/ZnS neutron coincidence counters with WSP sheets [4, 18] and ribbons [19]. PMT signals from a LiF/ZnS system with WSP ribbons were passed through pulse shape analysis modules. These modules produced an analog pulse with height proportional to the time between the crossings of two constant fraction discriminators (CFD). The results of a ^{252}Cf source with a CFD set from 90% to 50% of the peak amplitude of the trailing edge of pulses can be seen in Figure 2.3. This gamma-ray to neutron separation resulted in a γFoM greater than 5. These neutron and gamma-ray peaks were measured to be independent of neutron and gamma-ray energies [19].

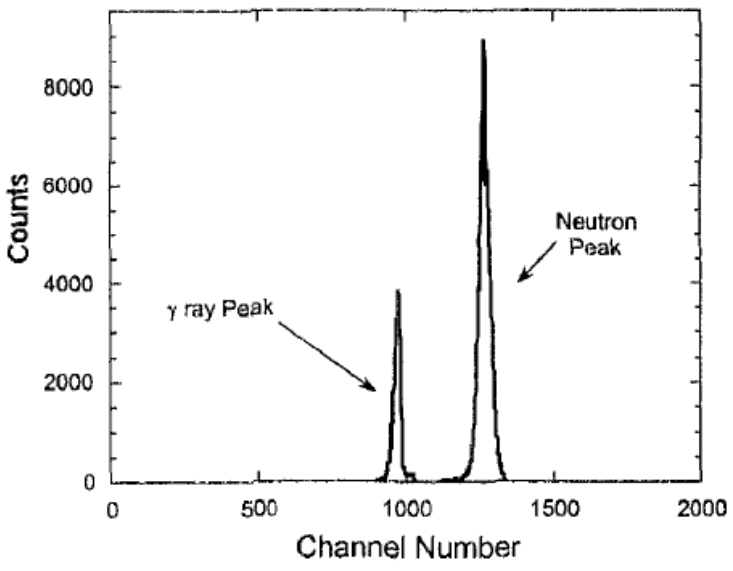

Figure 2.3 PSD spectra from ^{252}Cf with previous LiF/ZnS with WSP ribbons (figure from [19]).

Previous measurements of a LiF/ZnS system with WSP sheets summed the output of two PMTs into an Ortec 552 Pulse-Shape Analyzer in conjunction with an Ortec 566 Time-to-Amplitude Converter (TAC). The Ortec 552 was set to trigger at 90% and 20% of the peak input on the trailing edge. Results from these measurements can be seen in Figure 2.4. This set of measurements resulted in a γFoM of 1.23 [4].

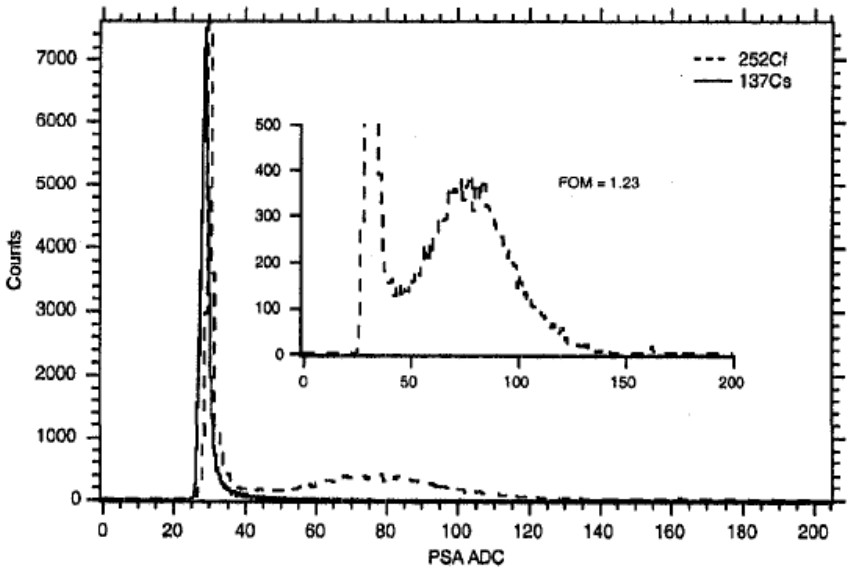

Figure 2.4 PSD spectra from ^{137}Cs and ^{252}Cf source with previous LiF/ZnS and WSP sheets (figure from [4]).

The same LiF/ZnS with WSP sheets system was also examined with a 2-dimensional PSD method of comparing pulse energy to pulse shape. This method resulted in a gamma rejection ratio (*GRR*) of 0.013, which was equivalent to a γFoM of 0.95 [4].

Despite the similar designs and PSD methods between the LiF/ZnS with the WSP sheets and the WSP ribbons, there was no explanation given for the dramatic difference between the gamma-ray discrimination abilities of the two measurements. From this, it may be inferred that small differences in design and methodology may result in large differences in gamma-ray discrimination, highlighting the importance of using sound assumptions and optimizing methods.

2.3 MCNP Methods

MCNP simulations were used by this project as well as by the Neutron Detection without Helium-3 project, described in section 2.4, to determine the most promising models for experimental testing and further development. The first simulation of the ENMC was conducted to ensure that results agreed with an already validated system. Further simulations modified the ENMC system to implement different neutron capture materials and geometry changes. The most promising of these simulations were then validated with experimental measurements.

Baseline simulations focused on reproducing the performance of the ENMC125 that was developed at LANL [20], which can be seen in Figure 2.5.

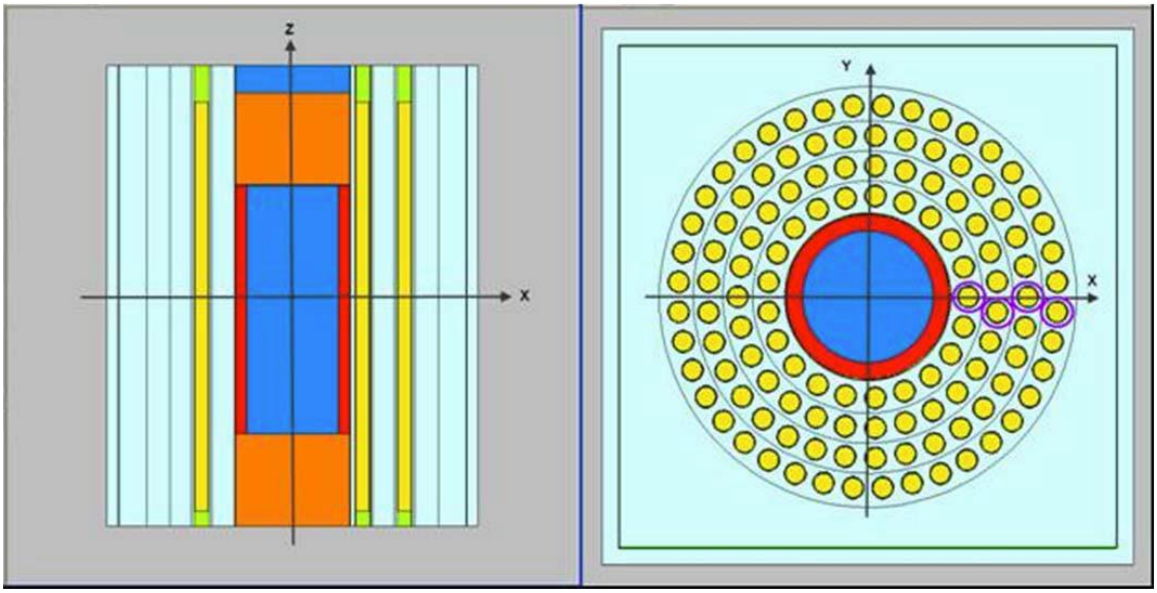

Figure 2.5 Screen captures showing the main components of the baseline ENMC125 model used for further development. (Left) Vertical profile. (Right) Horizontal profile, including the four (circled) tubes used to tally full-system "diagnostic" at the single-tube level [21].

As seen in Figure 2.5, the ENMC configuration consists of 121 identical ^{3}He tubes divided into four concentric rings of 21, 27, 33, and 40 tubes surrounding a cylindrical

sample chamber. The tubes are a standard size from G.E. Reuter-Stokes, with an outer diameter of 25.4 mm, active height of 711 mm, and 0.794 mm thick aluminum walls. Except for the top and bottom graphite end plugs and relatively thin inner and outer metal liners, the entire array of tubes are embedded within an 80.01 cm high, 65.112 cm square box filled with HDPE [21].

Neutron capture efficiency (NCE) was evaluated using the F4-type (track length) tally with a flux multiplier (FM4) to specify the reaction type. The results of this method gave the total number of neutron reactions per source-emitted neutron that took place in a given volume of material. As long as the material in which the neutron reaction occurred was the same as the signal-generating medium, then the NCE of the modeled detector can be equated to the total number of reactions per emitted neutron. This method has been shown to provide very accurate results for a variety of ^{3}He and BF_3-based systems, and was implemented with a VCF for LiF/ZnS simulations [21].

Neutron die-away time, τ, was determined with the neutron coincidence capture F8-CAP tally option. This option converts a pulse-height tally into a neutron capture tally that counts specified combinations of nuclides at the end of each history. By adjusting pre-delay and gate-width time values over a range, this option was used to simulate doubles NCE as a function of pre-delay and gate-width values [21]. An exponential function was fit to these doubles rate values, where τ was taken as the decay constant of the exponential. The doubles rate NCE as a function of gate-width for the LiNMC can be seen in Figure 2.6.

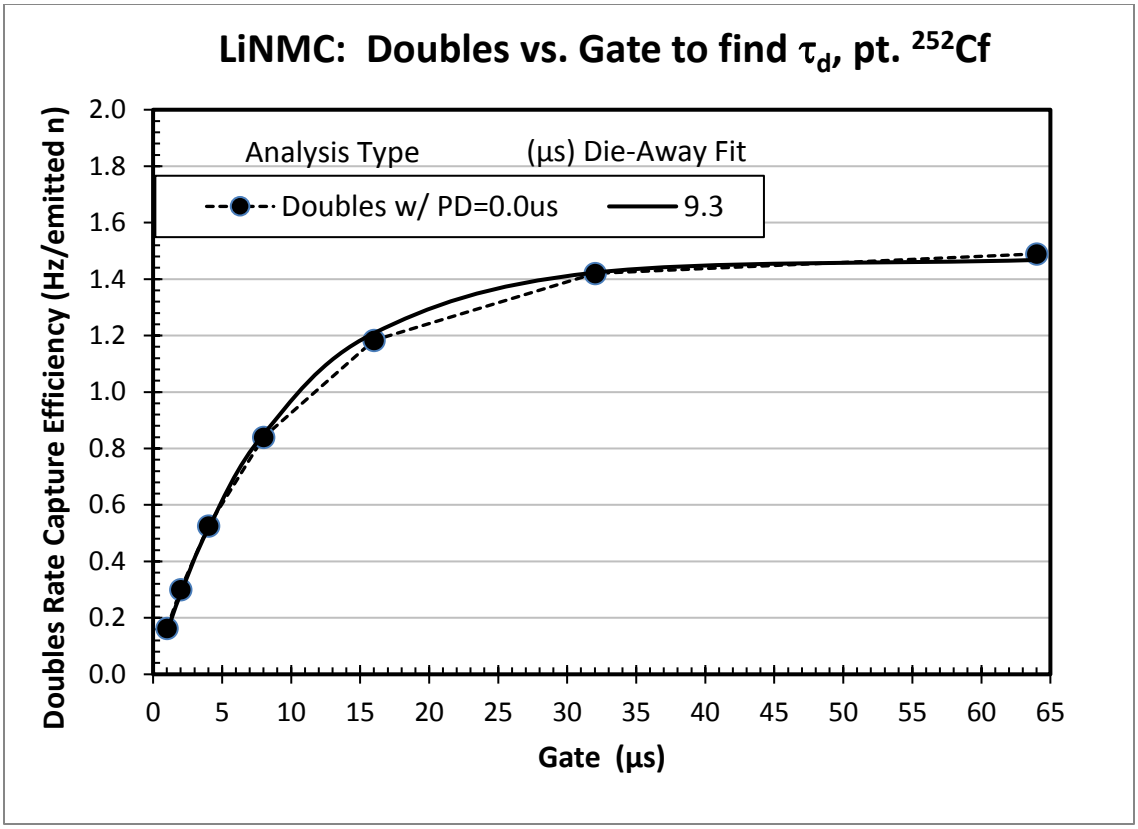

Figure 2.6 LiNMC doubles neutron capture efficiency as a function of gate-width time with associated exponential decay fit.

These MCNP methods were followed for ENMC, LiNMC, and all other ^{3}He alternative simulations and were used as the basis for NMC development. The MCNP input for the LiNMC is presented in Appendix 3: MCNP Model of LiNMC

2.4 Neutron Detection without Helium-3 Project

Collaborative research between Pacific Northwest National Laboratory (PNNL) and Los Alamos National Laboratory (LANL) has investigated the prospects of utilizing boron trifluoride (BF_3) proportional counters, boron-lined tube proportional counters, and LiF/ZnS sheets as alternatives to ^{3}He-based neutron multiplicity counters in the Neutron Detection without Helium-3 project. This research focused on using MCNP modeling to

determine the most promising detector technology and then building a demonstration unit. The Neutron Detection without Helium-3 Project was completed prior to my arrival at PNNL, but forms an important basis for LiNMC development.

The primary motivation for this Neutron Detection without Helium-3 Project was to investigate commercially available technologies that might be used in safeguards applications in the relatively near term as alternatives to ^{3}He-based neutron detectors, which is more fully detailed in the reports for the 'Neutron Detection without Helium-3 Project' [6, 10, 22-26]. Potential safeguards applications include determining the fissile content of declared and orphaned sources for treaty verification and nuclear stewardship. Alternative technologies were all compared to the Epithermal Neutron Multiplicity Counter (ENMC) because of its high capabilities and the assumption that any technology capable of comparable performance to the ENMC would also be capable of being used as an alternative to less capable ^{3}He-based systems, such as active well coincidence counters.

The first three years of this project focused on modeling and simulations of the ENMC with alternative technologies. The second half of the project was to develop a demonstration unit using the most promising alternative to demonstrate the technology in this type of application, validate the model and simulation results, and to discover any additional areas of research needs before this type of technology was used in a full-scale system. The three technologies investigated were boron trifluoride (BF_3) proportional tubes, boron-lined proportional tubes, and lithium fluoride mixed with zinc sulfide scintillator (LiF/ZnS). Although ^{10}B-based systems are insensitive to gamma rays, they had an inferior *FoM*'s compared to a ^{3}He or LiF/ZnS system with the ENMC's footprint [6].

According the Final Technical Report for the Neutron Detection without Helium-3 Project, "A baseline model of the ENMC in MCNP (developed and validated by LANL) was used as a starting point. The model was modified to support optimization investigations, and then used as a template to insert the various alternatives. Many parameters, such as the inner and outer liners, source insertion volume, and active height were maintained to minimize the configuration changes. The main changes that occurred were in the diameter or thickness of the detector material and moderator, which was optimized for each alternative technology. The main metrics used in the optimization of the modeling and simulations were the [neutron count] efficiency [ε] and the [neutron] die-away time [τ]. The efficiency is directly related to the signal collected, while the die-away time governs the necessary gate width to measure multiplicity, which is proportional to the accidental coincidence rate, or noise, of the system." [6]

In MCNP, ε was calculated by comparing the number of generated neutrons to the number of (n, t) reactions in ^{6}Li. The neutron die-away time was calculated by recording the time it took each neutron to be removed from the system. An exponential decay was fit to the neutron removal data set with a decay constant chosen to minimize the chi squared per degree of freedom between the exponential decay and the neutron removal data set. This exponential decay constant was taken to be τ for the modeled system.

Because neutron multiplicity counters can operate with a wide range of ε and τ values, a figure-of-merit (*FoM*) is generally used to compare different systems, where $FoM = \varepsilon^2/\tau$ [5, 6, 12]. The *FoM*s are useful to compare performance between configurations, but may not accurately predict system performance based on signal

collection, electronics, or data acquisition or analysis. Therefore, the *FoM* should only be used to estimate the approximate capabilities of systems.

For each of the technologies, simulations started with implementing configurations very similar to the ENMC, but with the new materials, and then investigating possible optimization approaches. The BF_3 system was optimized by increasing the volume of BF_3 gas with larger tubes and greater numbers of tubes. For the boron-lined tubes, the optimization involved increasing the surface area of the boron lining through decreasing the tube diameter and increasing the number of tubes. The LiF/ZnS material was sufficiently different from the proportional tubes that a layered design of the LiF/ZnS material and light guides was used, and the thickness and number of layers were optimized. Lithium fluoride was used since pure lithium is highly reactive with water, including moisture in the air, and is optically opaque [6].

Bounding designs were investigated for each technology that optimized the *FoM* while maintaining approximately the same footprint as the ENMC. The bounding design for the BF_3 proportional counters was 155 tubes filled with two atmospheres of BF_3 with a 5.08 cm (2 inch) diameter, which had a footprint approximately 55% larger than the ENMC. This is compared to the ENMC which has 121 tubes filled with ten atmosphere of ^3He with a 2.54 cm (1 inch) diameter [6]. A top view schematic of the optimized BF_3 is shown in Figure 2.7.

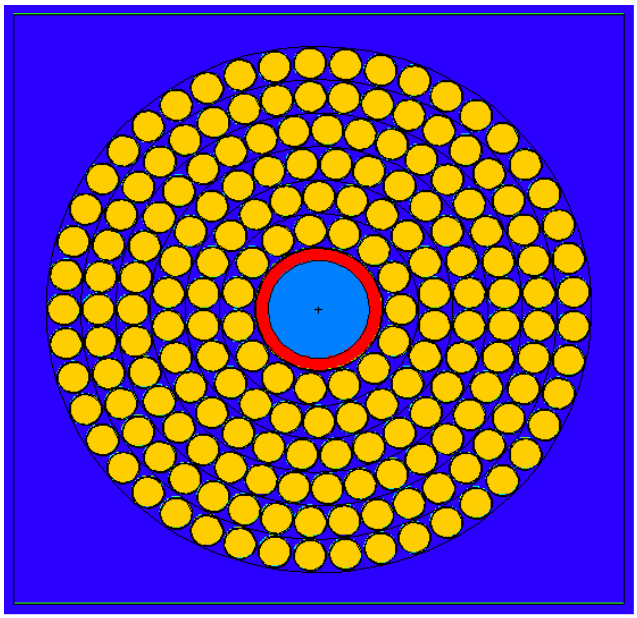

Figure 2.7 Bounding model for the BF_3 technology with 155 tubes in six rings, each tube 5.08 cm in diameter. The BF_3 system's footprint was 2.4 times larger than the ENMC, although both systems had the same height [27].

The bounding configuration for the boron-lined proportional counters was 4,725 tubes of 0.4 cm diameter, with the same footprint as the ENMC, and the boron lining thickness optimized to one micron [6]. A top view schematic of the optimized boron-lined proportional counter is shown in Figure 2.7.

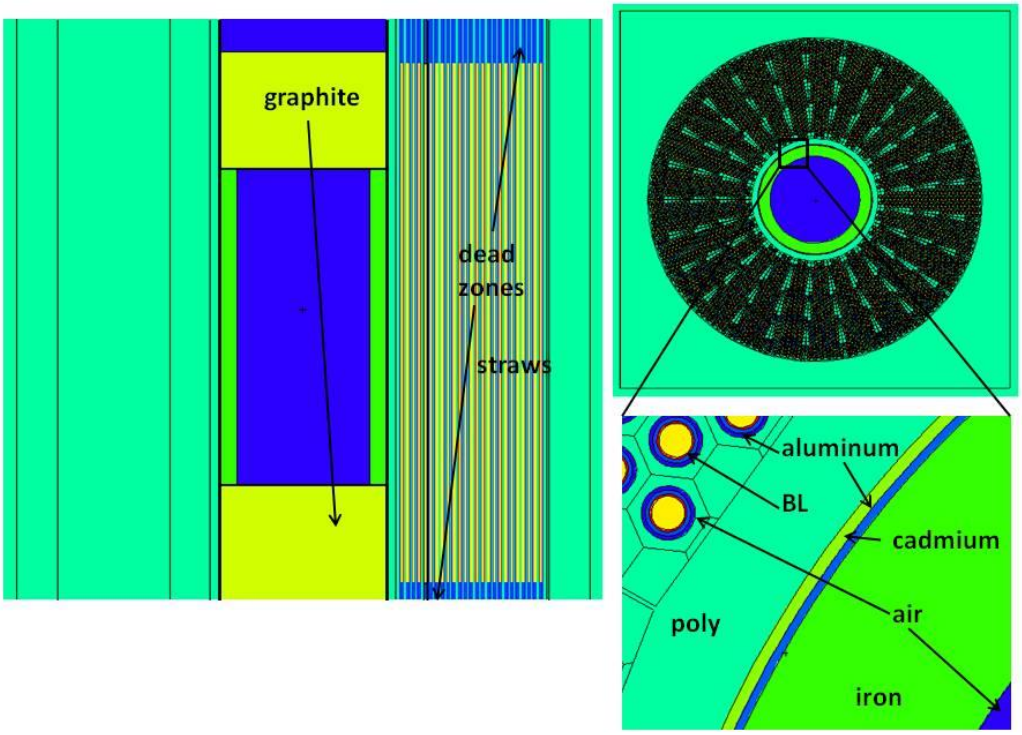

Figure 2.8 Bounding model of the boron-lined proportional counter technology with 4 mm tubes (4725 tubes) [6].

Two boron systems were modeled and validated as follows. Both systems incorporated boron-lined proportional counter tubes manufactured by General Electric (GE) Reuter-Stokes. The first of these comparisons was performed with bare tubes similar to the one depicted in Figure 2.9 which were surrounded with high density polyethylene (HDPE). The second system modeled and measured was a pre-built Neutron Detector Module (NDM) consisting of an array of 20 boron-lined proportional counter tubes embedded in a HDPE-filled panel, as shown in Figure 2.10 [22].

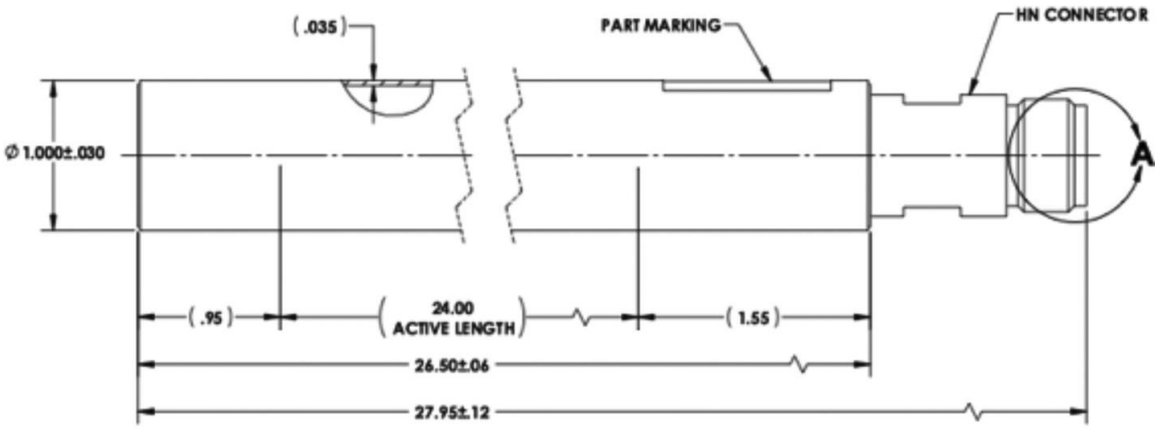

Figure 2.9 Schematic of a GE Reuter Stokes boron-lined proportional counter (units in inches) [22].

Figure 2.10 GE Reuter Stokes NDM panel containing an array of boron-lined proportional counters [22].

Simulations of pulse distributions from MCNP output, which are based on the energy deposition of the reaction products in the counting gas, were compared to experimental pulse height distributions. The correlation between simulated and experimental results was improved by accounting for the electric field and the electron avalanche within the boron-lined tubes with the Garfield program [28], and accounting for the boron-lining composition and experimental environment [22]. Experimental and simulated results agreed to better than 6% for all experiments [22].

The bounding condition for the LiF/ZnS configuration was optimized to 19 alternating layers of LiF/ZnS as the capture and scintillation material, and WSP as a light guide material. The LiF/ZnS and binder layer was 0.05 cm thick, while the WSP was optimized to 0.7 cm. The model employed a homogeneous mixture of LiF, ZnS, and a hydrogenous binder, which does not reflect the actual discreet distribution of the LiF and ZnS powders mixed with the binder. Therefore, the simulation was ended when the neutron captured in the lithium. The MCNP simulation counted neutron captures in the ^{6}Li and ignored real system inefficiencies relating to the inhomogeneous material mixture, light losses within the LiF/ZnS material, and light losses traveling from the LiF/ZnS material to the PMTs. These differences between simulated and actual measurements were compensated for with a validation correction factor (VCF) consisting of a measured result divided by the simulated result for that same system. Initially, the system used to obtain the VCF was the LiF/ZnS-based system developed by Innovative American Technologies (IAT) that was previously measured at PNNL [2]. The VCF value was 0.57 based on the IAT system (the demonstration model later built at PNNL had an estimated VCF of ~0.78), and the simulated efficiencies were multiplied by the VCF of the demonstration unit to

predict the total *FoM* of the bounded model. A top view of the full-scale simulated LiF/ZnS unit is depicted in Figure 2.11.

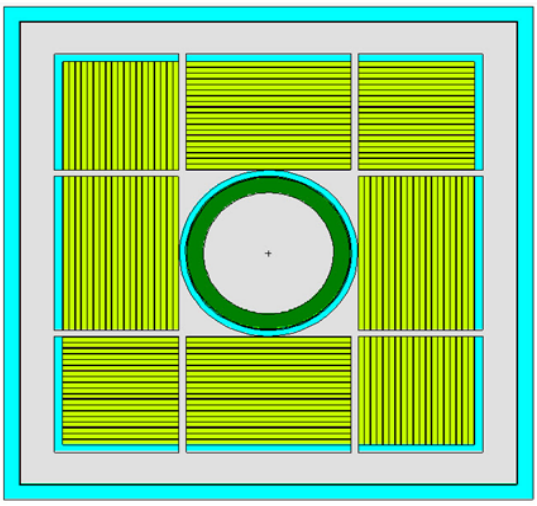

Figure 2.11 Bounding model of the LiF/ZnS alternative technology with 18 layers of LiF/ZnS material (0.05 cm) between 19 layers WSP light guides (0.7 cm).

The efficiency, die-away time, and *FoM* values of the simulated bounded alternative technologies are provided in Table 2.2.

Table 2.2 Simulated efficiencies and die-away times for the various alternatives. Note the LiF/ZnS results use the initial VCF of 0.57, which is lower than the VCF obtained from the demonstration system [6].

System Metrics	^{3}He	BF_3	Boron-Lined	LiF/ZnS
Count Efficiency (%)	66	57	39	44
Die-away time (μs)	23	44	37	10
***FoM* (ε^2/τ)**	189	74	41	194

*Uncertainty values were not reported for the ε or τ in the reference literature and therefore are not presented in this paper.

The high *FoM* of the LiF/ZnS technology prompted the development of a LiNMC system rather than a BF_3 or boron-lined neutron multiplicity counter.

2.5 LiF/ZnS Demonstration System development

Extensive modeling, simulating, and experimentation was performed in the development of the LiF/ZnS demonstration unit, which is more fully detailed in the reports for the 'Neutron Detection without Helium-3 Project'. The four detector stacks of the demonstration systems were each 71.12 cm tall by 15.24 cm wide by approximately 5.08 cm thick. The detector stack height was identical to the active detection height of the ENMC. The thickness was chosen as the largest area that would be fully viewable from a 5.08 cm diameter PMT, which was achieved by using five layers of LiF/ZnS sandwiched between six layers of WSP. The overall detector stack thickness depended on the thickness of the WSP, which varied from 3.5 cm (0.5 cm light guides) to 6.8 cm (0.9 cm light guides) [6].

The 500 μm sheets of LiF/ZnS(Ag) were composed of a 1:2 ratio of LiF:ZnS particles suspended in an organic binder with two 250 μm thick backings for structural support, resulting in each being 1,000 μm, or 1 mm, thick. These LiF/ZnS sheets were purchased from Eljen Technology. The lithium was enriched to 96% lithium-6. The LiF and ZnS grains were typically less than 10 μm in diameter as seen in Figure 2.12 [6].

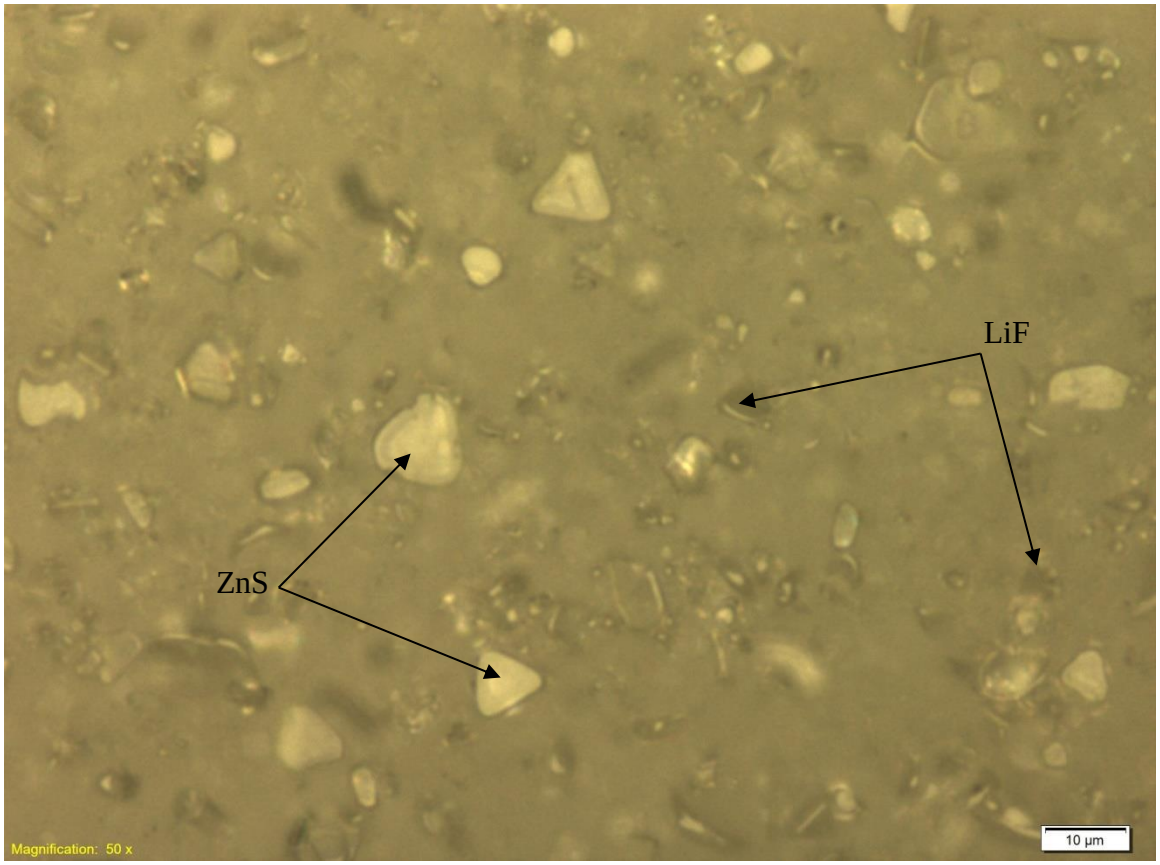

Figure 2.12 Magnified (50x) view of a section of a LiF/ZnS sheet showing the individual LiF and ZnS pieces suspended in the binder.

Two different light guide materials were tested: Poly-methyl methacrylate (PMMA) and wavelength shifting plastic (WSP) made from polyvinyl-toluene (PVT) with a wavelength shifting dye, as seen in Figure 2.13. The WSP is mildly sensitive to gamma rays as a scintillator, while the PMMA does not scintillate in response to gamma rays. A stack of alternating layers of LiF/ZnS with WSP and PMMA were constructed with a PMT attached to the end of the system. The WSP and PMMA light guides both transmitted light from the LiF/ZnS material to the PMTs on the ends, but differed in terms of light origin. The PMMA did not significantly alter the trajectory of the light emitted from the LiF/ZnS material, whereas the WSP isotropically reemitted light [6].

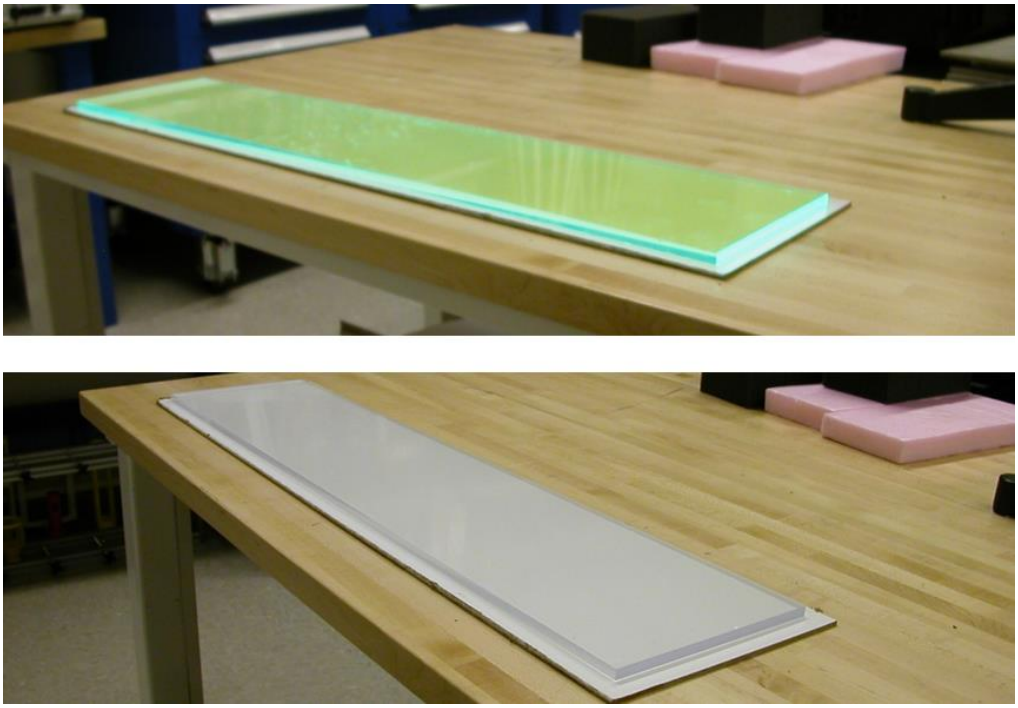

Figure 2.13 The WSP (top) and PMMA (bottom) sheets used for the bench-top test.

Results from measuring the neutron detection efficiency of the PMMA and WSP materials with one PMT can be seen in Table 2.3.

Table 2.3. Results from the ^{252}Cf measurements with 0.7 cm thick PMMA and WSP with a single PMT coupled directly to the end of the detector [6].

Measurement Configuration	Absolute Neutron Detection Efficiency
PMMA ^{252}Cf	0.016 ± 0.002
WSP ^{252}Cf	0.040 ± 0.006

The WSP transmitted more ZnS-generated light to the PMTs when 0.7 cm thick sheets of both materials were tested [6].

A second set of measurements was performed with the same detector configuration and PMTs on both ends of the detector system, as seen in Figure 2.14. Both PMTs were

voltage and gain matched to provide comparable performance and were connected to separate input channels of a Pixie-500 data acquisition system, which utilizes a 14 bit, 400 MHz ADC to digitize signals. The Pixie-500 was set to only record signals if both PMTs were triggered within 13.3 ns of each other, which was considered to be a coincidence most likely produced from a neutron capture. Coincidence measurements slightly decreased the neutron detection efficiency, but resulted in a greater suppression of the gamma-ray response, since gamma rays tend to produce less scintillation light than is emitted from neutron capture in ^{6}LiF/ZnS. The coincidence requirement reduced neutron detection efficiency by ~15% for the WSP and ~72% for the PMMA compared to the single PMT results above [6].

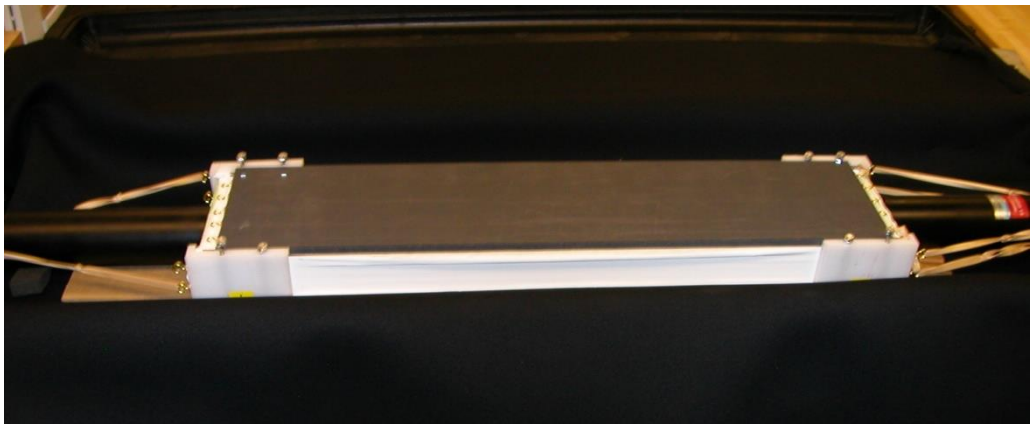

Figure 2.14 Bench-top test unit assembled on a support structure with two PMTs and no tapered light guides.

Results from measuring the neutron detection efficiency of the PMMA and WSP materials with PMTs in coincidence mode can be seen in Table 2.4.

Table 2.4 PMMA and WSP coincident PMT measurement results with a ^{252}Cf source centered on the detector. (2) Refers to a coincident PMT configuration [6].

Measurement Configuration	Absolute Neutron Detection Efficiency
PMMA ^{252}Cf (2)	0.0044 ± 0.0006
WSP ^{252}Cf (2)	0.034 ± 0.005

"The gamma-ray discrimination capability was determined by measuring two different gamma-ray fluxes on the detector for various configurations and data collection modes. The results are shown in Table 2.5. The PMMA had a better gamma-ray discrimination capability than the WSP, but had lower neutron detection efficiency, as seen above. The PMMA configuration would probably be useful only in high gamma-ray and high neutron flux applications." [6]

Table 2.5 Measurement summary with the 0.7 cm thick PMMA and 0.7 cm thick WSP. (H) indicates an incident gamma-ray rate of $5.9x10^7$ γ/s and (L) indicates an incident gamma-ray rate of 8.5×10^6 γ/s. In all cases the source was centered above the detector [6].

Measurement Configuration	Gamma-Ray Discrimination
PMMA ^{137}Cs (H)	$1.1\times10^{-5} \pm 1\times10^{-7}$
PMMA ^{137}Cs (L)	$3.7\times10^{-6} \pm 9\times10^{-8}$
WSP ^{137}Cs (H)	$1.8\times10^{-4} \pm 9\times10^{-7}$
WSP ^{137}Cs (L)	$4.8\times10^{-5} \pm 6\times10^{-7}$

The WSP was selected for additional optimization testing. Since increasing WSP thickness would increases ε by moderating neutrons, but decreases ε by moving the LiF/ZnS away from the neutron source, different thicknesses (0.5 cm, 0.7 cm, and 0.9 cm)

were tested to optimize the FoM. 0.7 cm thick WSP resulted in optimal ε, and was thus used for future designs. The results from experiments with the three different thicknesses of WSP can be seen in Table 2.6. The 0.9 cm thick WSP resulted in a 15% or greater neutron detection efficiency than the thinner sheets. Simulations indicated that 5% of the increase was due to the additional moderation, and 10% was due to improved light collection. The increased thickness provided increased efficiency, but also increased the die-away time. Simulations indicated that the die-away time of a full-scale system would increase by 18% from the 0.7 cm thickness to the 0.9 cm thickness. Using 0.9 cm thick instead of 0.7 cm thick WSP, the *FoM* would increase by approximately 5% overall. Simulations indicated that this small increase in *FoM* would drop off rapidly to a decrease in *FoM* for systems much larger than this bench-scale experiment; therefore, 0.7 cm thick WSP light guides were used for the demonstration unit [23].

Table 2.6 Measurement summary for a single PMT coupled directly to the detector with three different WSP thicknesses tested. The ^{252}Cf measurements were collected with the source centered over the detector [6].

Measurement Configuration	**Absolute Neutron Detection Efficiency**
WSP 0.5 cm ^{252}Cf	0.032 ± 0.005
WSP 0.7 cm ^{252}Cf	0.040 ± 0.006
WSP 0.9 cm ^{252}Cf	0.045 ± 0.007

Tapered light guides were added to the ends of detector stacks made of 0.7 cm thick WSP, 20 cm of length (10 cm from each light guide) to the system, as seen in Figure 2.15. The neutron detection efficiency for a single PMT was improved by 38% and the

coincidence detection efficiency was improved by 17% with light guides compared to measurements without light guides. Based on these measurement results, tapered light guides were included in the demonstrator system design [6].

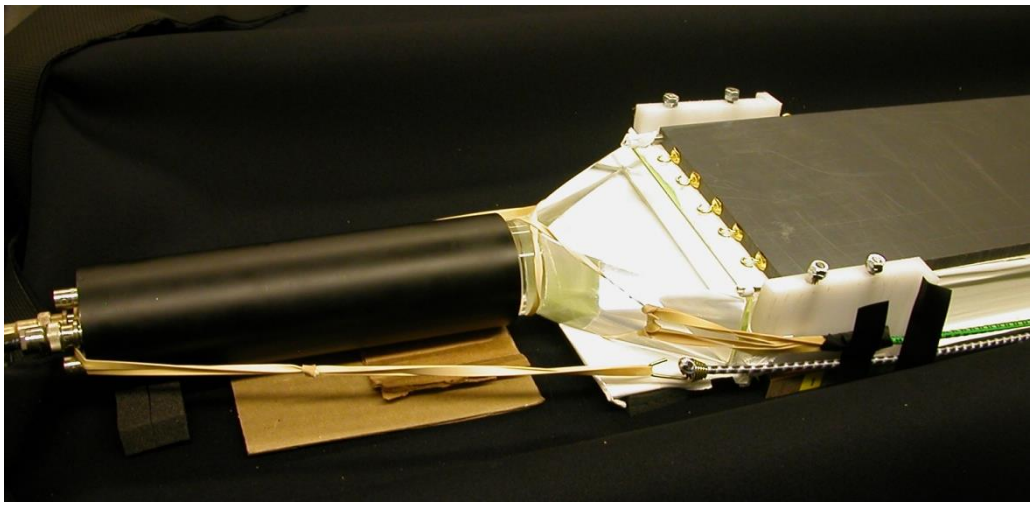

Figure 2.15 Test unit with tapered light guide attached.

The demonstration unit was designed to be a four detector stack system, each stack having the same active area as the bench-scale unit; that is, 71.12 cm active height by 15.24 cm active width. Each stack was filled with five layers of LiF/ZnS material sandwiched between six layers of 0.7 cm thick WSP. Non-scintillating PMMA light guides were glued onto the ends of the panels. The WSP and light guide stacks were then wrapped in Teflon tape followed by aluminum foil to mitigate light loss. The stacks were placed in a light-tight aluminum housing with external dimensions of 8.9 cm thick by 20.34 cm wide by 153.7 cm tall. Aluminum was chosen as a housing material because of its low neutron removal cross-section. Prior to assembly, PMT performance was measured with a NaI(Tl) crystal, and similar performing PMTs were paired together for each stack and attached to the ends of the light guides with a thin layer of optical grease between the PMT and the

light guide. A stand made from low density cellulose fiber and aluminum was centered between the panels to act as a source stand [6].

Initial simulations of this demonstration unit with a bare ^{252}Cf source gave an estimated $\varepsilon = 7.50\% \pm 0.08$. Measurements of this demonstration unit gave a $\varepsilon = 6.35\% \pm 0.95$, which led to a VCF of ~$0.85\% \pm 0.13$ [6].

3 Geometric Effects on Light Transport in Multiplicity Counter Design

Several aspects of geometry and optical materials were investigated to maximize the probability of detecting neutrons that capture in the ^{6}Li. Neutron captures in ^{6}Li produce alpha and triton particles, which generate scintillation light in the ZnS. Some scintillation light is lost in the LiF/ZnS mixture, at reemission in the WSP, at each scatter point, and at each optical interface. This reduces the probability that neutron-induced signals will surpass detection thresholds and be distinguishable from electronic noise.

This chapter is intended to summarize the key performance aspects of light transport and optical signal acquisition for full-scale detector design. The design aspects investigated were stack width, stack length, use of light guides, number of PMTs, PMT size and shape, overwrap material, and reducing WSP thickness on the sides of the stack. Results are given for simulated and experimental results as applicable.

3.1 Stack Width Comparison

Although previous detector stack measurements were conducted with 15.24 cm wide stacks, the LiNMC implemented larger, 20.32 cm wide stacks to match the ENMC's sample chamber size. MCNP simulations indicated that these larger stacks would also increase the LiNMC's ε. Therefore, measurements were conducted to compare the performance of 20.32 cm stacks to the performance of a 15.24 cm wide stack. At this time, Ni-quenched LiF/ZnS was being considered for implementation since it has a faster scintillation decay time than non-quenched (regular) LiF/ZnS; therefore, one 20.32 cm stack was constructed with Ni-quenched LiF/ZnS and another stack was constructed with

regular LiF/ZnS. The performance of all three stacks was compared using the same measurement methods, equipment, and electronic settings.

Total count rates were measured for each stack, which consisted of LiF/ZnS with WSP, light guides, and Teflon overwrap. Two PMTs were gain matched and fixed in place in a light-tight aluminum case. Each stack was placed in the middle of the aluminum case with the PMTs fixed 0.635 cm from the ends of the stack. The 0.635 cm air gaps were intentionally left between the PMTs and the light guides to facilitate quick swapping of the panels and improve repeatability of measurements by avoiding systematic uncertainties arising from non-uniform optical coupling between measurements. Although significant light leakage may have occurred between the stacks and PMTs, these measurements were intended to ascertain relative performance between stacks. Data sets from the PMTs were acquired with a Pixie-4 data acquisition system with settings that remained the same for all measurements. A ^{252}Cf neutron source was fixed to the top of the aluminum case, the aluminum case was fixed to a 2.54 cm thick HDPE sheet, and the HDPE sheet was fixed to a high density resin lab table, as depicted in Figure 3.1.

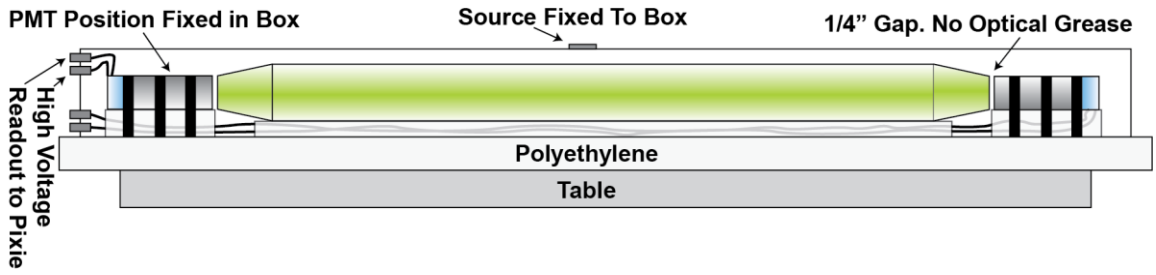

Figure 3.1 Schematic of the single panel experiments. The HDPE was intended to mitigate the effects of the unknown composition of the table and make measurements easier to compare to simulations.

Data sets were collected in one-minute runs at Pixie-4 thresholds of 5, 13, 21, and 29. After each run, the stack was rotated 180 degrees horizontally or vertically to minimize the effects of any asymmetries during construction and provide average performance over several measurements. These six sets of measurements were conducted for all four thresholds and all three stacks. The 15.24 cm wide stack was shorter than the 20.32 cm wide stacks; therefore, the PMTs were moved closer to the 15.24 cm wide stack to maintain the 0.635 cm air gaps.

Because of the high light losses from the 0.635 cm air gaps, results are reported in relative count rates rather than absolute count rates. The 15.24 cm wide stack, which has been tested in a full-scale demonstration unit in the past, was set to be the standard to compare the Ni-quenched and the regular 20.32 cm wide stacks against, since the 15.24 cm wide stack was already well understood. The results of these studies for six runs at four different Pixie-4 are shown in Figure 3.2.

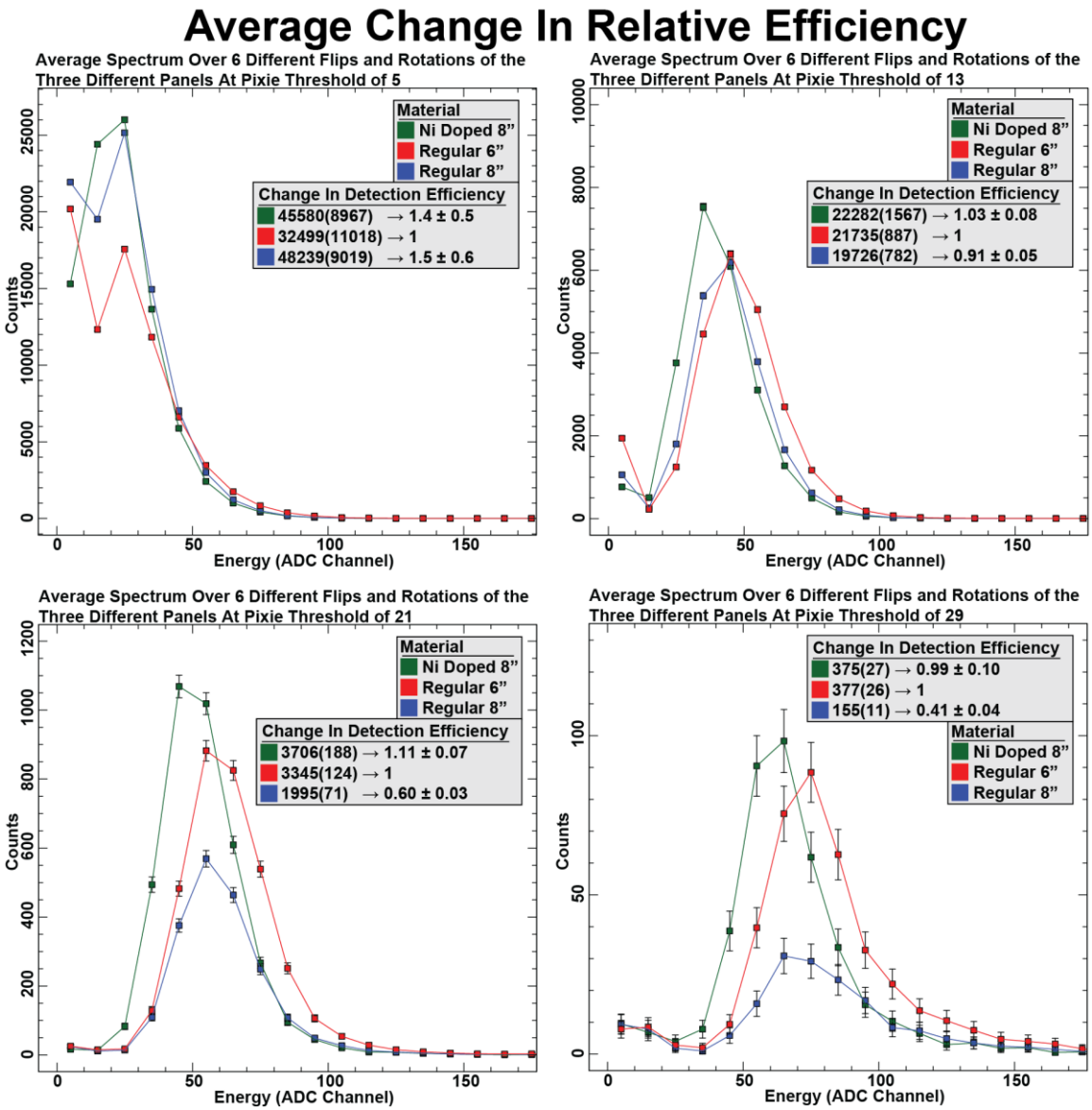

Figure 3.2 Relative efficiency of full-scale LiF/ZnS detector panels.

In all cases, except for very low thresholds, the 15.24 cm wide stack displayed superior ε to the regular 20.32 cm wide stack, as seen in Figure 3.2. The 20.32 cm wide Ni-quenched stack had an energy spectrum shift to lower energies across all thresholds, disregarding when the threshold = 5, which is consistent with the previous finding that the integrated energy of a given pulse for the Ni-quenched material was smaller than the

integrated energy of the pulses from the regular material. Key data from Figure 3.2 is presented in Table 3.1.

Table 3.1 Relative ε of Ni-quenched and regular 20.32 cm stacks averaged over both runs and compared to the regular 15.24 cm stack ε.

Threshold	Ni-Quenched Relative Efficiency	Regular Relative Efficiency	Ni-Quenched Relative / Regular Relative Efficiency
5	1.4 ± 0.5	1.5 ± 0.6	0.9 ± 0.8
13	1.03 ± 0.08	0.91 ± 0.05	1.13 ± 0.09
21	1.11 ± 0.07	0.60 ± 0.03	1.85 ± 0.08
29	1.0 ± 0.1	0.41 ± 0.04	2.4 ± 0.1

As thresholds increased, a systematic decrease in the count rate from the 20.32 cm wide stacks relative to the 15.24 cm wide stack was seen. This was unexpected, given that MCNP simulations indicated there would be a 33% increase in neutron capture in ^{6}Li under these experimental conditions.

A light ray trace analysis was performed by Bruce Bernacki to compare the light transport properties of the 15.24 cm wide stack against the 20.32 cm wide stacks. The light ray trace code conducted simulations and reported results, but did not report uncertainties associated with the results; therefore, no uncertainties are reported in this paper for light ray trace simulation results. Both stacks were simulated with light guides and Teflon overwrap, as used in the experiments. Since the presence of nickel doping in the LiF/ZnS does not significantly change any optical properties, only the geometric between the

15.24 cm wide stack and the 20.32 cm wide stacks were simulated, as seen in Figure 3.3 and Figure 3.4.

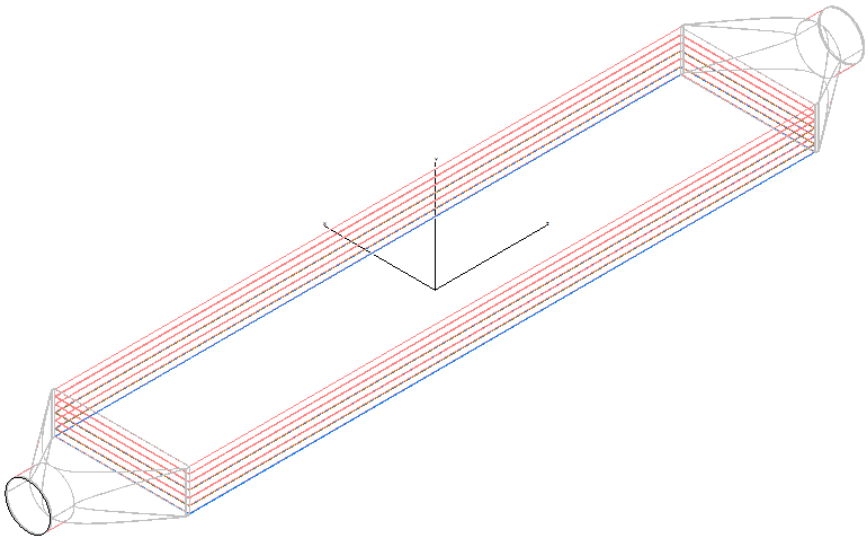

Figure 3.3 Model of 15.24 cm wide detector stack used for light ray trace simulations.

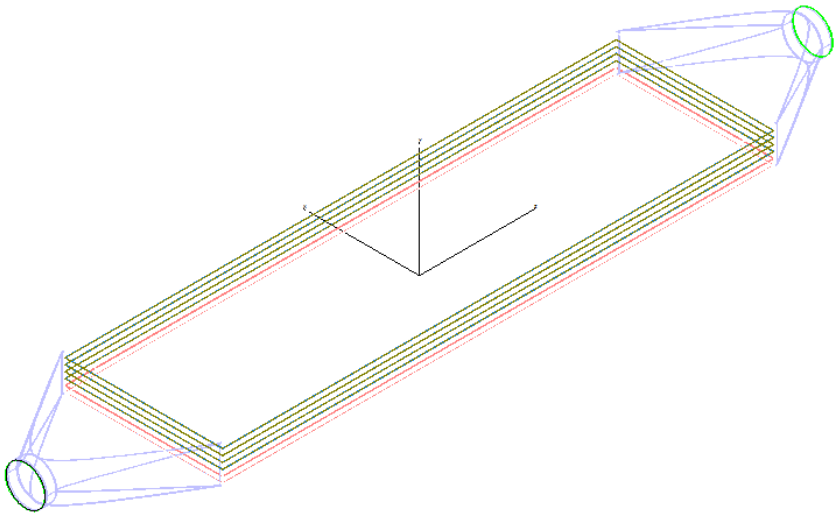

Figure 3.4 Model of the 20.32 cm wide detector stack used for light ray trace simulations.

For these simulations, the LiF/ZnS was treated as styrene and the WSP was treated as a polycarbonate polymer with fluorescent properties based on Invitrogen Alexa 430, which is similar to the Eljen EJ-280 WSP used in the physical construction. 40% more photons were generated in

the 20.32 cm wide stack simulations than in the 15.24 cm wide stack simulations, resulting in 41% more photons reaching the ends of the stack. Because the 20.32 cm wide stack produced more photons, and had more photons exiting than the 15.24 cm wide stack, the light guides were added to the models to determine the mechanics of light loss seen in the experiments.

Simulations that included the light guides with the stack showed that the 20.32 cm wide stack directed significantly more light back through the light guides than the 15.24 cm wide stack. The 20.32 cm wide stacks utilized longer and wider light guides than the 15.24 cm stacks, resulting in more light loss from scattering and more light being scattered away from the PMTs than for the 15.24 cm stacks. The 20.32 cm wide stack saw a 30% ± 1 reduction in the chances of light reaching the PMTs compared to the 15.24 cm wide stack.

Light rays that reached the PMTs were recorded in terms of the scattering modes they took to arrive at the PMTs. These light rays were recorded as being specular rays (rays that reflect according to Snell's Law and the Fresnel Equations), single scatter rays (rays that scatter from the overwrap just once before exiting), and multiple scattered rays (rays that scatter multiple times from the overwrap before exiting). Because some light was absorbed at each interface, increasing the number of multiple scatters decreased the total light that will reach the PMTs. Light rays that reached PMTs from specular and single scatters lost little light, producing more clearly countable signals from the PMTs. Simulations indicated that the 20.32 cm wide stack displayed a significant shift from specular and single scatters to multiple scatters compared to the 15.24 cm wide stack, as seen in Figure 3.5 and Figure 3.6.

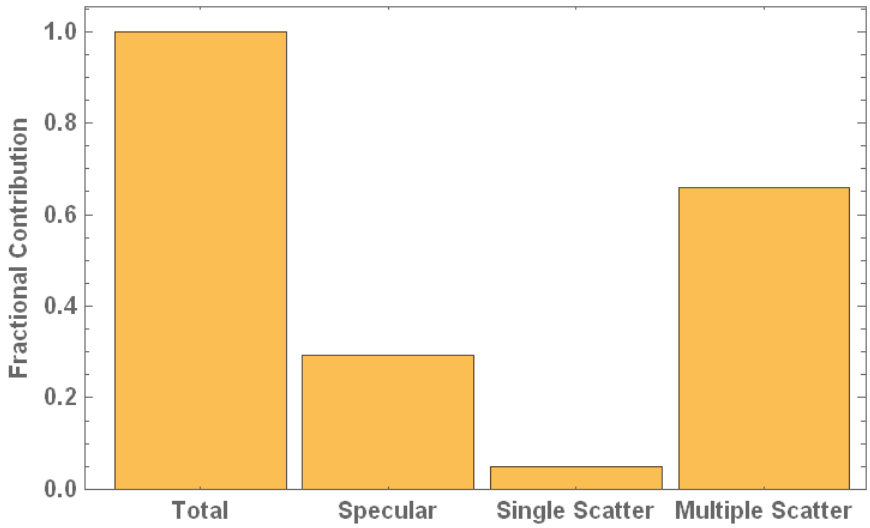

Figure 3.5 Simulation results of modes of light arriving at the PMTs from the 15.24 cm wide stack.

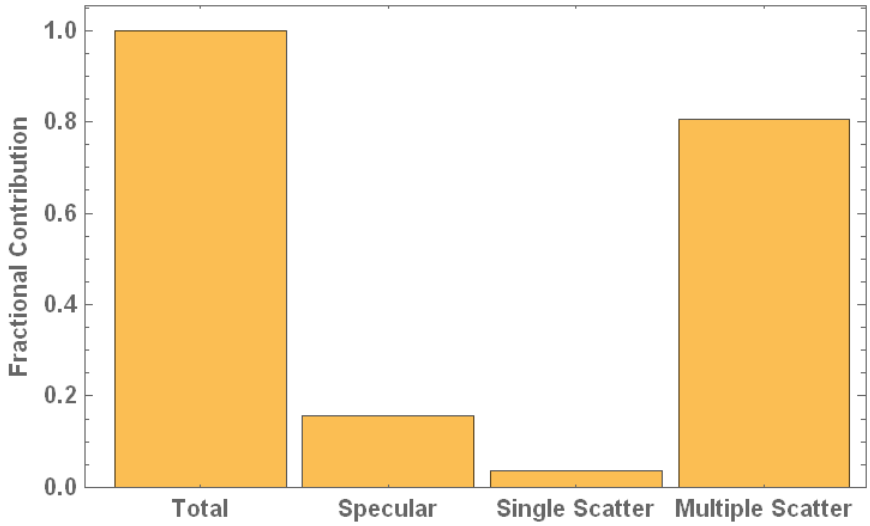

Figure 3.6 Simulation results of modes of light arriving at the PMTs from the 20.32 cm wide stack.

These simulations indicate that less light reached the PMTs of the 20.32 cm wide than the 15.24 cm stack due to increased losses from multiple scatterings and increased amounts of light being backscattered away from the PMTs.

3.2 Multiple PMT Comparison

Replacing the single PMT on each end of the stacks with multiple PMTs was considered as a means of increasing the light collection from each neutron capture event, and therefore increasing ε. Simulations were performed to estimate the increased light flux that would be detected from each event, and measurements were performed to ascertain the performance increase from measuring more light from each event.

It is important to note that all neutron capture events that result in scintillation either result in sufficient scintillation light to be detected, or scintillation light that is not sufficient to be detected. Light flux is related to pulses from particles, but these quantities do not necessarily have a linear relationship. For example, all pulses can be divided into two categories – pulses sufficient to be counted and pulses that are insufficient to be counted. A given increase in light from each pulse will have no counting effect on pulses that are already bright enough to be counted, nor will it have any counting effect on pulses that remain insufficient to be counted even with the increased in flux. The only effect that increasing the light flux from pulses has on counting pulses is from pulses that would otherwise be insufficient to be counted, but become sufficient to be counted from the increased light flux. Therefore, neutron detection measurements are required in addition to light simulations to determine performance changes from using multiple PMTs.

Detector models from Section 3.1 were modified to replace the single PMT on the end of each stack with two PMTs. Light ray trace simulations of the 20.32 cm wide stack with two PMTs (dual PMTs) on both ends were performed by Bruce Bernacki. Two of the simulations removed the light guides and placed the dual PMTs directly on the ends of the stack. Both simulations used a Teflon overwrap. The difference between the two models

was that one was bare on the ends, whereas the other included Teflon on the ends, except over the PMTs; both are depicted in Figure 3.7. The third model retained a light guide that had been modified to facilitate two PMTs instead of one, and maintained a Teflon overwrap over the entire stack, except where the PMTs contacted the stack, as depicted in Figure 3.8.

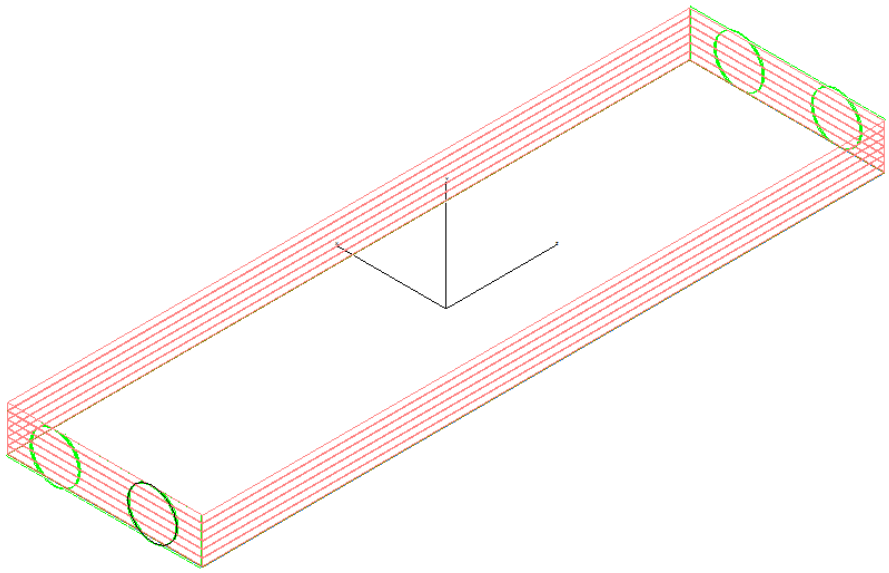

Figure 3.7 Simulation model of 20.32 cm wide detector stack with dual PMTs.

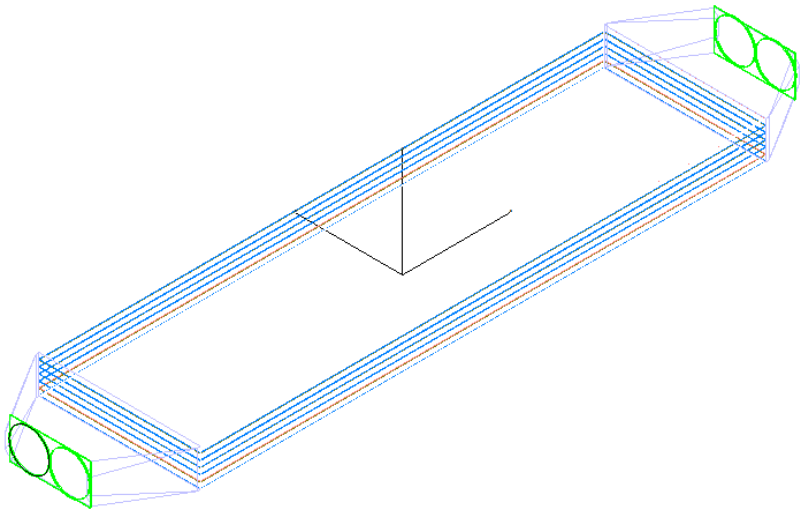

Figure 3.8 Simulation model of 20.32 cm wide detector stack with modified fishtail light guide and dual PMTs.

Simulations of all three stacks produced equal amounts of scintillation light and equal light fluxes exiting the ends of the stack. The light guide model directed some light rays to the PMTs while also giving the light rays a more tortuous path to the PMTs. Simulation results indicated that the 20.32 cm wide dual PMT system without light guides would experience a 28% increase in light flux compared to the 15.24 cm wide single PMT system with a light guide. The 20.32 cm wide dual PMT system with light guides was only predicted to experience a 19% increase in light flux compared to the 15.24 cm wide system with light guides, as seen in Table 3.2.

Table 3.2 Simulation results of light flux entering PMTs 20.32 cm wide dual PMT systems.

Configuration	Average Light Flux into PMTs (W)	Light Flux into PMTs relative to Original
15.24 cm, with light guide and single PMTs (Original)	0.0070351	1.0
20.32 cm, with light guide and single PMTs	0.0040782	0.58
20.32 cm, dual PMTs, no Light Guide	0.0089915	1.28
20.32 cm, dual PMTs, no Light Guide, no end wrap	0.0081146	1.15
20.32 cm, dual PMTs with Light Guide	0.0083879	1.19

These simulation results indicate that adding a second PMT to each end of the 20.32 cm wide stack would significantly improve light collection. As with previous simulations and measurements, light flux entering the PMTs was reduced by using light guides and also by removing the overwrap from the ends. Simulation results were verified by measuring count rates from a physical system very similar to the modeled system. Total count rates for the 20.32 cm wide stack were determined by placing the 20.32 cm wide stack, with Teflon overwrap, in the detector assembly. Two PMTs were fixed to each end of the stack and gain matched with a ^{252}Cf source. The experimental set up with the 15.24 cm wide stack and the 20.32 cm wide stack is depicted in Figure 3.9.

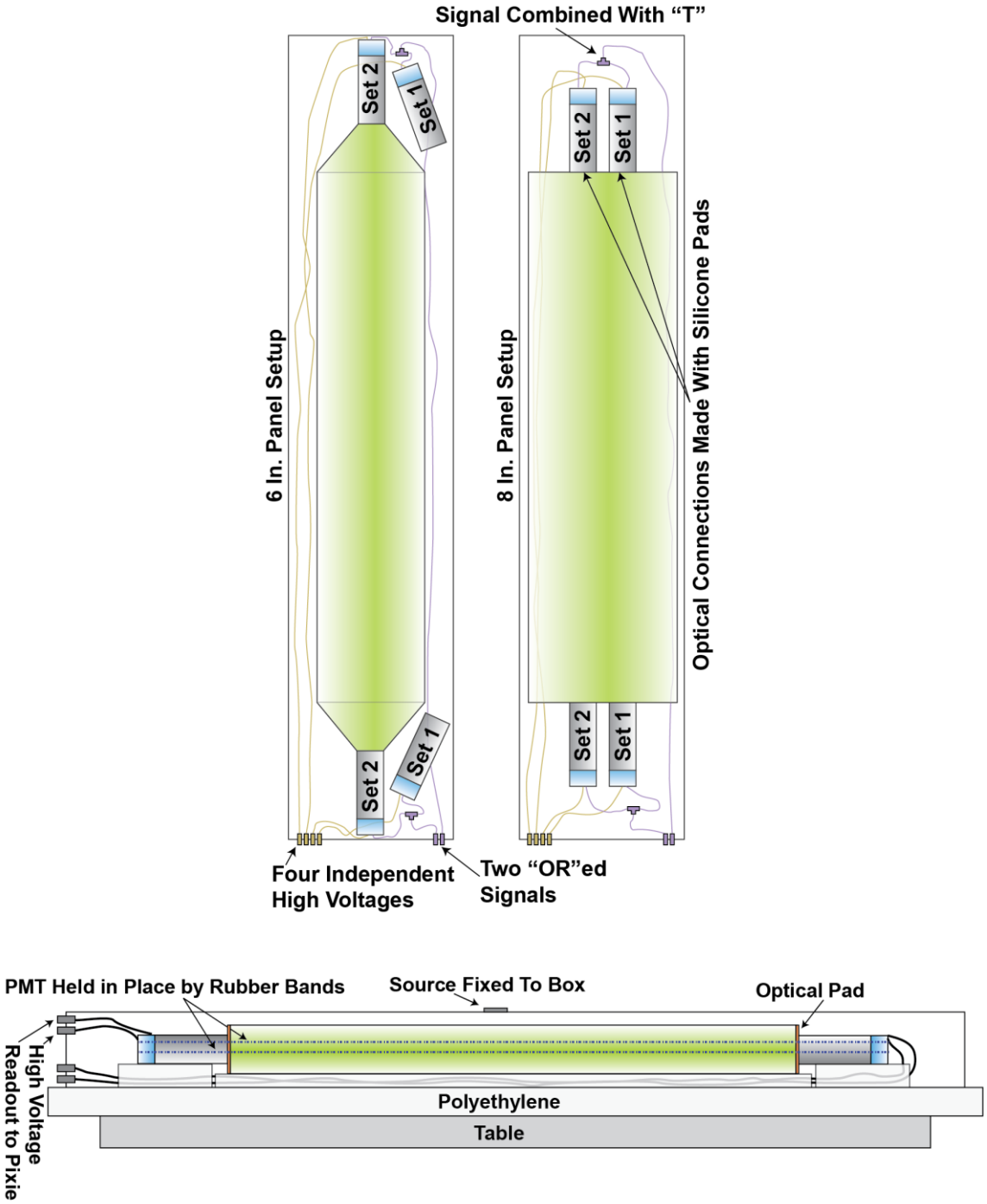

Figure 3.9 Experimental set up to measure the effects of multiple PMTs on the same detector stack. (Top) Top view of the experimental set up with the 15.24 cm wide stack and the 20.32 cm wide stack. (Bottom) Side view of the experimental set up with the 20.32 cm wide stack.

Count rate measurements were taken with each PMT set separately and then with both sets together and a ^{252}Cf source present. After the dual PMT measurements with the 20.32 cm wide stack were completed, the 20.32 cm wide stack was replaced with the 15.24 cm wide stack and measurements were taken with each PMT set.

In all cases, a single PMT set on the 20.32 cm wide stack displayed increased counts compared to one PMT set on the 15.24 cm wide stack. Two PMT sets on the 20.32 cm wide stack displayed a further increase in count rate compared to the 15.24 cm wide stack with a single PMT set, as seen in Figure 3.10.

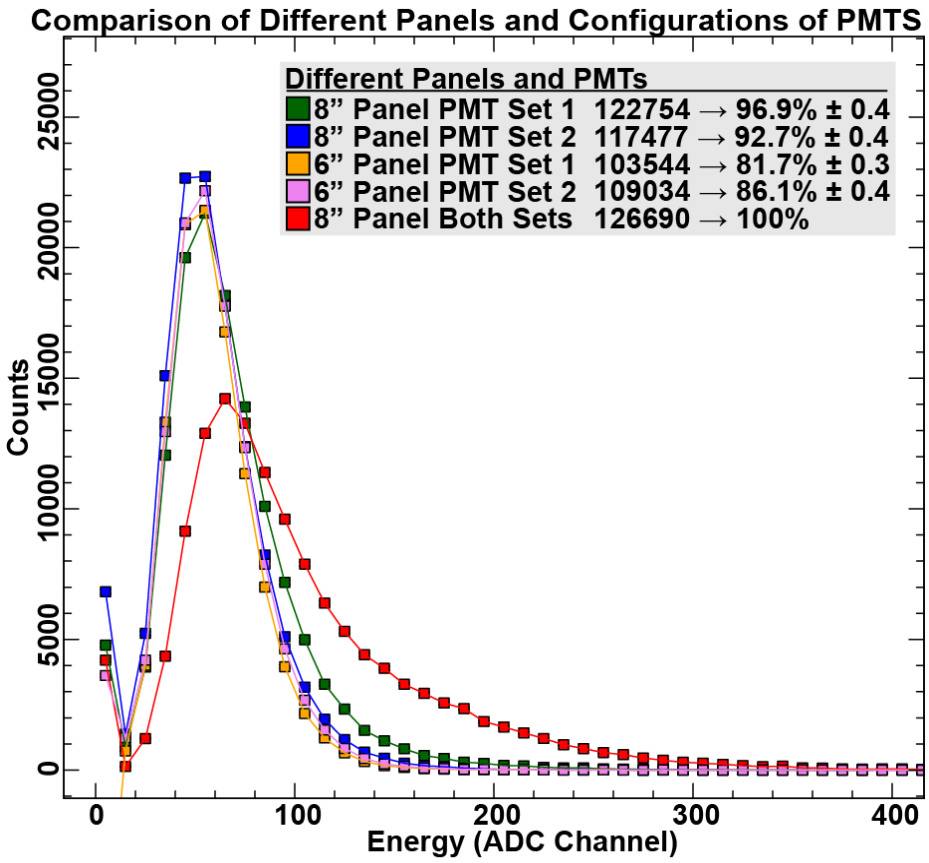

Figure 3.10 Counts vs Energy and total counts from the 15.24 cm wide stack and the 20.32 cm wide stack with data sets collected from both PMT sets.

From the data sets presented in Figure 3.10, the 20.32 cm wide stack with one PMT set displayed 13% ± 8 increased counts compared to the 15.24 cm wide stack with one PMT set. The 20.32 cm wide stack with dual PMTs displayed a 19% ± 8 increase in count compared to the 15.24 cm wide stack with one PMT set.

Results from these experiments cannot be directly quantitatively compared to simulation results, as the simulation results only counted total light flux and the measurements counted total pulses. There is no reason to assume that a 28% increase in light flux from each pulse will convert a number of uncounted pulses into counted pulses that exactly equal 28% of the counted pulses before the increase in light flux.

3.3 Enhanced Spectral Reflector

Because light is lost at each scatter event, simulations and measurements were performed to determine whether the average number of scatter events for photons to reach the PMTs could be reduced by replacing the Teflon overwrap, which is a diffuse reflector, with a specular reflector. Enhanced Spectral Reflector (ESR) was selected to compare to Teflon based on ESR's high specular reflectivity, availability, and workability.

Light ray trace simulations were performed comparing a 20.32 cm wide stack with Teflon overwrap to an identical stack with ESR. Teflon, which was used in previous measurements and simulations, has a diffuse reflectivity coefficient close to 1, depending on the thickness of the Teflon wrapping [29]. ESR is a specular reflector with a reflectivity of 0.985 across the visible light spectrum, which was developed by 3M [30]. ESR looks, feels, and behaves very similarly to aluminized Mylar. Without exact reflectivity information available for various frequencies of light and angles of incidence, ESR was assumed to have a reflectivity coefficient of 0.98 across all frequencies and angles.

ESR was modeled on a 20.32 cm wide stack with a single PMT set and light guides, as depicted previously in Figure 3.4, and on a 20.32 cm wide stack with dual PMTs, as depicted previously in Figure 3.7. The only changes to the models were to replace the Teflon overwrap with ESR overwrap.

Simulation results of modes of light reaching the PMTs indicated that the ESR overwrapped models compared to the Teflon overwrapped models displayed a significant increase in the proportion of specular reflected light while decreasing the single scatter light and the multiple scatter light. Simulation results of light reaching PMTs are displayed in Figure 3.11, Figure 3.12, Figure 3.13, and Figure 3.14. The results of the 15.24 cm wide stack are included for comparison purposes.

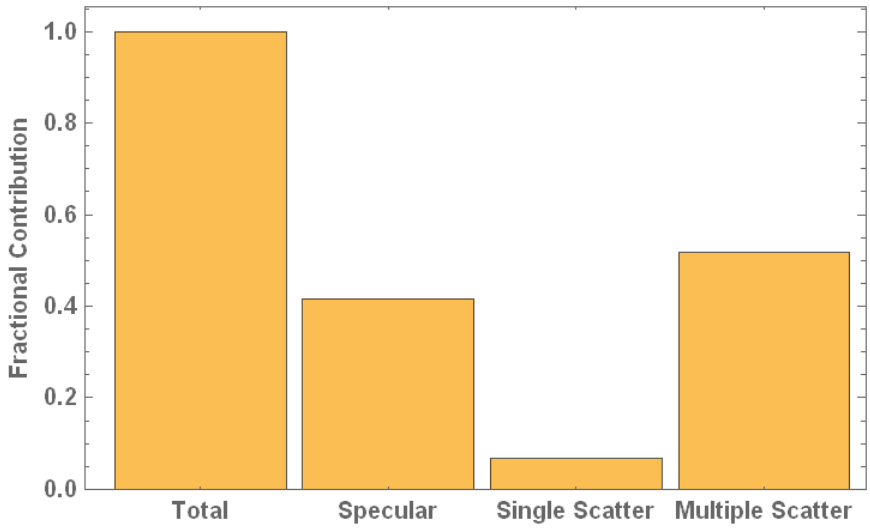

Figure 3.11 Modes of light arriving at the single PMTs from the 15.24 cm wide stack with a Teflon overwrap.

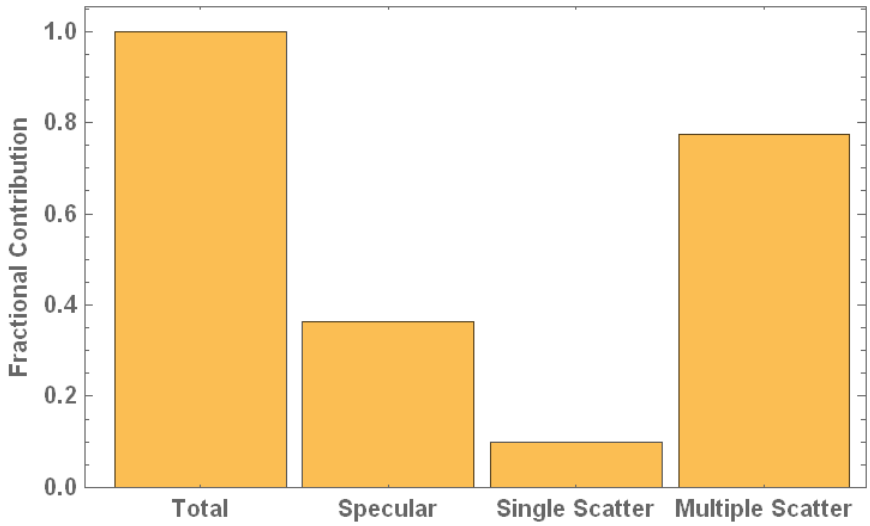

Figure 3.12 Modes of light arriving at the PMTs from the 20.32 cm wide stack with a Teflon overwrap.

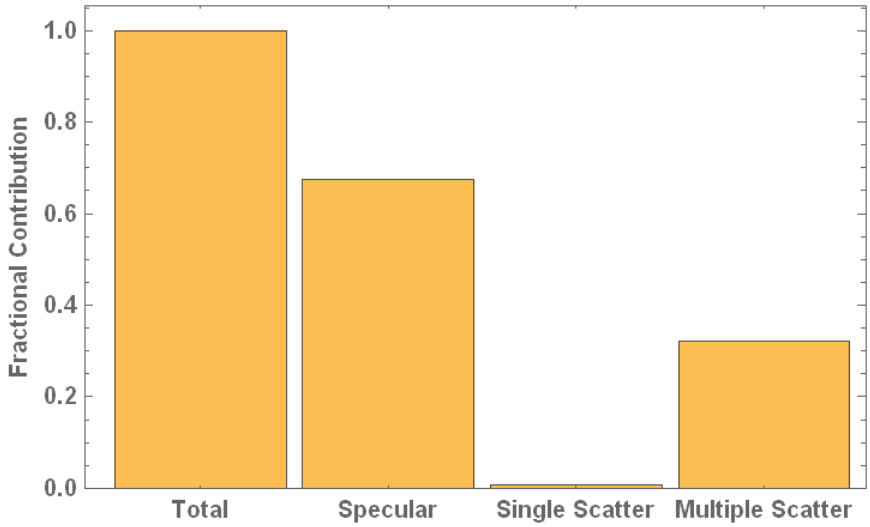

Figure 3.13 Modes of light arriving at the single PMTs from the 20.32 cm wide stack with an ESR overwrap.

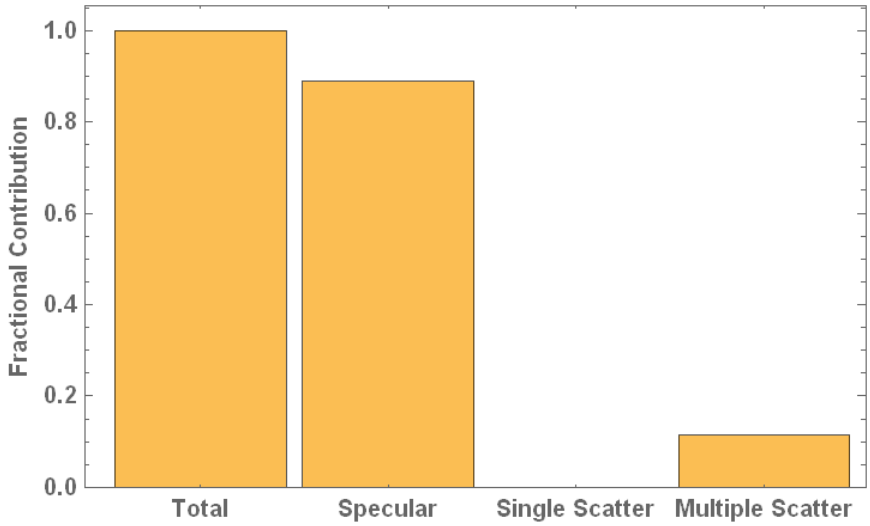

Figure 3.14 Modes of light arriving at the dual PMTs from the 20.32 cm wide stack with ESR overwrap.

A fraction of light is lost with every scatter event; therefore, reducing the proportion of single scatter and multiple scatter events for light modes entering the PMTs minimizes light loss within stacks. Simulations with ESR had reduced rates of single scatter and multiple scatter events compared to the Teflon overwrap simulations. In all cases, simulations with an ESR overwrap had increased light flux arriving at the PMTs compared to comparable models with a Teflon overwrap. Results from these simulations can be seen in Table 3.3.

Table 3.3 Light flux arriving at PMTs from ESR and Teflon overwrapped stacks.

Configuration	Average Light Flux into PMTs (W)	Light Flux into PMTs relative to Original
15.24 cm, with light guide, single PMTs and Teflon (Original)	0.0070351	1.0
20.32 cm, with light guide, single PMTs and Teflon	0.0040782	0.58
20.32 cm, Dual PMTs no Light Guide and Teflon	0.0089915	1.28
20.32 cm, with light guide, single PMTs and ESR	0.0062503	0.89
20.32 cm, Dual PMTs no Light Guide and ESR	0.0130189	1.85

Simulation results indicated that an ESR overwrap would increase light flux entering the PMTs of a single or dual PMT detector compared to a Teflon overwrap.

Experiments were performed to measure the effect of an ESR overwrap against a Teflon overwrap. A Ni-quenched 20.32 cm wide stack was prepared with a Teflon overwrap. No light guides were used and two PMTs were applied to each end of the stack. The stack and PMTs were placed in a light-tight aluminum case resting on a 2.54 cm thick HDPE sheet on a high density resin lab table. Data sets were collected with a Pixie-4 DAQ. A ^{252}Cf source was fixed to the top of the assembly and the four PMTs were gain adjusted until they all gave approximately the same count rate and energy spectrum. This experimental set up is depicted in Figure 3.15.

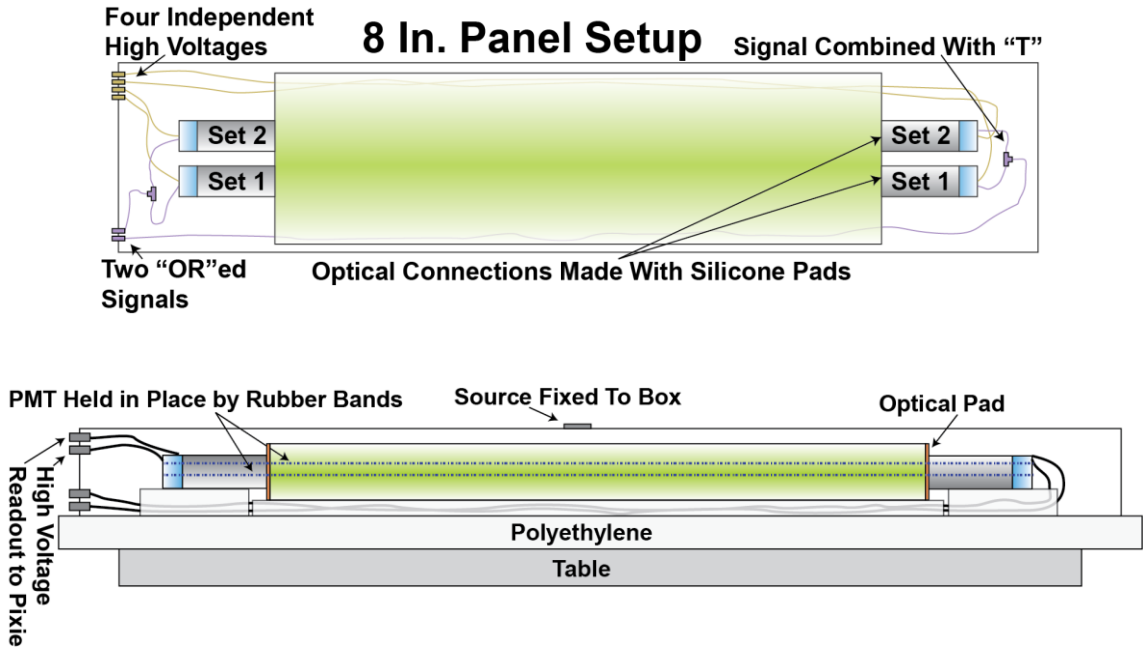

Figure 3.15 Experimental set up to compare ESR overwrap to Teflon overwrap. (Top) Top view of the experimental set up. (Bottom) Side view of the experimental set up.

Data sets were collected in this configuration with each set of PMTs first separately and then together. The aluminum case was then opened and the stack removed. The stack was completely unwrapped and an ESR overwrap was placed on the stack. Since ESR transmits very little light, no additional wrapping was placed on top the ESR; tape only was added to hold the ESR in place. This stack with the ESR overwrap was placed in the aluminum case and reconnected to the same PMTs as before. More data sets were collected with the individual and combined PMT sets. The count rates and energy spectra from these data sets can be seen in Figure 3.16.

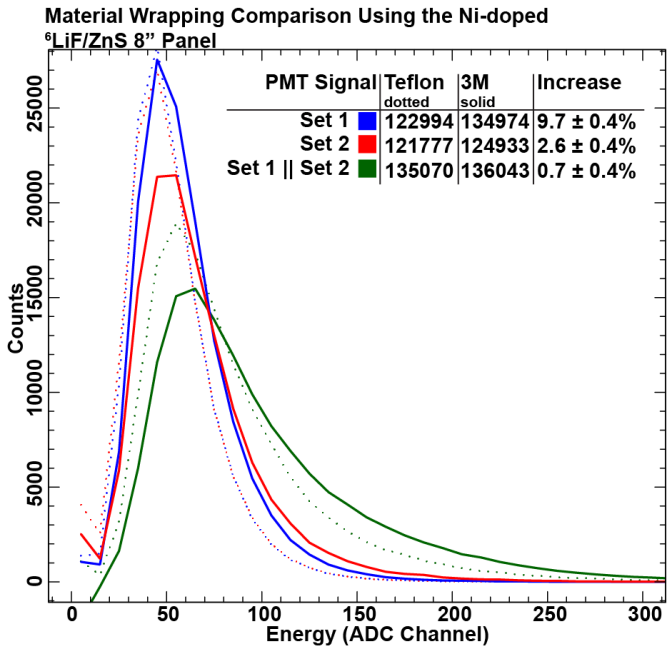

Figure 3.16 Counts and energy spectra from a 20.32 cm wide Ni-quenched stack with Teflon and ESR overwrap.

ESR overwrapped systems consistently had higher ε than equivalent Teflon overwrapped systems. The increased count rate from the ESR was more significant when only one PMT was active on each end than when two PMTs were active. Using ESR also increase the integrated energy recorded for events, indicating an increase in the number of photons counted per event, in agreement with light ray trace simulation results.

Using a dual PMT system or an ESR overwrapped system provided similar ε improvements, but applying a dual PMT and ESP overwrapped system together provide minimal ε improvements compared to either system alone. Either method alone improves light collection efficiency sufficiently to count nearly all neutron-induced scintillation events; therefore, applying both methods together can provide minimal additional ε.

3.4 Alternate Photomultiplier Tube Dimensions

Although using multiple PMTs on the ends of each stack was an effective way of increasing ε, it would have also doubled the number of electrical components for powering PMTs and processing their signals. An alternative way to achieve similar effect to multiple PMTs would be to use larger or square-faced PMTs. Simulations were performed to predict the increased detected light from implementing square PMTs or larger PMTs on each stack instead of 5.08 cm diameter PMTs. Although changes in light flux may not directly relate to changes in ε, these simulation results were used to determine which methods of improving light collection showed the most promise for further development.

Simulations were performed with first one and then two square PMTs placed on the ends of the 20.32 cm wide stack. Each square PMT was 5.08 cm wide on each side and located identically to the round PMTs of previous models, similarly to the model depicted in Figure 3.7. An ESR overwrap without light guides was used in these simulations, as these seemed like obvious improvements to apply to a final system, based on the findings shown in Section 3.3. Key data from these simulations can be seen in Table 3.4.

Table 3.4 Light flux entering 5.08 × 5.08 cm wide square PMTs from 20.32 cm wide stack.

Configuration	Average Light Flux into PMTs (W)	Light Flux into PMTs relative to Original
15.24 cm, with light guide, single PMTs and Teflon (Original)	0.0070351	1.00
20.32 cm, single round PMTs	0.0091609	1.30
20.32 cm, two round PMTs	0.0170062	2.42
20.32 cm, single square PMTs	0.0102090	1.45
20.32 cm, two square PMTs	0.0186325	2.65

A modest increase in light flux entering the PMTs is seen from simulations of the square PMTs compared to the round PMTs for both the single and dual PMT configurations. Previous comparisons between simulation results and measurements, as described in Section 3.2 and Section 3.3, indicated that measured increases in total counted events tend to be more modest than simulated increases in photon flux entering the PMTs from each event; therefore, using square PMTs rather than round PMTs would likely provide only a very modest increase in total counted events. Additionally, no square PMTs of similar performance and price to the R7724 Hamamatsu round PMTs [31] could be found; therefore, no measurements were performed to compare the performance of round PMTs to square PMTs on this system. Although the PLiNS used R7724 Hamamatsu PMTs, the completed LiNMC uses 9821KB07 ET Enterprises PMTs.

Light ray trace simulations were then performed that replaced a single 5.08 cm diameter round PMT with a 7.62 cm diameter PMT and then a 13.3 cm diameter PMT on

the center of a 20.32 cm wide stack. Key data from these simulations can be seen in Table 3.5.

Table 3.5 Light flux entering 7.60 and 13.3 cm diameter round PMTs from 20.32 cm wide stack.

Configuration	Average Light Flux into PMTs (W)	Light Flux into PMTs relative to Original
15.24 cm, with light guide and single PMTs and Teflon (Original)	0.0070351	1.00
20.32 cm, 5.08 cm round PMT	0.0091609	1.30
20.32 cm, 7.6 cm round PMTs	0.0133360	1.90
20.32 cm, 13.3 cm round PMT	0.0237050	3.37

Simulation results indicated that 7.62 cm and 13.3 cm diameter PMTs would increase photon detection by 46.2% and 159% respectively compared to a 5.08 cm diameter PMT on a 20.32 cm wide stack. These increases in light flux may provide a significant increase in the total event count rate relative to a single 5.08 cm diameter PMT and without the added complexity of a dual PMT system. These simulation results have not been compared to experimental measurements.

Implementing 7.62 cm or 13.3 cm diameter PMTs could require offsetting PMTs from the center of the stack; therefore, measurements were taken to determine the effects of offsetting PMT location on the count rates of a 20.32 cm wide stack. A 20.32 cm wide stack with ESR overwrap had one end covered with ESR and the other end left bare. A 5.08 cm diameter PMT was placed on the center of the bare end and a background rate was recorded for 60 seconds with a Pixie-4. A ^{252}Cf source inside an HDPE container was

placed on the assembly holding the 20.32 cm wide stack and an active rate was recorded for 60 seconds. The PMT was then relocated off-center of the stack to be half way between the center and the edge of the stack. Measurements were repeated for this configuration. The PMT was then located again at the edge of the stack while still being fully covered by the stack, and measurements were repeated. All three configurations are depicted in Figure 3.17. This set of three measurements was repeated six times to account for the systematic uncertainty of the system. Active and background measurement results are recorded in Table 3.6.

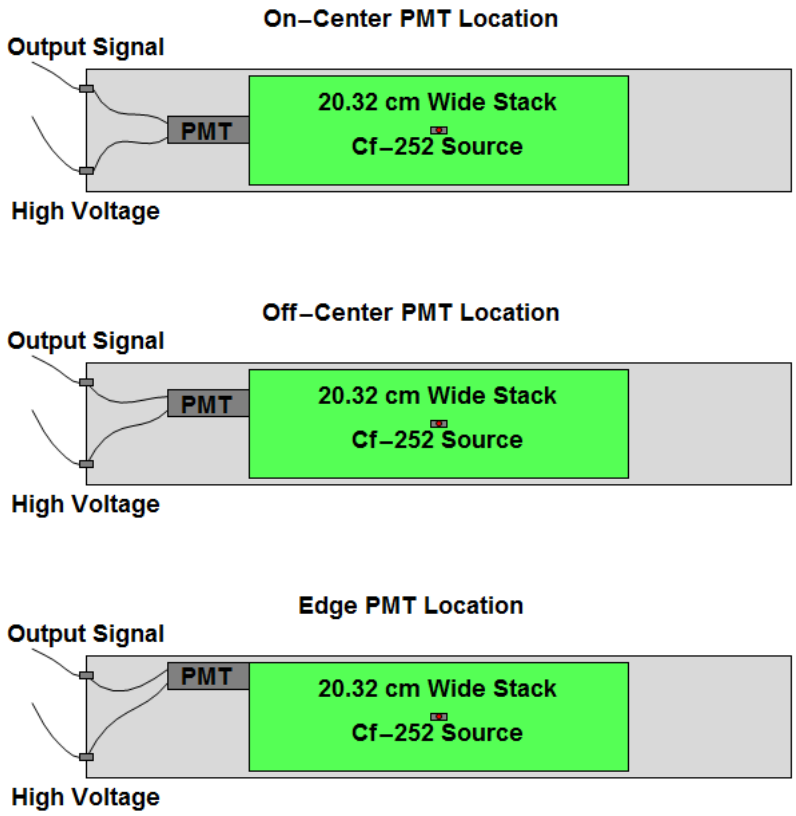

Figure 3.17 (Top) PMT located on-center of the 20.32 cm wide stack. (Middle) PMT located off-center of the 20.32 cm wide stack. (Bottom) PMT located on the edge of the 20.32 cm wide stack.

Table 3.6 Count rate measurement results of a PMT placed at different locations on a 20.32 cm wide stack.

Configuration	Active Count Rate (Hz)	Background Count Rate (Hz)	Background Subtracted Count Rate (Hz)
On-Center			
Run 1	1673 ± 5	30.54 ± 0.7	1642 ± 5
Run 2	1496 ± 5	25.1 ± 0.6	1471 ± 5
Run 3	1621 ± 5	28.3 ± 0.7	1592 ± 5
Run 4	1555 ± 5	20.6 ± 0.6	1534 ± 5
Run 5	1489 ± 5	19.8 ± 0.6	1470 ± 5
Run 6	1552 ± 5	20.8 ± 0.6	1532 ± 5
Off-Center			
Run 1	1541 ± 5	23.4 ± 0.6	1518 ± 5
Run 2	1824 ± 6	35.8 ± 0.8	1788 ± 6
Run 3	1501 ± 5	19.6 ± 0.6	1481 ± 5
Run 4	1562 ± 5	21.7 ± 0.6	1541 ± 5
Run 5	1602 ± 5	21.1 ± 0.6	1581 ± 5
Run 6	1627 ± 5	22.5 ± 0.6	1605 ± 5

Table continued on next page

Configuration	Active Count Rate (Hz)	Background Count Rate (Hz)	Background Subtracted Count Rate (Hz)
Edge			
Run 1	1444 ± 5	23.7 ± 0.6	1421 ± 5
Run 2	1538 ± 5	24.5 ± 0.6	1514 ± 5
Run 3	1636 ± 5	20.8 ± 0.6	1615 ± 5
Run 4	1556 ± 5	21.7 ± 0.6	1535 ± 5
Run 5	1535 ± 5	18.9 ± 0.6	1517 ± 5
Run 6	1622 ± 5	21.4 ± 0.6	1600 ± 5

The average count rate for each configuration was 1540 Hz ± 69 for the on-center configuration, 1586 Hz ± 110 for the off-center configuration, and 1533 Hz ± 71 for the edge configuration, as graphically represented in Figure 3.18.

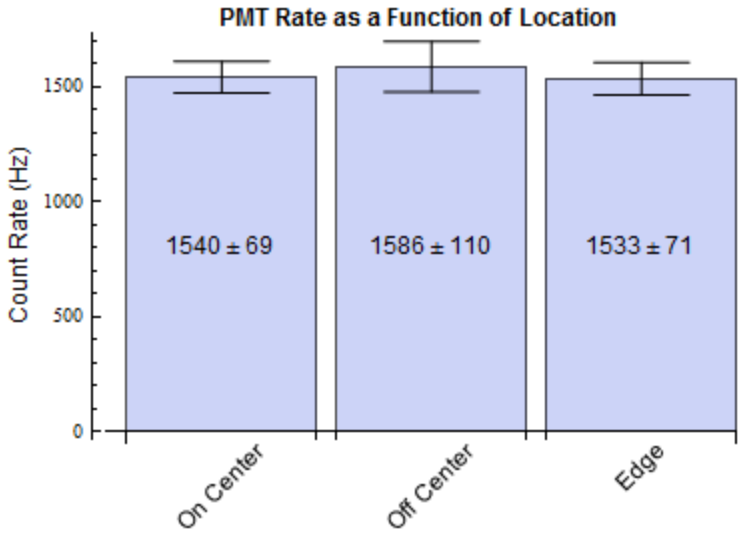

Figure 3.18 Averaged background subtracted count rates for different PMT locations on a 20.32 cm wide stack.

No statistically significant reduction in count rate was seen from relocating the PMT on the end of a 20.32 cm wide stack to any other location on the end of the stack, which is consistent with light simulation results that indicate a mostly uniform distribution of light flux at the ends of detector stacks. Therefore, if a PMT were placed off-center, there would be no significant reduction in counts as a consequence. Since the count rates of a 5.08 cm diameter PMT remained static regardless of location, it can be assumed that larger PMTs will have similar characteristics and will not see significant count rate reductions from being placed off-center.

3.5 Alternate Dimensions of Wavelength Shifting Plastic

The wavelength shifting plastic (WSP) is important to the LiNMC as a neutron moderator, a medium for light transport, and for the distance it removes the LiF/ZnS from the source therefore, simulations and measurements were performed to maximize the *FoM* based on WSP dimensions.

A model of a 20.32 cm wide stack with reduced WSP thicknesses was developed to reduce τ with a minimal reduction of ε. MCNP simulations indicated that a modest reduction in WSP from each stack would improve the *FoM* by 10.1%. Therefore, a light ray trace model was developed of a 20.32 cm wide stack with the first and last sheets of WSP 0.35 cm thick instead of 0.7 cm thick. All other sheets of WSP remained 0.7 cm thick. This model implemented dual PMTs, a Teflon overwrap, and light guides. Other than reducing the thickness of the first and last sheets of WSP, this model was identical to the model depicted in Figure 3.8.

The reduction of material between the LiF/ZnS sheets and the overwrap does increase the number of scatters required for photons to reach a PMT, but unlike surface scatters associated with light guides, this increase in surface scattering does not necessarily increase the probability of photons scattering away from the PMTs. The amount of overwrap was reduced while the amount of LiF/ZnS was maintained; therefore, this simulation can be seen as a perturbation of the system, increasing the ratio of LiF/ZnS scatters to Teflon scatters. Light entering the PMTs of the model with the 0.35 cm thick first and last WSP sheets increased slightly compared to the same model with 0.7 cm thick first and last WSP sheets, indicating that surface scattering from LiF/ZnS may be more effective at directing light to PMTs than the Teflon overwrap. Increasing the ratio of LiF/ZnS to overwrap material may be an effective means of reducing light losses in detector stacks. Results from these simulations can be seen in Table 3.7.

Table 3.7 Light flux entering dual PMTs of a 20.32 cm wide stack with 0.35 cm thick WSP first and last sheets.

Configuration	Average Light Flux into PMTs (W)	Light Flux into PMTs relative to Original
15.24 cm, with light guide, single PMTs and Teflon (Original)	0.0070351	1.0
20.32 cm, dual PMTs with Light Guide	0.0083879	1.19
20.32 cm, dual PMTs with Light Guide and thin WSP	0.0093295	1.33

Simulations indicate that implementing 0.35 cm thick WSP first and last sheets on the stack will increase light flux entering the PMTs by 11.8% in a 20.32 cm wide stack with Teflon overwrap, dual PMTs, and a light guide. Therefore, reducing the first and last WSP sheets thickness to 0.35 cm shows promise for improving total optical performance while reducing the overall footprint and weight of the detector system, bringing the LiF/ZnS closer to the radiation source to increase neutron capture efficiency, and reducing materials costs for stacks and cases.

A separate model was developed to determine if a net increase in neutron capture efficiency could be achieved by increasing the amount of LiF/ZnS through extending the length of the stacks without excessive optical losses. This model extended the 20.32 cm wide stack from 71.12 cm long to 101.28 cm, extending the length of LiF/ZnS, WSP, and overwrap. The model used 0.7 cm wide sheets of WSP, a single PMT on both ends, Teflon overwrap, and no light guides. Key data from these simulations can be seen in Table 3.8.

Table 3.8 Light flux entering the PMTs of a 20.32 cm wide stack with extended length.

Configuration	Average Light Flux into PMTs (W)	Light Flux into PMTs relative to Original
15.24 cm, with light guide and single PMTs and Teflon (Original)	0.0070351	1.0
20.32 cm, single PMT, ESR overwrap	0.0091609	1.30
20.32 cm, single PMT, ESR overwrap, 101.28 cm height	0.0067120	0.95

Simulations of a 101.28 cm long, 20.32 cm wide stack without a light guide shows a 26.7% reduction in light flux entering the PMTs. To further understand the reason for this decrease in light flux entering the PMTs, light mode histories entering the PMTs were examined and compared to non-extended stack light ray histories, as seen in Figure 3.19 and Figure 3.20.

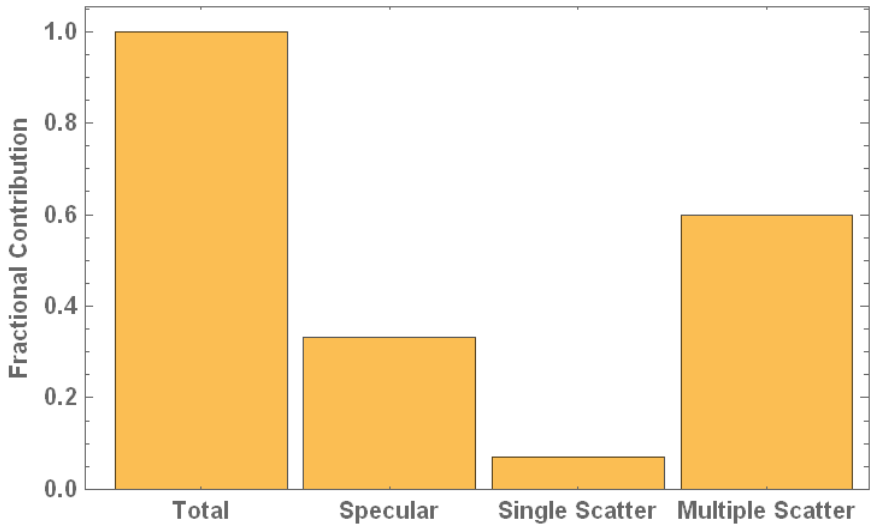

Figure 3.19 Modes of light arriving at the PMTs from a 20.32 cm wide, 71.12 cm long stack.

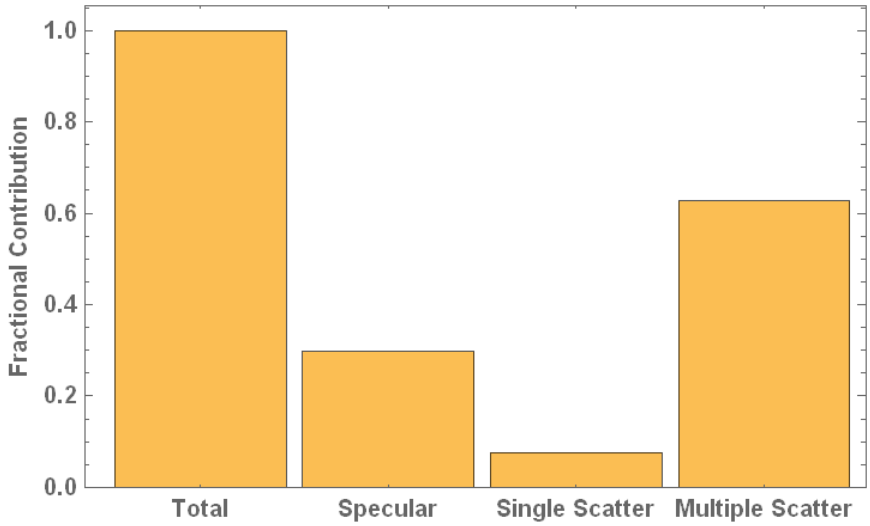

Figure 3.20 Modes of light arriving at the PMTs from a 20.32 cm wide, 101.82 cm long stack.

From these light ray histories, it can be seen that the extended stack has slightly decreased specular scatters and slightly increased multiple scatters compared to the non-extended stack. It appears that the longer stack offers significantly greater opportunity for scattering and attenuation and reduced opportunity for specular (unscattered) light to reach the PMTs. From these simulation results, it was determined that the extended length stack lacked sufficient promise to justify further modeling or physical experimentation.

For future development, MCNP and light tracking simulations may be used to optimize the length of the detector stacks.

3.6 LiNMC Evolution

The initial LiNMC design by the end of the Neutron Detection without Helium-3 Project, as discussed in Section 2.4, evolved to the current design based on engineering and financial constraints. Development was guided by a combination of the most promising simulation and experimental results.

The initial design, as depicted in Figure 2.11, called for 18 layers of LiF/ZnS sandwiched between 19 layers of WSP. Although this entire area could have its scintillations light detected with a single large area PMT on both ends, the dead time and signal pileup would have resulted in long assay times. Therefore, the detector regions were divided into four smaller detector regions that had five sheets of LiF/ZnS and six sheets of WSP. These smaller regions each had their own pair of PMTs on both ends to reduce pulse pileup effects, dead time, and particle misidentification associated with large detector stacks. Based on diminishing performance to cost benefits, only 12 of the 16 detector stacks were constructed and installed.

Since the detector stacks needed to be optically isolated from each other to limit cross talk, each stack was built separately and covered with a reflective overwrap to prevent optical signal loss or spurious optical signal introduction. Making each stack from five sheets of LiF/ZnS and six sheets of WSP increased the total amount of WSP in the system and thus the neutron moderation and τ. This increase in τ was mitigated by reducing the thickness of the first and last WSP sheets in each stack by half, as described in section 3.4.

The active detector regions in the four corners of the LiNMC were removed based on budgetary constraints. Rather than leave the corners bare, MCNP simulations were conducted that replaced the detector regions with other neutronically sensitive materials. Simulations indicated that HDPE wedges would provide neutron moderation and reflection, increasing ε and τ, for an overall increased *FoM*. Before these wedges were implemented, further simulations determined that 7.5% lithiated HDPE would provide a similar ε increase but less increase in τ than non-lithiated HDPE, resulting in superior *FoM* [32].

HDPE shielding is not typically sold in wedges, but is typically sold in 5.08 cm × 10.16 cm × 20.32 cm and 5.08 cm × 10.16 cm × 15.24 cm blocks; therefore, simulations were performed to compare the wedge configuration to an "L" configuration in the corners. The difference in *FoM* between these two configurations was not significant, indicating that the additional material in the wedge configuration was not needed. Therefore, the corners were constructed from 5.08 cm × 10.16 cm × 20.32 cm and 5.08 cm × 10.16 cm × 15.24 cm blocks arranged in an "L" configuration. Additional advantages of the "L" configuration were that the standard blocks were less expensive and faster to produce than wedge-shaped blocks.

Most of these beneficial designs features that were incorporated into the LiNMC came after simulating many inferior designs features to optimize a specific parameter space. The MCNP input for the LiNMC is presented in Appendix 3: MCNP Model of LiNMC The LiNMC's performance may be further improved through continued optimization of materials and geometries.

3.7 Conclusions

Initial experiments and simulations indicated that a 20.32 cm wide stack with light guides had reduced ε compared to a 15.24 cm wide stack with similar light guides. Simulations indicated that light traversing a 20.32 cm wide stack with light guides experienced significantly more multiple scatters and had more light scattered away from the PMTs than the 15.24 cm wide stack. Once the light guides were removed from the 20.32 cm wide stack, the 20.32 cm wide stack displayed increased ε compared to the 15.24 cm wide stack.

Similar increases in measured and simulated counts were seen from using dual PMTs on the ends of the stacks and from using an ESR overwrap instead of a Teflon overwrap. Although increased counts from both these methods were significant, the increases from the methods were generally not additive with each other. Therefore, either method alone is approximately as useful as both methods together, therefore, there is little reason to implement both methods in a full-scale system.

Simulations indicated that light detection could be modestly increased by using square PMTs instead of similar round PMTs; however, square PMTs with similar performance and cost to the round Hamamatsu R7724 PMTs used in the PLiNS could not be found as of the time this was written, and the modest increases in light detection from using square PMTs would not justify the cost of having custom PMTs built.

Simulation results indicated that using 7.62 cm diameter or 13.3 cm diameter PMTs would significantly increase the signal from to the data acquisition systems from each scintillation event. This increased signal may be similar to the increased signal gained from using multiple PMTs but without the need to double power supply and data acquisition channels.

Simulation results indicated that decreasing the thickness of the first and last sheets of WSP from 0.70 cm to 0.35 cm would provide a small increase in scintillation light entering the PMTs, while also reducing τ and without having a significant effect on ε.

Simulation results indicated that extending the length of the detector stack from 71.12 cm to 101.28 cm would significantly decrease the light flux entering the PMTs. This model did not provide sufficient promise to be considered worth further pursuit at this time.

Considering the optical simulation and experimental results, the full-scale LiNMC was designed to utilize 20.32 cm wide 71.12 cm tall detector stacks without light guides. The detector stacks were designed to incorporate 5 sheets of LiF/ZnS sandwiched between 6 sheets of WSP. The first and last sheets of WSP were 0.35 cm thick and all other sheets of WSP were 0.70 cm thick. The stacks received an ESR overwrap and had a single 7.62 cm diameter PMT placed off-center at both ends, with a silicone optical pad between the PMT face and the stack end.

4 Gamma-Ray Discrimination Methods

Because shift register results are based on the assumption that all signals are from neutron captures, misidentifying gamma rays as neutrons could results in assay errors. High rates of gamma-ray signals may also contribute to pulse pileup, reducing reliability at high signal rates. Therefore, reducing gamma-ray signals without significantly affecting neutron signals is required for neutron multiplicity counters to reliably perform sample assays. Since LiF/ZnS-based neutron detector systems are not inherently gamma-ray insensitive, various methods were investigated to reduce gamma-ray-like signals without significantly affecting overall systems performance.

This chapter is intended to summarize gamma-ray discrimination methods and key performance results that were applied to a single 20.32 cm wide Ni-quenched detector panel. Particular attention was given to pulse shape discrimination (PSD) methods. The results investigated were gamma Figure-of-Merit (γFoM), estimated gamma rejection ratio (*GRR*), neutron counts, gamma-ray counts, and calculations time. Iterative methods were used to determine the *GRR* optimized parameters for each PSD method.

Scintillators tend to produce light with different characteristics depending on how they are stimulated. The characteristic shapes of these pulses can be used to distinguish between the reactions involved in generating these pulses, and therefore the particle interactions that caused the pulses, permitting particle identification based on pulse shape [17].

PSD is based on the existence of multiple decay mode fluorescence. In addition to the prompt decay mode, there is usually a slower emission. The fast mode results from the direct radiative de-excitation of excited states in the scintillator, while the slower modes

originate from the collision interactions of pairs of molecules and low excited states [33, 34]. The short range of the energetic charged particles produced from neutron, alpha, and triton collisions yield a high number of triplets compared to the longer range of the electrons from gamma-ray interactions. The greater number of triplets produced from neutron, alpha, and triton interactions leads to greater delayed emissions than from gamma-rays [17].

Data sets to test with PSD methods were obtained by placing a 20.32 cm wide detector panel inside an aluminum case and placing PMTs near both ends of the panel. The PMTs were not physically connected to the detector stack to reduce systematic uncertainties associated with optical interfaces, and to improve reproducibility. The aluminum case was placed on 27.4 × 27.4 × 7.6 cm wood blocks. The wood blocks were placed on a 2.54 cm thick sheet of high density polyethylene (HDPE) on a high density resin table. An elevated geometry was used to reduce the neutron reflection from the HDPE and table, thereby increasing the detected gamma-ray to neutron ratio, to provide sufficient gamma-ray waveforms for pulse shape analysis. Measurements were taken with one ^{252}Cf, one ^{60}Co, and three ^{137}Cs sources simultaneously fixed to the top of the aluminum case, as depicted in Figure 4.1.

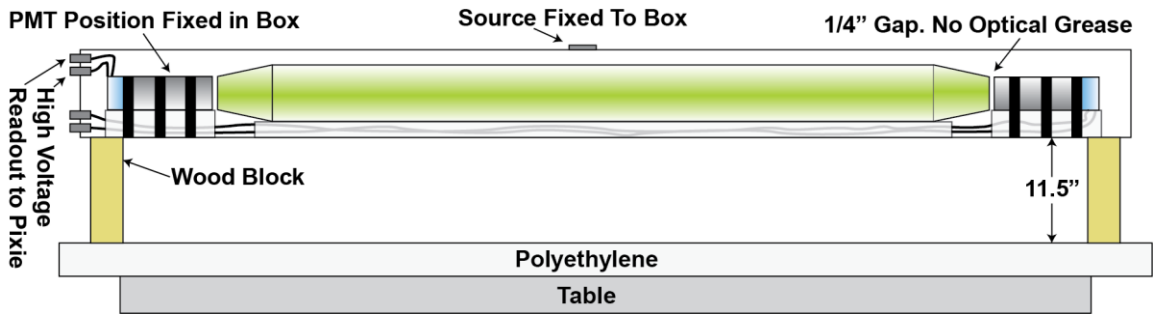

Figure 4.1 20.32 cm wide detector panel raised above a table with ^{252}Cf, ^{60}Co, and ^{137}Cs sources.

Signals from the PMTs were collected with a Pixie-4 DAQ. The Pixie-4 used time bins of 13.3 ns for data collection; therefore, time parameters were set as multiples of 13.3 ns. Each pulse was analyzed with a trace length of 6666.7 ns (500 bins), including a 507.7 ns (38 bins) trace delay. All PSD methods were performed using the same Pixie-4 data set and settings[1]. All methods employed a simple discrimination against multiple pulses by discarding any pulses with a maximum pulse height not within 333.3 ns (25 bins) of the trigger pulse. All methods also employed a base-line-correction that averaged the first 266.7 ns (20 bins) of the pulse and then subtracted that average from the value of each energy bin in the pulse.

4.1 Pulse Shape Discrimination Methods

PSD is a popular method for distinguishing between events that tend to produce different signals in a system. Neutron captures in LiF/ZnS tend to produce a sharp increase in scintillation light with a long tail that returns to baseline over several microseconds, whereas gamma rays tend to produce a single sharp peak of scintillation light that rapidly returns to zero over tens of nanoseconds. PSD can be used to automatically sort waveforms via an algorithm, as being either neutron-like or gamma-ray-like, allowing gamma-ray-like signals to be discarded from a neutron detector. A brief review of PSD is found in Section 2.2.

[1] Pixie-4 settings: Energy Rise Time = 0.0533333 μs; Energy Flat Top = 1.89333 μs; Trigger Rise Time = 0.08 μs; Trigger Flat Top = 0.4 μs; Trigger Threshold = 5; Voltage Gain (channel 1) = 4.99996; Voltage Gain (channel 2) = 5.79997, Voltage Offset (channel 1) = -0.173874; Voltage Offset (channel 2) = -0.162506, Trace Length = 6.70667 μs; Trace Delay = 0.50667 μs.

Multiple PSD methods were applied to the same data set to compare between different methods[2]. Each waveform was analyzed by each method to produce a single numeric result, which was usually a charge ratio. These individual charge ratios were accumulated into histograms, depicted below. Double Gaussian functions were fit to these histograms, with one Gaussian fit to the neutron-like pulses and the other Gaussian fit to the gamma-ray-like pulses, as seen in Equation 4.1.

Equation 4.1 $\text{Double Gaussian Function} = \frac{A}{\sigma_1\sqrt{2\pi}} e^{-\frac{1}{2}(\frac{x-\mu_1}{\sigma_1})^2} + \frac{B}{\sigma_2\sqrt{2\pi}} e^{-\frac{1}{2}(\frac{x-\mu_2}{\sigma_2})^2}$

where A and B are the scaling constants for both Gaussians, σ_1 and σ_2 are the standard deviations for both Gaussians, and μ_1 and μ_2 are the centroids for both Gaussians. Noting that for a Gaussian with zero skewness, the centroid is also the mean of the Gaussian. The gamma figure-of-merit (γFoM) was then determined by calculating the separation between the means, or centroids, of the two Gaussian functions, and then dividing by the sum of the full-width-at-half-maximum (FWHM) of both Gaussian functions, as in Equation 4.2.

Equation 4.2 $\gamma FoM = \frac{S}{\delta_n + \delta_\gamma}$

$$\gamma FoM = \frac{\mu_1 - \mu_2}{(\sigma_1 + \sigma_2)2\sqrt{2\ln(2)}}$$

where S is the separation between the two Gaussians functions, δ_n is the FWHM of the neutron pulses, and δ_γ is the FWHM of the gamma-ray pulses. Assuming that parameters

[2] All PSD Methods were performed on a Dell Precision 690 computer running Windows 7, through an Oracle VM Virtual Box (version 4.3.30) running CentOS 6.3 x64. The virtual machine had 6 Gb of memory, 1 thread of an Intel Xeon DP 5060 CPU, and 64 Mb of video memory. All PSD Methods were written and run in ROOT version 5.34/09 with C/C++ interpreter version 5.18.00.

are uncorrelated with each other, uncertainties for each of the *γFoM* parameters can be propagated to determine a *γFoM* uncertainty, as seen in Equation 4.3.

Equation 4.3 $$\delta\gamma FoM^2 = \delta\mu_1^2\left(\frac{d\gamma FoM}{d\mu_1}\right)^2 + \delta\mu_2^2\left(\frac{d\gamma FoM}{d\mu_2}\right)^2 + \delta\sigma_1^2\left(\frac{d\gamma FoM}{d\sigma_1}\right)^2 + \delta\sigma_2^2\left(\frac{d\gamma FoM}{d\sigma_2}\right)^2$$

$$\delta\gamma FoM = \sqrt{\delta\mu_1^2(\frac{d\gamma FoM}{d\mu_1})^2 + \delta\mu_2^2(\frac{d\gamma FoM}{d\mu_2})^2 + \delta\sigma_1^2(\frac{d\gamma FoM}{d\sigma_1})^2 + \delta\sigma_2^2(\frac{d\gamma FoM}{d\sigma_2})^2}$$

$$\delta\gamma FoM = \sqrt{\frac{\delta\sigma_1^2(\mu1-\mu2)^2}{8(\sigma_1+\sigma_2)^4 ln(2)} + \frac{\delta\mu_2^2(\mu1-\mu2)^2}{8(\sigma_1+\sigma_2)^4 ln(2)} + \frac{\delta\sigma_1^2}{8(\sigma_1+\sigma_2)^2 ln(2)} + \frac{\delta\sigma_2^2}{8(\sigma_1+\sigma_2)^2 ln(2)}}$$

where $\delta\gamma FoM$ is the uncertainty of the *γFoM*, $\delta\mu_1$ and $\delta\mu_2$ are the uncertainties of the centroids of the Gaussians, and $\delta\sigma_1$ and $\delta\sigma_2$ are the uncertainties of the Gaussians. $\delta\gamma FoM$ would require additional terms if parameters were correlated with each other, which have been excluded since σ_1 and σ_2 only depend on the spread of the sorted waveforms. μ_1 and μ_2 only depend on the mean of the sorted waveforms, which are all independent values. The *γFoM* was related to a gamma rejection ratio (*GRR*) by Mitchell Myjak [35], which is the ratio of gamma-rays detected as neutrons to the number of incident gamma-rays [36], through Equation 4.4.

Equation 4.4 $$GRR = \frac{1}{2}erfc(2\gamma FoM\sqrt{\ln(2)})$$

where erfc is the complimentary error function. This *GRR* is only a rough estimate of the actual performance of these methods. A final *GRR* should be based on actual performance measurements of the completed system, including shielding, coincidence between PMTs, and PSD methods.

Once a PSD method is applied to the waveforms, neutron and gamma-ray counts were calculated by setting a cutoff point in the charge ratio data set at the minima between the neutron and gamma-ray peaks. Any events on the neutron dominant side of the cutoff

point were counted as neutrons and any events on the gamma-ray dominant side of the cutoff point were considered to be gamma-rays. The better the separation between the neutron and gamma-ray regions, the lower the *GRR* and the higher the γFoM.

The run time for each method was recorded to give an estimate of the relative time each method will require to implement, which may be important if PSD analysis is conducted in real time rather than offline.

4.2 Method 1

Method 1 utilized a short gate – long gate technique, which sorts waveforms according to the total integrated energy and the tail integrated energy of events [17, 37, 38]. Using an interactive approach to optimize the γFoM, the short gate was defined as the integrated energy from 440.0 ns (bin 33) to 506.7 ns (bin 38), and the long gate was defined as integrated energy from 520.0 ns (bin 39) to 1053.3 ns (bin 79). The charge ratio was the long gate divided by the sum of the long gate and short gate, as seen in Equation 4.5.

Equation 4.5 $$\text{Charge Ratio} = \frac{\text{Long Gate}}{\text{Long Gate+Short Gate}}$$

$$\text{Charge Ratio} = \frac{\int_{520.0ns}^{1053.3ns} \text{Pulse Energy}\, dt}{\int_{440.0ns}^{506.7ns} \text{Pulse Energy}\, dt + \int_{520.0ns}^{1053.3ns} \text{Pulse Energy}\, dt}$$

where t is time, and the Pulse Energy is the time binned energy recorded for each pulse. The charge ratio data set and the fit double Gaussian function for Method 1 can be seen in Figure 4.2.

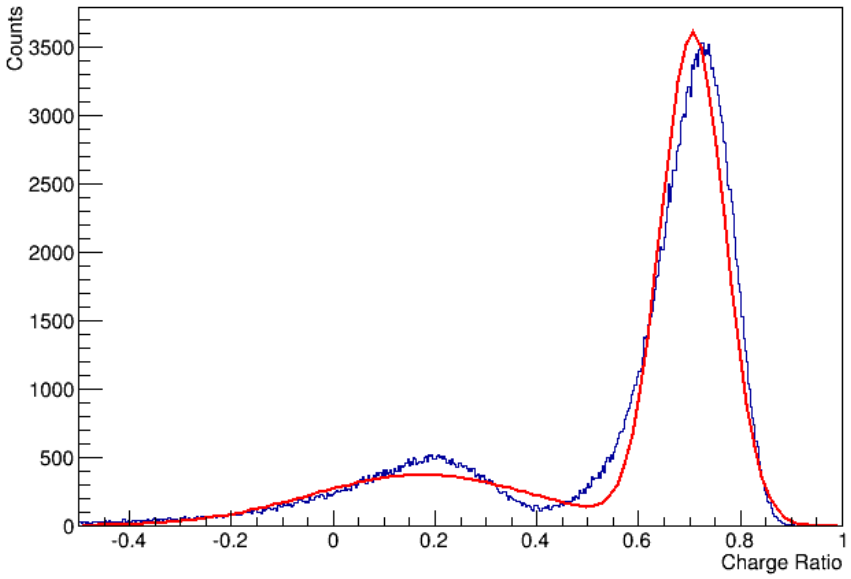

Figure 4.2 Waveforms were analyzed via Method 1 and counted as a function of their charge ratio (blue) and then fit with a double Gaussian function (red) which was used to quantify the neutron to gamma-ray separation from Method 1.

Pulses with charge ratios less than 0.4075 were counted as gamma-rays; all other pulses were counted as neutrons. The double Gaussian function parameters associated with Method 1 can be seen in Table 4.1.

Table 4.1 Double Gaussian parameters for Method 1.

Parameters	Values
A	3590 ± 10
σ_1	0.0631 ± 0.0001
μ_1	0.7069 ± 0.0002
B	374 ± 2
σ_2	0.176 ± 0.001
μ_2	0.022 ± 0.001

Performance results for Method 1 can be seen in Table 4.2.

Table 4.2 Performance results for Method 1.

Results	Values
γFoM	1.216 ± 0.007
GRR	$2.1\times10^{-3} \pm 1\times10^{-4}$
Neutrons	213043
Gamma-Rays	66418
Run Time (s)	25.6 ± 0.1

Method 1 had a superior speed but inferior *γFoM* and *GRR* compared to other PSD methods described below. Method 1 would be easy to implement due to its speed, but would provide minimal gamma-ray rejection.

4.3 Method 2

Method 2 utilized a dynamic short gate – long gate technique. The short gate was defined as the integrated energy from 40.0 ns (3 bins) before peak energy to 26.7 ns (2 bins) after peak energy; the long gate was defined as the integrated energy for 533.3 ns (40 bins) after the end of the short gate. The charge ratio was the value of the long gate divided by the sum of the long gate and short gate, as seen in Equation 4.6.

Equation 4.6 $$\text{Charge Ratio} = \frac{\text{Long Gate}}{\text{Long Gate}+\text{Short Gate}}$$

$$\text{Charge Ratio} = \frac{\int_{Peak+40.0ns}^{Peak+533.3ns} \text{Pulse Energy}\, dt}{\int_{Peak-40.0ns}^{Peak+26.7ns} \text{Pulse Energy}\, dt + \int_{Peak+40.0ns}^{Peak+533.3ns} \text{Pulse Energy}\, dt}$$

where *Peak* is the bin with maximum energy. The charge ratio data set and fit double Gaussian function for Method 2 can be seen in Figure 4.3.

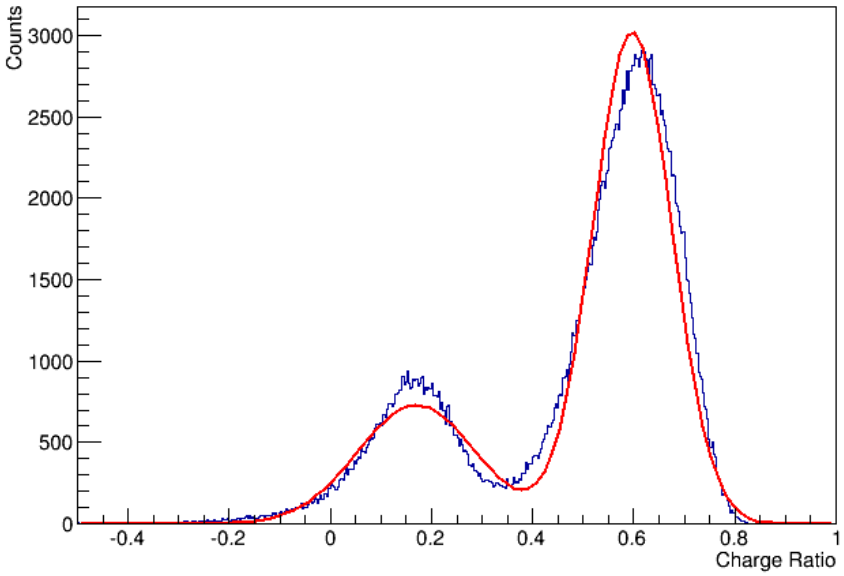

Figure 4.3 Waveforms were analyzed via Method 2 and counted as a function of their charge ratio (blue) and then fit with a double Gaussian function (red) which was used to quantify the neutron to gamma-ray separation from Method 2.

Pulses with charge ratios less than 0.3475 were counted as gamma rays; all other pulses were counted as neutrons. The double Gaussian function parameters associated with Method 2 can be seen in Table 4.3.

Table 4.3 Double Gaussian parameters for Method 2.

Parameters	Values
A	3024 ± 8
σ_1	0.0779 ± 0.0001
μ_1	0.5970 ± 0.0002
B	729 ± 4
σ_2	0.1167 0.0006
μ_2	0.1702 ± 0.0005

Performance results for Method 2 can be seen in Table 4.4.

Table 4.4 Performance results for Method 2.

Results	Values
γFoM	0.931 ± 0.004
GRR	$1.42\times10^{-2} \pm 3\times10^{-4}$
Neutrons	210071
Gamma Rays	69390
Run Time (s)	29.2 ± 0.2

Method 2 had inferior *γFoM*, *GRR*, and longer run time compared to Method 1.

4.4 Method 3

Method 3 utilized a peak to long gate energy technique to distinguish between pulse types. The peak energy was taken as the energy of the maximum energy bin within a pulse.

The long gate was calculated by integrating the pulse energy from 40.0 ns (3 bins) before the pulse maximum to 266.7 ns (20 bins) after the pulse maximum). The charge ratio was determined by dividing the long gate by the sum of the long gate and the peak energy, as seen in Equation 4.7.

Equation 4.7 $$\text{Charge Ratio} = \frac{\text{Long Gate}}{\text{Long Gate+Peak Energy}}$$

$$\text{Charge Ratio} = \frac{\int_{Peak-40.0ns}^{Peak+266.7ns} \text{Pulse Energy } dt}{\int_{Peak-40.0ns}^{Peak+266.7ns} \text{Pulse Energy } dt + \text{Peak Energy}}$$

where *Peak* is the bin with maximum energy, and Peak Energy is the value of the maximum energy bin. The charge ratio data set and the fit double Gaussian function for Method 3 can be seen in Figure 4.4.

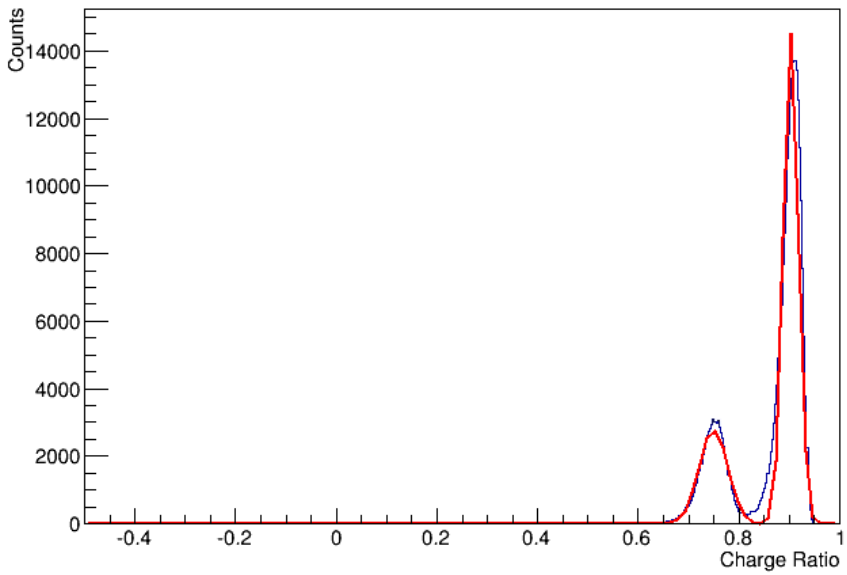

Figure 4.4 Waveforms were analyzed via Method 3 and counted as a function of their charge ratio (blue) and then fit with a double Gaussian function (red) which was used to quantify the neutron to gamma-ray separation from Method 3.

Pulses with charge ratios less than 0.8185 were counted a gamma rays; all other pulses were counted as neutrons. The double Gaussian function parameters associated with Method 3 can be seen in Table 4.5.

Table 4.5 Double Gaussian parameters for Method 3.

Parameters	Values
A	2760 ± 10
σ_1	0.01504 ± 0.00003
μ_1	0.90318 ± 0.00006
B	14530 ± 40
σ_2	0.0285 ± 0.0001
μ_2	0.7493 ± 0.0001

Performance results for Method 3 can be seen in Table 4.6.

Table 4.6 Performance results for Method 3.

Results	Values
γFoM	1.501 ± 0.003
GRR	$2.06\times10^{-4} \pm 7\times10^{-6}$
Neutrons	212215
Gamma Rays	67246
Run Time (s)	33.7 ± 0.9

These results indicated that Method 3 was slightly slower than Method 1 and Method 2, but had a much better *γFoM* and *GRR*.

Because of the high promise of Method 3 for full-scale application, Method 3 was later refit with a Gaussian plus a skewed Gaussian function to better estimate the *γFoM*, as seen in Equation 4.8 and Equation 4.9. The input into Equation 4.2 was modified to replace μ_1 with the mean of the skewed Gaussian ($Mean_1$), and replaced σ_1 multiplied by a constant with the full-width-at-half-maximum ($FWHM_1$) of the skewed Gaussian.

Equation 4.8 $$\text{Gaussian plus skewed Gaussian} = \frac{e^{-\frac{(x-\mu_2)^2}{2\mu_2^2}}}{\mu_2\sqrt{2\pi}} + \frac{e^{-\frac{(x-\sigma_1)^2}{2\mu_1^2}}\,\text{erfc}\left[-\frac{\alpha_1(x-\sigma_1)}{\mu_1\sqrt{2}}\right]}{\mu_1\sqrt{2\pi}}$$

where α1 is the skewness of the skewed Gaussian and all other parameters are the same as in Equation 4.1.

Equation 4.9 $$\gamma\text{FoM} = \frac{S}{\delta_n + \delta_\gamma}$$

$$\gamma\text{FoM} = \frac{Mean_1 - \mu_2}{FWHM_1 + \sigma_2 \times 2\sqrt{2\ln(2)}}$$

where $Mean_1$ is the mean of the skewed Gaussian, since the mean of a skewed Gaussian is not generally the centroid of the skewed Gaussian, $FWHM_1$ is the full-width-at-half-maximum of the skewed Gaussian, and all other parameters are the same as in Equation 4.2. Uncertainties for the $Mean_1$ and $FWHM_1$ were not determined, as these parameters could only be determined numerically, not symbolically.

The Gaussian plus skewed Gaussian fit with the data set from Method 3 can be seen in Figure 4.5.

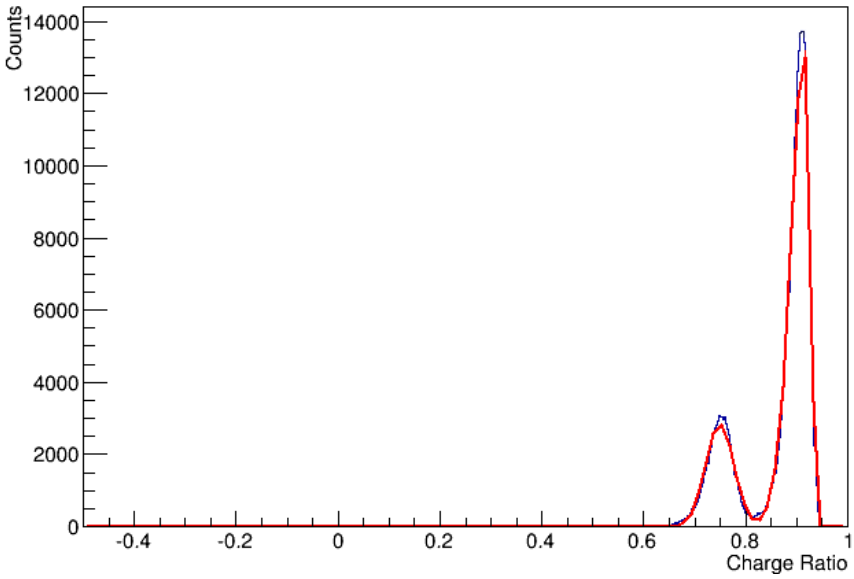

Figure 4.5 Waveforms were analyzed via Method 3 and counted as a function of their charge ratio (blue) and then fit with a Gaussian plus skewed Gaussian function (red) which was used to quantify the neutron to gamma-ray separation from Method 3.

The application of a skewed Gaussian improves the fit between the function and the data set. The Gaussian plus skewed Gaussian function parameters associated with Method 3 can be seen in Table 4.7, where α_1 is the skewness of the skewed Gaussian.

Table 4.7 Gaussian plus skewed Gaussian parameters for Method 3.

Parameters	Values
A	632 ± 1
σ_1	0.03218 ± 0.00008
μ_1	0.92634 ± 0.00006
α_1	-3.96 ± 0.03
B	2820 ± 10
σ_2	0.0277 ± 0.0001
μ_2	0.7490 ± 0.0001

Results for the *γFoM*, *GRR*, neutron count, gamma ray count, and run time for Method 3 with a skewed Gaussian fit can be seen in Table 4.8.

Table 4.8 Results for Method 3 with a Gaussian plus skewed Gaussian fit.

Results	Values
γFoM	1.41 ± 0.003
GRR	$4.4\times10^{-4} \pm 1\times10^{-5}$
Neutrons	212215
Gamma Rays	67246
Run Time (s)	33.7 ± 0.9

Estimates of the *γFoM* and *GRR* worsened for Method 3 with a Gaussian plus Gaussian fit, but remain superior to most other PSD methods. Method 3 showed high

promise for development and implementation as a method of gamma-ray discrimination in LiF/ZnS systems.

4.5 Method 4

Method 4 utilized a dynamic short gate – long gate technique. The short gate was defined as the integrated energy from the 35% rising edge to the 35% falling edge of each pulse. The long gate was defined as the integrated energy from the start of the short gate and extending five times as far as the short gate. The charge ratio was the value of the long gate divided by the sum of the long gate and the short gate, as in Equation 4.10.

Equation 4.10

$$\text{Charge Ratio} = \frac{\text{Long gate}}{\text{Long Gate+Short Gate}}$$

$$\text{Charge Ratio} = \frac{\int_{-0.35\text{Max}}^{5(+0.35\text{Max}+(-0.35\text{Max}))} \text{Pulse Energy}\ dt}{\int_{-0.35\text{Max}}^{5(+0.35\text{Max}+(-0.35\text{Max}))} \text{Pulse Energy}\ dt + \int_{-0.35\text{Max}}^{5(+0.35\text{Max}} \text{Pulse Energy}\ dt}$$

where +0.35Max is the 35% rising energy edge, and -0.35Max is the 35% falling energy edge. The charge ratio data set and fit double Gaussian function for Method 4 can be seen in Figure 4.6.

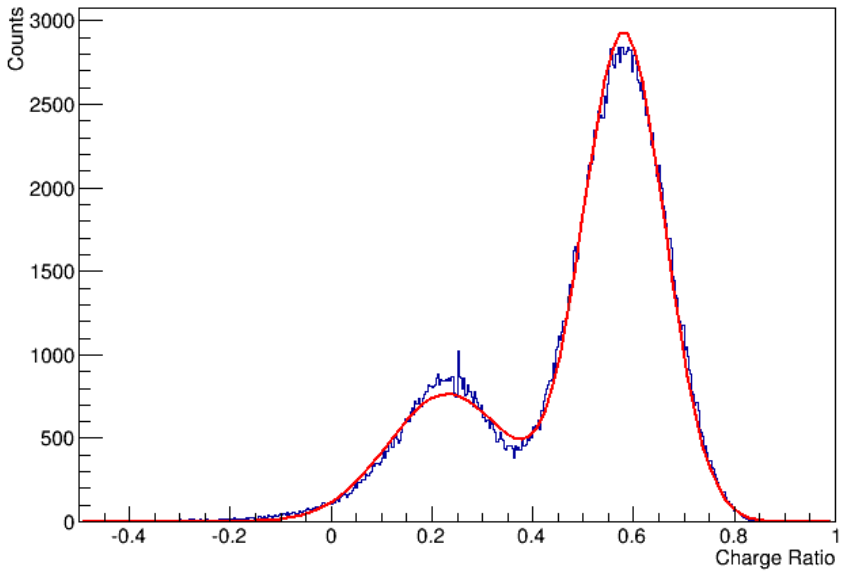

Figure 4.6 Waveforms were analyzed via Method 4 and counted as a function of their charge ratio (blue) and then fit with a double Gaussian function (red) which was used to quantify the neutron to gamma-ray separation from Method 4.

Pulses with charge ratios less than 0.3640 were counted as gamma rays; all other pulses were counted as neutrons. The double Gaussian function parameters associated with Method 4 can be seen in Table 4.9.

Table 4.9 Double Gaussian parameters for Method 4.

Parameters	Values
A	766 ± 4
σ_1	0.1201 ± 0.0007
μ_1	0.2314 ± 0.0007
B	2920 ± 8
σ_2	0.0813 ± 0.0002
μ_2	0.5807 ± 0.0002

Performance results for Method 4 can be seen in Table 4.10.

Table 4.10 Performance results for Method 4.

Results	Values
γFoM	0.736 ± 0.003
GRR	$4.15\times10^{-2} \pm 6\times10^{-4}$
Neutrons	209490
Gamma Rays	69971
Run Time (s)	45.7 ± 0.3

Method 4 was slow and provided inferior *γFoM* and *GRR* compared to most other methods. Method 4 had minimal promise for further development or implementation.

4.6 Method 5

Method 5 utilized a bin counting technique rather than an energy integration technique to distinguish between neutron and gamma-ray pulses. The charge ratio was replaced by counting the number of bins from peak energy to the 25% falling edge, as seen in Equation 4.11.

Equation 4.11 $\text{Falling Bin Count} = \sum_{i=\text{Max}}^{+0.25\text{Max}} \text{Pulse Energy}_i$

where +0.25Max is the 25% falling energy edge. The falling bin count data set and fit double Gaussian function for Method 5 can be seen in Figure 4.7.

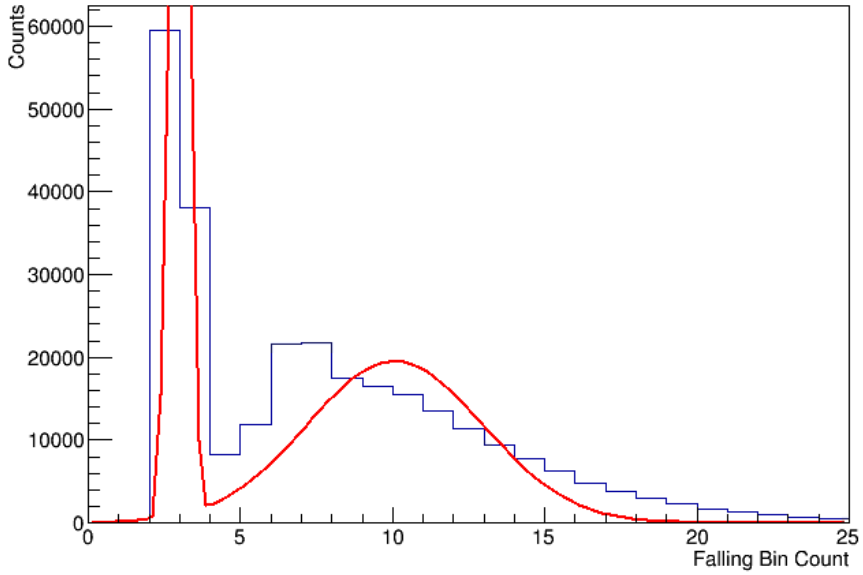

Figure 4.7 Waveforms were analyzed via Method 5 and counts as a function of width in bins (blue) and then fit with a double Gaussian function (red) which was used to quantify the neutron to gamma-ray separation from Method 5.

Pulses with bin counts less than 4 were counted as gamma rays; all other pulses were counted as neutrons. The double Gaussian function parameters associated with Method 5 can be seen in Table 4.11.

Table 4.11 Double Gaussian parameters for Method 5.

Parameters	Values
A	19540 ± 70
σ_1	2.892 ± 0.007
μ_1	10.07 ± 0.02
B	600000 ±200000
σ_2	0.22 ± 0.02
μ_2	2.977 ± 0.004

Performance results for Method 5 can be seen in Table 4.12.

Table 4.12 Performance results for Method 5.

Results	Values
γFoM	0.968 ± 0.007
GRR	$1.13\times10^{-2} \pm 5\times10^{-4}$
Neutrons	181799
Gamma Rays	97662
Run Time (s)	51 ± 1

Method 5 had an intermediate *γFoM* and *GRR* compared to most other methods, but it did have a long run time and its gamma-ray and neutron counts were significantly different from all other methods. The high quantization of Method 5 prevented it from having the level of detail required to accurately differentiate between neutron and gamma-ray pulses. If quantization of time bins could be reduced, such as through the use of shorter time bins, then Method 5 may be promising for further development, but 13.3 ns bins show little promise for further development or implementation.

4.7 Method 6

Method 6 distinguished between gamma-ray and neutron pulses by combining features from Method 3, Method 4, and Method 5. The long gate was calculated by integrating the pulse energy from the 8.4% rising energy to the 15% falling edge plus 3.66 times the number of bins from the 8.4% rising edge to the 15% falling edge. This values was added to 4.77 times the number of bins from the 8.4% rising edge to the 15% falling

edge squared. The charge ratio was calculated by dividing the long gate by the sum of the long gate and the peak energy, as seen in Equation 4.12.

Equation 4.12 $\text{Charge Ratio} = \frac{\text{Long Gate}}{\text{Long gate+Peak Energy}}$

$$\text{Charge Ratio} = (0.277 \int_{+0.084Max}^{-0.15Max+3.62(-0.15Max-(+0.084Max))} \text{Pulse Energy}\, dt + 4.79\big(-0.15Max - (+0.084Max)\big)^2)/(\text{Peak Energy} + 0.277 \int_{+0.084Max}^{-0.17Max+3.62(-0.15Max-(+0.084Max))} \text{Pulse Energy}\, dt + 4.79(-0.15Max - (+0.084Max))^2)$$

where +0.084Max is the 8.4% rising energy edge, -0.15Max is the 15% falling energy edge, and Peak Energy is the value of the bin with maximum energy. The charge ratio and the fit double Gaussian function for Method 6 can be seen in Figure 4.8.

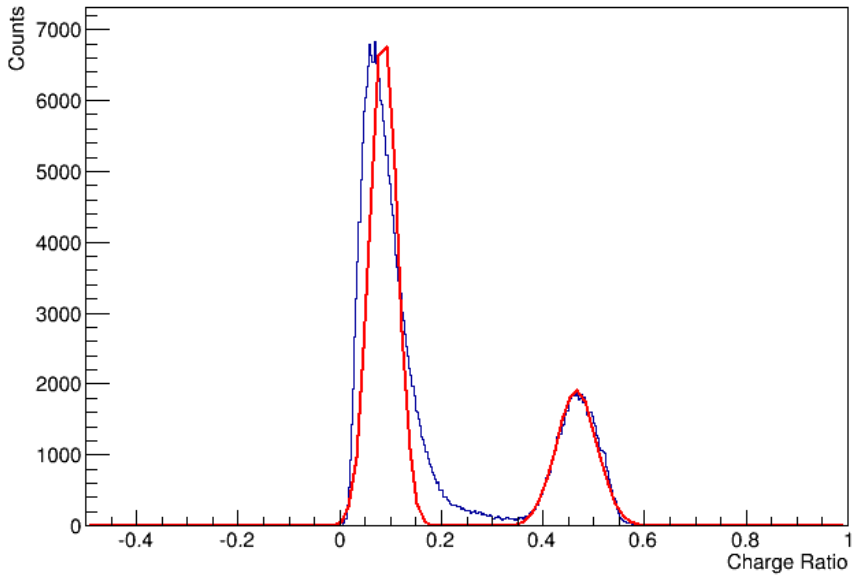

Figure 4.8 Waveforms were analyzed via Method 6 and counted as a function of their charge ratio (blue) and then fit with a double Gaussian function (red) which was used to quantify the neutron to gamma-ray separation from Method 6.

Pulses with charge ratio values less than 0.3400 were counted as gamma rays; all other pulses were counted as neutrons. The double Gaussian function parameters associated with Method 6 can be seen in

Table **4.13**.

Table 4.13 Double Gaussian parameters for Method 6.

Parameters	Values
A	6970 ± 20
σ_1	0.02681 ± 0.00003
μ_1	0.0858 ± 0.0001
B	1911 ± 9
σ_2	0.0400 ± 0.0001
μ_2	0.4659 ± 0.0002

Performance results for Method 6 can be seen in Table 4.14.

Table 4.14 Performance results for Method 6.

Results	Values
γFoM	2.42 ± 0.04
GRR	$6.0\times10^{-9} \pm 4\times10^{-10}$
Neutrons	214142
Gamma Rays	65319
Run Time (s)	55.5 ± 0.2

Method 6 had a superior γFoM and GRR compared to all other methods, and similar neutron and gamma-ray counts to most other methods, but also had the highest run time of any methods.

Because of the high potential of Method 6 for application, Method 6 was later refit with a Gaussian plus a skewed Gaussian function to better estimate the γFoM, as seen in Equation 4.8 and Equation 4.9, where the input into Equation 4.2 was modified to replace μ_1 with the mean of the skewed Gaussian ($Mean_1$), and replaced σ_1 multiplied by a constant with the FWHM of the skewed Gaussian. The Gaussian plus skewed Gaussian fit with the data set from Method 6 can be seen in Figure 4.9.

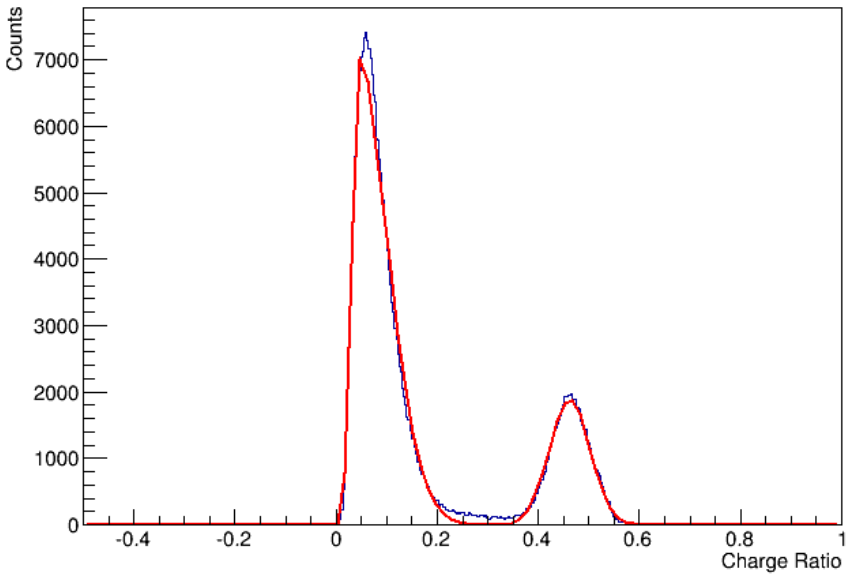

Figure 4.9 Waveforms were analyzed via Method 6 and counted as a function of their charge ratio (blue) and then fit with a Gaussian plus skewed Gaussian function (red) which was used to quantify the neutron to gamma-ray separation from Method 6.

Pulses with charge ratios less than 0.305332 were counted a gamma rays; all other pulses were counted as neutrons. The application of a skewed Gaussian can be seen to improve the fit between the function and the data set. The Gaussian plus skewed Gaussian

function parameters associated with Method 6 can be seen in Table 4.15, where α_1 is the skewness of the skewed Gaussian.

Table 4.15 Gaussian plus skewed Gaussian parameters for Method 6.

Parameters	Values
A	628 ± 1
σ_1	0.0667 ± 0.0002
μ_1	0.0298 ± 0.0001
α_1	6.75 ± 0.06
B	191 ± 1
σ_2	0.0402 ± 0.0001
μ_2	0.4619 ± 0.0002

Performance results for Method 6 with a skewed Gaussian plus Gaussian function can be seen in Table 4.16.

Table 4.16 Performance results for Method 6 with a skewed Gaussian plus a Gaussian fit.

Results	Values
γFoM	2.141 ± 0.004
GRR	$2.3\times10^{-7} \pm 1\times10^{-8}$
Neutrons	213981
Gamma Rays	65480
Run Time (s)	55.5 ± 0.2

Estimates of the *γFoM* and *GRR* worsened for Method 6 with a Gaussian plus Gaussian fit, but remain superior to all other PSD methods. Method 6 had some of the most promise for implementation as a method for gamma-ray discrimination in a LiF/ZnS system; however, it had a very high run time, and would be difficult to implement on an FPGA.

4.8 Coincidence Method

The coincidence method is a non-PSD method for discriminating against gamma rays that takes advantage of the fact that neutrons pulses in the detector stacks tend to be visible from longer distances away from the PMTs than gamma-ray pulses. Thermalized neutrons capturing in lithium have a Q-value of 4.78 MeV and produce ~160,000 photons from captures in LiF/ZnS, while fission gamma rays have ~0.9 MeV on average and produce ~75,000 photons from captures in LiF/ZnS [3, 39, 40]. Therefore neutron captures tend to produce brighter signals than gamma-ray captures. Demanding a coincidence between two PMTs on opposite sides of the detector stack can therefore be used to preferentially detect brighter neutron pulses compared to dimmer gamma-ray pulses.

Some advantages of the coincidence method are that it can be used alone or in conjunction with any PSD methods, it can allow some data acquisition systems to operate at decreased thresholds, more than overcoming the reduced count rate inherent to this method, and when it is used in conjunction with PSD, the PSD run time may be significantly reduced, as many of the pulses may be eliminated. Implementing higher gain or wider aperture PMTs may reduce the effectiveness of the coincidence method.

The *GRR* for the coincidence method was determined by sorting pulses with Method 6, because of the excellent separation between gamma rays and neutrons. A

106 ns coincidence window was applied. The ratio of gamma rays to neutrons in coincidence was compared to the ratio of gamma rays to neutrons in singles to determine the *GRR*. The charge ratio data set from Method 6 in singles and coincidence can be seen in Figure 4.10. The total number of counts in coincidence mode is seen to decrease since two pulses in coincidence are required for a single count.

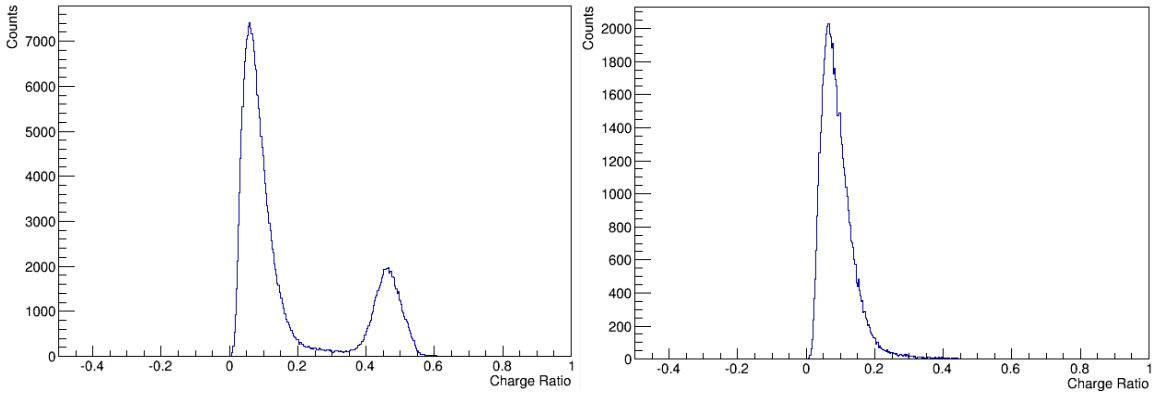

Figure 4.10 Waveforms collected from either PMT and analyzed via Method 6 (left) have a much larger gamma-ray region than waveforms that were only collected when coincidence was required between both PMTs and analyzed via Method 6 (right).

The gamma-ray pulse peak, clearly visible for singles pulses, was entirely gone for coincidence pulses. Because no gamma-ray pulse peak was visible, the same threshold of 0.305332 was used from Method 6 with a Gaussian plus a skewed Gaussian fit as a means to judge between gamma-ray pulses and neutron pulses. Performance results for Method 6 with the coincidence method can be seen in Table 4.17.

Table 4.17 Performance results for Method 6 with the coincidence method.

Results	Values
Neutrons	60718
Gamma Rays	373
Run Time (s)	30.2 ± 0.1

Averaging the neutron and gamma-ray counts from all PSD methods (excluding Method 5), a ratio of gamma rays to neutrons was estimated for this data set. The ratio of gamma-ray to neutron pulses from the coincidence method was compared to the ratio of gamma-rays to neutron pulses from PSD methods to determine the *GRR* of the coincidence method, as seen in Equation 4.13.

Equation 4.13 $$\text{PSD Gamma to Neutron Ratio} = \frac{\text{Gamma counts}}{\text{Neutron counts}} = \frac{66418+69390+67246+69971+65480}{213043+210043+212215+209490+213981} = 0.319715$$

$$\text{Coincidence Gamma To Neutron Ratio} = \frac{\text{Gamma Counts}}{\text{Neutron Counts}} = \frac{373}{60718} = 0.00614315$$

$$\frac{\text{Coincidence Gamma To Neutron Ratio}}{\text{PSD Gamma To Neutron Ratio}} = \frac{0.00614315}{0.319715} = 0.0192145$$

Comparing the gamma ray to neutron ratio of coincidence to singles provided a *GRR* of 1.92×10^{-2}, which is equivalent to a γFoM of 0.879.

Alternatively, the *GRR* was also estimated by manually counting the number of gamma-ray pulses in the set of coincident pulses. Since a prohibitively large number of pulses were in the data set, 1540 pulses were inspected, which included 10 pulses that were visually identified as being gamma-ray pulses. This gamma-ray to neutron ratio was compared to the gamma-ray to neutron ratio from singles pulses, as seen in Equation 4.14.

Equation 4.14 $\text{Coincident Gamma to Neutron Ratio} = \frac{10}{1530} = 0.00653695$

$$\frac{\text{Coincidence Gamma To Neutron Ratio}}{\text{Singles Gamma To Neutron Ratio}} = \frac{0.00653695}{0.319715} = 0.0204462$$

Comparing manually counted gamma-rays to neutrons provides a *GRR* of 2.04×10^{-2}, which is equivalent to a *γFoM* of 0.868.

Both techniques for estimating provided similar *GRR* values, which were averaged to a *GRR* of 1.98×10^{-2}, and an equivalent *γFoM* of 0.874.

The *GRR* and *γFoM* from the coincidence method may be superior to the results estimated, since the pulses counted as gamma-rays may have been neutron pulses with exceptionally short tails. A better estimate could have been reached if enough gamma-ray pulses were visible to produce a clear peak region in the charge ratios, which could have been achieved by dramatically increasing the gamma-ray to neutron ratio of the source(s). By the time this deficiency was discovered, the experimental set up that collected the original data sets had been dismantled. Because a minimum level of performance had been estimated, it was determined that rebuilding and rerunning the experiment was unnecessary.

4.9 Passive Shielding Method

Passive shielding is commonly used to reduce ionizing photon doses for a wide variety of applications. Passive shielding has the advantages that it can reduce gamma-ray and x-ray exposure to the detector system and operators, reduce gamma-ray contributions to pulse pile up affects, reduce background signals from the detector system, and reduce the total number of particles producing signals, allowing PSD methods with long run times to more easily operate. Passive shielding also tends to be inexpensive, and requires nothing

on the part of the operator to function, and requires minimal support and maintenance other than a sturdy structure to hold it.

The ability of materials to attenuate gamma-rays is roughly proportional to atomic number. The high density and low cost of lead and iron make lead and iron common gamma-ray and x-ray shielding materials. Lead and iron were the only passive shielding materials seriously considered for this project. Attenuation and build-up properties of materials change with gamma-ray energies, therefore 0.5, 1.0, 1.5, 2.0, 3.0, and 4.0 MeV gamma-rays were considered. Gamma-rays above ~4.0 MeV are uncommon from most fission sources and very rare from most non-fission sources and were therefore not considered here [40-42]. Gamma-rays are attenuated through Compton scattering, both reducing photon energy and redirecting photons away from the detector. The inverse of the mean free path (μ) of particles in a material is the linear attenuation coefficient. The total linear attenuation is a function of μ, material thickness (x), photon energy, and material. μx values for lead and iron can be seen in Table 4.18. In order to account for photons that are not removed by Compton scattering or that are directed into the detector as a result of scattering it is convenient to introduce a buildup factor $B(\mu x)$. The total photon dose φ (collided and uncollided) at a distance x from a monodirectional monoenergetic source $\varphi 0$ can be determined by Equation 4.15.

Table 4.18 Linear attenuation and mean free path data for lead and iron [43].

Photon Energy (MeV)	Linear Attenuation Coefficients (μ) (cm^{-1})	Mean Free Path (cm)	μx for 1.27 cm	μx for 2.54 cm	μx for 3.81 cm	μx for 5.08 cm
		Lead				
0.5	1.83	0.547	2.23	4.48	6.97	9.29
1.0	0.805	1.24	1.02	1.97	3.07	4.09
1.5	0.592	1.69	0.752	1.45	2.26	3.01
2.0	0.522	1.91	0.663	1.28	1.99	2.65
3.0	0.480	2.08	0.610	1.18	1.83	2.44
4.0	0.476	2.10	0.605	1.17	1.81	2.42
		Iron				
0.5	0.663	1.51	0.841	1.62	2.52	3.37
1.0	0.472	2.12	0.599	1.16	1.80	2.40
1.5	0.384	2.60	0.488	0.942	1.46	1.95
2.0	0.336	2.98	0.426	0.823	1.28	1.71
3.0	0.285	3.51	0.362	0.699	1.09	1.45
4.0	0.261	3.83	0.331	0.639	0.994	1.32

Equation 4.15 $\phi(x) = \phi_0 B(\mu x) e^{-\mu x}$ [40]

In principle the buildup factor can be applied to gamma-rays and neutrons, but will not be applied to neutrons here as the neutron removal cross sections of lead and iron are

low and lead and iron also provides a small amount of neutron moderation, providing little net change in neutron counts compared to gamma-ray counts [40].

B(μx) is tabulated for various *μx* values in Table 4.19, from Health Physics and Radiological Health, Table 6.8.1, with relevant values presented in Table 4.20.

Table 4.19 Gamma-ray exposure buildup factors *B(μx)* for lead and iron [44].

Photon Energy (MeV)	**μx**									
	0.5	1.0	2.0	3.0	4.0	5.0	6.0	7.0	8.0	10.0
					Lead					
0.5	1.14	1.24	1.39	1.52	1.62	1.71	1.80	1.88	1.95	2.10
1.0	1.20	1.38	1.68	1.95	2.19	2.43	2.66	2.80	3.10	3.51
2.0	1.21	1.40	1.76	2.14	2.52	2.91	3.32	3.74	4.17	5.07
3.0	1.23	1.40	1.73	2.10	2.50	2.93	3.40	3.89	4.41	5.56
4.0	1.21	1.36	1.67	2.02	2.40	2.82	3.28	3.79	4.35	5.61
					Iron					
0.5	1.48	1.99	3.12	4.44	5.96	7.68	9.58	11.7	14.0	19.1
1.0	1.41	1.85	2.85	4.00	5.30	6.74	8.31	10.0	11.8	15.8
2.0	1.35	1.71	2.49	3.34	4.25	5.22	6.25	7.33	8.45	10.8
3.0	1.32	1.64	2.28	2.96	3.68	4.45	5.25	6.09	6.96	8.80
4.0	1.30	1.57	2.12	2.68	3.29	3.93	4.60	5.31	6.05	7.60

Assuming a linear progression between adjacent B(μx) values, B(μx) values can be calculated for each μx values from Table 4.18. Referencing Table 4.18 and Table 4.19 and

applying weights from the μx values in Table 4.18, B(μx) values were calculated and are presented in Table 4.20.

Table 4.20 Gamma-ray exposure buildup factors for 1.27-5.08 cm of lead and iron.

Photon Energy (MeV)	**μx for 1.27 cm**	**μx for 2.54 cm**	**μx for 3.81 cm**	**μx for 5.08 cm**
		Lead		
0.5	1.43	1.68	1.88	2.05
1.0	1.39	1.69	1.97	2.21
1.5	1.30	1.56	1.80	2.05
2.0	1.27	1.52	1.76	2.01
3.0	1.27	1.47	1.67	1.89
4.0	1.24	1.42	1.61	1.82
		Iron		
0.5	1.83	2.76	3.81	5.00
1.0	1.50	2.05	2.65	3.31
1.5	1.37	1.76	2.19	2.63
2.0	1.30	1.60	1.93	2.26
3.0	1.23	1.46	1.70	1.93
4.0	1.20	1.39	1.57	1.75

With μx and $B(\mu x)$ values, assuming that gamma-ray flux is approximately equivalent to dose $\varphi(x)$, and assuming $\varphi_0 = 1$, gamma-ray flux can be calculated for various

photon energies and shielding thicknesses. This provides a *GRR* for given gamma-ray energies and shielding thicknesses, as presented in Table 4.21.

Table 4.21 Gamma-ray flux through lead shielding.

Photon Energy (MeV)	**φ(1.27)**	**φ(2.54)**	**φ(3.81)**	**φ(5.08)**
		Lead		
0.5	0.140	0.0161	1.77×10^{-3}	1.89×10^{-4}
1.0	0.499	0.219	0.0914	0.0370
1.5	0.612	0.346	0.189	0.101
2.0	0.655	0.403	0.240	0.141
3.0	0.689	0.435	0.269	0.165
4.0	0.678	0.425	0.263	0.162
		Iron		
0.5	0.788	0.513	0.305	0.173
1.0	0.822	0.618	0.438	0.301
1.5	0.841	0.663	0.507	0.373
2.0	0.848	0.684	0.536	0.411
3.0	0.858	0.709	0.572	0.453
4.0	0.861	0.716	0.580	0.465

Because the average prompt fission gamma-ray has an energy of approximately 0.93 MeV [40, 41], and the *GRR* between different photon energies is clearly not a linear progression, it will be assumed that most prompt fission gamma-rays are ~1 MeV.

Gamma-rays from neutron capture in cadmium and from non-fission disintegrations are dominated by significantly lower than 1 MeV energy gamma-rays [42, 45] therefore it will be assumed that most non-fission are ~0.5 MeV. These conservative *GRR* and *γFoM* equivalent values are presented in Table 4.22, where lead and iron are given in cm of shielding thickness.

Table 4.22 *GRR* and *γFoM* for 1.0 MeV photons with lead shielding.

Shielding Parameters	**1.27 cm**	**2.54 cm**	**3.81 cm**	**5.08 cm**
	Lead			
***GRR* (1 MeV)**	0.499	0.219	0.0914	0.0370
γFoM Equivalent (1 MeV)	0.00140	0.330	0.566	0.759
***GRR* (0.5 MeV)**	0.140	0.0161	1.77×10^{-3}	1.89×10^{-4}
γFoM Equivalent (0.5 MeV)	0.458	0.909	1.24	1.51
	Iron			
***GRR* (1 MeV)**	0.822	0.618	0.438	0.301
γFoM Equivalent (1 MeV)	-0.392[1]	-0.127[1]	0.0658	0.222
***GRR* (0.5 MeV)**	0.788	0.513	0.305	0.173
γFoM Equivalent (0.5 MeV)	-0.340[1]	-0.014[1]	0.216	0.401

[1] Because $\gamma FoM = \frac{\text{InverseErfc}(2\times GRR)}{2\sqrt{\ln(2)}}$, a negative *γFoM* indicates that less than half of the gamma ray are rejected. This would be a significant problem for PSD method since a higher ratio of gamma rays would be counted as neutrons than actual neutrons would be counted as neutrons. No such problem exists for shielding though.

Iron shielding was simulated with MCNP to estimate the effect of iron shielding on gamma ray mitigation. Gamma rays were generated in simulations and counted with a surface tally on the first LiF/ZnS sheets. The model universe ended just beyond the tally surface to prevent scattering and multiple counting of the same particles. A simple model was used to determine the effect of iron shielding on a pencil beam of monoenergetic gamma rays. A more realistic model was developed that incorporated an isotropic monoenergetic gamma-ray source as well as the relevant graphite, aluminum, and high density polyethylene from the LiNMC. The final model was identical to the realistic model but had 0.635 cm iron plates above and below the 2.54 cm thick iron ring. All models are depicted in Figure 4.11.

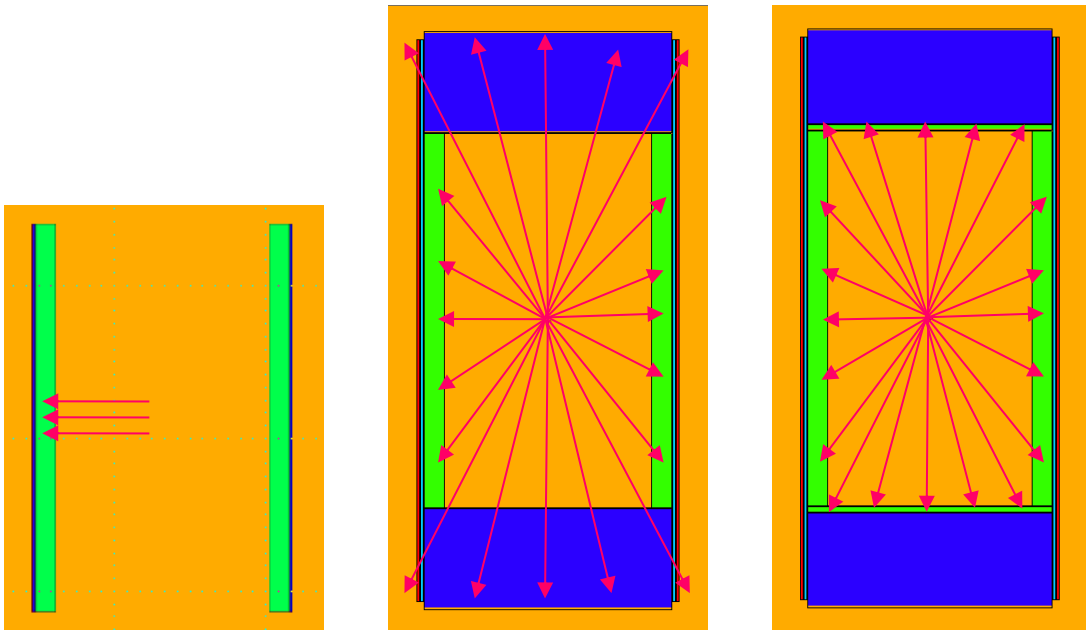

Figure 4.11 (Left) Simple iron shielding modeling with pencil beam neutron source. (Middle) Realistic iron shield model with isotropic source. (Right) Realistic iron shield model with top and bottom iron plate and an isotropic source.

Simulation results from these models can be seen in Figure 4.12.

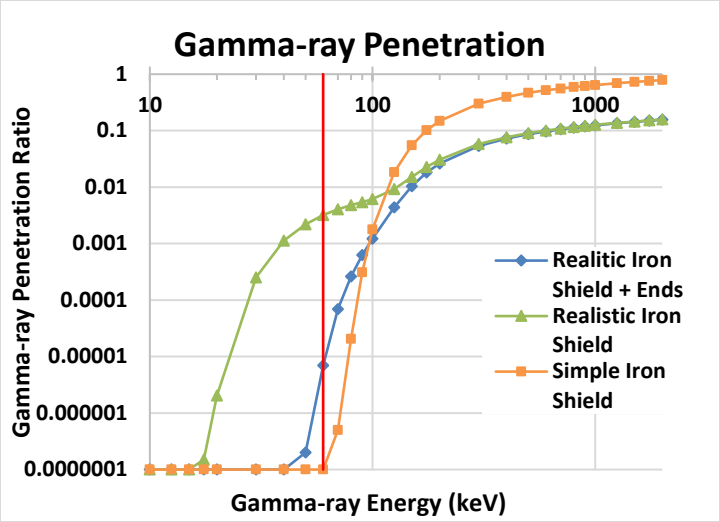

Figure 4.12 Simulation results of gamma-ray penetration probability as a function of gamma-ray energy and shielding configuration. Red line indicates dominant ^{241}Am gamma-ray peak.

Although low energy gamma-rays rarely penetrated through the iron shielding they were able to scatter off or penetrate through the graphite to reach the detection region. Even 0.635 cm iron plates above and below the sample chamber were sufficient to dramatically reduce low energy gamma rays from reaching the detector stacks. The top and bottom iron shielding reduced the 60 keV gamma-ray peak associated with ^{241}Am, which is often the dominant gamma-ray peak in plutonium samples, by more than two and half orders of magnitude.

The source in the realistic models was replaced with an energy spectrum from a steel encapsulated 198.73 g 98.25% pure plutonium metal source. Results from simulating the realistic models with the isotropic Pu source indicated that addition of 0.635 cm thick iron plates above and below the sample chamber reduced gamma-ray penetration by 9.3 ± 0.9 %.

These simulations indicate that placing 0.635 cm thick iron plates above and below the sample chamber will be very effective at reducing gamma-ray penetration from

minimally shielded or self-shielded sources, especially if ^{241}Am is the dominant gamma ray emitting isotope in the source. Conversely, top and bottom iron plates will provide minimal gamma-ray reduction from high shielded or self-shielded sources. Therefore even modest shielding plates immediately above and below the primary shield may greatly reduce gamma-ray penetration from some source, but provide minimal gamma-ray reduction from other sources.

Although lead and iron shielding provides inferior *GRR*s compared to other methods, they can reduce pulse pileup associated with high gamma-ray rates, do not require electronic or technical expertise, and can reduce dose to operators.

A 2.0 cm iron shield was selected for LiNMC construction based on the use of a 2.0 cm iron shield in the ENMC as a neutron scatterer, and based on the reduced weight of an iron shield (~140 kg) compared to a lead shield (~200 kg). MCNP simulation results indicate that a 2.0 cm iron ring in a full scale detector system will provide a *GRR*(1 MeV) of $0.5099 \pm 3\times10^{-4}$ and a *GRR*(0.5 MeV) of $0.6684 \pm 3\times10^{-4}$.

4.10 Gamma-Ray Detection Efficiency

A lower limit was set on the gamma-ray detection efficiency of the full scale system by investigating the rate of detected gamma-rays from gamma-ray sources with a 20.32 cm wide detector panel inside an aluminum box with PMTs on both ends, and extrapolating results to a full scale system. Gamma-ray detection efficiency calculations used the same data set used for PSD methods, as described near the beginning of this chapter and depicted in Figure 4.1.

Events were only counted and analyzed from one PMT channel to avoid event double counting. PSD Method 3 was used to distinguish between neutron and gamma-ray

events. Gamma-ray detection data for the active and background measurements can be seen in Table 4.23.

Table 4.23 Active and background gamma-ray detection data from 20.32 cm wide detector panel.

Source Configuration	Total Gamma-ray counts (γ)	Live Time(s)	Live Time corrected Gamma-ray Counts (γ/s)
Active	67,248	158.053	425.478
Background	68,016	262.243	259.362

Subtracting the background gamma-ray count rate from the active gamma-ray count rate gives a gamma-ray count rate just from the radiation sources of 166 γ/s.

Assuming the five radiation sources were an average of 1.27 cm from the center of the 72.12 cm × 20.32 cm active detector face and using the following equation for the solid angle of a rectangle:

Equation 4.16 $$\Omega = 4 \times \arcsin(\sin(\arctan(\frac{h}{2d})) \times \sin(\arctan(\frac{w}{2d})))$$

where *h* is the height of the active detector region, *w* is the width of the active detector region, and *d* is the distance from the center of the active detector region to the radiation source [46]. The detector subtends a solid angle of 5.77 steradians. A full scale detector system with four such detector panels that are each 10.16 cm from the central source subtends a solid angle of 12.0 steradians. The ratio of solid angles of a full scale system to this experimental system is 2.07 or a 207% increase in solid angle. Therefore a full scale system would be anticipated to measure

$$166.115 \frac{\gamma}{\text{s}} \times 2.07 = 344.670 \frac{\gamma}{\text{s}}$$

On the day of the measurement the radiation source had the activities displayed in Table 4.24.

Table 4.24 Gamma-ray detection efficiency radiation source isotope data [42, 47].

Isotope	Declared Activity (μCi)	Declaration Date	Activity on 23 march 2015 (μCi)	Mean Gamma-rays per decay (γ/decay)	Total Gamma-ray emission rate (γ/s)
Co-60	11.05	1 June 1999	1.382	2.000	102,300
Cs-137	9.630	1 Feb 2007	7.987	0.9304	275,000
Cs-137	10.18	1 June 2006	8.315	0.9304	286,200
Cs-137	10.16	1 June 2006	8.298	0.9304	285,700
Cf-252	19.00	15 Feb 2013	11.88	0.6348	260,100

Collectively the sources emitted 1.209×10^{6} γ/s. The anticipated gamma-ray detection efficiency limit (ε_γ) of a full scale system is given in Equation 4.17.

Equation 4.17 $$\varepsilon_\gamma = \frac{344.670\,\gamma_{detected/s}}{1.209\,x\,10^{6}\,\gamma_{emitted/s}} = 2.850\times10^{-4}\,\frac{\gamma_{detected}}{\gamma_{emitted}}$$

Since the system used for this experiment is optically inferior to the full scale system, lacking Enhanced Spectral Reflector, optical pads and a firm connection between the active detector region and the PMTs, a full scale system cannot be expected to have a lower gamma-ray detection efficiency than 2.850×10^{-4}. Further reducing the detected gamma-ray to emitted gamma-ray rate and therefore the misidentified gamma-ray to detected neutron rate requires coincidence between PMTs, PSD, shielding, or improving neutron detection efficiency. Measuring the gamma-ray detection efficiency of a full scale

system is required to fully account for misidentified gamma-rays and definitively determine gamma-ray and neutron detection efficiencies.

5 Effects of Gamma Rays on Neutron Multiplicity Counting

Multiplicity counting and coincidence counting rely on both time correlated and uncorrelated events to determine sample properties. Gamma-ray misidentification as neutrons may have different effects on sample property assays depending on the abundance of correlated and uncorrelated gamma-rays. Therefore experimental measurements and analysis were conducted to quantify the relative importance of correlated and uncorrelated gamma-rays on sample parameter assay.

Experiments used the NCC-12, a custom built neutron coincidence counter made from 12 Reuter Stokes # P/N PS P4 1634 204 ^{3}He tubes, as displayed in Figure 5.1, to measure counts from ^{252}Cf sources [48, 49]. A ^{3}He-based multiplicity counter was used because of its inherent insensitivity to gamma-rays. Time correlated signals, representing correlated gamma-rays, were introduced with an Ortec 905-4 (3" × 3") NaI(Tl) detector [50], as depicted in Figure 5.2. Uncorrelated signals, representing uncorrelated gamma-rays, were introduced with a CAEN DT5800D Dual Channel Desktop Digital Detector Emulator with channel correlation [51]. The uncorrelated signal experiment was physically set up similarly to Figure 5.2 but without the NaI(Tl) detector.

Figure 5.1 (Left) top view and (right) side view of the NCC12 multiplicity counter (set up for an unrelated polyethylene experiment) [49].

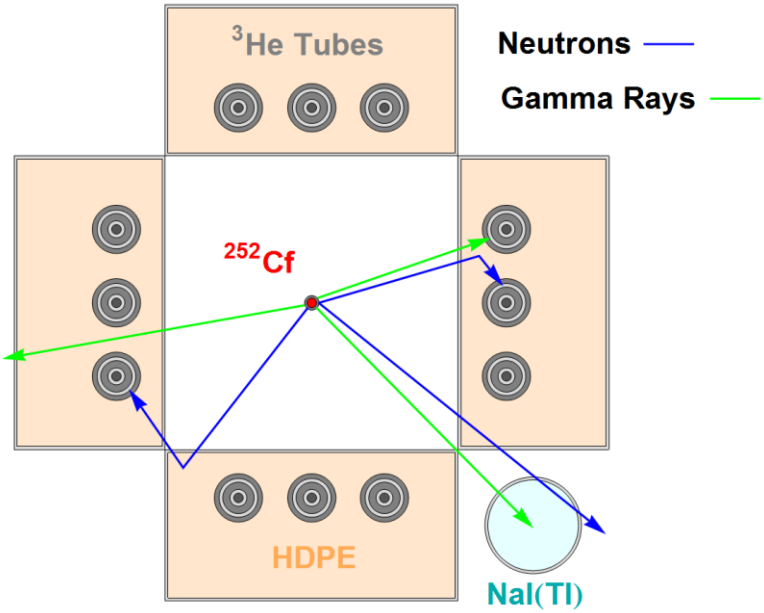

Figure 5.2 Diagram of NCC12 with NaI(Tl) detector. Neutrons (blue) scatter and thermalize in HDPE until they capture in the ^{3}He and produce signals, or escape. Gamma-rays absorbed in ^{3}He are discriminated against, and gamma-rays absorbed in NaI(Tl) produce time correlated signals.

Because neutron signals after a fission event follow a Rossi-alpha distribution, too short of a pre-delay results in excessive dead time from pulse pileup, and too long of a pre-delay results in missing excessive signals and decreasing detection efficiency. The optimal NCC-12 pre-delay was determined by measuring the doubles rate as a function of pre-delay and selecting the pre-delay with the maximum doubles rate. A ^{252}Cf neutron source was placed in the center of the NCC-12. Data sets were collected with a JSR-14 shift register [52] and analyzed with INCC 5.1.2 software [53]. The pre-delay was set to a value in the INCC software and data sets were collected for 10 minutes. This process was followed to collect doubles rate data sets over a range of pre-delays. Pre-delay and doubles rates data can be seen in Table 5.1. The NCC-12 pre-delay was set to 3.25 μs to maximize doubles.

Table 5.1 NCC-12 doubles rates as a function of pre-delay data.

Pre-delay (μs)	Doubles rate (Hz)
1.0	1382 ± 5
1.5	1386 ± 5
2.0	1403 ± 4
2.5	1411 ± 4
2.75	1417 ± 4
3.0	1423 ± 5
3.25	1428 ± 3
3.5	1402 ± 4
4.0	1207 ± 7
4.5	1071 ± 3
5.0	938 ± 2
5.5	851 ± 4

Because neutron signals from a fission event die-away exponentially with time, too short of a collection gate will result in missing excessive numbers of neutrons, and too long of a gate will result in accepting excessive numbers of accidental neutrons, increasing the multiplicity uncertainty. The optimal NCC-12 gate time was determined by measuring the doubles rate over a range of gate lengths and fitting a decay curve to those doubles, where the decay constant was the die-away time (τ). A ^{252}Cf neutron source was used along with a JSR-14 shift register and INCC 5.1.2 software. The gate length was set to a value in the

INCC software and data sets were collected for 10 minutes. This process was followed to collect doubles rate data sets over a range of gate lengths. Gate length and doubles rates data can be seen in Table 5.2.

Table 5.2 NCC-12 doubles rates as a function of gate length.

Gate Length (μs)	Doubles rate (Hz)
8	787 ± 2
16	924 ± 2
24	1043 ± 3
32	1152 ± 3
40	1242 ± 5.
48	1328 ± 5
56	1401 ± 5
58	1428 ± 6
60	1440 ± 8
64	1481 ± 3
72	1536 ± 7
80	1590 ± 5
88	1645 ± 7
86	1685 ± 6
104	1723 ± 6

Following the exponentially decaying neutron population, as modeled by Equation 2.1, an exponential decay was fit to the doubles rates as a function of gate length, as depicted in Figure 5.3. To account for measurement uncertainty, each data point was weighted by the inverse of the associated uncertainty squared. Following the exponential decay equation

Equation 5.1 $Doubles\ Rate = A + R^{-G/\tau}$,

values of *A*, *R*, and τ are given in Table 5.3 [5].

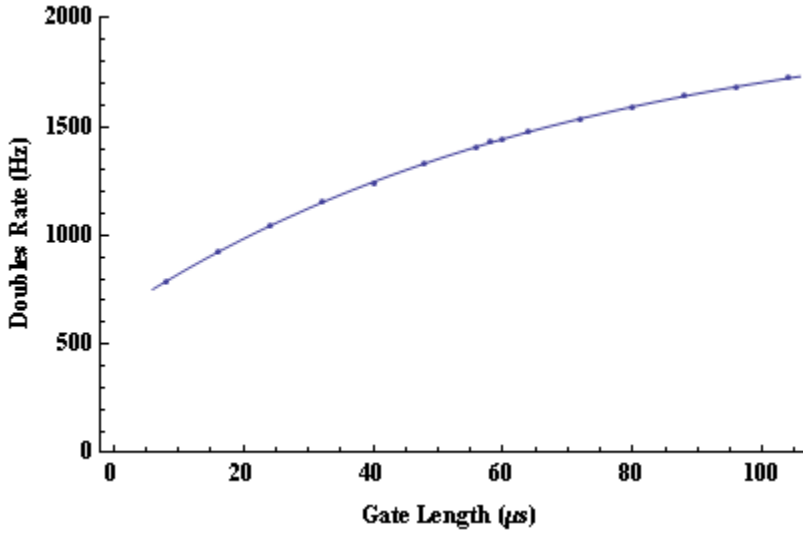

Figure 5.3 Exponential decay function fit to doubles rate as a function of gate length data set for the NCC-12.

Table 5.3 NCC-12 doubles rate as a function of gate length constants.

Constant	Value
A **(doubles per second)**	2050 ± 10
R **(doubles per second)**	1410 ± 10
τ **(micro seconds)**	70.7 ± 1.1

R is related to the gate width *G* and the neutron die-away time τ as $(1 - e^{G/\tau})$, and has a relative error that is minimized for a given τ by Equation 5.2, as derived by Norbert Ensslin in Passive Nondestructive Assay of Nuclear Material [12].

Equation 5.2 $\text{Gate Length} = \tau(e^{\text{Gate Length}/\tau} - 1)/2 \approx 1.256\tau$

For a die-away time of 70.7 μs the optimal gate length is 88.9 μs or approximately 89 μs, therefore 89 μs was be used for the NCC-12 gate length.

5.1 Uncorrelated Gamma Rays

Uncorrelated gamma rays, which are produced from non-fission disintegration events, may also be spuriously identified as uncorrelated neutrons, and result in sample property miscalculations. The following experiments and analysis were performed to document the effects of uncorrelated gamma-rays on neutron multiplicity counting. A neutron multiplicity counter assay was performed with a ^{3}He-based system, as a gamma-ray insensitive baseline, which was then followed by assays with the same system but with some gamma-ray-like signals being interpreted as neutron signals. These assays that interpreted some gamma-ray-like signals as neutron signals were compared to the baseline assay to determine the effects of misidentifying uncorrelated gamma-rays as neutrons on neutron multiplicity counting.

The NCC-12 was used as the base system, and a CAEN DT5800D Dual Channel Desktop Digital Detector Emulator with channel correlation was selected as a surrogate uncorrelated gamma-ray source for its ability to generate similar pulse shapes and rates as the NaI detector but with a Poisson distribution in time.

A ^{252}Cf source was placed in the center of the NCC-12 and a data set was collected from just the NCC-12 as a baseline for neutron events. Signals from the detector emulator were then added to the NCC-12 signal with a CAEN N454 Logic Fan-in/Fan-out. These combined signals were passed to an ORTEC GG8020 Octal Gate Generator to provide a TTL signal for the JSR-14 and analyzed with INCC 5.1.2 software. The rate of the detector emulator was changed to match the rate of the NaI detector under similar conditions and the measurements with the NCC-12 and detector emulator were repeated until there were detector emulator measurements for each NaI measurement for all ^{252}Cf source combinations (Strong, Weak, and Both). At the time of the assays, the Strong ^{252}Cf source had 9.58 μCi of activity and emitted 37,500 n/s, and the Weak ^{252}Cf source had 1.27 μCi of activity and emitted 3,710 n/s.

Given the singles, doubles, and triples rates and Equation 2.9 through Equation 2.16, the sample self-multiplication (M), ratio of (α, n) neutron to spontaneous fission neutrons (α), and mass were determined for the NCC-12 only data set and the NCC-12 with detector emulator data sets. A regression line was fit to the ratio of these sample parameter calculations to determine the effects of uncorrelated spurious neutron signals, with results that can be seen in Figure 5.4, Figure 5.5, and Figure 5.6. The regression line was calculated from all data points and was constrained to pass through the origin since the

origin represents the unmodified system, which must therefore have no measurement error from gamma-ray-like signals.

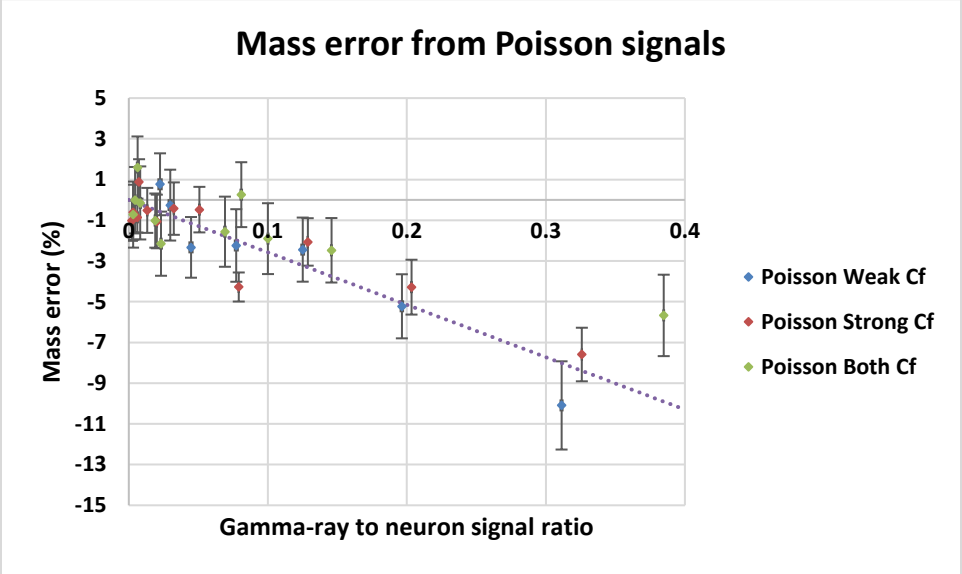

Figure 5.4 Sample mass error from uncorrelated gamma rays as a function of gamma-ray to neutron ratio from three different ^{252}Cf source combinations.

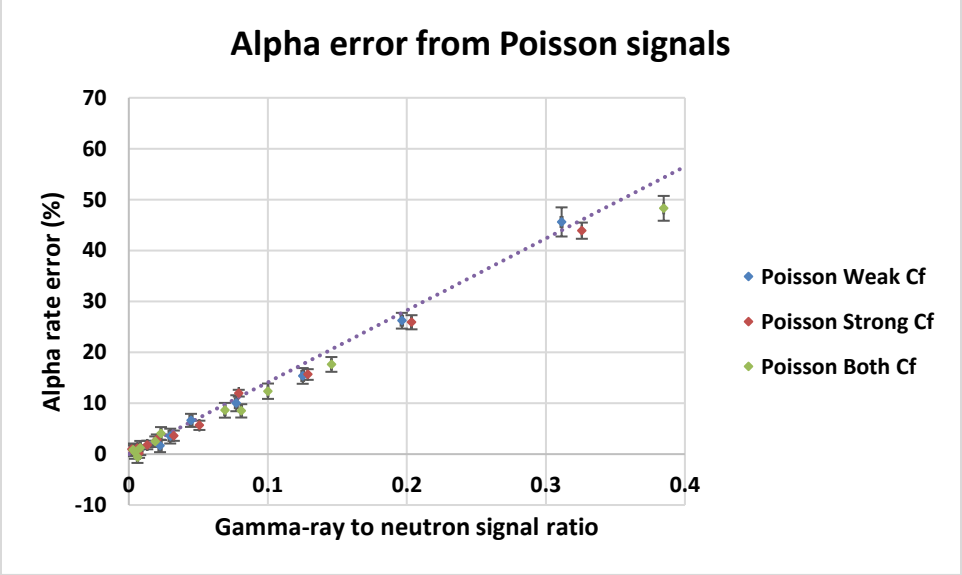

Figure 5.5 Sample *alpha* error from uncorrelated gamma rays as a function of gamma-ray to neutron ratio from three different ^{252}Cf source combinations.

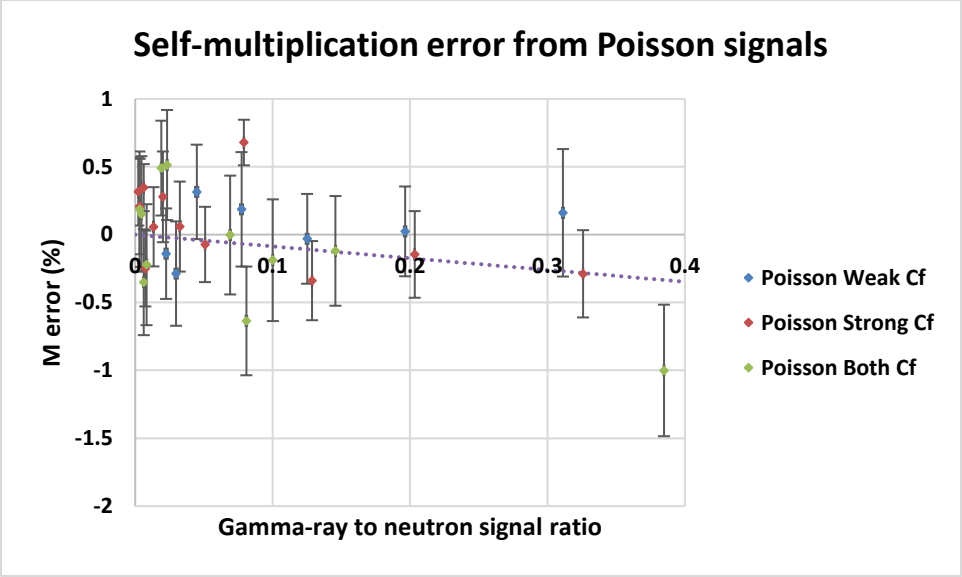

Figure 5.6 Sample self-multiplication error from uncorrelated gamma rays as a function of gamma-ray to neutron ratio from three different ^{252}Cf source combinations.

The regression lines were of the form

Equation 5.3 $$Error\ (\%) = A \times \frac{gamma\text{-}ray\ signall\ rate}{total\ neutron\ signal\ rate},$$

with results that can be seen in Table 5.4. There is no constant term because the regression line was constrained to pass through the origin so that the zero point would correspond with no assay error from gamma-ray-like signals.

Table 5.4 Sample parameter error coefficients from uncorrelated gamma-rays.

Sample Parameter	$A_{uncorrelated}$	χ^2/degree of freedom
M	-0.868 ± 0.108	5.47
α	141 ± 4	0.489
Mass	-25.8 ± 0.77	0.430

Spurious neutrons from uncorrelated gamma-ray signals have a strong tendency to produce mass underestimates, a weak tendency to produce self-multiplication underestimates, and a strong tendency to produce α overestimates.

5.2 Correlated Gamma Rays

Determining the effects of correlated gamma rays on sample assays involves a comparison of assays with and without gamma-ray-like signals, and a deconvolution of the correlated and uncorrelated gamma-ray signals, since the ^{252}Cf sources produced a combination of correlated and uncorrelated gamma rays.

A similar set of measurements was conducted for a combination of correlated and uncorrelated gamma-ray signals from ^{252}Cf sources as for the uncorrelated gamma-ray-like signals above. The previous baseline assay with the NCC-12 system was compared to assays of the same systems but with some gamma-ray signals being interpreted as neutron signals. These assays that interpreted some gamma-ray signals as neutron signals were compared to the baseline assay to determine the effects of misidentifying ^{252}Cf gamma-rays as neutrons on neutron multiplicity counting.

A NaI(Tl) detector was selected as a gamma-ray detector because of its reasonably short scintillation decay time, good gamma-ray detection efficiency, neutron insensitivity, and availability. The detected gamma-ray rate was controlled by moving the NaI(Tl) detector away from the ^{252}Cf sources. Since the location of the NaI(Tl) detector effected the neutronics of the system, a new baseline assay was also performed for each NaI(Tl) detector location. Otherwise the procedure, equipment, and settings were identical to those used for the uncorrelated gamma-ray-like assays above.

Given the singles, doubles, and triples rates and Equation 2.9 through Equation 2.16, *M*, *alpha*, and *mass* were calculated for the NCC-12 only data sets and the NCC-12 with NaI data sets. A regression line was fit to the ratio of these sample parameter calculations to determine the effects of time correlated spurious neutron signals, with results that can be seen in Figure 5.7, Figure 5.8, and Figure 5.9. The regression line was calculated from all data points and was constrained to pass through the origin since the origin represents the unmodified system, which must therefore have no measurement error from gamma-ray-like signals.

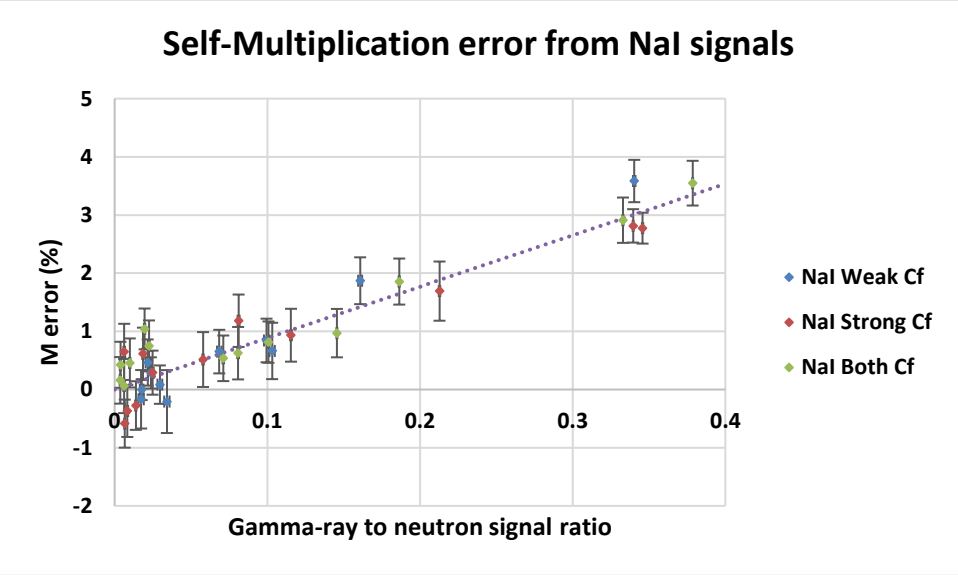

Figure 5.7 Sample self-multiplication error from gamma rays as a function of gamma-ray to neutron ratio from three different ^{252}Cf source combinations.

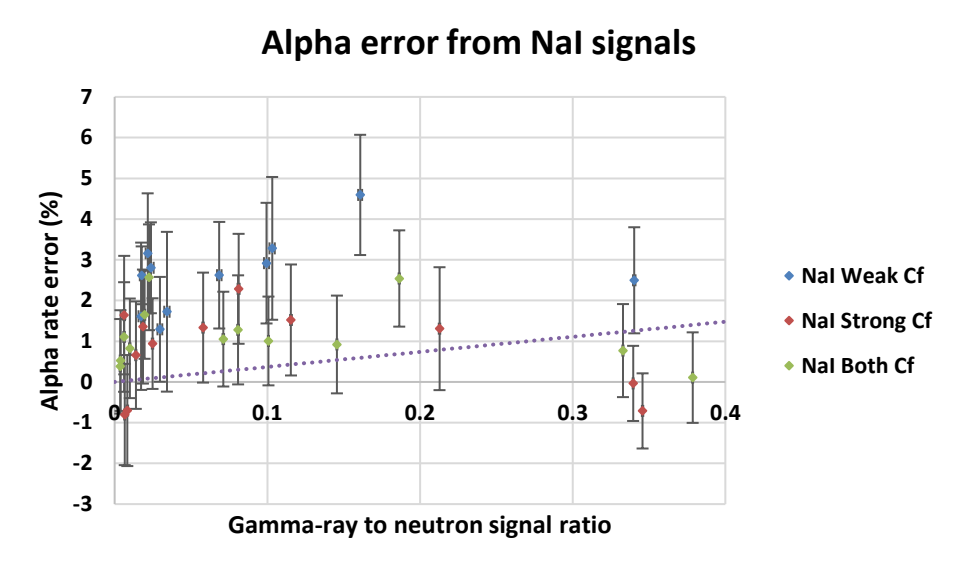

Figure 5.8 Sample *alpha* error from gamma rays as a function of gamma-ray to neutron ratio from three different ^{252}Cf source combinations.

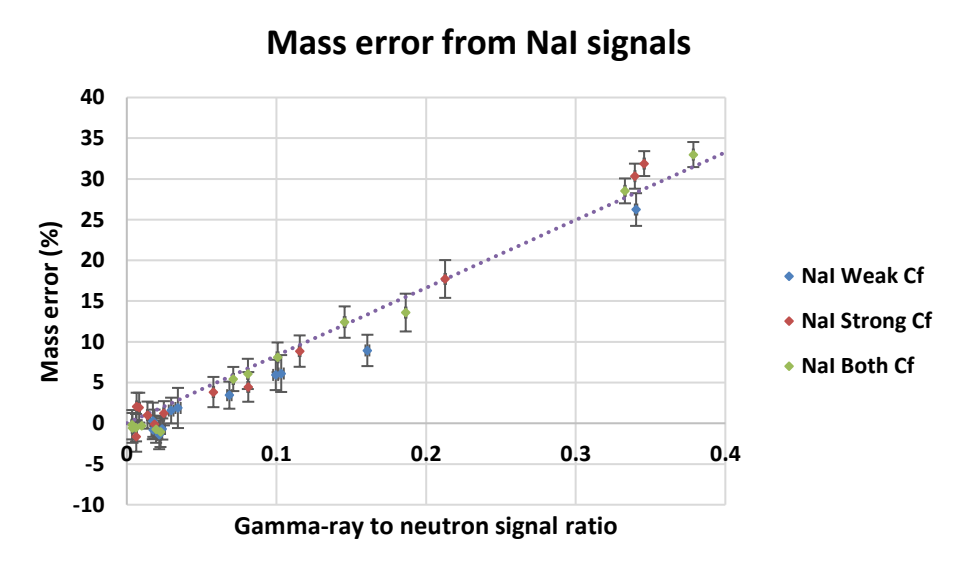

Figure 5.9 Sample mass error from gamma rays as a function of gamma-ray to neutron ratio from three different ^{252}Cf source combinations.

The regression lines were of the same form as Equation 5.3,

$$Error\ (\%) = A \times \frac{gamma\text{–}ray\ signal\ rate}{total\ neutron\ signal\ rate},$$

with results that can be seen in Table 5.5. There is no constant term because the regression line was constrained to pass through the origin so that the zero point would correspond with no assay error from gamma-ray-like signals.

Table 5.5 Sample parameter error coefficients from ^{252}Cf gamma-rays.

Sample Parameter	$A_{convolved}$	χ^2/degree of freedom
M	8.84 ± 0.39	0.737
α	3.70 ± 1.73	22.6
Mass	83.2 ± 2.3	0.401

Spurious neutrons from ^{252}Cf gamma-ray signals have a high tendency to produce mass overestimates, a weak tendency to produce self-multiplication overestimates, and a weak and highly uncertain tendency to produce α overestimates.

Cf-252 sources emit a combination of correlated and uncorrelated gamma rays, therefore the uncorrelated gamma rays must be deconvolved to isolate the effects of correlated gamma-rays on parameter measurements. The deconvolution was performed by collecting a neutron time stamp data set from the NCC-12, then artificially adding combinations of correlated and uncorrelated events to the time stamp data set, and adjusting the ratio of artificial correlated to uncorrelated time stamps to match parameter predictions based on results from Table 5.5. This ratio of correlated to uncorrelated gamma rays was used to deconvolve the uncorrelated gamma-rays from the ^{252}Cf sample parameter error coefficients.

The NCC-12 with the JSR-14 collected data sets for 10 minutes with a ^{252}Cf source. This data stream was split into two identical data streams with an ORTEC GG8020 Octal

Gate Generator. One data stream was passed to the INCC software while the other data stream was passed to the Pixie-4. The data streams to the INCC and Pixie-4 were both analyzed to determine the singles, doubles, and triples moments and correction factors were applied to the Pixie-4 data stream to ensure that the singles, doubles, and triples moments matched between both systems, as seen in Table 5.6.

Table 5.6 Neutron multiplicity moments and correction factor from the INCC and Pixie-4.

Sample Parameter	INCC	Pixie-4	Correction Factor
Singles Moment	762 ± 2	758 ± 1	1.005 ± 0.002
Doubles Moment	204 ± 1	199.2 ± 0.7	1.024 ± 0.007
Triples Moment	40.6 ± 0.6	36.1 ± 0.5	1.12 ± 0.02

The minor discrepancies between singles, doubles, and triples moments were assumed to result from dead time differences between the two systems.

Since prompt and delayed gamma rays from fission events are emitted approximately instantaneously and have much shorter die-away times than neutrons in the NCC-12, they may cause multiplicity counting to start before the first neutron from a fission is counted. From Figure 5.10 and Figure 5.11, it can be seen that most prompt gamma-rays are emitted within a few nanoseconds of fission and most delayed gamma-rays are emitted within a few microseconds of fission, which may collectively be misidentified as a single neutron event before any of real neutrons have thermalized and captured [54, 55].

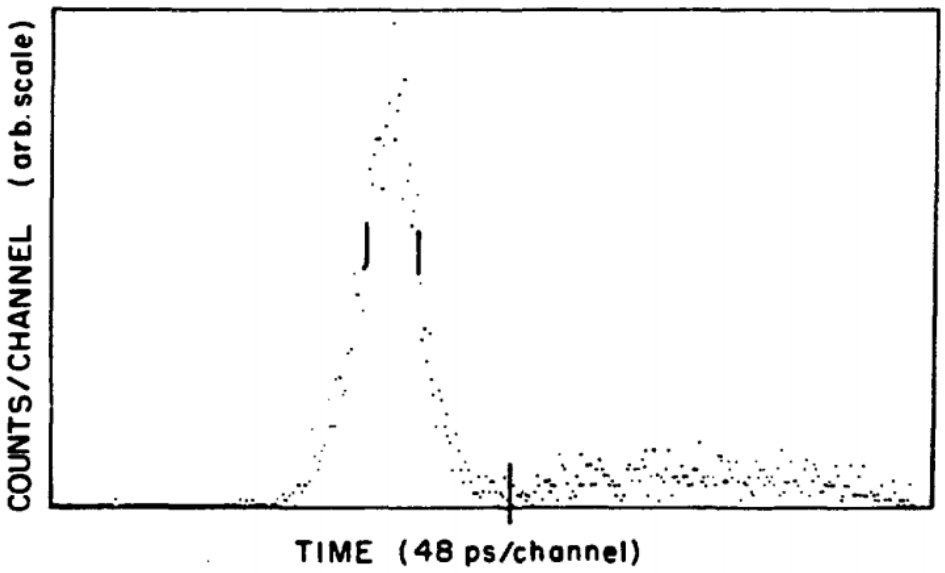

Figure 5.10 Time distribution of pulses following Cf-252 spontaneous fission. The upper two markers indicate a resolution of 1 nanosecond at half maximum. The lower marker indicates the approximate point of partition between the gamma-rays and fast neutrons [55].

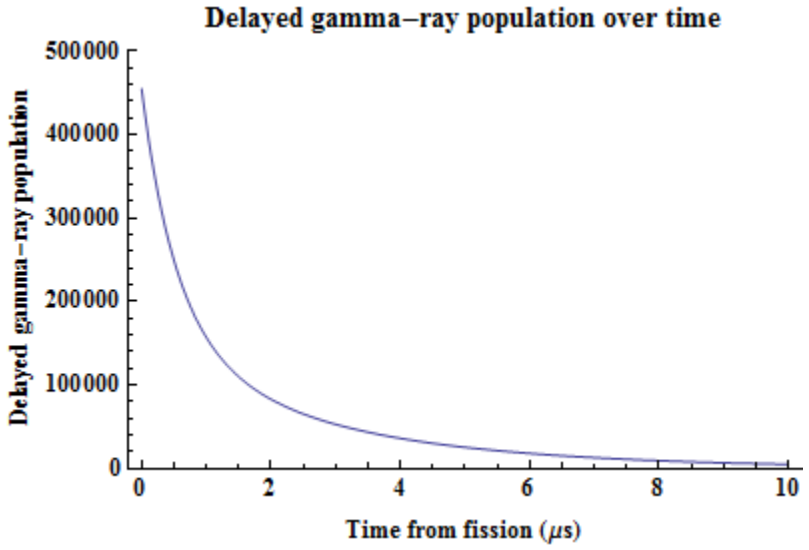

Figure 5.11 Time distribution of delayed gamma-ray population following Cf-252 spontaneous fission [54].

Since the majority of all correlated gamma rays are emitted within a few nanoseconds of fission, and the majority of the delayed gamma-rays are emitted within a few microseconds of fission, long before most neutrons have thermalized and captured, correlated gamma rays were assumed to produce a pre-trigger relative to groups of neutron events. Correlated gamma-ray events were simulated by modifying the Pixie-4 time stamp list with an additional time stamp before each set of timestamps that occurred within one gate length. Uncorrelated gamma-rays were simulated by modifying the Pixie-4 time stamp list by adding Poisson distributed time stamps over the length of the entire time stamp list.

Initially the Pixie-4 time stamp data was only modified with artificial uncorrelated events from Table 5.4 and correction factors from Table 5.6. Measured INCC and artificially modified Pixie-4 results matched each other with results that can be seen in Table 5.7.

Table 5.7 Neutron multiplicity moments and parameter errors between INCC and Pixie 4 data with artificial correlated events.

Sample Parameter	INCC	Pixie-4 + Uncorrelated events
Singles Moment	762 ± 2	918 ± 1
Doubles Moment	204 ± 1	204 ± 1
Triples Moment	40.6 ± 0.6	40.7 ± 0.3
***Mass* Difference (%)**	0.62 ± 1.25	
***Alpha* Difference (%)**	0.74 ± 3.51	
***M* Difference (%)**	-0.058 ± 0.251	

Agreement between measured INCC and modified Pixie-4 data sets gave confidence that modifying Pixie-4 data set with extra time stamps was a viable method of simulating gamma-ray events in data.

Since the ratio of detected correlated to uncorrelated gamma-ray events was unknown and the pre-trigger time was unknown, the difference between predicted results from Table 5.5 and artificial results were compared over a range of correlation ratios and pre-trigger times for *mass*, *alpha*, and *M* as seen in Figure 5.12, Figure 5.13, and Figure 5.14, where red planes mark where artificial data sets and measured data set results match.

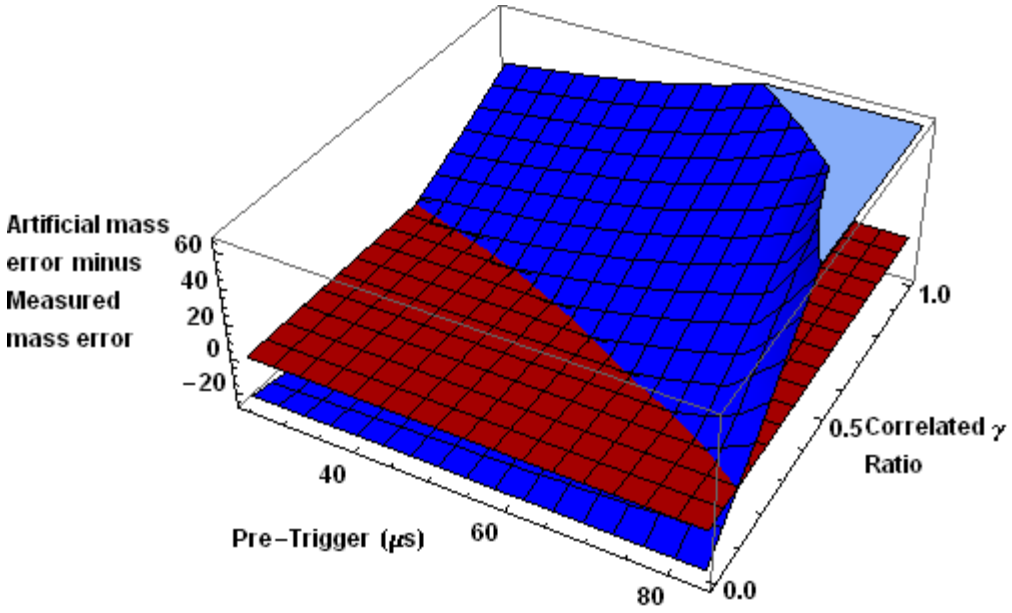

Figure 5.12 Artificial mass error minus measured mass error as a function of pre-trigger time and the ratio of correlated gamma-rays to uncorrelated gamma-rays. Red plane displayed to indicate where artificial mass error and measured mass error have identical values.

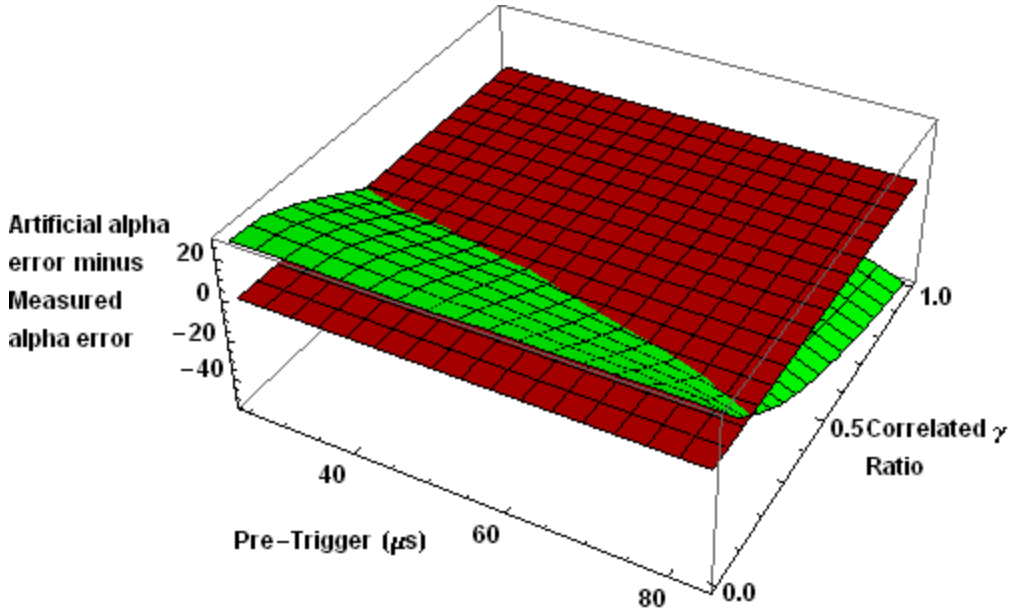

Figure 5.13 Artificial *alpha* error minus measured *alpha* error as a function of pre-trigger time and the ratio of correlated gamma rays to uncorrelated gamma rays. Red plane displayed to indicate where artificial *alpha* error and measured *alpha* error have identical values.

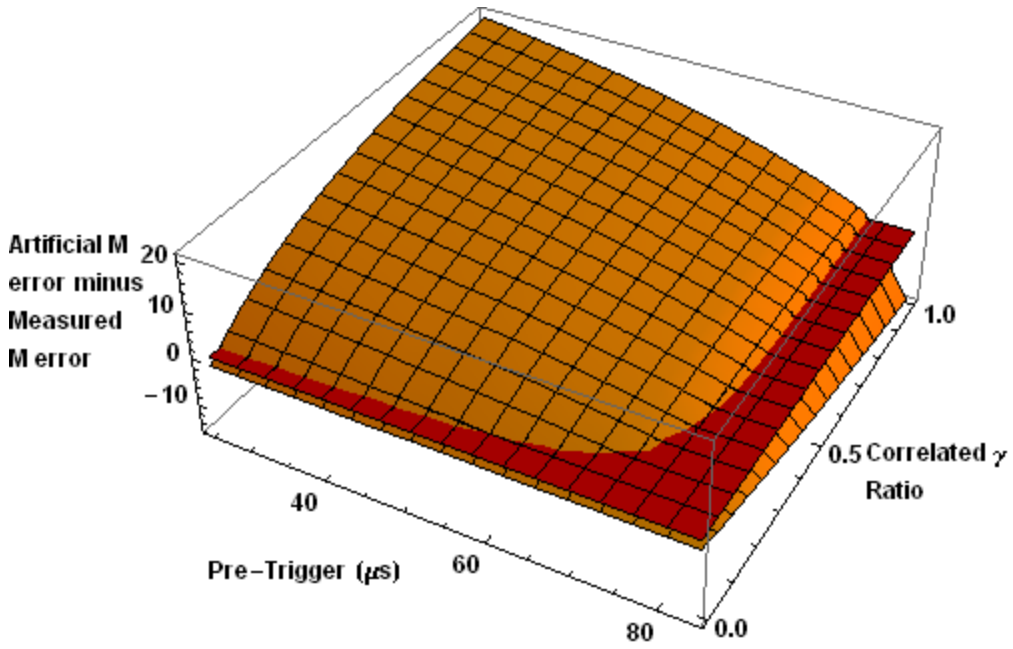

Figure 5.14 Artificial self-multiplication error minus measured self-multiplication error as a function of pre-trigger time and the ratio of correlated gamma-rays to uncorrelated gamma-rays. Red plane displayed to indicate where artificial self-multiplication error and measured self-multiplication error have identical values.

All parameter difference results were overlaid to determine the unique correlation ratio and pre-trigger time where all parameter differences were simultaneously identical between artificial and measured results, as seen in Figure 5.15 and Figure 5.16.

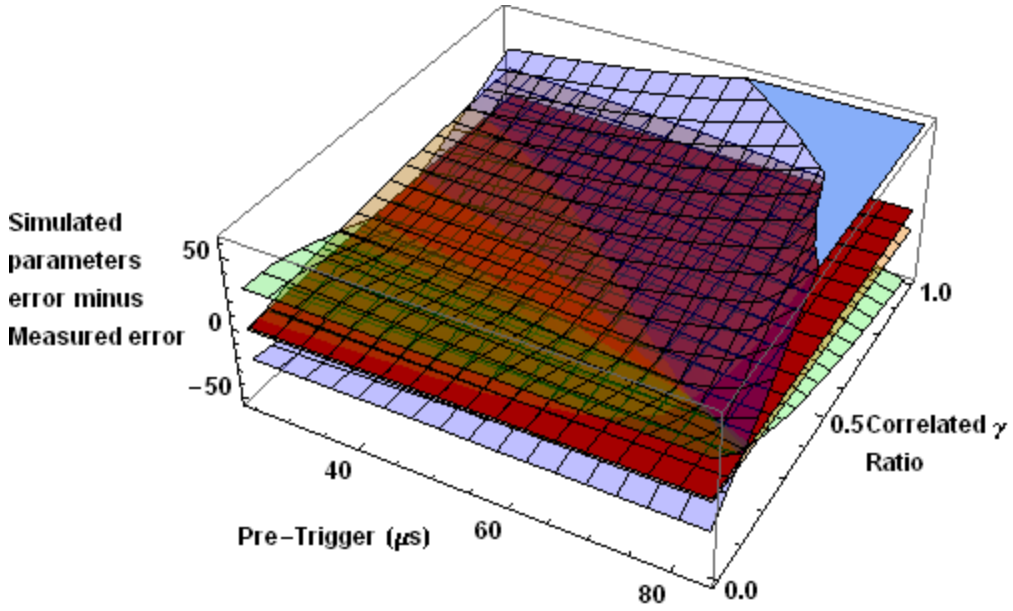

Figure 5.15 Diagonal view of all artificial parameter errors minus measured parameter errors overlaid. *Mass* is displayed in blue, *alpha* is displayed in green, *M* is displayed in orange, and a red plane indicates where artificial and measured values are identical.

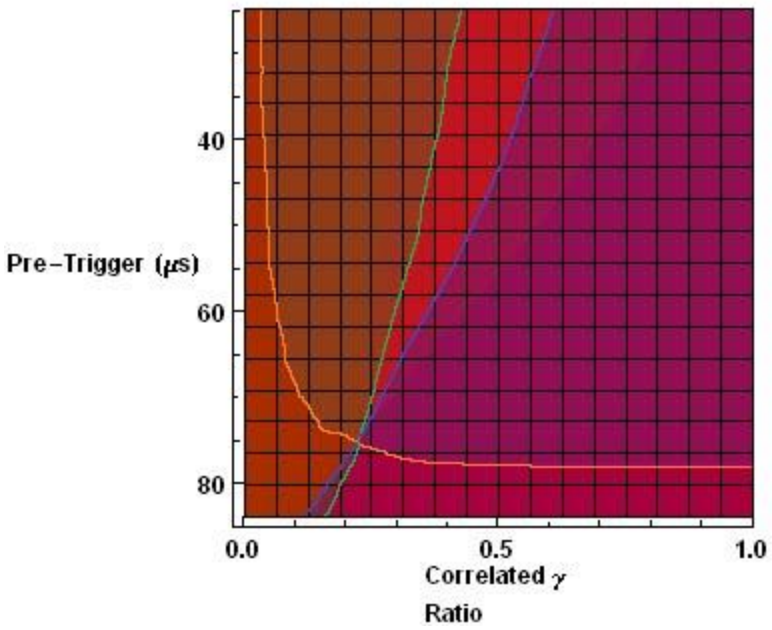

Figure 5.16 Top view of all artificial parameter errors minus measured parameter errors overlaid with intersection lines traced. *Mass* is displayed in blue, *alpha* is displayed in green, *M* is displayed in orange, and a red plane indicates where artificial and measured values are identical.

Correlation ratio and pre-trigger points around the intersection of the difference plots and the zero difference plane were investigated and a correlated to uncorrelated gamma-ray ratio of 0.226 ± 0.002 with a pre-trigger time of 74.8 μs was discovered as an optimal intersection point. Measured INCC and the Pixie-4 data set that was modified with a 0.226 correlation ratio and a 74.8 μs pre-trigger time results matched with each other with results that can be seen in Table 5.8.

Table 5.8 Neutron multiplicity moments and parameter errors between INCC and Pixie-4 data with artificial gamma-rays with a 0.226 correlation ratio and 74.8 μs pre-trigger.

Sample Parameter	INCC	Pixie-4 + Artificial events
Singles Moment	762 ± 2	918 ± 1
Doubles Moment	204 ± 1	254.1 ± 0.6
Triples Moment	40.6 ± 0.6	54.7 ± 0.3
***Mass* Difference (%)**	0.184 ± 2.23	
***Alpha* Difference (%)**	0.0238 ± 1.59	
***M* Difference (%)**	0.176 ± 0.206	

Because the convoluted gamma-ray error coefficient ($A_{convoluted}$) is a linear combination of the correlated gamma-ray error ($A_{correlated}$) and the uncorrelated gamma-ray error ($A_{uncorrelated}$),

Equation 5.4 $A_{convoluted} = (1 - CorrelationRatio)A_{correlated} + CorrelationRatio \times A_{uncorrelated}$,

the deconvolved correlated gamma-ray error coefficient ($A_{correlated}$) is given by Equation 5.5.

Equation 5.5 $A_{correlated} = \frac{A_{convoluted} - (1 - Correlation\ Ratio) \times A_{uncorrelated}}{Correlation\ Ratio}$

The results for the *mass*, *alpha*, and *M* error coefficients for correlated gamma-ray effects on sample assay can be seen in Table 5.9.

Table 5.9 Sample parameter error coefficients from correlated gamma-rays.

Sample Parameter	$A_{correlated}$
M	42.1 ± 1.6
α	-467 ± 18
Mass	456 ± 11

Spurious neutrons from correlated gamma-ray signals have a very high tendency to produce mass overestimates, a high tendency to produce self-multiplication overestimates, and a very strong and tendency to produce *α* underestimates.

5.3 Correlated and Uncorrelated Gamma-Ray Effects Applications

Gamma rejection ratio requirements for each sample parameter can be determined from Equation 5.3 as a function of desired assay uncertainty (*δMass*, *δα*, or *δM*), total neutron signal rate (*N*), neutron and gamma-ray detection efficiency (ε_n, ε_γ), and total correlated and uncorrelated gamma-ray rates ($\gamma_{cor}, \gamma_{un}$), as seen in Equation 5.6, Equation 5.7, and Equation 5.8.

Equation 5.6 $$GRR = \frac{\delta Mass\ (\%) \times N\varepsilon_n}{\varepsilon_\gamma}(456\gamma_{cor} - 25.8\gamma_{un})^{-1}$$

Equation 5.7 $$GRR = \frac{\delta \alpha\ (\%) \times N\varepsilon_n}{\varepsilon_\gamma}(-467\gamma_{cor} + 141\gamma_{un})^{-1}$$

Equation 5.8 $$GRR = \frac{\delta M\ (\%) \times N\varepsilon_n}{\varepsilon_\gamma}(42.1\gamma_{cor} - 0.868\gamma_{un})^{-1}$$

From Equation 5.3, *Error (%)*, becomes the desired parameter uncertainty limit, the gamma-ray signal rate is replaced with

If correlated and uncorrelated gamma-ray to neutron rates are approximately constant for each sample type, such as PuO, Pu metal, LANL salt scrubs, etc. then Equation

5.6, Equation 5.7, and Equation 5.8 can be used along with a gross gamma ray rate measurements to determine the *GRR* requirement for each sample type, parameter of interest, and assay accuracy. If correlated and uncorrelated gamma-ray to neutron rates are not approximately constant for each sample type, the correlated and uncorrelated gamma-ray rates will need to be ascertained to determine *GRR* requirement for each sample, parameter of interest and assay accuracy. If the system's *GRR* is insufficient for some samples, then a lead insert or other modification could be applied specifically for high error sample types.

Knowledge of parameter error may also be used to compensate for gamma-ray induced error, allowing for reduced gamma-ray error regardless of *GRR*. If a system is capable of actively discriminating between gamma-rays and neutrons, and the neutron counting efficiency and gamma-ray counting efficiency are known, and the ratio of correlated to uncorrelated gamma rays in approximately uniform, then for every identified gamma-ray a known number of gamma-rays will be misidentified and their effect on the sample assay can be determined. If the effects of gamma-rays on sample assay are known then they can be accounted for and the parameters adjusted to compensate for the presence of misidentified gamma rays.

Parameter assay error can also be determined as a function of *GRR*, as seen in Equation 5.9, Equation 5.10, and Equation 5.11.

Equation 5.9 $\delta Mass\ (\%) = \varepsilon_\gamma GRR \frac{456\gamma_{cor} - 25.8\gamma_{un}}{N\varepsilon_n}$

Equation 5.10 $\delta\alpha\ (\%) = \varepsilon_\gamma GRR \frac{-467\gamma_{cor} + 141\gamma_{un}}{N\varepsilon_n}$

Equation 5.11 $\delta M\ (\%) = \varepsilon_\gamma GRR \frac{42.1\gamma_{cor} - 0.868\gamma_{un}}{N\varepsilon_n}$

For example, given a sample this is 0.0134 w% ^{238}Pu, 93.8143 w% ^{239}Pu, 5.9389 w% ^{240}Pu, 0.1797 w% ^{241}Pu, and 0.1118 w% ^{241}Am, which has an uncorrelated gamma-ray rate of 1.6×10^{11} Hz, a correlated gamma-ray rate of 1.7×10^{5} Hz (assuming that all of the correlated gamma rays from a fission event can only misidentified as a single neutron), and a neutron rate of 4.8×10^{5} Hz, and assuming a detector with ε_γ of 1.0×10^{-6}, ε_n of 0.50, and a *GRR* of 0.01, then assay uncertainties would be as follows:

$$\delta Mass\ (\%) = 1.0 \times 10^{-6} \times 0.01 \frac{456 \times 1.7 \times 10^{5} - 25.8 \times 1.6 \times 10^{11}}{0.50 \times 4.8 \times 10^{5}} = -0.17\%$$

$$\delta \alpha\ (\%) = 1.0 \times 10^{-6} \times 0.01 \frac{-467 \times 1.7 \times 10^{5} + 141 \times 1.6 \times 10^{11}}{0.50 \times 4.8 \times 10^{5}} = 0.94\%$$

$$\delta M\ (\%) = 1.0 \times 10^{-6} \times 0.01 \frac{42.1 \times 1.7 \times 10^{5} - 0.868 \times 1.6 \times 10^{11}}{0.50 \times 4.8 \times 10^{5}} = -0.0058\%$$

6 Construction and Operation

The LiNMC's construction and operational development was completed based on experimental and modeling guidance, as discussed in previous chapters and the appendices, in addition to budgetary and time constraints. Initial development was based on the ENMC design and MCNP simulations. An iterative process was applied to development between developing models, validating the most promising models with experimental measurements, and updating models according the most promising measurement results.

The final LiNMC design houses 12 stacks of WSP and LiF/ZnS with 24 PMTs in four aluminum boxes. The sample chamber consisted of an aluminum platform surrounded by cadmium sheets. Above and below the sample chamber were graphite plugs, and the corners of the LiNMC had blocks of lithium doped HDPE. The entire assembly was mounted on a rolling aluminum frame and is depicted in Figure 6.1 and Figure 6.2.

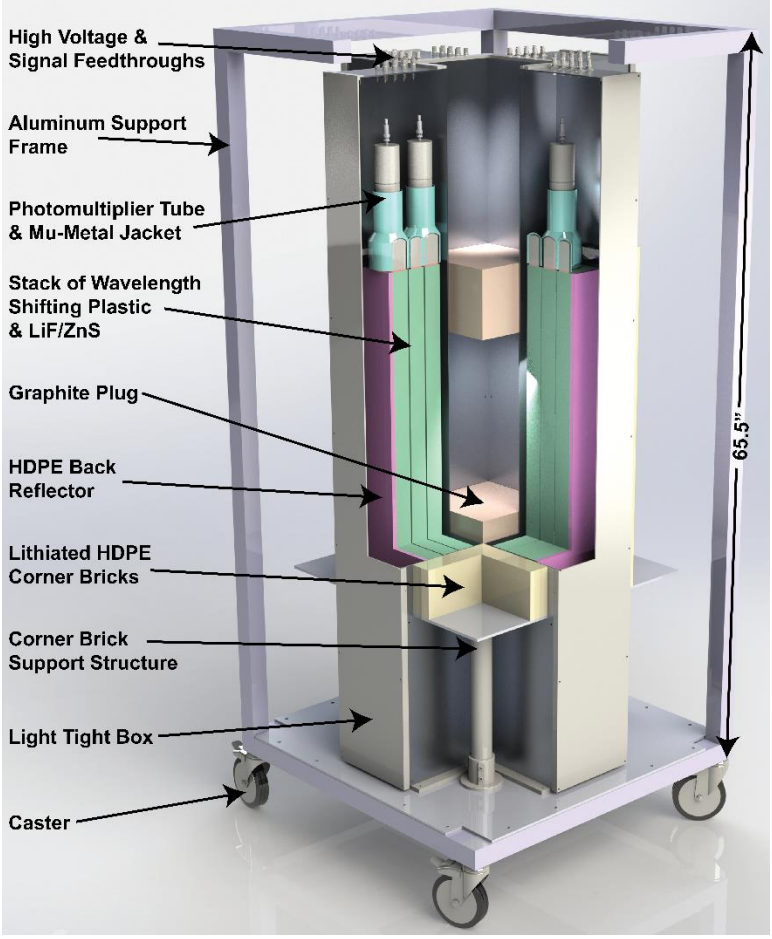

Figure 6.1 LiNMC schematic.

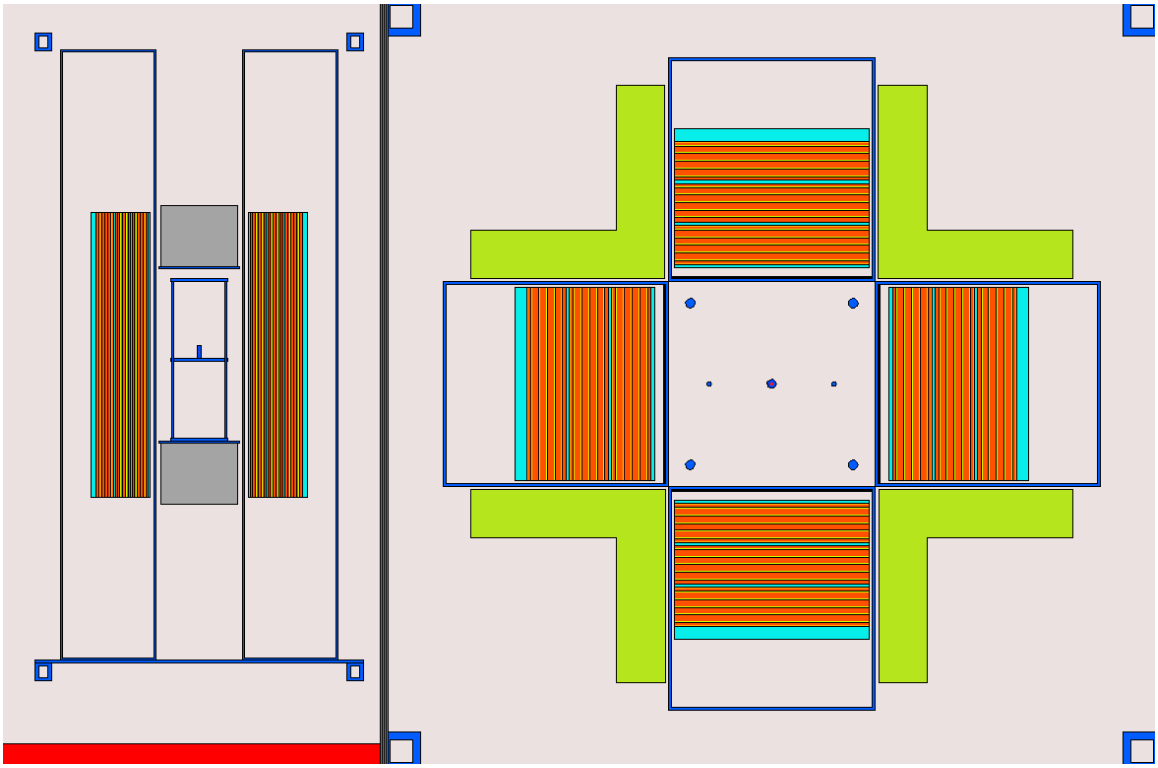

Figure 6.2 Diagram of the LiNMC. (Left) Vertical slice view through the center of the LiNMC. (Right) Horizontal slice through the center of the LiNMC. Concrete and the source are red, aluminum and iron are blue, air is light grey, graphite is dark grey, WSP is orange, LiF/ZnS is yellow, HDPE is teal, and lithiated HDPE is green.

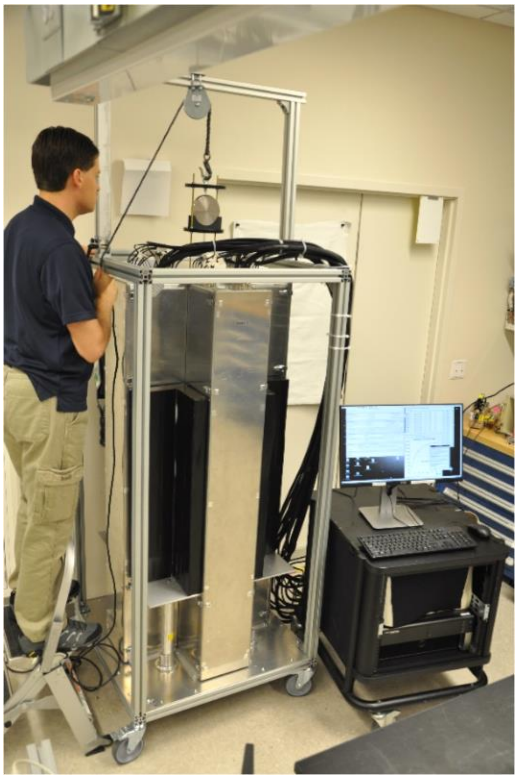

Figure 6.3 Photograph of the completed LiNMC and associated DAQ. A sample is on the sample holder and ready to be lowered into the sample chamber.

6.1 LiNMC Construction

The sample chamber consisted of a stand with three aluminum plates that could be vertically adjusted. The central aluminum plate was adjusted so that samples sitting on it would be at the center of the LiNMC. Cadmium and graphite were placed around the sample chamber to provide neutron reflection and reduce the τ, based on similar features in the ENMC. The cadmium liner design was based on the Cd annulus around the ENMC sample chamber [56]. The cadmium between the sample chamber and the stacks was 0.889 mm thick, and the cadmium above and below the sample chamber was 0.635 mm thick. The top and bottom cadmium sheets were attached to 0.3175 cm thick aluminum plates and 15.24 cm thick graphite blocks. The aluminum plates acted as a support

structure and the graphite moderated and reflected escaping neutrons into the active detection regions.

Four stacks of lithiated HDPE (7.56 wt% Li) were placed outside the sample chamber in the LiNMC's four corners in "L" configurations, which are approximately 76.8 cm tall, 5.08 cm thick, and have 20.3 cm long arms. Lithiated HDPE was selected for its ability to moderate and reflect neutrons that would otherwise escape detection, while also eliminating neutrons that spend excessive amounts of time in the reflector [32]. MCNP simulations indicated that this lithiated HDPE resulted in a superior *FoM* compared to standard HDPE. The lithiated HDPE blocker were placed on a 0.635 cm thick aluminum plate and supported with an aluminum tube that was connected to the LiNMC's base plate.

The decision to use lithiated HDPE in the corners was based on the original design, which had active detector stacks in the four corners. When budgetary constraints eliminated the possibility of implementing stacks in the corners, simulations were performed to replace the stacks with other neutronically significant materials, including HDPE, graphite, and lithiated HDPE in "L" and wedge geometries. A lithiated HDPE "L" shape was discovered as a promising and cost effective alternative to stacks in the corners.

The four aluminum boxes were 0.3175 cm thick and measured 153.7 cm × 23.5 × 21.0 cm, which were designed to be sufficient to hold four detector stack each and the associated PMTs and cables with minimal unused space. The boxes were each attached to 0.635 cm thick aluminum plate that were fastened to the LiNMC's base plate. The tops of the boxes were rigidly attached together with a square ring that was screwed into each box to fix the positions of the boxes and prevent the sample chamber from being deformed. To ensure light tightness, holes in the boxes were covered with two

layers of aluminized tape, BNC feedthroughs were covered with BNC caps, eight latches were attached to the lids to ensure tight sealing, a two layer thick BK5 Blackout Fabric curtains were installed, and excess PMT face areas were covered with Enhanced Spectral Reflector (ESR).

The detector stacks were housed in aluminum boxed based on the low density of aluminum compared to other common metals.

Starting closest to the sample chamber, the boxes were loaded with 0.889 mm thick cadmium, as previously mentioned, followed by a 0.9525 cm thick air gap, 0.3175 cm of HDPE, and a stack of WSP and LiF/ZnS followed by two more alternating sheets of 0.3175 cm of HDPE and detector stacks, with 0.9525 cm of HDPE in the back. The air gap was placed between the cadmium and the first sheet of HDPE to offset the first detector stack, allowing the first PMT to cover more of the first stack than if the stack had been moved all the way forward, thus improving the optical coverage on the first stack, as depicted in Figure 6.4 and Figure 6.5. The sheets of HDPW were used to provide neutron moderation and reflection with a minimal effect on die-away time (τ).

The airgap was added based on single stack measurements of neutron detection efficiency as a function of air gap. When the air gap was minimized the neutron capture efficiency was maximized since the stack was moved closer to the source. When the air gap was increased to center the PMT on the stack, the probability of detecting each neutron capture was maximized. These competing aspects of neutron capture efficiency and detecting each neutron capture were balanced to maximize neutron detection efficiency when the air gap was approximately 3/8” or 0.9525 cm. These measurements and results are depicted in Figure 6.4 and Figure 6.5.

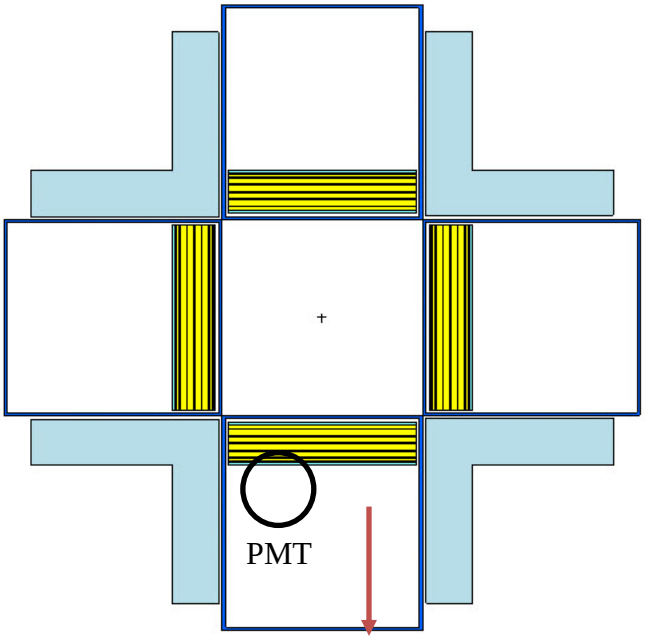

Figure 6.4 Diagram of LiNMC with four stacks. The stacks were moved away from the source without moving the PMTs, giving the PMTs better coverage of the stacks and reducing the neutron capture efficiency of the stacks.

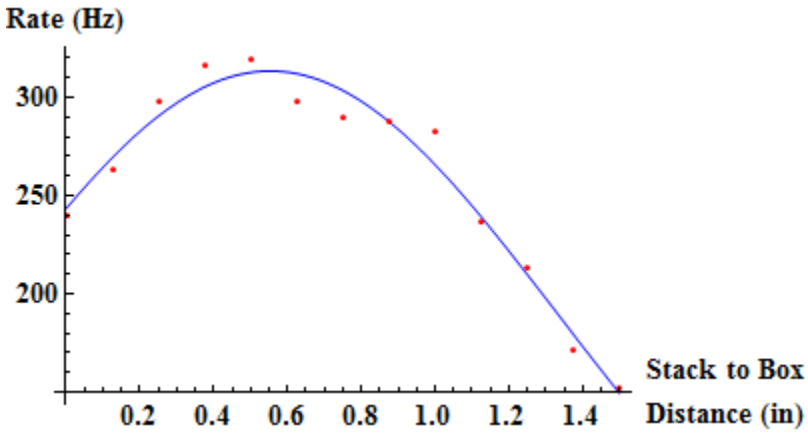

Figure 6.5 Measured neutron detection rate as a function of stack position from the front of the aluminum boxes. Blue line follows Gaussian function fit to the data points. Rates were maximized when the stack was offset from the box front with a 3/8" to 5/8" air gap.

The detector stacks within the boxes were composed of alternating layers of WSP and LiF/ZnS sheets wrapped in ESP and adhesive coated fabric. Each stack had one sheet of 3.5 mm thick WSP followed by 4 sheets of 7.0 mm thick WSP and another 3.5 mm thick sheet of WSP. A sheet of LiF/ZnS was placed between each sheet of WSP. The sheets of LiF/ZnS were each 1.0 mm thick, including 0.5 mm of backing material and 0.5 mm of powdered LiF and ZnS:Ag mixed in a hydrogenous binder. They were acquired from Eljen Technology as EJ-426HD2, which is enriched to 95 atom% ^{6}Li, and has a ^{6}LiF:ZnS mass ratio of 1:2 [57]. The LiF/ZnS and WSP were all 20.32 cm × 71.12 cm, and the completed detector stacks were each 20.32 cm × 71.12 cm × 3.50 cm.

5.0 mm, 7.0 mm, and 9.0 mm thicknesses of WSP had been tested in the past without altering the number of LiF/ZnS sheets. Measurements and simulations found that ε and τ increased with WSP thickness. Simulations indicated that 7.0 mm thick WSP would provide the optimal *FoM* between the three options [23]. The end sheets of WSP were cut down to a thickness of 3.5 mm based on MCNP simulations that indicated that such a reduction in WSP would reduce τ without significantly effecting ε. The 1.0 mm thick sheets EJ-426HD2 LiF/ZnS were compared to LiF/ZnS sheets from other vendors and was selected based on simulations that it would produce a system with the highest total neutron capture efficiency [23].

EJ-280 WSP was used for its ability to efficiently absorb the light from the ZnS scintillation and isotropically reemit the light with a wavelength that can be efficiently detected by the PMTs [11]. The isotropic reemission was also important for reducing the number of scatters required for photons to reach the PMTs and therefore increasing the probability of neutron events being counted compared to non-isotropically reemitting

media [6]. ZnS's wavelength of maximum emission is 450 nm [3]; the wavelengths of maximum absorption and emission of EJ-280 WSP are 427 nm and 490 nm, respectively [11]; the wavelength region of maximum PMT sensitivity is approximately 325-450 nm [58].

The detector stacks were wrapped in ESR to maximize the probability of photons to reach the PMTs. Although sufficiently thick Teflon has a diffuse reflectivity of 1.000 ± 0.006, the ESR has a specular reflectivity of 0.985 and provided superior neutron detection in measurements and superior photon transport in simulations [29, 30]. A 7.62 cm × 4.0 cm hole was left in both ends of the detector stacks for PMT placement.

9821KB photomultiplier tubes from ET Enterprises were selected based on their 7.62 cm wide faces, ~16% quantum efficiency for 490 nm light emitted by the WSP, and high gain to maximize the probability of counting neutron events [58]. Strips of ESR were placed over the PMT faces to only admit light from the holes on the ends of the detector stacks. A 7.6 cm × 4.3 cm, EJ-560 optical pad was placed on the end of each stack, between the stack and the PMT to minimize photon loss at the optical interface between the stacks and the PMTs. EJ-560 optical pads were selected because their flexible nature allowed them fill in the gaps created by stacking different materials together while providing a more level surface than optical grease for the PMT faces to rest against.

Once the PMTs were attached to the ends of the stacks a double layered curtain of BK5 rubberized blackout fabric from Thorlabs was placed between the stacks with the PMTs and the box opening to help ensure the detector's light tightness. The opening to each box was fastened shut with a form fitting lid that were each tightly held shut with eight latches.

The tops of the aluminum boxes were held together with a square ring that screwed into each of the boxes. The bottoms of the boxes were held together by attaching them to 0.635 cm thick aluminum baseplates which were then screwed into the LiNMC's baseplate. The LiNMC baseplate was a 0.635 cm thick aluminum plate held in a Bosch railing frame. The frame around the boxes and sample chamber was composed of 4.445 cm × 4.445 cm thick Bosch railing that formed a 188.0 cm × 81.3 cm × 81.3 cm cuboid on wheels. A loop with a pulley was attached to the top of the frame for moving the sample holder into and out of the LiNMC sample chamber with a rope and hook. The loop attached to the frame with a swivel joint to allow easier movement of the entire system through standard height doorways. The pulley mount increased the height of the LiNMC to 246.4 cm when it was up, but could be swiveled down for transportation.

The MCNP input for the LiNMC is presented in Appendix 3: MCNP Model of LiNMC

6.2 Data Acquisition System and LiNMC Operation

The LiNMC receives electronic and data acquisition support from devices mounted on a cart that can be moved along with the LiNMC. The cart mounted equipment includes a power supply, a DAQ and a personal computer, from which the power supply and the DAQ could be controlled.

The high voltage power for the PMTs was supplied by a CAEN SY5527LC Universal Multichannel Power Supply System with two custom built power supply modules [59]. The anode signals of the PMTs were digitized with a 4DSP FMC116 16-channel analog-to-digital converter (ADC), which was part of a Linear Technology's LTC2175-14, quad channel, 14-bit, 125-MHz (8 ns time bins) ADC chip. The ADC was

built on the same chip as a Xilinx Kintex-7 field programmable gate array (FPGA). The digitized signals from the ADC were passed to the FPGA, where a threshold filter, rate filter, and digital constant fraction discriminator were applied. These filter results were passed across the component interconnect express (PCIe) to a personal computer, which ran on Redhat Enterprise Linux 6.6, where further analysis was performed.

The FPGA pulse height threshold was determined by down sampling values from the raw data stream for each channel separately and building a histogram of those values. These histograms were fit with a Gaussian curve, where the centroid matched with the baseline signal. The pulse height threshold was then set as the value four standard deviations above the Gaussian mean, discriminating against 99.994% of baseline noise. A similar method was used to generate a rate filter. A traveling 2 μs time window incremented a rate value for every bin that entered the window that was above the pulse height threshold and decremented the rate value for every bin leaving the window above the pulse height threshold, producing a filter of the sum of all time bins over the pulse height threshold within a moving time window, as demonstrated in Figure 6.6. These rate values were made into a histogram and fit with an exponential decay function. A threshold was applied to the exponential decay to eliminate 99% of the events with the lowest rate values. Since baseline noise and gamma-ray events tend to be short in time, this filter was used to discriminate against non-neutron-like signals, including baseline noise, electronic noise, and gamma-ray signals. Finally a digital constant fraction discriminator (CFD) was implemented to mitigate time walk. The CFD creates a copy of the rate filter that is delayed by 2 μs and the 10% to 90% rise time of the pulse is added to the rate filter, and the zero crossing of this signal is taken as the event time and is read out. A raw waveform with a

rate filter and CFD are displayer in Figure 6.6. Although the FPGA is capable of implementing PSD methods, trapezoidal filters, and triangular filters, these methods and filters had not been optimized and validated with the FPGA by the end of the project and were therefore not implemented.

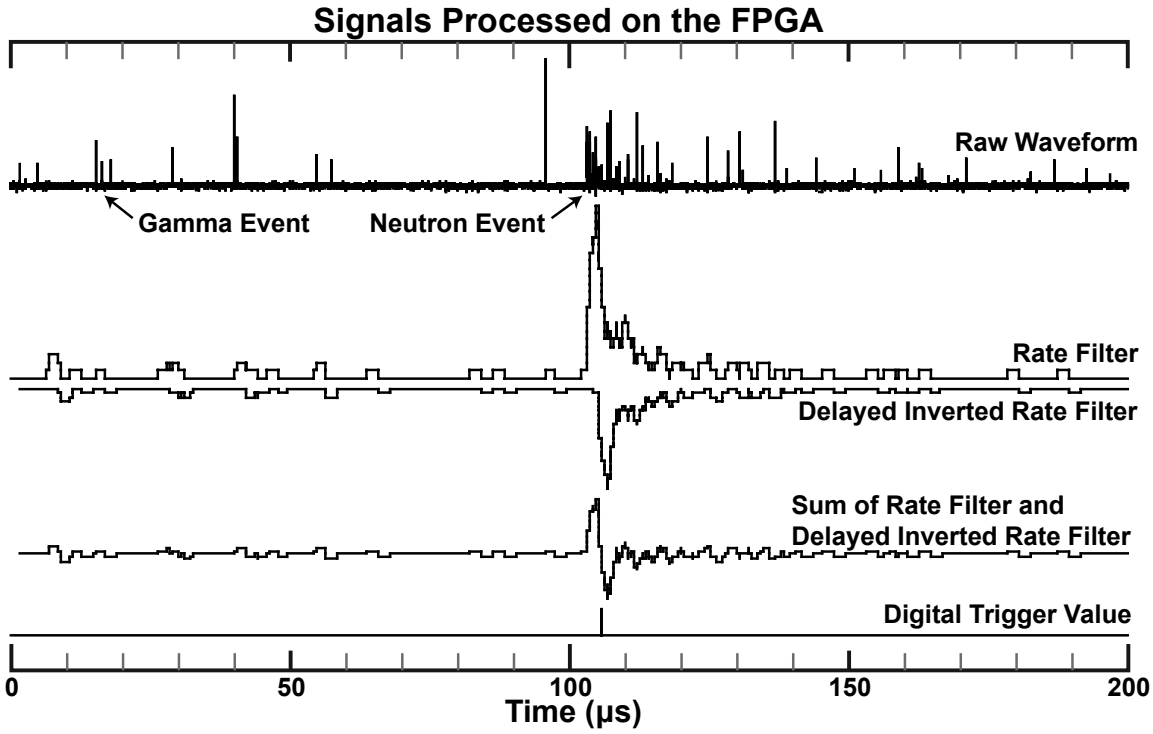

Figure 6.6 Waveform and signals computed on the FPGA. The rate filter is the sum of all of the time bins over a threshold within a moving window. The delayed inverted rate filter signal is then added to the rate filter to produce a digital constant fraction signal that is compared to a second threshold. The trigger time is taken as the zero crossing of this signal after it has gone over threshold.

Once the zero point cross is determined, an event package, consisting of a 48-bit timestamp and a 16-bit channel number, is passed from the FPGA to its own associated a first in first out (FIFO) list, which can each hold 8192 packets. When any of the FIFOs are filled, the 4DSP firmware transfers the data from each of the FIFOs across the PCIe bus to

the computer, where a Linux kernel module buffers the data for the user space. During this transfer process, the FIFOs are blocked from receiving new data to ensure identical live time for all channels, and therefore simpler live time correction. Once the computer receives and verifies the data sets, the FIFOs are re-enabled and the data sets are removed from the communication thread of the computer.

The data sets are then reordered and time sorted for each channel. A coincidence filter between upper and lower PMTs is applied to the time list data sets with a 200-600 ns window, depending on PMT pair performance. The remaining time stamps are compiled into a single time stamp list and saved as a TTree in a ROOT file.

The results of these data sets are also displayed online for user observation so that setting changes can be monitored in real time. A labeled screenshot of the graphic user interface between the user and the firmware is displayed in Figure 6.7. This software supported real-time histograms of various measurements including down samples of the raw and filtered waveforms and doubles as a function of gate length. These histograms are generated on a separate thread from the hardware communication and have been shown to not affect live time. The histograms are displayed as TCanvas object ROOT objects into Qt (a graphics user interface code) objects that are periodically updated (typically about once per second).

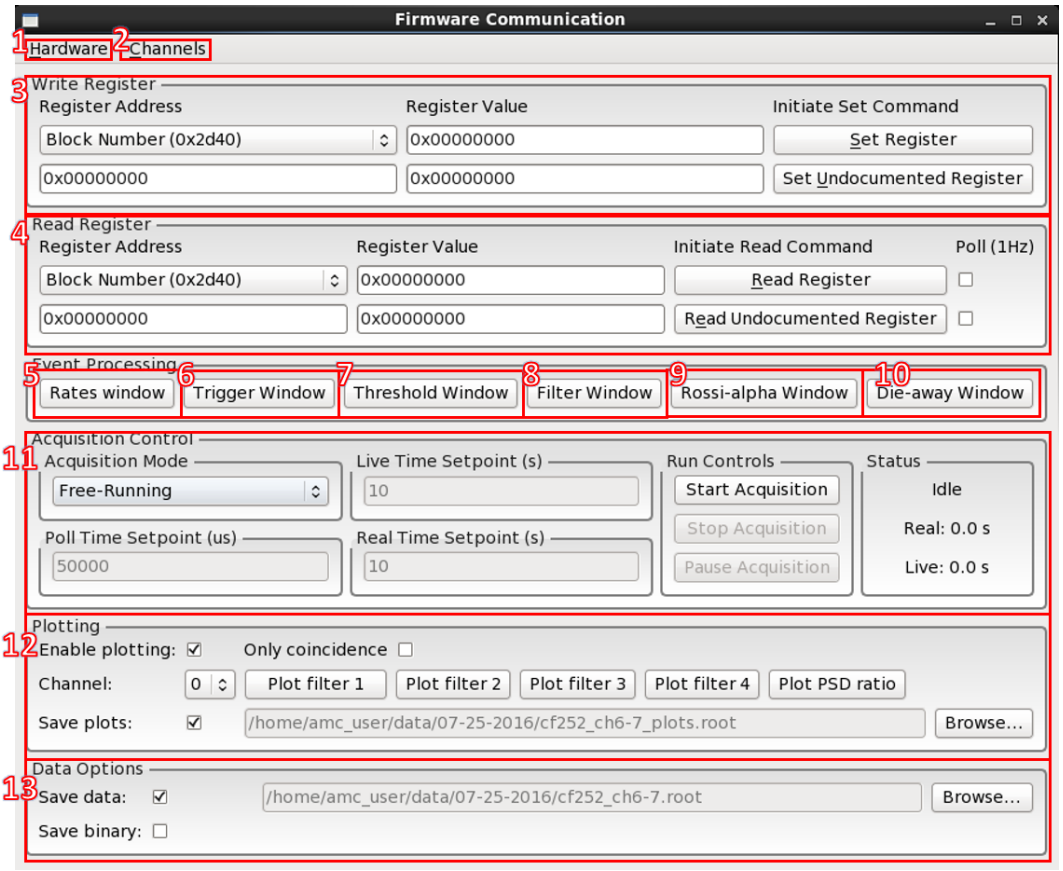

Figure 6.7. Screenshot of the data acquisition software developed to control the LiNMC.

1. **Hardware:** saves and loads hardware (FPGA) parameters; replay data file
2. **Channels:** enable or disable channels; enable or disable coincidence
3. **Write Register:** write an arbitrary hexadecimal value to an arbitrary FPGA register address
4. **Read Register:** read an hexadecimal value from an arbitrary FPGA register address
5. **Rate Window:** view the trigger rates for each channel
6. **Trigger Window:** adjust the trigger parameters
7. **Threshold Window:** adjust threshold parameters
8. **Filter Window:** adjust trapezoidal filter shape times
9. **Rossi-alpha Window:** show plot of Rossi-α distribution

10. **Die-away Window:** plot the doubles count rate as a function of gate length
11. **Acquisition Control:** start and stop data collection; set run time parameters; view current data run's real and line time
12. **Plotting:** enable histogram plotting from different channels; save histograms plots
13. **Data Options:** save data

The DAQ records list mode data sets in a PTR32 format, which keeps track of time between events rather than absolute event time, to reduce the size of list files. The PTR32 format was selected since that is the format used by our LANL partners, and using the same format would help to ensure compatibility between our systems.

These timestamp lists can then be analyzed with a shift register to determine the singles (*S*), doubles (*D*), and triples (*T*) neutron rates, which can in turn be analyzed to determine the ^{240}Pu *mass*, neutron self-multiplication (*M*), and (α, n) to fission neutron ratio (α) from samples. For more information about shift registers and how time stamps are used to determine sample characteristics, see Section 2.1.

The DAQ is fully operational to the point described above although it does require expertise to operate. Future development would be required to 1) fine tune the automation of thresholding features, 2) implement filters and additional PSD methods, 3) optimize operations between the FPGA, FIFOs, and computer, and 4) simplify DAQ operation.

7 Calibration Results

Because the LiNMC is intended to assay the same kinds of samples as the ENMC, it was calibrated with ^{252}Cf, similarly to the ENMC, which is standard practice for neutron multiplicity counters [5, 12, 56]. Neutron detection efficiency (ε) and neutron die-away time (τ) were measured with a ^{252}Cf source.

7.1 Californium Calibration

Calibrations were performed with ^{252}Cf because of the high availability of ^{252}Cf as a fission neutron source compared to Pu sources, and because ^{252}Cf tend to lower gamma-ray activity that Pu sources, allowing for more pure neutron measurements.

The ε and τ were determined by placing a steel encapsulated ^{252}Cf source (32,550 n/s) in the center of the sample chamber, collecting data with the 4DSP data acquisition system (DAQ), and analyzing the collected data set. Detected events were compared to emitted neutrons to determine ε, and the doubles rate as a function of gate width (G) was fit with an exponential to determine τ. Pulse shape analysis and coincidence between PMTs was applied to discriminate against gamma-ray signals. The signal rates from each pair of data channels were compared to the neutron emission rate to determine the neutron detection efficiency and validation correction factor (VCF), as seen in Table 7.1.

Table 7.1 LiNMC neutron detection performance by detector element with ^{252}Cf source. Data collected with 4DSP DAQ operating in coincidence with pulse shape analysis.

Detector Region	Neutron detection efficiency (ε)	VCF
Box 0 Stack 0	0.030	0.73
Box 1 Stack 0	0.028	0.67
Box 2 Stack 0	0.035	0.84
Box 3 Stack 0	0.025	0.59
Box 0 Stack 1&2	0.068	0.82
Box 1 Stack 1&2	0.067	0.80
Box 2 Stack 1&2	0.065	0.78
Box 3 Stack 1&2	0.074	0.89
All	0.39	0.77

The detected doubles rate from all of the detector elements was recorded and calculated as a function G. G was varied from 2 μs to 64 μs in 2 μs increments to ensure adequate coverage of the gate space. An exponential decay was fit to this data set with the decay constant as τ, as seen in Figure 7.1.

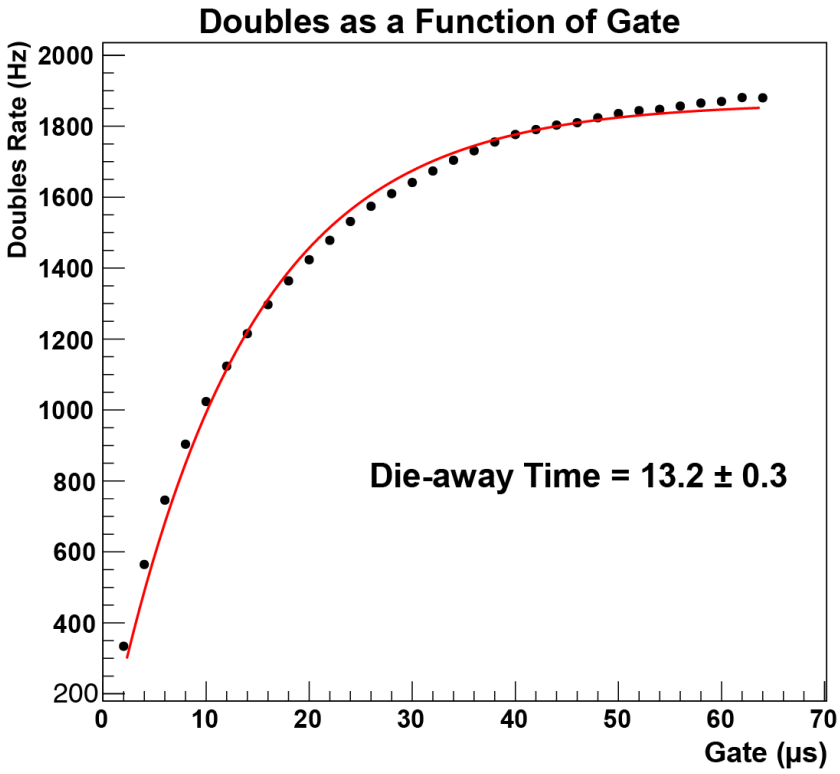

Figure 7.1 Detected doubles rate as a function of gate width. Exponential decay constant indicates neutron die-away time. Data collected with LiNMC, ^{252}Cf source, and the 4DSP DAQ.

The ε and τ are used to determine a neutron multiplicity counter's figure-of-merit (FoM), which is used as a general performance metric for neutron multiplicity counters and allows systems with different ε and τ to be compared to each other. FoM is defined as

Equation 7.1 $$FoM = \frac{\varepsilon^2}{\tau},$$

where ε_n is in percent and τ is in μs.

The 39% ε and 13.2 μs τ of the LiNMC give FoM = 120. By comparison typical Epithermal Neutron Multiplicity Counters (ENMSs) have 62.5-65% ε and 19.1-22 μs τ [56, 60], and a FoM of ~200. Based on these values, the LiNMC is anticipated to be able to perform assays similarly to an ENMC but take 67% longer to perform assays than the

ENMC. Although the LiNMC have somewhat inferior assay time than the ENMC, it remains superior to most neutron multiplicity and coincidence counters.

Measurements with a Pixie-4 data acquisition system resulted in $\varepsilon = 0.357 \pm 0.006$, a $\tau = 11.7 \pm 0.1$ μs, a $\varepsilon_\gamma = 1.5\times10^{-3} \pm 2\times10^{-4}$ (with a 107 μs coincidence window and no PSD), and FoM = 109 ± 4, similarly to the results from the data acquisition system built for the LiNMC.

8 Conclusion

The LiNMC is one of the first LiF/ZnS-based neutron multiplicity counters and has evolved and been optimized over a wide range of parameters to achieve similar performance to an ENMC [6, 10, 18, 23, 25, 26, 61-64]. This is an innovative neutron multiplicity counter design with very promising preliminary results and with potential safeguards applications that include material verification, accountancy, and identification. With a 39% ε and 13.2 μs τ the LiNMC has a FoM of 120, indicating that the LiNMC should take 67% longer to perform assays than the ENMC. Although the LiNMC has somewhat inferior assay time than the ENMC, it remains faster than most neutron multiplicity and coincidence counters. A LiNMC-like design could also be modified for effective active interrogation of challenging samples, such as gadolinium loaded nuclear fuel, as described in Appendix 1: Modeling Gd Fuel in the Demonstration System [64]. LiF/ZnS-based neutron detectors may also find applications as a substitute for ^{3}He neutron detectors outside of U.S. government based applications, such as universities, non-government laboratories, and laboratories outside of the U.S., where ^{3}He supplies are extremely limited.

This project has successfully designed, built, and tested a lithium fluoride with zinc sulfide based neutron multiplicity counter with a high neutron detection efficiency, short neutron die-away time, and low gamma-ray sensitivity. By the end of the project the LiNMC's basic components have been brought together and validated, achieving technological readiness level four, and providing strong evidence that LiF/ZnS-based neutron detection is viable technology for development into high performance ^{3}He-free neutron detectors.

8.1 Potential Future Improvements

Although these tests with the LiNMC have been sufficient to show that lithium based neutron detectors may be a viable alternative to many ^{3}He based neutron coincidence and multiplicity counters, ^{3}He technologies have been optimized over many decades and lithium based neutron multiplicity counting, as an emerging technology, still has many avenues for potential improvement. Future research could be performed to improve the LiNMC's performance in a variety of ways. The following methods show promise for improving LiNMC performance:

- The four corners of the detector could be replaced with four more aluminum boxes filled with detector stacks and PMTs, increasing neutron detection efficiency and reducing neutron die-away time.
- Adding a fourth detector stack to each box is expected to increase ε while only having a small effect on the neutron die-away time.
- The number of WSP sheets could be increased while the thickness of the WSP sheets is decreased, increasing the number of LiF/ZnS sheets that could be placed in a stack, thus increasing ε and reducing τ, although the signal rate per channel would also increase.
- Replacing regular LiF/ZnS with Ni-quenched LiF/ZnS may be useful for reducing the effects of pulse pileup and therefore allow operation at higher rates while only having a small effect on gamma-ray rejection, see Appendix 2: Comparison of Ni-Quenched to Non-Quenched LiF/ZnS for more details.
- Replacing the standard 7.62 cm circular PMTs with larger numbers of small square silicon photomultipliers would reduce the height of the boxes required to house the

detector stacks and reduce the effects of pulse pileup since each PMT would be associated with fewer LiF/ZnS sheets.

- Installing a lead ring around the sample chamber may increase the gamma-ray rejection while only having a small effect on ε and τ.
- Coupling MCNP simulation output to light simulation input may allow improved optimization of detector stack geometry.
- Optimizing the geometry and composition of neutron modifying materials may allow improvements to neutron detection efficiency and/or neutron die-away time.

Replacing the lithiated HDPE in the LiNMC's corners with boxes filled with detector stacks and PMTs would double the number of neutron capture sites. Simulations indicate that placing active detector components in the corners may increase ε by ~16% and reduce τ by ~33% [26]. This could dramatically improve the *FoM*, although it would also require doubling many of the construction materials and electrical components.

Adding a fourth detector stack and pair of PMTs to each box would increase the number of neutron capture site and moderation in the LiNMC. Simulations indicate that adding a fourth detector stack to each box will increase ε by ~5% and increase τ by ~1%, resulting in an improved *FoM*, although it would require increasing the number of many construction and electrical components by 33%.

An experiment was conducted that replaced all of the 7.0 mm WSP sheets in a stack with two 3.5 mm sheets of WSP and one sheets of LiF/ZnS to build a stack with the same amount of WSP but 45% more LiF/ZnS than a standard stack. The neutron detection efficiency of the stack was tested with two 5.08 cm wide PMTs on each end of the stack operating in coincidence. A standard stack was then tested and the ε of the two stacks were

compared. With statistical uncertainties, the modified stack had a 72% ± 1 increase in counts, or 90% ± 1 of the rate increase anticipated from the addition of the extra LiF/ZnS, indicating ε scales up approximately with LiF/ZnS sheet packing density, at least down to 3.5 mm WSP sheet thicknesses. It should be noted that the modified stack was 4 mm thicker than the regular stack, reducing the light transmission from some layers of the stack to the PMTs. Stacks with increased LiF/ZnS sheet packing densities may be able to increase the neutron capture rate of each stack and therefore increase ε while reducing τ, which may result in a dramatically improved *FoM*, although it would increase the signal rate and pulse pileup associated with each channel.

Ni-quenched LiF/ZnS has a faster light decay time than regular LiF/ZnS and may therefore be useful for reducing the amount of time required to distinguish separate events. At low thresholds, the Ni-quenched LiF/ZnS was also less sensitive to gamma rays than the regular LiF/ZnS. Replacing regular LiF/ZnS with Ni-quenched LiF/ZnS may reduce the effects of pulse pileup and increase gamma-ray rejection, although the Ni-quenched LiF/ZnS is approximately 50% more expensive than regular LiF/ZnS. For more information on Ni-quenched LiF/ZnS see Appendix 2: Comparison of Ni-Quenched to Non-Quenched LiF/ZnS.

The 7.62 cm diameter PMTs have good light collection from each stack, but they are also 29 cm tall and are each responsible for detecting the light emitted by five sheets of LiF/ZnS. Replacing the PMTs with silicon photomultipliers, which are typically less than 1 cm tall, could allow the LiNMC's aluminum boxes to be redesigned by as much as 56 cm. Silicon photomultipliers also have much smaller faces than 7.62 cm diameter PMTs, allowing each photomultiplier to monitor fewer sheets of LiF/ZnS, thus reducing

pulse pileup effects if more readout channels are implemented. They also tend to operate at much lower voltages, reducing power requirements per photomultiplier. But silicon photomultipliers are still much more expensive than PMTs and would require many more channels of power and signal processing, therefore silicon photomultipliers may only become a viable option when their prices and the prices of the associated electronics decrease.

Installing a high Z material ring with a high density around the sample chamber could be an effective means of improving gamma-ray rejection and pulse pileup associated with gamma rays. An iron ring was used in the ENMC as a neutron scatterer, although lead could perform a similar role. Lead is an inexpensive gamma-ray attenuator but would significantly increase the weight of the LiNMC. Tungsten and depleted uranium would also be effective gamma-ray shielding materials, although they would be even heavier than lead.

The validation correction factor (VCF) has been important to guiding development and predicted performance since the VCF is a means of quantifying the ε difference between the simulated and physical LiNMC. Since neutron simulations were performed with MCNP and light ray-trace simulations were performed with another software suite, coupling the output of the MCNP simulations to the input of the light ray-trace simulations would improve the overall realism of the simulations and allow simulation based optimization of materials that are neutronically and optically important. For example, the thickness of the WSP, the width of the detector stacks, and the height of the detector stacks could all be optimized. Although simulation work can be expensive, it is often the easiest

way to optimize between many geometry options that would be too expensive and time consuming to individually test.

Simulations and measurements could be performed to further optimize neutronically significant materials in the LiNMC. The locations, dimensions, and compositions of neutron moderators, reflectors, and poisons, such as HDPE, graphite, and cadmium, could be varied to maximize the *FoM*. Many of the assumptions that went into the LiNMC were based on the ENMC and may need to be modified for the LiNMC's specific neutronics. Simulations and measurements can be time consuming, and improvements to the *FoM* may be modest, but these materials are inexpensive and alterations would generally be easy to implement.

In sum, there are many viable methods for further improving various characteristics of the LiNMC. Based on development experience and current equipment costs, I anticipate that the greatest performance increases for their cost will come from increasing the packing density of the LiF/ZnS sheets in conjunction with installing a lead lining around the sample chamber, followed by coupling MCNP simulation outputs to light ray-trace inputs to further optimizing detector stack geometry and the geometry and composition of other neutronically significant materials. I anticipate that the LiNMC is mostly likely to exceed ENMC performance by replacing the lithiated HDPE with active detector stacks in the corners, adding a fourth detector stack to each box, and increasing the LiF/ZnS packing density in each stack.

9 References

1. Goorley, T., et al., *Initial MCNP 6 Release Overview.* Los Alamos National Laboratory, 2012. LA-UR-11-07082.

2. Kouzes, R.T., et al., *Full Scale Coated Fiber Neutron Detector Measurements.* Pacific Northwest National Laboratory, 2010. PNNL-19264.

3. Knoll, G.G., *Radiation Detection and Measurements*. 3rd ed. 2000: John Wiley & Sons.

4. Browne, M.C., et al., *Prototype Neutron-Capture Counter for Fast-Coincidence Assay of Plutonium in Residues* Los Alamos National Laboratory, 2001. LA-UR-01-2164.

5. Ensslin, N., et al., *Passive Nondestructive Assay of Nuclear Materials.* Los Alamos National Laboratory, 2007. LA-UR-07-1402.

6. Ely, J.H., et al., *Final Technical Report for the Neutron Detection without Helium-3 Project.* Pacific Northwest National Laboratory, 2013. PNNL-23011.

7. Belian, A.P., et al., *Characterizing the Detector Response and Testing the Performance of a New Well Counter for Neutron Coincidence Measurments of Plutonium Residues.* Los Alamos National Laboratory, 2001. LA-UR-01-3848.

8. Li, S.F., et al., *Fast-neutron multiplicity analysis based on liquid scintillation.* Applied Radiation and Isotopes, 2016. **110**: p. 53-58.

9. Chichester, D.L., et al., *MPACT Fast Neutron Multiplicity System Prototype Development.* Idaho National Laboratory, 2013. INL/EXT-13-30279.

10. Ely, J.H., A.T. Lintereur, and E. Sicialiano, *Interim Report on the Optimization and Feasibility Studies for the Neutron Detection without Helium-3 Project.* Pacific Northwest National Laboratory, 2012. PNNL-20952.

11. Eljen Technology. *Wavelength Shifting Plastic*. [product specification] 2016; [Available from: http://www.eljentechnology.com/images/products/data_sheets/EJ-280_EJ-282_EJ-284_EJ-286.pdf.

12. Reilly, D., et al., *Passive Nondestructive Assay of Nuclear Materials.* Los Alamos National Laboratory, 1991. LA-UR-90-732.

13. Bohnel, K., *The Effects of Multiplication on the Quantitative-determination of Spontaneously Fisioning Isotopes by Neutron Correlation-Analysis.* Nuclear Science and Engineering, 1985. **90**(1): p. 75-82.

14. Cifarelli, D.M. and W. Hage, *Models for a Three-parameter Analysis of Neutron Signal Correlation Measurements for Fissile Material Assay.* Nuclear Instruments and Methods in Physics Research Section A, 1986. **251**(3): p. 550-563.

15. Langner, D.G., et al., *Application Guide to Neutron Multiplicity Counting.* Los Alamos National Laboratory, 1998. LA-13422-M.

16. Brooks, F.D., *A Scintillation Counter with Neutron and Gamma-Ray Discriminators.* Nuclear Instruments & Methods, 1959. **4**(3): p. 151-163.

17. Zaitseva, N., et al., *Pulse Shape Discrimination in Impure and Mixed Single-Crystal Organic Scintillators.* Ieee Transactions on Nuclear Science, 2011. **58**(6): p. 3411-3420.

18. Lintereur, A.T., et al., *Neutron and Gamma Ray Pulse Shape Discrimination with Polyvinyltoluene.* Pacific Northwest National Laboratory, 2012. PNNL-21609.

19. Geist, W.H., et al., *Testing of a Fiber/Scintillator Neutron-capture Detector*. Proceedings of the Sixth International Conference on Facility Operations-Safeguards Interface. 1999, La Grange Park: Amer Nuclear Soc. 126-132.

20. Swinhow, M.T., J.S. Hendricks, and D.R. Mayo, *MCNPX for Neutron Multiplicity Detector Simulation.* Los Alamos National Laboratory, 2004. LA-UR-04-8025.

21. Ely, J.H., E.R. Sicialiano, and M.T. Swinhoe, *Alternatives to Helium-3 for Neutron Multiplicity Detectors*. 2011, Pacific Northwest National Laboratory and Los Alamos National Laboratory: Richland, WA and Los Alamos, NM.

22. Lintereur, A.T., E.R. Siciliano, and R.T. Kouzes, *Boron-10 Lined Proportional Counter Model Validation.* Pacific Northwest National Laboratory, 2012. PNNL-21501.

23. Ely, J.H., et al., *Modeling and Simulation Optimization and Feasibility Studies for the Neutron Detection without Helium-3 Project.* Pacific Northwest National Laboratory, 2013. PNNL-22228.

24. Robinson, S., et al. *Adaptive Pulse Shape Discrimination Techniques for Multiplicity Counting*. in *IEEE-NSS*. 2014. Seattle, WA.

25. Stave, S., et al. *Progress in Development of a 6LiF/ZnS-based Neutron Multiplicity Counter*. in *IEEE-NSS 2014*. 2014. Seattle, WA.

26. Stave, S.C., et al., *Improving Neutron Measurements Venture: PNNL FY14 Year-End Report.* Pacific Northwest National Laboratory, 2014. PNNL-23835.

27. Kouzes, R.T., *The 3He Supply Problem.* Pacific Northwest National Laboratory, 2009. PNNL-18388.

28. Veenhof, R. *Garfield - Simulations of Gaseous Detectors*. 2010 7 Sep 2010 [cited 2014 3 December]; Available from: http://garfield.web.cern.ch/garfield/.

29. Janecek, M. and W.W. Moses, *Optical Reflectance Measurements for Commonly Used Reflectors.* Ieee Transactions on Nuclear Science, 2008. **55**(4): p. 2432-2437.

30. CS Hyde Company. *ESR Reflector Film*. 2012; Available from: http://catalog.cshyde .com/viewitems/films/esr-reflector-film.

31. Hamamatsu Photnics Corperation. *Photomultiplier Tube R7724*. Available from: http://www.hamamatsu.com/us/en/R7724.html.

32. Shieldwerx. *SWX-215*. [product specifications] Nov. 2015; Available from: http://www.shieldwerx.com/assets/swx-215.pdf.

33. Brooks, F.D., *Development of Organic Scintillators.* Nuclear Instruments & Methods, 1979. **162**(1-3): p. 477-505.

34. Brooks, F.D., *A Scintillation Counter with Neutron and Gamma-ray Discriminators.* Nuclear Instruments and Methods, 1959. **4**(3): p. 151-163.

35. Myjak, M.J., *Converting Figure of Merit to Gamma Rejection ratio*. 2013, Pacific Northwest National Laboratory: Richland, WA.

36. Kouzes, R.T., et al., *Introduction to Neutron Coincidence Counter Design Based on Boron-10.* Pacific Northwest National Laboratory, 2012. PNNL-21090.

37. Ivanova, A.A., et al., *Fast Neutron Flux Analyzer with Real-time Digital Pulse Shape Discrimination.* Nuclear Instruments and Methods in Physics Research Section A, 2016. **827**: p. 13-17.

38. Zhmurin, P.N., et al., *Polystyrene-based Scintillator with Pulse-shape Discrimination Capability.* Nuclear Instruments and Methods in Physics Research Section A, 2014. **761**: p. 92-98.

39. Van Eijk, C.W.E., *Inorganic Scintillators for Thermal Neutron Detection.* Radiation Measurements, 2004. **38**(4-6): p. 337-342.

40. Glasstone, S. and A. Sesonske, *Nuclear Reactor Engineering*. 3rd ed. 2010: XanEdu.

41. Verbinsk, V., et al., *Prompt Gamma Rays from 252Cf (Spontaneous Fission) 235U(n f) and 239Pu(n f).* Bulletin of the American Physical Society, 1968. **13**(11).

42. Chu, S.Y.F., L.P. Ekstrom, and R.B. Firestone. *The Lund/LBNL Nuclear Data Search*. 1999; Available from: http://nucleardata.nuclear.lu.se/toi/.

43. Berger, M.J., et al. *XCOM: Photon Cross Section Database*. 2010; Available from: http://www.nist.gov/pml/data/xcom/.

44. Johnson, T.E. and B.K. Birky, *Health Physics and Radiological Health*. 4th ed. 2012: Lippincott Williams & Wilkins.

45. International Atomic Energy Agency, *Database of Prompt Gamma Rays from Slow Neutron Capture for Elemental Analysis*. 2007, Vienna, Austria: International Atomic Energy Agency.

46. Zaluzec, N.J., *Analytical Formulae for Calculation of X-Ray Detector Solid Angles in the Scanning and Scanning/Transmission Analytical Electron Microscope.* Microscopy and Microanalysis, 2014. **20**(4): p. 1318-1326.

47. Be, M.M. and V. Christe, *252Cf - Comments on Evaluation of Decay Data*. 2007, Laboratoire National Henri Becquerel.

48. Switzer, T., et al., *Neutron Detection Authentication Case Study: Revised Edition*. Pacific Northwest National Laboratory, 2003. PNNL-14222.

49. Aguayo, E., R.T. Kouzes, and E.R. Siciliano, *Ship Effect Neutron Measurements And Impacts On Low-Background Experiments*. Pacific Northwest National Laboratory, 2013. PNNL-22953.

50. ORTEC. *905 Series NaI(Tl) Scintillation Detectors*. [cited 2016 6 Jan]; Available from: http://www.ortec-online.com/download/905-Series.pdf.

51. CAEN. *DT5800D User Manual*. 2013; Available from: www.detectoremulator.com/DOC/userman11.pdf.

52. Canberra. *Model of JSR-14 Neutron Analysis Shift Register*. 2012; Available from: http://www.canberra.com/products/waste_safeguard_systems/pdf/JSR-14-SS-C37278.pdf.

53. Kroick, M. and W.H. Geist, *INCC Software Users Manual*. Los Alamos National Laboratory, 2009. LA-UR-10-6227.

54. Ajitanand, N.N., *Delayed Gamma-ray Emission in the Spontaneous Fission of 252Cf*. Nuclear Physics A, 1971. **164**(2): p. 300-306.

55. Brunson, G.S.J., *Multiplicity and Correlated Energy of Gamma Rays Emitted in the Spontaneous Fission of Californium-252*. Los Alamos National Laboratory, 1982. LA-9408-T.

56. Menlove, H.O., et al., *Manual for the Epithermal Neutron Multiplicity Detector (ENMC) for Measurement of Impure MOX and Plutonium Sample*. Los Alamos National Laboratory, 2004. LA-14088.

57. Eljen Technology. *Thermal Neutron Detector EY-426*. [product specifications] 2016; 2/8/2016:[Available from: http://www.eljentechnology.com/images/products/data_sheets/EJ-426.pdf.

58. Electrontube Enterprises. *78 mm (3") photomultiplier 9821B series data sheet*. [product specifications] 2012; 1/23/2012:[Available from: https://my.et-enterprises.com/pdf/9821B.pdf.

59. CAEN. *SY5527-SY5527LC Power Supply System User's Manual*. 2014; [Available from: file:///C:/Users/cowl193/Downloads/SY5527_rev10.pdf.

60. Stewart, J.E., et al., *The Epithermal Neutron Multiplicity Counter Design and Performance Manual: More Rapid Plutonium and Uranium Inventory Verifications by Factors of 5-20*. Los Alamos National Laboratory, 2000. LA-13743-M.

61. Stave, S.C., et al., *Improving Neutron Measurements Venture: PNNL FY15 Year-End Report*. Pacific Northwest National Laboratory, 2015. PNNL-24895.

62. Lintereur, A.T., *Neutron Multiplicity Counter Design without Helium-3*, in *Nuclear Engineering*. 2013, University of Flourida.

63. Kouzes, R.T., A.T. Lintereur, and E.R. Siciliano, *Progress in Alternative Neutron Detection to Address the Helium-3 Shortage.* Nuclear Instruments and Methods in Physics Research Section A, 2015. **784**: p. 172-175.

64. Cowles, C.C., R.T. Kouzes, and E.R. Siciliano, *Simulations of Lithium-Based Neutron Coincidence Counter for Gd-Loaded Fuel.* Pacific Northwest National Laboratory, 2014. PNNL-23921.

65. Rogers, T., et al., *Optimization of PWR Fuel Assembly Radial Enrichment and Burnable Poison Location based on Adaptive Simulated Annealing.* Nuclear Engineering and Design, 2009(239): p. 1019-1029.

66. Soba, A., et al., *Simulation of the Behaviour of Nuclear Fuel under High Burnup Conditions.* Annals of Nuclear Energy, 2014(70): p. 147-156.

67. Mikus, J.M., *Power Distribution Gradients in WWER Type Cores and Fuel Failure Root Causes.* Nuclear Engineering and Design, 2014(267): p. 207-217.

68. Evans, L.G., et al., *A New Fast Neutron Collar for Safegaurds Inspection Measurements of Fresh Low Enriched Uranium Fuel Assemblies Containing Burnable Poison Rods.* Nuclear Instruments and Methods in Physics Research A, 2013(729): p. 740-746.

10 Appendix 1: Modeling Gd Fuel in the Demonstration System

The current LiNMC is a passive system that relies on spontaneous fission from sources to determine sample characteristics, but fresh nuclear fuel has a very how spontaneous fission rate, especially since many power plants are starting to gadolinium loaded fuel, which is a neutron poison. Active neutron coincidence well counters are the standard method for assaying fresh fuel. The LiNMC has some similarities to a well counter, but will require modifications to fit tightly around fuel bundles and to implement an active source to generate induced fission in sample fuel.

Modeling and simulations of the LiNMC demonstration unit were used to compare detector performance with and without gadolinium loaded pressurized water reactor (PWR) fuel, which is more fully detailed in the report 'Simulations of Lithium-Based Neutron Coincidence Counter for Gd-Loaded Fuel' [64].

Nuclear reactor research has led to an interest in loading light water reactor (LWR) fuel with gadolinium for use as a burnable neutron poison to provide improved power balance throughout a reactor core and therefore permit increased cycle length and/or increased average power density [65-67]. Safeguards applications therefore require neutron coincidence counters capable of assaying Gd loaded LWR fuel assemblies in a reasonable time. MCNP simulations of the LiNMC demonstration unit were conducted with a pressured water reactor (PWR) fuel assembly with and without Gd-loaded fuel. These LiNMC simulations were compared to simulations and measurements the UNCL-II, a ^{3}He based system. A modified LiNMC demonstration system, referred to as PLNS3A-R1, showed strong promise for assaying Gd loaded fuel to 1% precision in 10 minutes,

with better performance (in simulation) than a UNCL-II modified to measure Gd-loaded fuel.

Currently, the International Atomic Energy Administration (IAEA) uses active well coincidence counters based on ^{3}He, but particularly for assemblies with high Gd content, systematic errors can be high and measurement times can be very long (hours), in contrast to about ten minutes for non-Gd loaded fuel. A new uranium neutron coincidence collar (UNCL) design based on high-pressure ^{3}He tubes was developed to overcome this problem [68].

A schematic of the LiNMC demonstration unit can be seen in Figure 10.1 with a ^{252}Cf point source situated on the top center of the source stand. Modeling this detector, referred to as PLNS-2013, obtained agreement with previously reported results [6, 64].

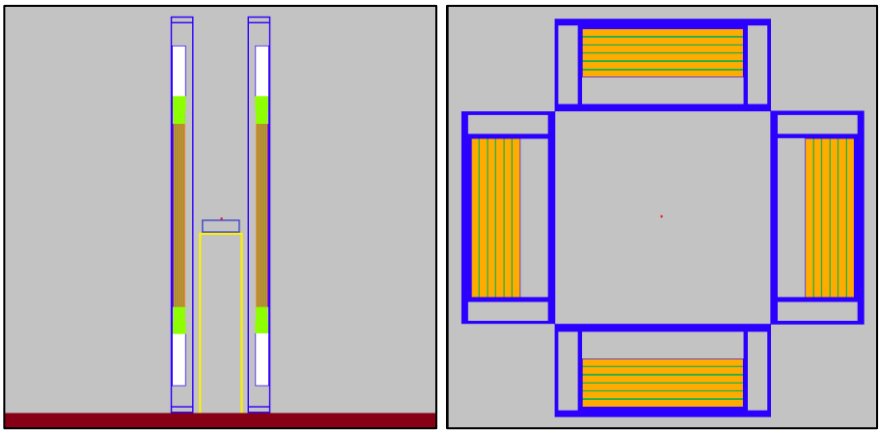

Figure 10.1 Model of the PLNS-2013 system used as a baseline for model comparison. The small red dot depicts the location of the ^{252}Cf point source.

Previous research indicated a Validation Correction factor (VCF) of 0.78 ± 0.03 [6, 64]. This VCF was applied to the results of modeling for this project. The PLNS-2013 model was modified to account for the steel encapsulated ^{252}Cf source used in experiments

and the replacement of the cardboard and aluminum source stand with a polyurethane foam source stand to better match the experimental set up, which was referred to as PLNS4. The model was then modified with simple additions of high-density polyethylene (HDPE) and polyvinyl toluene (PVT) to maximize the *FoM* of PLNS4, one such configuration is depicted in Figure 10.2.

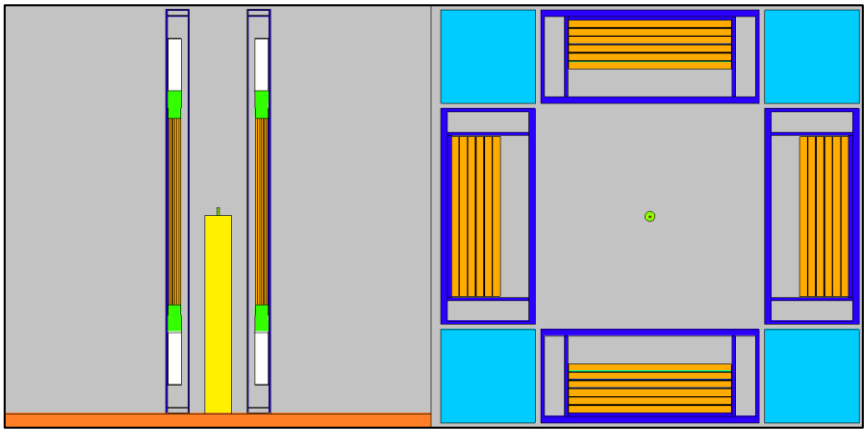

Figure 10.2 PLNS4 with ^{252}Cf source, polyurethane foam stand, and HDPE corners.

The *FoM* optimized configurations for a four panel system with a polyurethane foam stand was to move the active detector region close to the center of the system, add HDPE blocks to the corners, and to add 1.5 centimeters of HDPE to the interior and exterior, as depicted in Figure 10.3. No further optimization was pursued for the PLNS4 type systems.

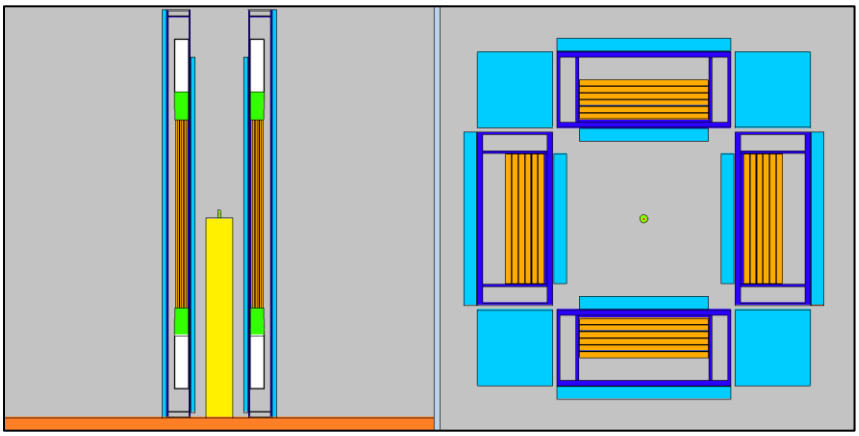

Figure 10.3 PLNS4 with detector regions moved close to the center and 1.5 cm HDPE lining and backing.

Although the modified PLNS4 had a predicted *FoM* of 24.8 ± 1, compared to the measured *FoM* of 4.4 for the UNCL-II, the PLNS4 type models were abandoned because of their very low doubles capture efficiency for fresh PWR fuel compared to the UNCL-II, which utilized active interrogation to increase the neutrons given off from the fuel. The PNLS4 was modified to an active interrogation configuration by replacing one detector panel with a slab of HDPE with a cavity for a neutron source, referred to as the PLNS3A. This active configuration was then optimized by simulating it corner pieces, inner lining, outer linings, and varying slab thicknesses of HDPE and PVT. Of the models simulated, the optimal configuration was to move the detector regions closer to the source, add 1.0 cm of HDPE inner lining, 1.5 cm HDPE outer lining, and add HDPE wedges to the corners, as depicted in Figure 10.4, which was referred to as PLNS3A-R1, and had an estimated *FoM* of 18.7 ± 1.

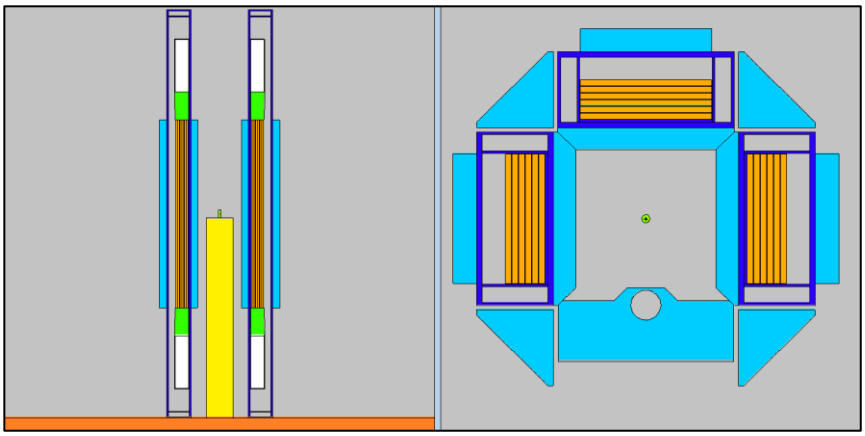

Figure 10.4 PLNS3A-R1, optimized active interrogation model.

To determine and compare the die-away times of the PLNS3A-R1 and the UNCL-II, both models were simulated with an encapsulated ^{252}Cf source centered on a polyurethane foam (PUF) stand. To show the differences in capture behavior between the fully moderated ^{3}He system and the LiF/ZnS system, the simulated total capture efficiencies (TCE) of both models were evaluated as a function of time. The results are shown in Figure 10.5, where the straight lines are chi-squared fits for a single exponential function.

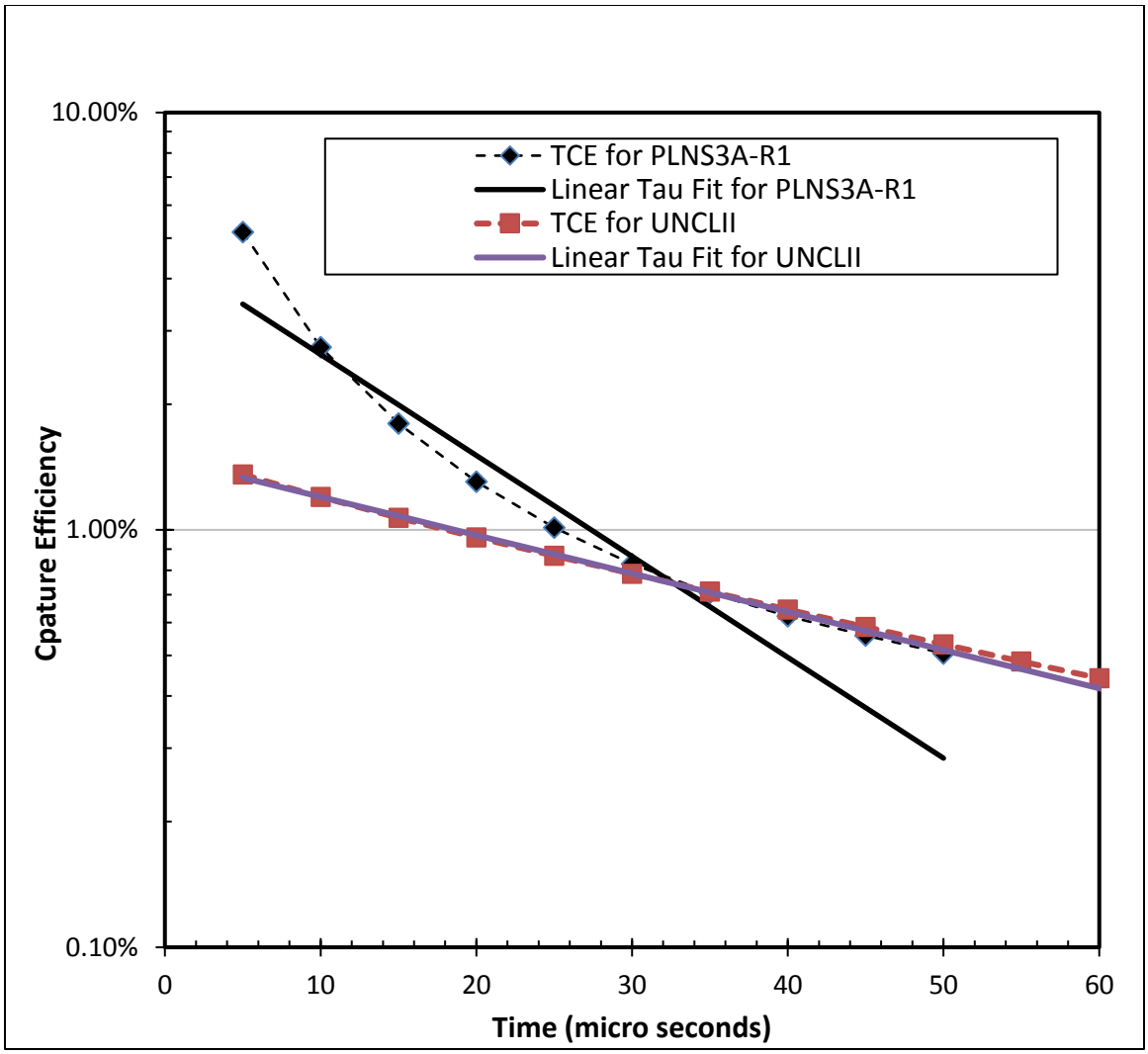

Figure 10.5 Total capture efficiency of the PLNS3A-R1 and the UNCL-II as a function of time.

As seen from this chart, the captures in the UNCL-II follows a single exponential decay over the full range of time, while the PLNS3A-R1 has a more rapid decay that changes times, providing it with a significantly higher total capture efficiency for the first few tens of microseconds, suggesting that the PLNS3A-R1 should be capable of the same performance as the UNCL-II but with a shorter gate time.

The gate length that gives the lowest relative error for a coincidence counter is roughly 1.26 τ [15]. This is a very broad and shallow minimum, so setting the gate width

to the nearest convenient value, considering hardware and software limitations, is usually sufficient [15]. For a die-away time of 18.0 μs for the PLNS3A-R1, the recommended die-away gate width is 22.7 μs, which was rounded to 24.0 μs, which was used for the remainder of the study. The pre-delay had specific optimal point, so it was picked to be short because of the fast fie-away time, but longer than a typical pulse. The pre-delay was chosen as 1.5 μs.

The PLNS3A-R1 and UNCL-II models were then modified to include a PWR fuel assembly, and the fuel was modified to include Gd loaded WPR fuel for select rods. These Gd burnable-poison fuel arrays were inserted into the PLNS3A-R1 and UNCL-II models to estimate the doubles capture efficiency and assay time of the PLNS3A-R1 and UNCL-II for various fuel configurations. The PLNS3A-R1 with a non-poisoned fuel array is depicted in Figure 10.6. Three configurations of positioning Gd loaded fuel within fuel arrays were used, as depicted in Figure 10.7. Arrays one through three contain four, eight, and sixteen Gd loaded fuel rods respectively. Each Gd loaded fuel rod contains 2.0w% ^{235}U and an amount of Gd that varies from 0-12w%. These simulations were run with the normal fuel rods containing 3.2% LEU and 4.5% LEU in an array of 72 total rods. Empty places in the array were reserved for instruments and coolant flow through a reactor core.

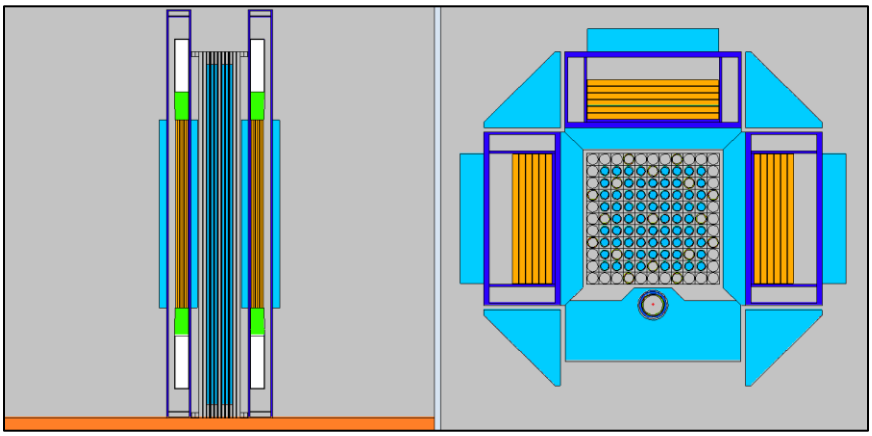

Figure 10.6 PLNS3A-R1 with full WPR fuel array and an active source.

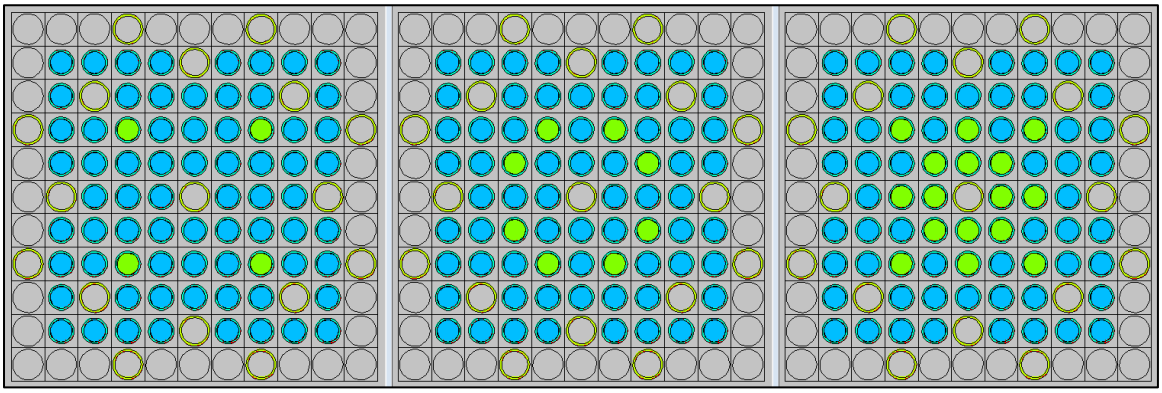

Figure 10.7 Fuel arrays with blue PWR fuel, green Gd loaded fuel, and empty regions for tools and coolant flow.

The full data set will not be provided here, but there was a significant increase in doubles capture efficiency when going from the UNCL-II to the PLNS3A-R1 across all fuel configurations, enrichments, and Gd concentrations, as depicted in Figure 10.8. All fuel array configurations showed very similar trends in performance between the UNCL-II and the PLNS3A-R1.

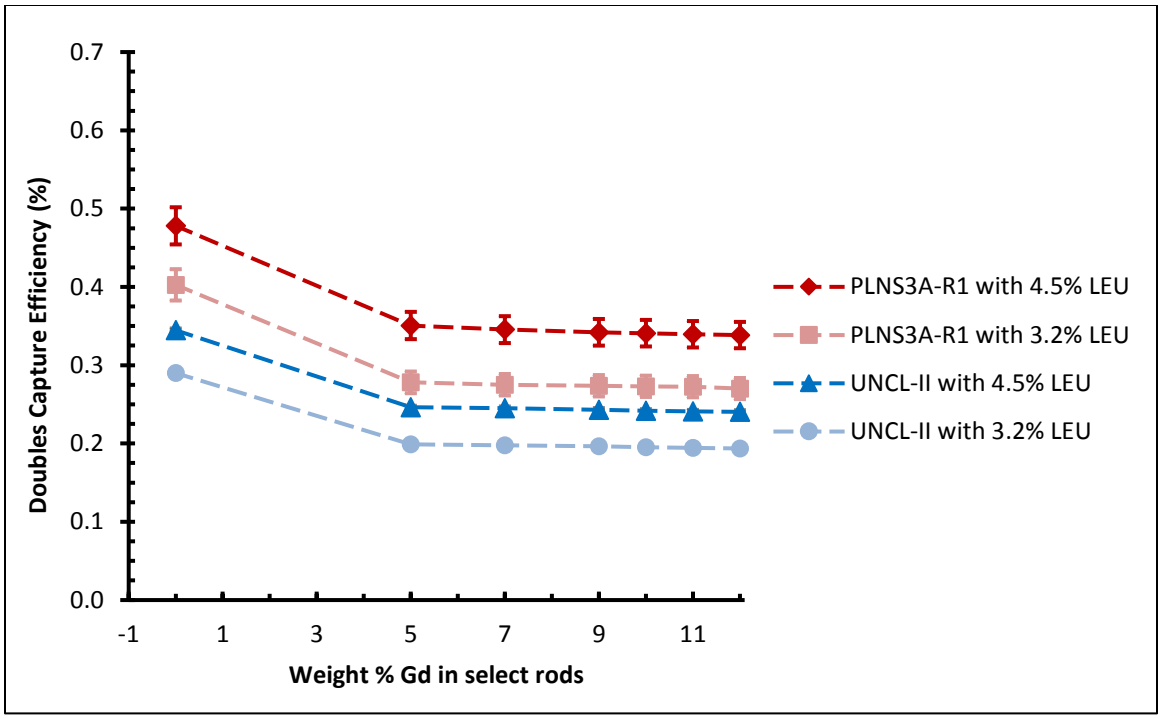

Figure 10.8 Array 3: Double capture efficiency per fission.

The UNCL-II and PLNS3A-R1 both displayed a rapid saturation trend in response to increasing Gd concentrations in fuel. Additional Gd beyond 5% into fuel did not significantly reduce the doubles capture efficiency of either system.

The statistical precision of assay measurements was estimated for an AmLi source of 2×10^4 n/s, for 600 second (10 minute) period and the predicted doubles capture efficiency, in the normal manner as the square root of counts over counts, as in Equation 10.1.

Equation 10.1 Assay Precision $= (\sqrt{\varepsilon_{Doubles} A t})^{-1}$

Where ε_{Double} is the predicted doubles count efficiency, A is the AmLi source activity, and t is the assay time. Assay precision estimates were performed over the range for all configurations. The UNCL-II had a statistical uncertainty of 0.5 - 0.7 % for assays, and the PLNS3A-R1 had a statistical uncertainty of 0.4 – 0.6 % for assays.

The PLNS3A-R1 model displayed the most promise as a potential system capable of meeting or exceeding UNCL-II performance for passive and active coincidence counting. The PLNS3A-R1 had a *FoM* of 18.7, four times greater than the UNCL-II's *FoM* of 4.4. The PLNS3A-R1 also displayed improved performance in counting fission events from Gd loaded fuel compared the UNCL-II. The results of this study indicate that a lithium-based coincidence counter, with a short die-away time, may be capable of making measurements of Gd-loaded low enriched uranium fuel in a reasonable period of time.

11 Appendix 2: Comparison of Ni-Quenched to Non-Quenched LiF/ZnS

Nickel-quenched LiF/ZnS was proposed by Eljen as an alternative to non-quenched (regular) LiF/ZnS with similar properties but faster scintillation decay times, which could reduce the effects of pulse pileup at high event rates. Pileup occurs when an event occurs and then a second event occurs before signal from the first event is completed, making the two events indistinguishable. Reducing the time scintillation time associated with each event reduces the time required to process each event and thus allow events to occur more closely in time before pileup occurs.

This chapter is intended to summarize the key scintillation performance aspects of Ni-quenched LiF/ZnS compared to regular LiF/ZnS. The performance aspects investigated are the light emission, the pulse height of signals, the pulse shape of signals, the total count rate associated with neutron and gamma-ray sources, gamma-ray discrimination, threshold dependence, and effects of pileup on neutron detection. Results will be given for experiments involving small bare samples of quenched and regular LiF/ZnS and for full-scale detector panels.

11.1 Material Selection Introduction

The performance of bare samples of Ni-quenched and non-quenched (regular) LiF/ZnS were measured to determine the relative characteristics of the two materials without potentially confounding aspects of more complex systems. Small bare sample experiments were performed by placing 5.1 cm × 5.1 cm (2” × 2”) samples of Ni-quenched and regular LiF/ZnS in source holders within a light tight box. A photomultiplier tube (PMT) on a stand was placed approximately 1 cm from the bare sample, facing the sample.

The PMT, PMT stand, and sample stand were all fixed in placed. Some high density polyethylene (HDPE) was placed within the light tight box near the sample to provide neutron moderation and reflection. The light tight box was sealed shut. Tests were performed with and without overhead lights on in the lab to ensure that no significant amounts of light were entering the light tight box and triggering the PMTs.

Neutron scintillation was measured by recording signals from the PMT when a ^{252}Cf source (~4,740 n/s) was near a bare LiF/ZnS sample. The encapsulated ^{252}Cf was placed outside the light tight box with 5.1 cm of lead between the source and the LiF/ZnS sample to shield the sample from gamma rays. A HDPE cave was constructed around the ^{252}Cf source and part of the light tight box, to moderate and reflect neutrons. Data sets were then collected in five minute runs with Pixie-4 thresholds of 5, 13, 21, and 29, which span reasonable threshold values. Pixie-4 thresholds are correlated with pulse height, but do not map to specific millivolt values. The ^{252}Cf source was then replaced with four ^{137}Cs and one ^{60}Co source and the 5.1 cm lead shield was removed. Data sets were collected again from five minute runs across the same Pixie-4 thresholds as previously stated. This process of data set collection occurred for the Ni-quenched and the regular samples back-to-back.

The regular sample displayed significant phosphorescence and was given about five minutes to de-excite after being placed in the light tight box before and data was collected. The Ni-quenched sample was not given time to de-excite since it has never displayed any significant phosphorescence.

Up to 250 neutron and gamma-ray induced pulses were manually selected from each of these runs. Gamma-ray runs with thresholds above 5 provided fewer than 250

gamma-ray pulses. The gamma-ray pulses from these runs were used instead of the 250 counts used for neutron pulses statistics. The gamma-ray runs with a threshold = 29 provided too few gamma-ray pulses to be statistically significant; therefore pulses from these runs are not reported.

Once measurements were completed on Ni-quenched and regular bare sample of LiF/ZnS, full scale detector stacks were constructed to measure the scintillation performance differences between the Ni-quenched and regular LiF/ZnS. Two detector stacks were constructed that were identical except that one incorporated regular LiF/ZnS and the other incorporated Ni-quenched LiF/ZnS. Both stacks were 20.32 cm wide. Scintillation measurements were performed by placing either stack alone into a light tight box with PMTs facing the optical openings on the stacks. The PMTs were removed 0.635 cm from the surfaces of the stacks so that every measurement with both stacks would have the same optical medium and distance between the stacks and the PMTs. Although a high portion of scintillation photons may have been lost due to the 0.635 cm gap between the stacks and the PMTs, these measurements were intended to examine the relative performance between the two stacks, which would be unaffected if all measurements lost the same fraction of photons between the stacks and PMTs. The detector assembly was centered on sheets of HDPE measuring 2.54 × 62.2 × 163 cm. The detector assembly was fixed to the HDPE and the HDPE was fixed to a lab table. Tests were performed with and without lights on in the lab to ensure that no significant amounts of light were entering the assembly and triggering the PMTs.

A ^{252}Cf source capsule was centered and placed horizontally on the assembly. No additional shielding or HDPE was placed around the source or assembly. Data sets were

then collected in five minute runs with Pixie-4 thresholds of 5, 13, 21, and 29. The ^{252}Cf source was then replaced with three ^{137}Cs sources. Data sets were collected again from five minute runs across the same Pixie-4 thresholds as previously stated. All sources were removed and background measurements were collected across all thresholds for five minutes each. This process was carried out for the Ni-quenched stack and the regular stack.

To improve the spatial isolation of the stacks from the materials in the room what are difficult to account for in MCNP simulations, the assembly was then elevated by placing its ends on wooden stands that measure 27.62 × 27.62 × 7.62 cm. All previous measurements with all sources, thresholds, and stacks were repeated for these elevated conditions. Measurements were compared to MCNP simulation results at various stages of the Alternative Multiplicity Counter project as a means of validating the MCNP models that were guiding detector development.

A dead-time free system was used to collect data sets separately from the measurements used above. The dead-time free system utilized an ATS9626 field programmable gate array to continuously stream data signals from one PMT to 16 different hard drives. Although this system was able to record dead-time free waveforms, the generated files where prohibitively large to save and analyze for more than a few seconds of data collection time. Using this system the 20.32 cm Ni-quenched panel was centered on a lab table without a source and a two seconds of full waveform background data set was collected. A ^{252}Cf source was centered horizontally on the detector panel and another two second full waveform data set was collected. This was repeated with four ^{137}Cs and one ^{60}Co sources acting as a single gamma-ray source, and repeated again with all of the sources placed on the detector panel. These data sets were used to create a catalog of Ni-

quenched neutron and gamma-ray pulses. Previously collected data sets were used to create a catalog of neutron and gamma-ray pulses from regular LiF/ZnS.

11.2 Light Emission from Bare Materials

The amount of light output per average neutron from small samples for each material was calculated by three different methods. The first method was to fit functions to the rise and decay time of neutron pulses and then integrate over these functions. The second was to average the neutron pulses and gamma-ray pulses over the four thresholds and then sum over these averaged pulses. The third was to stimulate the samples with ultraviolet light and record the amount and wavelength of light emitted from the samples.

Equations for the threshold averaged neutron pulse rise times and decay times NiQ_{ND}, $NiQ_{NR,}$ Reg_{ND}, and Reg_{NR} (Equation 11.3, Equation 11.5, Equation 11.5, and Equation 11.6) were used to calculate the ratio of light from Ni-quenched to regular LiF/ZnS. Ni-quenched neutron rise times were integrated over 106.7 ns or 8 Pixie-4 time bins; regular neutron rise times were integrated over 120.0 ns, or 9 Pixie-4 time bins. Ni-quenched and regular neutron decay times were integrated over 6,173.3 ns, or 463 Pixie-4 time bins. The light from the neutron pulse rise time and the neutron pulse decay time were summed to estimate the total light collected from neutron pulses for each materials. These total light values were compared to estimate the light collection change of Ni-quenched compared to regular LiF/ZnS, as seen in Equation 11.1.

Equation 11.1 $$\frac{\text{Total Neutron Light from Ni}-\text{Quenched}}{\text{Total Neutron Light from Regular}} = \frac{NiQ_{NR}+NiQ_{GD}}{Reg_{NR}+Reg_{GD}} = \frac{2140.96+46259.5}{2151.35+50951.3} = 0.911$$

The neutron pulses from the Ni-quenched material tended to be 8.90% less luminous than the regular material.

This process was repeated for the gamma-ray equations NiQ_{GD}, $NiQ_{GR,}$ Reg_{GD}, and Reg_{GR} (Equation 11.8, Equation 11.9, Equation 11.10, and Equation 11.11) to estimate the ratio of gamma-ray induced light from Ni-quenched to regular LiF/ZnS. The rise times and decay times of gamma-ray pulses in both materials was approximately 100 ns. The ratio of the total light from the gamma-ray pulses rise and decays can be seen in Equation 11.2.

Equation 11.2 $$\frac{\text{Total Gamma}-\text{Ray Light from Ni}-\text{Quenched}}{\text{Total Gamma}-\text{Ray Light from Regular}} = \frac{NiQ_{GR}+NiQ_{GD}}{Reg_{GR}+Reg_{GD}} = \frac{1333.53+1486.38}{1344.83+1219.41} = 1.10$$

The gamma-ray pulses from the Ni-quenched material tended to be 10.0% more luminous than the regular material.

The second method for estimating the light between materials was to sum the threshold averaged neutron and gamma-ray pulses from each material. The ratio of these sums was taken to estimate the change in light collected from neutron pulses between Ni-quenched and regular LiF/ZnS, as seen in Table 11.1.

Table 11.1 Light collection from averaged neutron pulses across multiple threshold, for Ni-quenched and regular LiF/ZnS. Although the light collection was is in arbitrary units, the gain was unchanged between measurements so that the values are comparable.

Neutron Pulse Threshold	Ni-Quenched Light Collection (Arbitrary Intensity)	Regular Light Collection (Arbitrary Intensity)	Ni-Quenched Light / Regular Light
5	34300	37700	0.907
13	45100	51300	0.880
21	53600	56900	0.942
29	60400	66500	0.909
Averaged	48300	53100	0.910

The threshold averaged neutron pulses from the Ni-quenched material were 9.0% ± 1.3 less intense than the regular material.

The previous analysis was repeated for gamma rays with results that can be seen in Table 11.2.

Table 11.2 Light collection from averaged gamma-ray pulses across multiple threshold, for Ni-quenched and regular LiF/ZnS. Although the light collection was is in arbitrary units, the gain was unchanged between measurements so that the values are comparable.

Gamma-Ray Pulse Threshold	Ni-Quenched Light Collection (Arbitrary Intensity)	Regular Light Collection (Arbitrary Intensity)	Ni-Quenched Light / Regular Light
5	894	668	1.35
13	2340	2250	1.04
21	3780	2610	1.05
Averaged	2340	2170	1.15

The threshold averaged gamma-ray pulses from the Ni-quenched material were 15% ± 10 more intense than the regular material.

The last technique used to quantify the light output was to measure the light with an instrument specifically designed for the task. The study was performed by Dr. Zheming Wang using a Horiba laser spectrometer system from the Environmental Molecular Science Laboratory facility at PNNL. In the first step of the process the excitation laser frequency is scanned while monitoring the total number of photons given off by the material. In the second step of the process the laser frequency is locked at the frequency that gave the maximum response and the wavelength of the emitted photons are resolved. The LiF/ZnS material chosen for use in the full-scale neutron multiplicity counter system will have a 250 μm polyester backing on both sides. This material affects both the excitation and the light output. For this reason, the comparison of the samples was done with the 250 μm

polyester backing in place. A comparison of the wavelength spectrum for emitted photon from the two materials is shown in Figure 11.1.

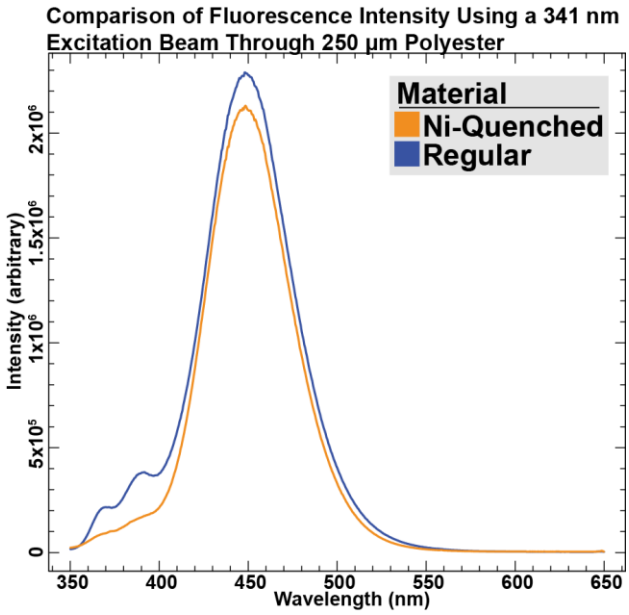

Figure 11.1 Comparison of the light output as a function of wavelength for Ni-quenched and regular LiF/ZnS.

The relative light emission from both materials was determined by taking the difference between the light emissions over the entire investigated spectra and at the peak emission wavelength. The Ni-quenched material emits 13.948% ± 0.007 less total scintillation light than the regular material, and 6.94% ± 0.09 less at the peak emission wavelength. In both cases the error bars are purely statistical.

11.3 Pulse Height from Bare Materials

The pulse height of the bare LiF/ZnS samples was investigated to determine how easily neutron events and gamma-ray events can be detected between the regular and Ni-quenched LiF/ZnS. These analyses used the same waveform data sets as were used in Section 11.2 that was collected from PMTs and bare samples in a light tight box with a

radiation source nearby. Since the optimal signal threshold was unknown, data sets were collected over a range of reasonable thresholds. The data sets from each threshold were averaged together, and then the average was taken between the four sets. The ratio of these averages was taken to estimate the change in neutron pulse height between Ni-quenched and regular LiF/ZnS, as seen in Table 11.3.

Table 11.3 Neutron pulse height across multiple thresholds, for Ni-quenched and regular LiF/ZnS. Although the pulse height was is in arbitrary units, the gain was unchanged between measurements so that the values are comparable.

Pixie-4 Threshold	Ni-Quenched Neutron Pulse Height (Arbitrary Intensity)	Regular Neutron Pulse Height(Arbitrary Intensity)	Ni-Quenched Pulse Height / Regular Pulse Height
5	833	676	1.23
13	1160	974	1.19
21	1340	1080	1.24
29	1570	1290	1.21
Averaged	1220	1000	1.22

The threshold averaged neutron pulses from the Ni-quenched material had 22% ± 1 greater pulse height than the regular material.

The maximum pulse height of the averaged gamma-ray-induced pulses from the small samples was recorded. The ratio of the averages was taken to estimate the change in gamma-ray pulse height between Ni-quenched and regular LiF/ZnS, as seen in Table 11.4.

The threshold averaged gamma-ray pulses from the Ni-quenched material had 35% ± 11 greater pulse height than the regular material.

Table 11.4 Gamma-ray pulse height across multiple thresholds, for Ni-quenched and regular LiF/ZnS. Although the pulse height was is in arbitrary units, the gain was unchanged between measurements so that the values are comparable.

Pixie-4 Threshold	Ni-Quenched Gamma-Ray Pulse Height (Arbitrary Intensity)	Regular Gamma-Ray Pulse Height (Arbitrary Intensity)	Ni-Quenched Pulse Height / Regular Pulse Height
5	185	120	1.54
13	529	461	1.15
21	694	513	1.35
Averaged	469	365	1.35

The bare Ni-quenched LiF/ZnS displayed greater pulse height from neutron-induced signals and from gamma-ray induced signals than the regular LiF/ZnS.

11.4 Pulse Shape Analysis for Bare Materials

The waveforms from the bare Ni-quenched and regular LiF/ZnS materials were analyzed to determine the neutron rise time, neutron decay time, gamma-ray rise time, and gamma-ray decay time. 250 neutron and gamma-ray waveforms were manually selected from each materials data set and then averaged to obtain an average neutron and gamma-ray waveform for each threshold. The average waveforms from the four thresholds were then averaged together to obtain overall average neutron and gamma-ray waveforms. Polynomial functions were then fit to the rising edge and the falling edge of these

waveforms to determine and compare the neutron rise time, neutron decay time, gamma-ray rise time, and gamma-ray decay time between the Ni-quenched and regular LiF/ZnS.

11.4.1 Neutron Pulse Shape Analysis

Typical neutron waveforms for each threshold were obtained by averaging the 250 manually selected neutron waveforms from each threshold's data set for the Ni-quenched and regular LiF/ZnS, which are displayed in Figure 11.2. The typical waveforms from the four data sets were averaged together to provide an overall comparison of the Ni-quenched to regular LiF/ZnS waveforms, as seen in Figure 11.3.

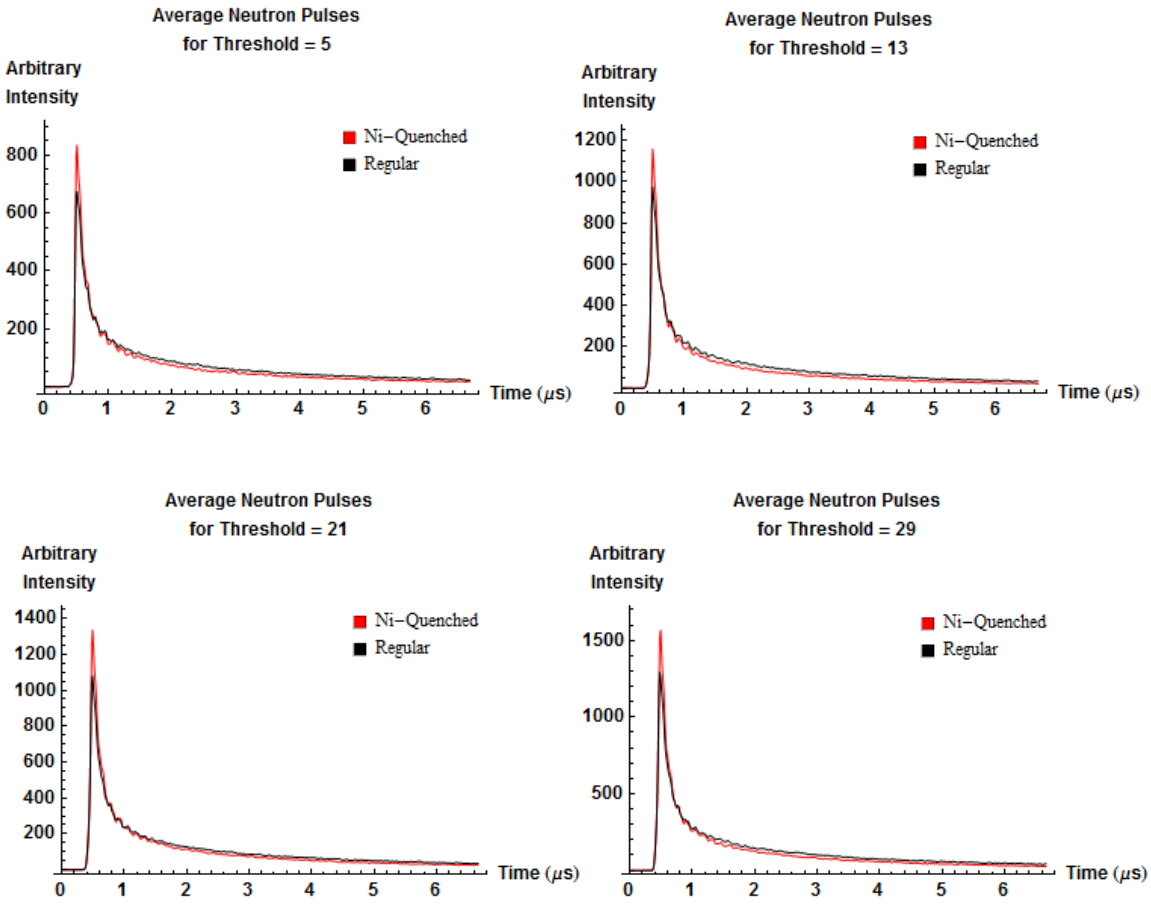

Figure 11.2 Average neutron waveforms for each of four thresholds, for Ni-quenched and regular LiF/ZnS. Although intensities are in arbitrary units, no gain changes occurred between measurements, so the intensities are comparable.

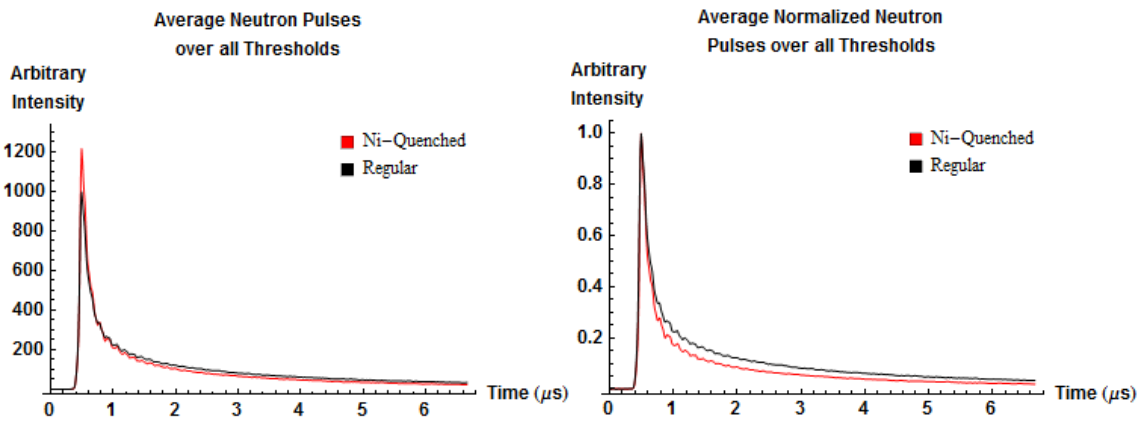

Figure 11.3 (Left) unnormalized threshold averaged neutron pulse shapes for Ni-quenched and regular LiF/ZnS. Right: normalized threshold averaged neutron pulse shapes for Ni-quenched and regular LiF/ZnS.

The neutron pulse decay time for these threshold averaged neutron waveforms was estimated by fitting a double exponential decay to the neutron waveforms from the peak pulse height to the end of the waveforms. This peak to end data set and the fit function were plotted with uncertainty bands at 1 standard deviation (sigma), as seen in Figure 11.4 for Ni-quenched and Figure 11.5 for regular LiF/ZnS. The uncertainty bands are small enough to be difficult to see. The equation fit to the Ni-quenched neutron decay time NiQ_{ND} can be seen in Equation 11.3, the equation fit to the regular neutron decay time Reg_{ND} can be seen in Equation 11.4, where time t is in picoseconds.

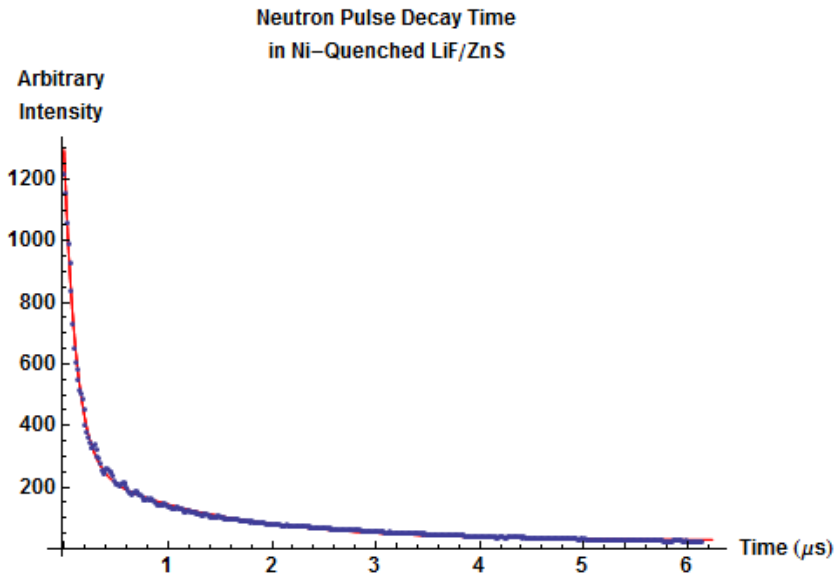

Figure 11.4 Ni-quenched threshold averaged neutron pulse tail with NiQ_{ND} and 1 sigma uncertainty bands overlapped.

Equation 11.3 $NiQ_{ND} = 26.4 + 256e^{-0.776t} + 1086e^{-8.65t}$

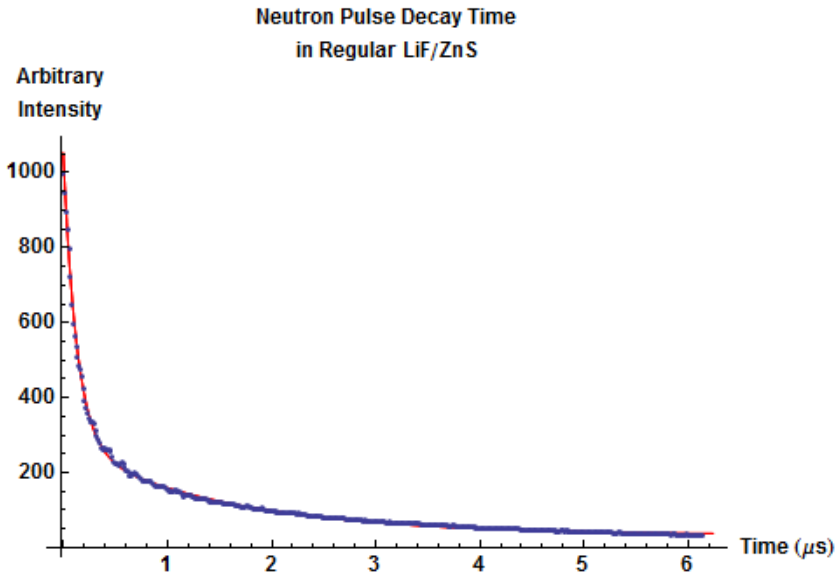

Figure 11.5. Regular threshold averaged neutron pulse tail with Reg_{ND} and 1 sigma uncertainty bands overlapped.

Equation 11.4 $Reg_{ND} = 33.6 + 244e^{-0.659t} + 826e^{-7.73t}$

NiQ$_{ND}$ and *Reg*$_{ND}$ and their respective 1 sigma uncertainty bands were plotted together to inspect the expected behavior of neutron decays between both materials together, as seen in Figure 11.6.

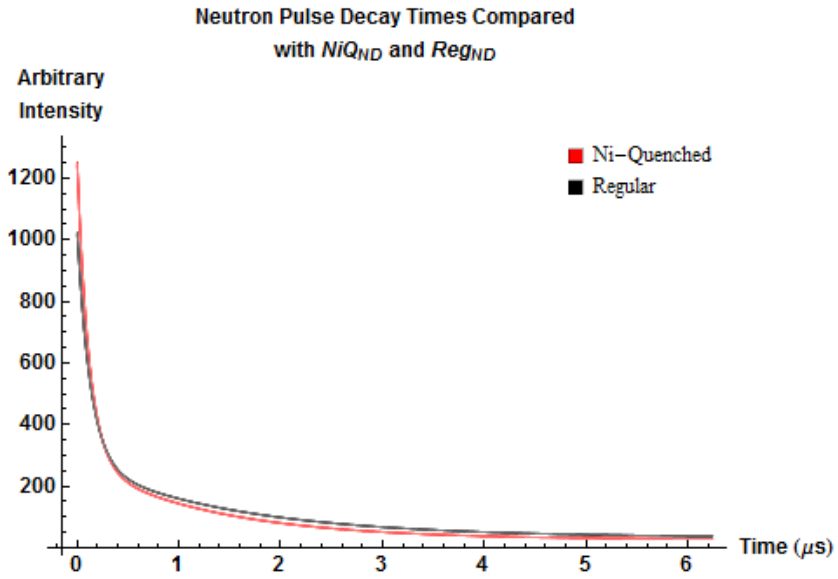

Figure 11.6 Comparison of average neutron pulse decay times for Ni-quenched and regular LiF/ZnS with *NiQ*$_{ND}$ and *Reg*$_{ND}$.

Constants and uncertainties of values in *NiQ*$_{ND}$ and *Reg*$_{ND}$ can be seen in Table 11.1.

Table 11.5 Constants and uncertainties of NiQND and RegND, where both equations are of the form $a + b^{ct} + d^{et}$.

Constants	NiQ_{ND}	Reg_{ND}
a (Arbitrary Intensity)	26.4 ± 0.8	33.6 ± 0.7
b (Arbitrary Intensity)	256 ± 3	244 ± 2
c (ps^{-1})	-0.78 ± 0.02	-0.66 ± 0.01
d (Arbitrary Intensity)	1086 ± 6	826 ± 4
e (ps^{-1})	-8.65 ± 0.09	-7.73 ± 0.07

The Ni-quenched ^{6}LiF/ZnS demonstrated a peak to 20% neutron pulse decay time of 351 ns ± 2, and the regular sample displayed a peak to 20% neutron pulse decay time of 524 ns ± 3. Peak to 20% decay time was selected as a standard for the decay time as opposed to the more typical 90% to 10% decay time since these waveforms have a much more clearly defined peak point rather than a 90% point, and they have long energy tails that return to 10% relatively slowly compared to 20%. This analysis shows that Ni-quenched LiF/ZnS has a faster neutron decay time than the regular LiF/ZnS.

Because waveforms are composed of a rise time and a decay, to fully determine the typical neutron pulse time for Ni-quenched and regular LiF/ZnS, the analysis that was described above was repeated for the neutron rise times for both materials. A third order polynomial was fit to the average neutron rise time of the Ni-quenched and the regular LiF/ZnS. The polynomials were fit from the beginning of the neutron pulses rise to the peak, and include 1 sigma statistical uncertainty bands, as seen in Figure 11.7 for Ni-quenched and Figure 11.8 for regular LiF/ZnS. The equation fit to the Ni-quenched

neutron rise time NiQ_{NR} can be seen in Equation 11.5, the equation fit to the regular neutron rise time Reg_{NR} can be seen in Equation 11.6. NiQ_{NR} and Reg_{NR} were plotted together for comparison in Figure 11.9.

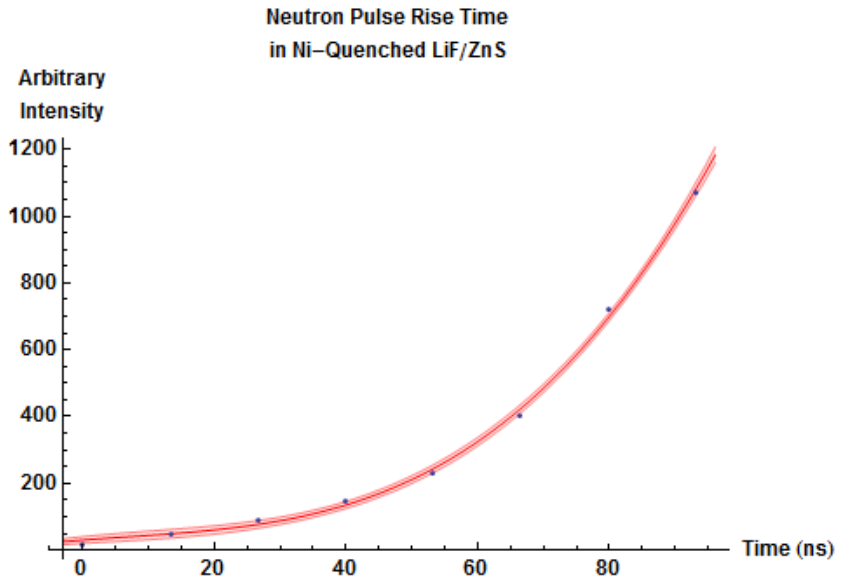

Figure 11.7 Ni-quenched threshold averaged neutron pulse rise with NiQ_{NR} and 1 sigma uncertainty bands overlapped.

Equation 11.5 $NiQ_{NR} = 3.22t - 1.21t^2 + 0.259t^3$

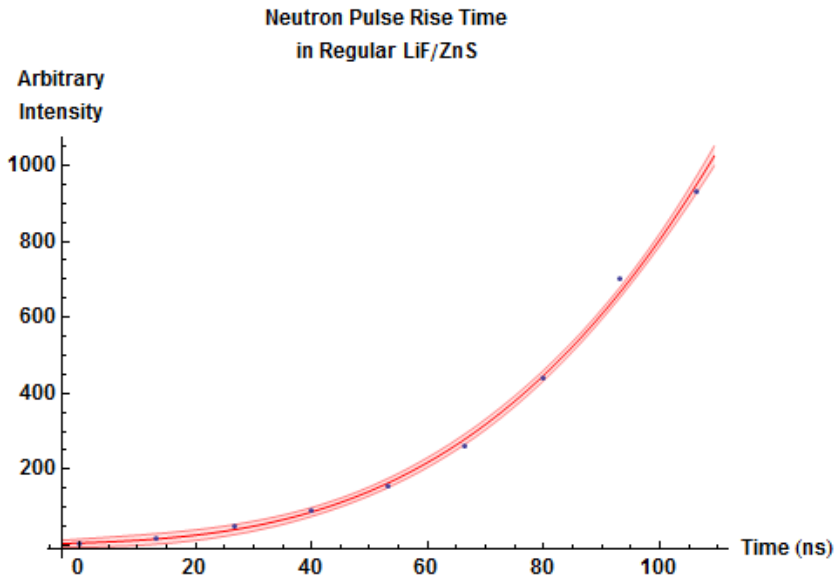

Figure 11.8 Regular threshold averaged neutron pulse rise with Reg_{NR} and 1 sigma uncertainty bands.

Equation 11.6 $Reg_{NR} = 0.491t - 0.146t^2 + 0.108t^3$

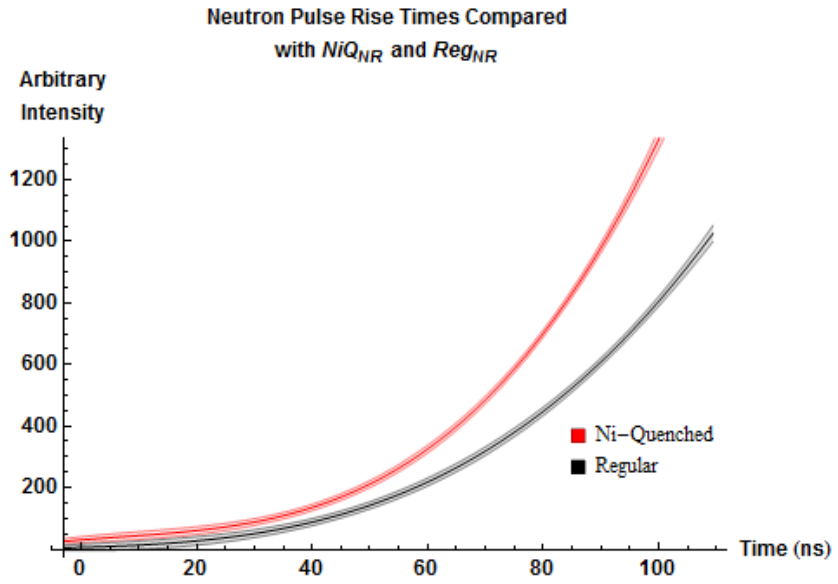

Figure 11.9 Comparison of average neutron pulse rise times for Ni-quenched and regular LiF/ZnS with NiQ_{NR} and Reg_{NR}.

Constants and uncertainties of values in NiQ_{NR} and Reg_{Nr} can be seen in Table 11.6.

Table 11.6. Constants and uncertainties of NiQNR and RegNR, where both equations are of the form $at + bt^2 + ct^3$.

Constants	NiQ_{ND}	Reg_{ND}
a (Arbitrary Intensity / ns)	3 ± 1	0.5 ± 0.9
b (Arbitrary Intensity / ns^2)	-1.2 ± 0.4	-0.1 ± 0.3
c (Arbitrary Intensity / ns^3)	0.26 ± 0.03	0.11 ± 0.02

The Ni-quenched ^{6}LiF/ZnS demonstrated a 20% to peak neutron pulse rise time of 64 ns ± 1, and the regular sample displayed a 20% to peak neutron rise time of 70 ns ± 2. This analysis shows that Ni-quenched LiF/ZnS has a slight faster neutron rise time than the regular LiF/ZnS.

Comparing the ratio of the total neutron pulse rise times and decay times for both materials, as seen in Equation 11.7, the Ni-quenched material completes an average neutron pulse in 70% of the time as the regular material. Taking the inverse of this value and subtracting one, the Ni-quenched material is expected to have similar neutron pile-up effects at rates 49% higher than the regular material.

Equation 11.7 $\frac{\text{Ni−quenched pulse time}}{\text{Regular pulse time}} = \frac{64\ ns+351\ ns}{70\ ns+524\ ns} = 0.699$

11.4.2 Gamma-Ray Pulse Shape Analysis

Typical gamma-ray waveforms for each threshold were obtained by averaging the 250 manually selected gamma-ray waveforms from each threshold's data set for the Ni-quenched and regular LiF/ZnS, which are displayed in Figure 11.10. The typical waveforms from the three data sets were averaged together to provide an overall comparison of the Ni-quenched to regular LiF/ZnS waveforms, as seen in Figure 11.11. A

statistically insignificant number of gamma-ray like waveforms were present in the data sets collected with threshold = 29, therefore no data from the threshold measurements will be presented in this section.

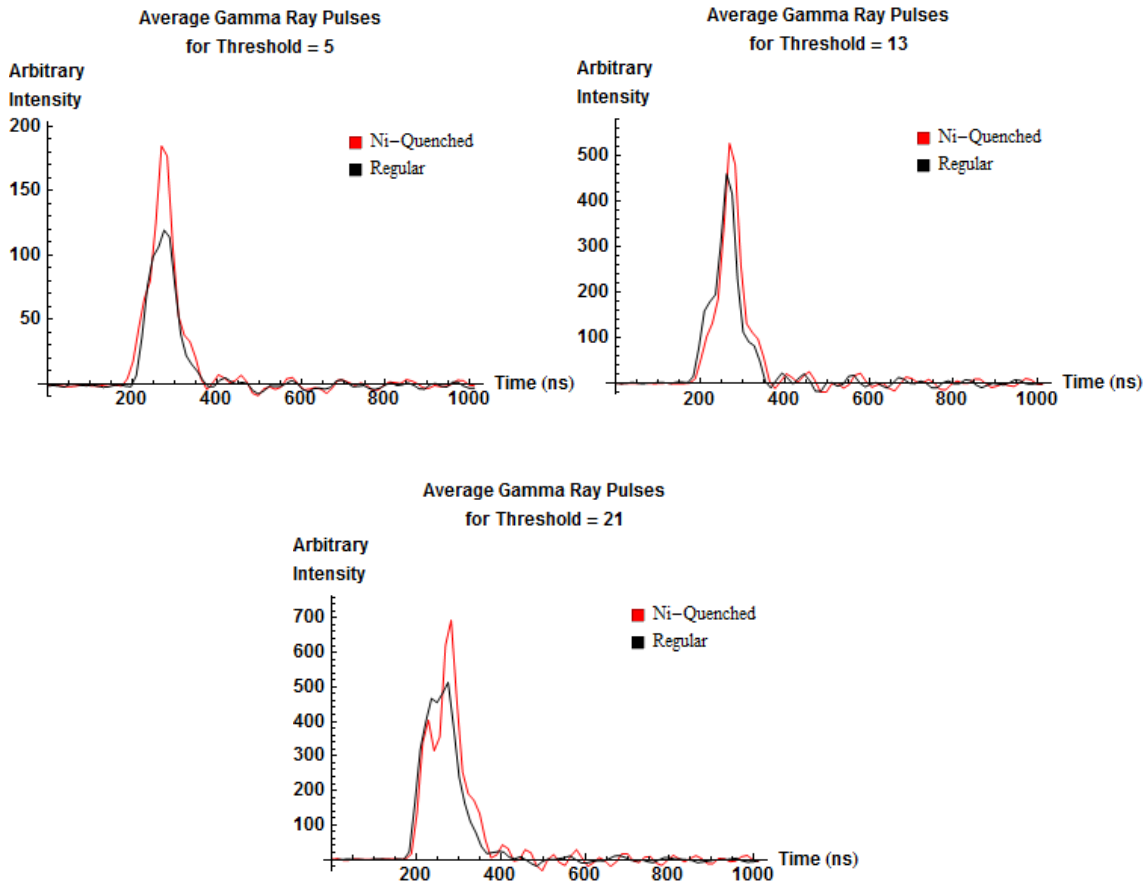

Figure 11.10 Average gamma-ray waveforms for each threshold, for Ni-quenched and regular LiF/ZnS. Although the intensities are in arbitrary units, no gain changes occurred between measurements, so the intensities are comparable.

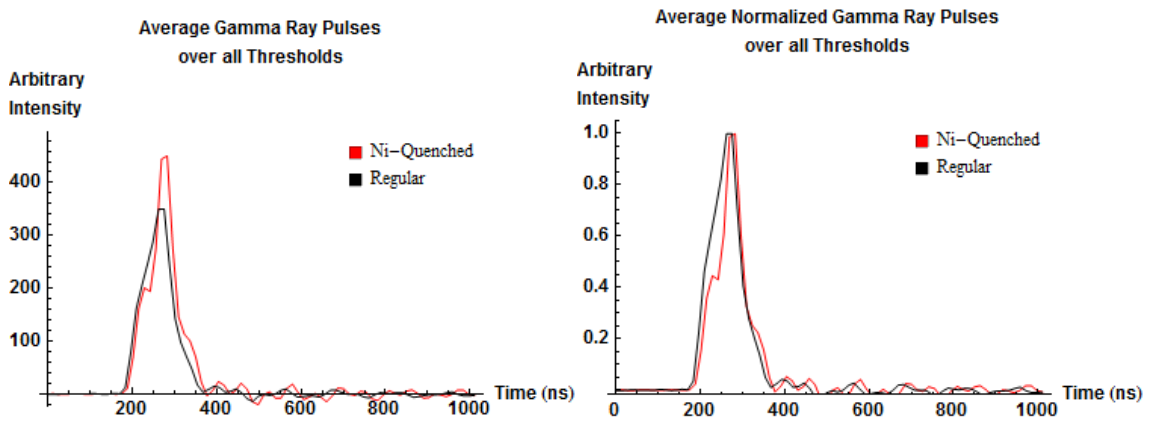

Figure 11.11 (Left) unnormalized threshold averaged neutron pulse shapes for Ni-quenched and regular LiF/ZnS. (Right) normalized threshold averaged neutron pulse shapes for Ni-quenched and regular LiF/ZnS.

The gamma-ray decay time for these averaged gamma-ray waveforms was determined by fitting an exponential decay to the gamma-ray waveform data set from the peak of the pulse until the pulse returned to zero. This peak to zero data set and the fit function were plotted with 1 sigma statistical uncertainty bands as seen in Figure 11.12 for Ni-quenched and Figure 11.13 for regular LiF/ZnS. The gamma-ray decay times were fit to first order polynomials, as seen in Equation 11.8 for the Ni-quenched gamma-ray decay time NiQ_{GD}, and in Equation 11.9 for the regular gamma-ray decay time Reg_{GD}, where time is in picoseconds.

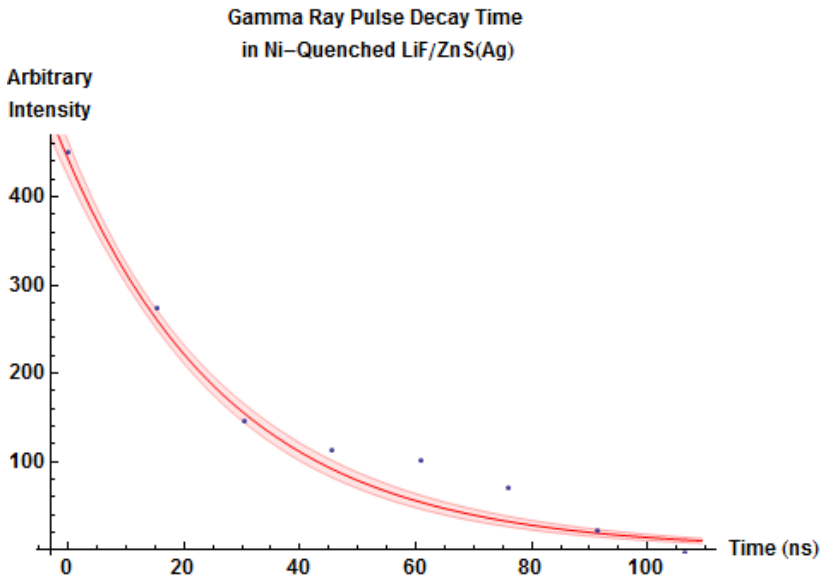

Figure 11.12 Ni-quenched threshold averaged gamma-ray pulse decay with NiQ_{GD} and 1 sigma statistical uncertainty bands overlapped.

Equation 11.8 $NiQ_{GD} = 442e^{-0.0346t}$

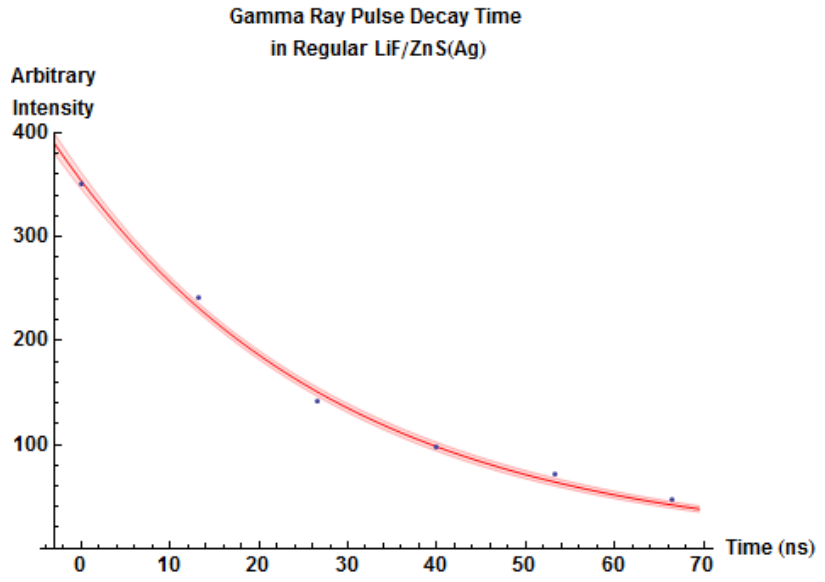

Figure 11.13. Regular threshold averaged gamma-ray pulse decay with Reg_{GD} and 1 sigma statistical uncertainty bands overlapped.

Equation 11.9 $Reg_{GD} = 354e^{-0.0322t}$

NiQ$_{GD}$ and *Reg*$_{GD}$ and their respective 1 sigma statistical uncertainty bands were plotted together to compare the behaviors of gamma-ray decays between both materials together, as seen in Figure 11.14.

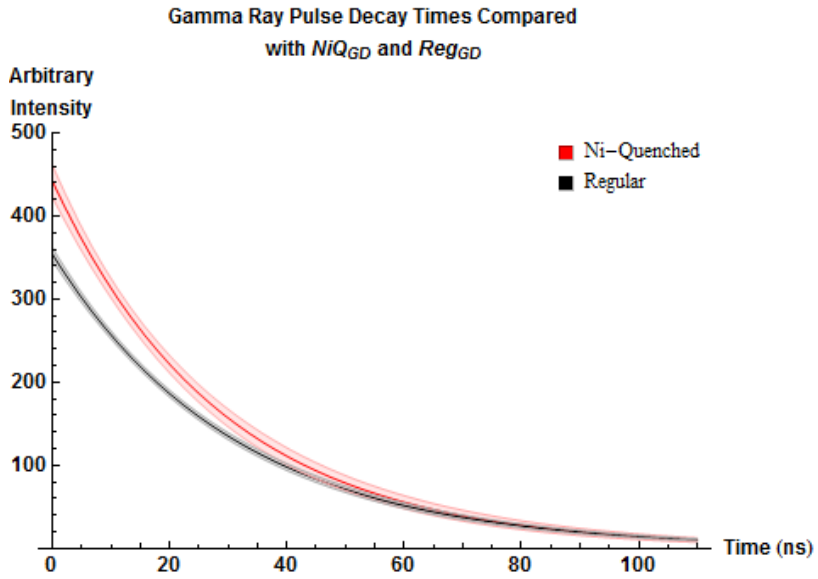

Figure 11.14 Comparison of average gamma-pulse decay times for Ni-quenched and regular LiF/ZnS with *NiQ*$_{GD}$ and *Reg*$_{GD}$.

Constants and uncertainties of values in *NiQ*$_{GD}$ and *Reg*$_{GD}$ can be seen in Table 11.7.

Table 11.7 Constants and uncertainties of NiQGD and RegGD, where both equations are of the form ae^{-bt}.

Constants	**NiQ$_{ND}$**	**Reg$_{ND}$**
b (Arbitrary Intensity)	440 ± 20	350 ± 1
c (ns^{-1})	0.0346 ± 0.003	0.0322 ± 0.002

The Ni-quenched material displayed a 46 ns ± 6 peak to 20% falling edge time, and the regular material displayed a 50 ns ± 7 peak to 20% falling edge time. This analysis was inconclusive since each decay time is within the statistical uncertainty of the other decay time. If the Ni-quenched LiF/ZnS does have a faster gamma-ray decay time than the regular LiF/ZnS, it is not significantly faster.

Because waveforms are composed of a rise time and a decay, to fully determine the typical gamma-ray pulse time for Ni-quenched and regular LiF/ZnS, the analysis that was described above was repeated for the gamma-ray rise times for both materials. A first order polynomial was fit to the threshold averaged gamma-ray pulse rise time of both materials. This zero to peak gamma-ray rise data set and the fit function were plotted with 1 sigma statistical uncertainty bands, as seen in Figure 11.15 for Ni-quenched and Figure 11.16 for regular LiF/ZnS. The equation fit to the Ni-quenched neutron decay time NiQ_{GR} can be seen in Equation 11.10, the equation fit to the regular neutron decay time Reg_{GR} can be seen in Equation 11.11, where time t is in nanoseconds. NiQ_{GR} and Reg_{GR} and their respective 1 sigma uncertainty bands were plotted together for comparison in Figure 11.17.

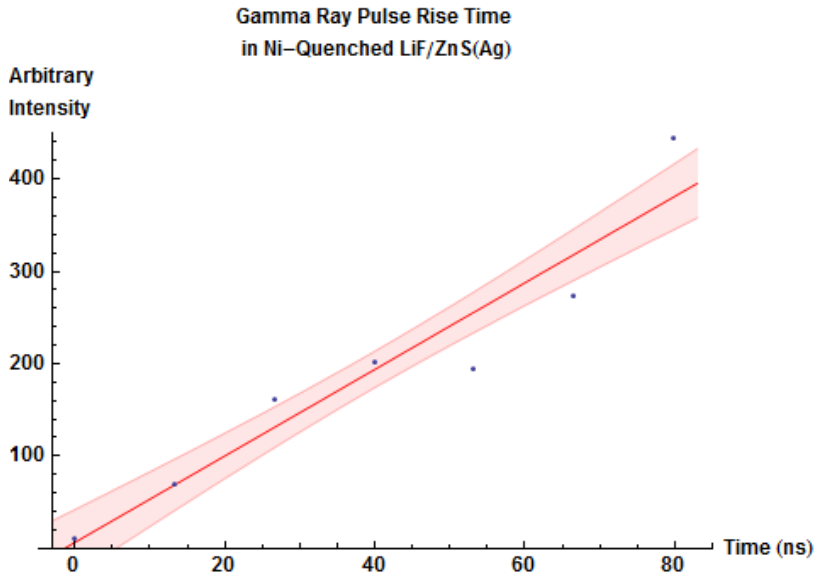

Figure 11.15 Ni-quenched threshold averaged gamma-ray pulse rise with fit function overlapped.

Equation 11.10 $NiQ_{GR} = 10.6 + 4.99t$

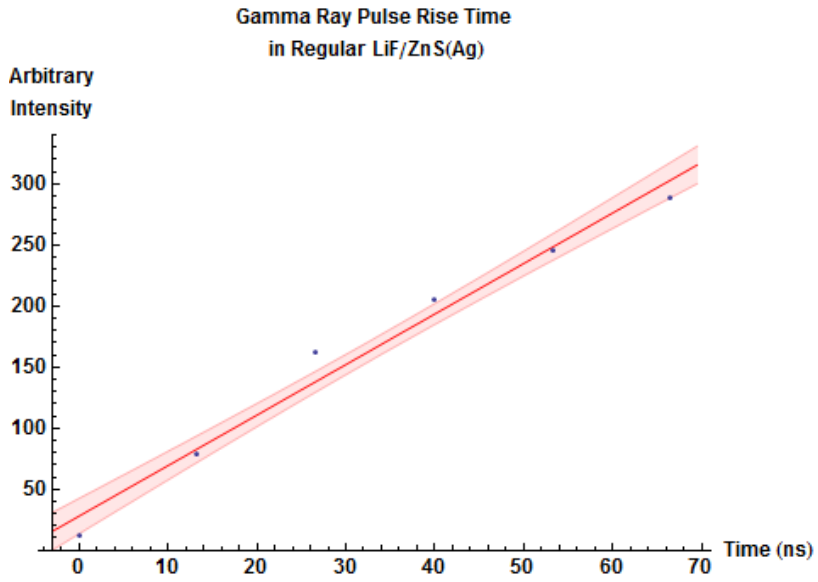

Figure 11.16 Regular threshold averaged gamma-ray pulse rise with fit function overlapped.

Equation 11.11 $Reg_{GR} = 28.0 + 4.13t$

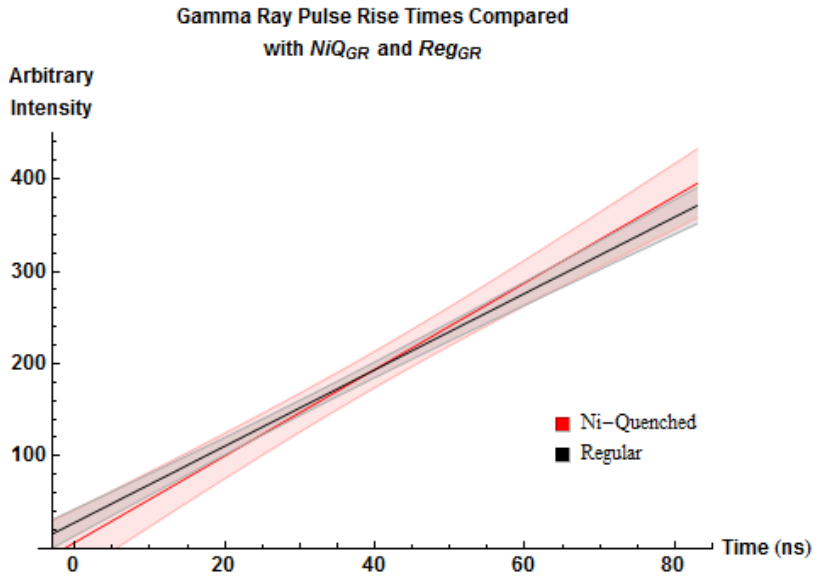

Figure 11.17 Comparison of average gamma-ray pulse rise times for Ni-quenched and regular LiF/ZnS with NiQ_{GR} and Reg_{GR}.

Constants and uncertainties of values in NiQ_{GR} and Reg_{GR} can be seen in Table 11.8.

Table 11.8 Constants and uncertainties of NiQGR and RegGR, where both equations are of the form $a + bt$.

Constants	NiQ_{ND}	Reg_{ND}
a (Arbitrary Intensity)	10 ± 2	28 ± 2
b (Arbitrary Intensity / ns)	5.0 ± 0.6	4.1 ± 0.4

The Ni-quenched material displayed a 66 ns ± 7 20% rising edge to peak time, and the regular material displayed a 59 ns ± 4 20% rising edge to peak time. This analysis shows that the Ni-quenched LiF/ZnS has a slightly faster gamma-ray decay time than the regular LiF/ZnS, similarly to the neutron induced pulses.

From this data set it can be seen that both materials have similar rise times, although the Ni-quenched material may have a slightly faster gamma-ray rise time than the regular material.

Equation 11.12
$$\frac{\text{Ni−quenched pulse time}}{\text{Regular pulse time}} = \frac{66\ ns + 46\ ns}{59\ ns + 50\ ns} = 1.03$$

The Ni-quenched material displayed a 3% ± 11 reduced 20% rising edge to 20% falling edge relative to the regular material.

11.5 Total Count Rate

Total count rates from the small samples were determined by reading the Pixie-4 output files (.ifm files), as seen in Table 11.9. No background runs were taken since test runs indicated very low and consistent rates between both samples. All pulses from a lead

shielded ^{252}Cf source were assumed to be from neutron interactions, and all pulses from four bare ^{137}Cs and one ^{60}Co were assumed to be from gamma-ray interactions.

Table 11.9 Total neutron and gamma-ray counts from small samples for Ni-quenched and regular LiF/ZnS.

Threshold	Pulse Type	Ni-Quenched Count Rate (Hz)	Regular Count Rate (Hz)	Ni-Quenched Count Rate / Regular Count Rate
5	Neutron	101	118	0.862
13	Neutron	70.2	70.4	0.997
21	Neutron	54.4	54.0	1.01
29	Neutron	44.5	42.1	1.06
Average	Neutron	67.6	71.1	0.982
5	Gamma-Ray	7.69	178	0.0431
13	Gamma-Ray	0.558	0.434	1.29
21	Gamma-Ray	0.186	0.150	1.24
Average	Gamma-Ray	0.372	0.292	1.26

The average neutron count rate of the Ni-quenched material decreased by 1.8% ± 4.2 compared to the regular material. The average gamma-ray count rate of the Ni-quenched material increased by 26% ± 2 compared to the regular material, excluding the threshold = 5 results. The Ni-quenched LiF/ZnS neutron sensitivity is not statistically significantly different from the regular LiF/ZnS, although Ni-quenched LiF/ZnS is more sensitive to gamma-rays at most thresholds.

Total neutron counts for a full-scale stack were determined by constructing two 20.32 cm wide stacks, one with Ni-quenched LiF/ZnS and the other with non-doped LiF/ZnS. These stack were placed in an aluminum box on a table, with PMTs facing the ends of the stacks, as described in the introduction of chapter 4 and depicted in Figure 4.1. Data sets were collected with both stacks at Pixie threshold of 5, 13, 21, and 29 as described in chapter 4, with results presented in Table 11.10.

Table 11.10 Relative neutron detection rates of Ni-quenched and regular LiF/ZnS full-scale stacks.

Threshold	**20.32 cm Ni-Quenched Count Rate (Hz)**	**20.32 cm Regular Count Rate (Hz)**	**15.24 cm Regular Count Rate (Hz)**
Elevated			
5	1523 ± 3	1468 ± 3	1207 ± 2
13	304 ± 1	269 ± 1	268 ± 1
21	43.3 ± 0.4	26.7 ± 0.3	35.9 ± 0.3
29	4.6 ± 0.1	2.22 ± 0.09	4.1 ± 0.1
Un-Elevated			
5	2288 ± 4	2156 ± 5	1771 ± 3
13	497 ± 1	405 ± 1	405 ± 1
21	71.7 ± 0.5	38.3 ± 0.4	50.0 ± 0.4
29	7.5 ± 0.2	3.1 ± 0.1	4.9 ± 0.1

At threshold = 5, the threshold most representative of the threshold used in the fully operation system, the Ni-quenched had a 4% ± 2 increase in neutron count rate compared to the 20.32 cm wide regular panel.

At higher thresholds the Ni-quenched material had increased ε compared to the regular LiF/ZnS for both small and full-scale measurements. At the lowest threshold, the Ni-quenched material had inferior ε for the bare sample and slightly superior ε for the full-scale samples. A full system constructed with Ni-quenched LiF/ZnS is anticipated to have slightly improved ε compared to a Ni-free system.

11.6 Gamma-Ray Discrimination

Because LiF/ZnS and wavelength shift plastic (WSP) are inherently sensitive to gamma ray, as scintillators, gamma-ray sensitivity was analyzed for bare samples of Ni-quenched and regular LiF/ZnS. Bare analyzed based on manually selected gamma-ray-like waveforms.

Pulse shape discrimination (PSD) was applied to full-scale stacks with LiF/ZnS with Ni-quenched and regular material. These analyses were conducted before the PSD development that is documented in chapter 4, therefore Method 1 was the only PSD method used for the analyses in this section. PSD information is only briefly reviewed in this section, with more complete information available in Chapter 4 and Section 2.2. After waveforms were analyzed with Method 1 a double Gaussian function was fit to the charge ratios. The standard deviation of the two Gaussians and their distance apart was used to determine the gamma-ray discrimination figure-of-merit, allowing the gamma-ray sensitivity of the stacks to be compared.

11.6.1 Small Sample Gamma-Ray Discrimination

Manually selected gamma-ray pulses from the bare samples were collected and counted, as seen in Table 11.11, for comparing gamma-ray sensitivity. The ratios of the number of Ni-quenched gamma-ray pulses to the number of regular gamma-ray pulses over the same period of time is used to estimate the relative sensitivity of the Ni-quenched material to the regular LiF/ZnS.

Table 11.11 Manually selected gamma-ray pulses from 5 minutes of data collection.

Threshold	Ni-Quenched Gamma-Ray Pulses	Regular Gamma-Ray Pulses
5	>250	>250
13	145	110
21	44	30

Comparing the file sizes of the threshold = 13 data set to the threshold = 5 data set, it becomes apparent that manually selecting all gamma-ray pulses from the threshold = 5 files would take a prohibitively long period of time and was therefore not performed. The number of gamma-ray-like events within the first 250 total events, from the threshold = 13 data set and the threshold = 21 data set, was 39% ± 7 higher from the Ni-quenched material compared to the regular material.

When the ^{252}Cf source was placed near the source with 5.08 cm of lead between the source and the sample, very few gamma-ray-like waveforms were observed, therefore no gamma-ray pulses are reported from the runs utilizing the ^{252}Cf source for the bare samples.

Gamma-ray measurements of bare samples were compared to gamma-ray measurements of the PMT looking at two sheets of WSP without any LiF/ZnS, to estimate the number of gamma-ray-like waveforms generated from the WSP relative to the LiF/ZnS. Because all waveforms collected from WSP alone were gamma-ray-like a count rate was used instead of manually selected events to compared gamma-ray sensitivities between different thresholds. The total rates from the WSP measurements without samples were multiplied by 5/12 to adjust for the thickness of WSP used in the measurements and the ratio of WSP to LiF/ZnS used in the stacks. These measurements, as read directly from Pixie-4 output files (.ifm files) can be seen in Table 11.12. .Ifm files are human readable files that include information about summarize a Pixie-4 data collection run, including count rate.

Table 11.12 Gamma-ray count rates of WSP, Ni-quenched, and Regular samples compared.

Threshold	Ni-Quenched Count Rate (Hz)	Regular Count Rate (Hz)	WSP Count Rate	Ni-Quenched + WSP / Ni- Regular + WSP
5	7.69	178	6.68	0.0777
13	0.558	0.434	0.0966	1.23
21	0.186	0.150	0.0367	1.19

Accounting for the gamma-ray and neutron sensitivity of the WSP, which only produce gamma-ray0like signals, these analysis of threshold = 13 data sets and threshold = 21 data sets show that full-sized Ni-quenched LiF/ZnS stacks are expected to be 22% ± 2 more sensitive to gamma rays than regular LiF/ZnS stacks.

11.6.2 Full-Scale Gamma-Ray Discrimination

Spencer Behling led research to quantify the gamma-ray discrimination of full-scale detector stacks, to determine how a more realistic system would perform than the bare sample examined above. Full-scale detector stacks with either Ni-quenched or regular LiF/ZnS were placed in a light tight box with PMTs facing each of the ends to collect sctillation light. A ^{252}Cf source was placed on the light tight box and data sets were collected from one PMT for 5 minutes with both stacks. A Pixie-4 was used as the data acquisition systems, operating in waveform mode so that PSD could be performed. The same settings, equipment, and procedure was followed for both stacks. The process used is as follows:

1. The 500 bin waveforms from a single PMT were used in the PSD algorithm.
2. The first 25 bins, which occur before the trigger event, were averaged and then subtracted from all bins within the waveform, as a means of baseline subtraction.
3. The next 20 bins after background subtraction where summed. This sum is what will be referred to as the short gate.
4. The last 455 bins after background subtraction where summed. This sum is what will be referred to as the long gate.
5. The ratio of long gate / short gate was recorded of for each waveform with a histogram. These histograms have two peaks in them, one originating from gamma-ray events (peaked around zero) and the other coming from neutron events (peaked around 5), as seen in Figure 11.18.
6. The histogram for each material was normalized so that it could be viewed as the probability of observing a background or real event.

7. Then the distribution was fit with two Gaussians and the area of the overlap region between the two Gaussians was calculated as a percent of the total area. This figure quantifies our ability to distinguish between gamma-ray and neutron events.
8. The errors for these measurements were estimated by generating 1000 new fit curves and measuring the overlap region in each case and taking the standard deviation of these 1000 values. Each new fit value was generated by drawing Gaussian distributed random numbers for each of the 6 fit parameters. Where the mean and standard deviation of each Gaussian were taken as the central value and standard error for each fit parameter at its best-fit value.

This procedure was carried out on data sets from the full-scale Ni-quenched stack, the full-scale regular stack, and a ¾ scale regular stack, which left over from previous AMC project studies [6, 62]. The results of this procedure are shown in Figure 11.18.

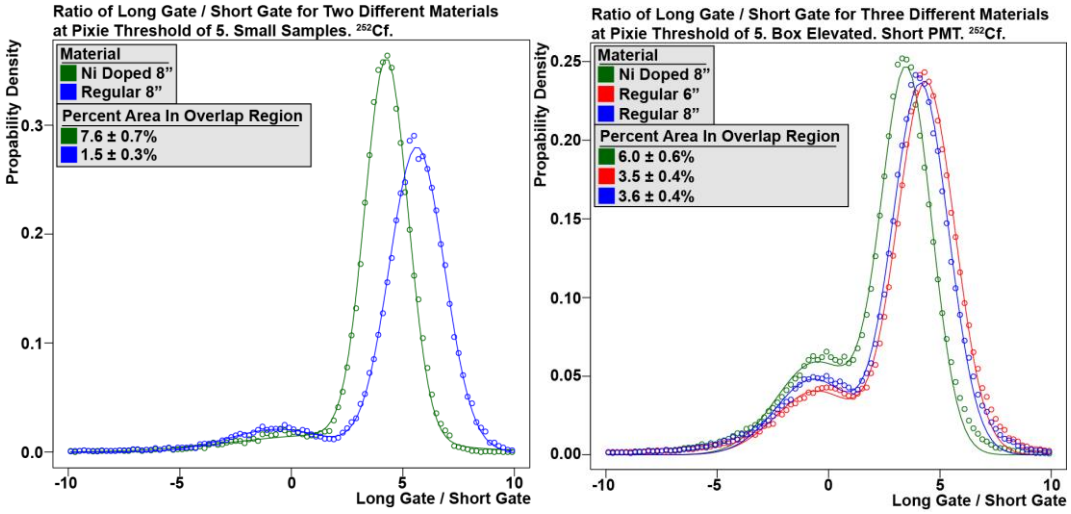

Figure 11.18 The two Gaussian fits for the background and source peaks for the three panels and the small samples.

The Ni-quenched stack constantly had greater overlap between the neutron region and the gamma-ray region of the probability density plots than either of the regular LiF/ZnS stacks. This study revealed that the Ni-quenched material is similar but slightly worse at discriminating between neutron and gamma-ray events than regular LiF/ZnS for an arbitrary set of long-gate-short-gate parameters.

A similar study was conducted over a wider long-gate-short-gate parameter space to compare the gamma-ray discrimination of both materials under more optimal conditions. The pulse peak of average gamma-ray pulses was determined to be at the 39^{th} time bin, or 518.7 ns. The short-gate centered on the 39^{th} time bin and was expanded out by one time bin, or 13.3 ns, both before and after the central bin until the short-gate was 21 bins, or 279.3 ns long, which is longer than a typical gamma-ray pulse. The long-gate was started in the time bin immediately following the last time bin of the short-gate. The long-gate was tested over a range of 10-100 bins, or 133-1330 ns.

The long-gate-short-gate data set was then plotted in a histogram of counts vs. long-gate over long-gate plus short-gate, as seen in Figure 11.19. Two Gaussian functions were fit to the two peaks from the gamma-ray and neutron region. The distance between the centroids of these Gaussians and their full-width-at-half-maximum were used to determine a gamma-ray discrimination figure-of-merit (γFoM), as seen in Equation 11.13 [17, 34].

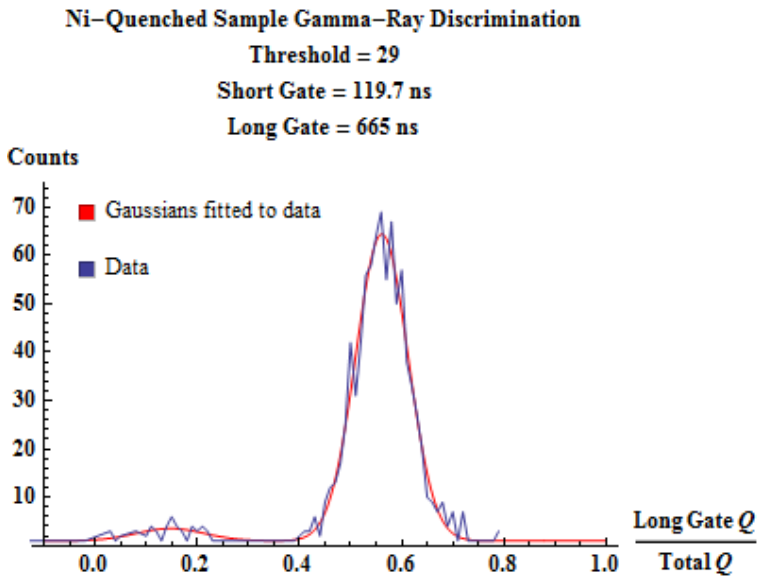

Figure 11.19 Long-gate-short-gate histogram with fit Gaussian functions.

Equation 11.13 $$\gamma FoM = \frac{S}{\delta_{neutron}+\delta_{gamma-ray}}$$

Where *S* is the separation distance between the centroids of the two Gaussians, and $\delta_{neutron}$ and $\delta_{gamma-ray}$ are the full-width-at-half-maximum of the neutron and gamma-ray Gaussians. This process was followed for the complete data set from one PMT of the Ni-quenched and regular threshold = 5 runs, which were chosen since they were expected to have the highest ratios of gamma-ray to neutron pulses. This gamma-ray *FoM* can be seen in Figure 11.20 and Figure 11.21, where the gamma-ray *FoM* is plotted over long-gate and short-gate parameters.

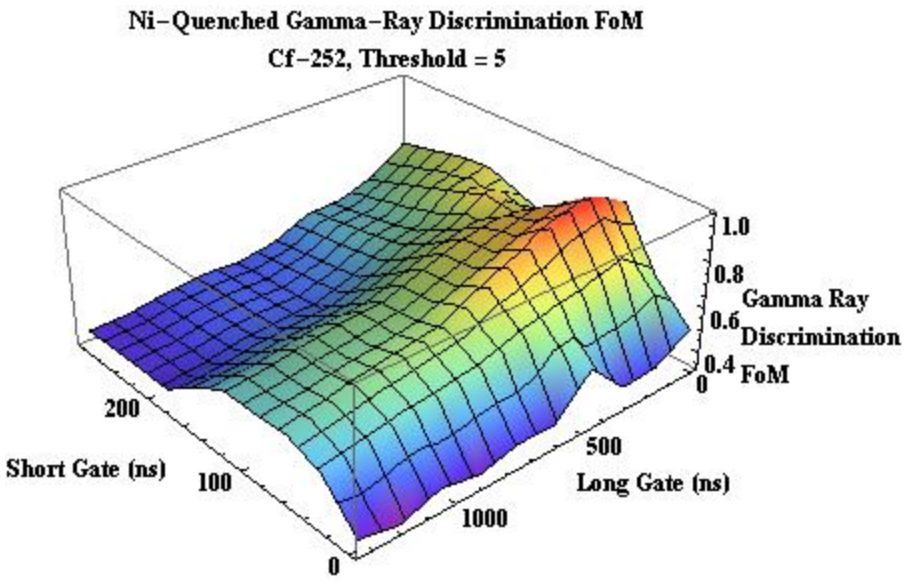

Figure 11.20 Ni-quenched gamma-ray *FoM* contour plots over long-gate and short-gate space.

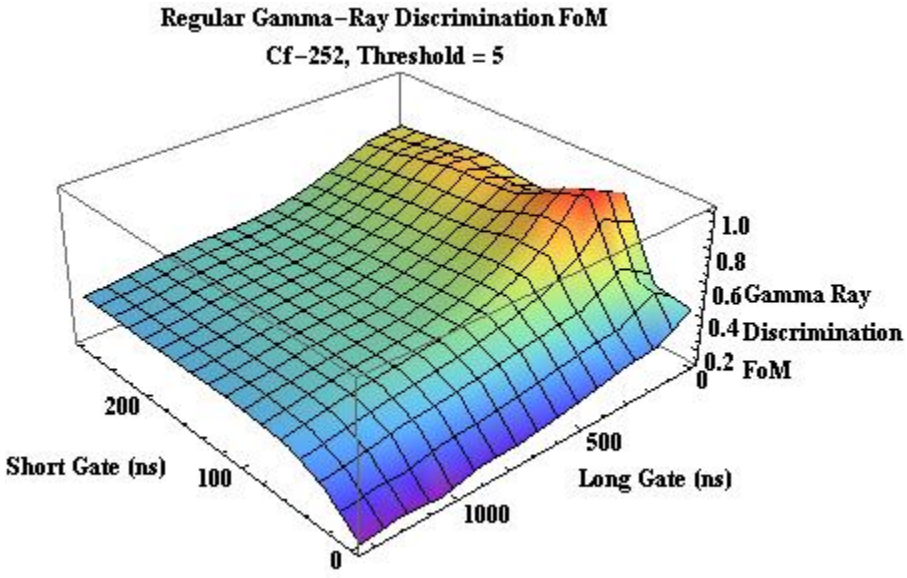

Figure 11.21 Regular gamma-ray *FoM* contour plots over long-gate and short-gate space.

The mean and maximum gamma-ray *FoM* from both materials can be seen in Table 11.13.

Table 11.13 Ni-quenched and regular gamma-ray *FoM* under optimal and average parameters.

Material	Maximum FoM	Mean FoM
Ni-quenched	1.00	0.60
Regular	1.02	0.53

This analysis shows that there is no significant difference between the optimal gamma-ray *FoM* of the Ni-quenched and regular materials, therefore any change in gamma-ray sensitivity between the materials is anticipated to correspond to an identical change in gamma-ray detection, assuming optimal long-gate-short-gate parameters.

11.7 Pulse Pileup

Sean Robinson led research on the effects of pules pileup between the Ni-quenched and regular LiF/ZnS were studied using to determine which materials could operate at high event rates. Initially a catalog of manually selected gamma-ray-like and neutron-like waveforms was compiled, which was later replaced by a catalog of PSD selected gamma-ray-like and neutron-like waveforms. Data sets from the Ni-quenched and regular stacks were collected with a dead-time free data acquisition system. Examples of gamma-ray-like and neutron-like waveforms can be seen in Figure 11.22.

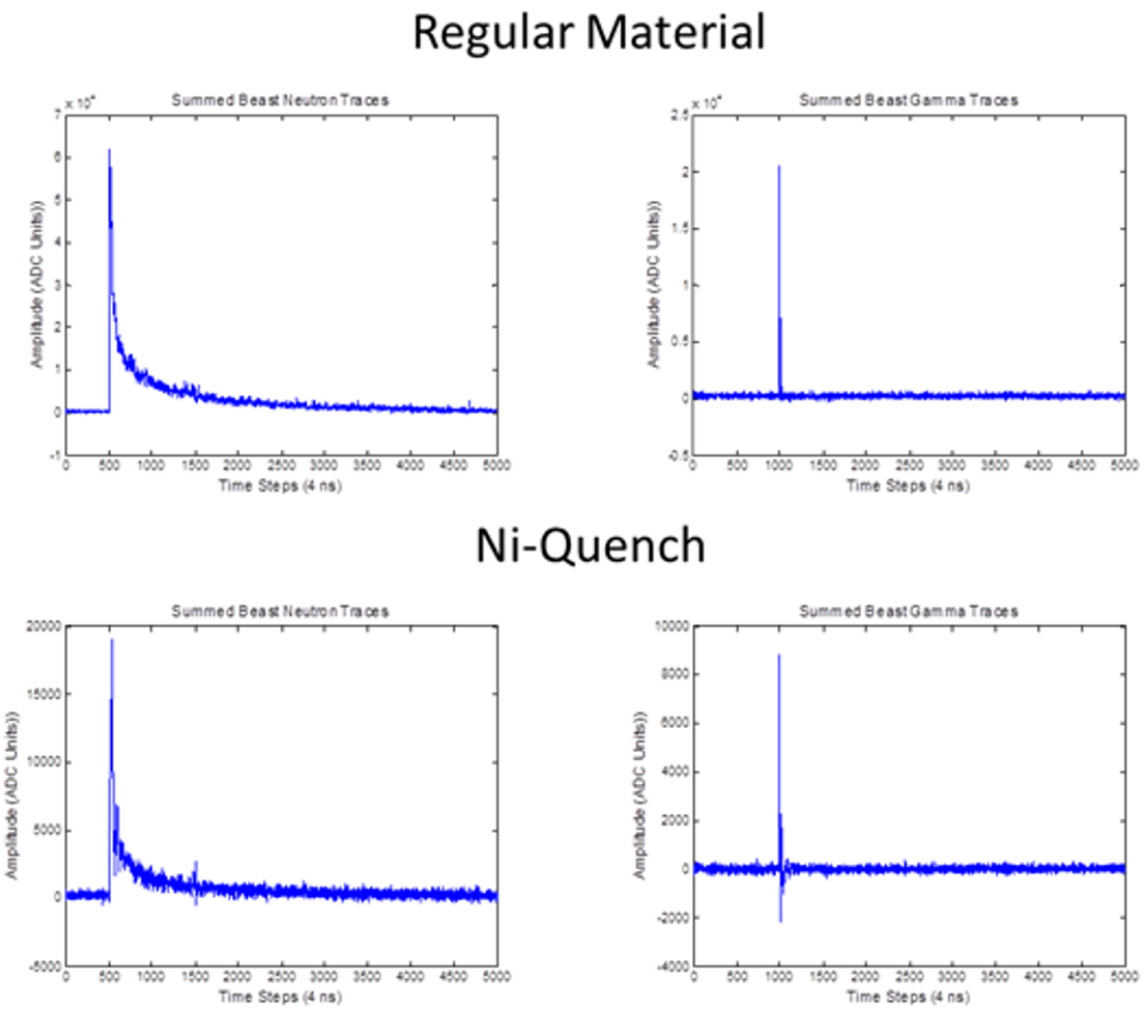

Figure 11.22 Averaged neutron and gamma-ray pulses from Ni-quenched and regular LiF/ZnS detector stacks.

These catalogs were then used to produce synthetically piled-up data set, which was in turn evaluated using a tuned coincidence-based neutron discrimination technique, and the results were compared with one another, as seen in Figure 11.23.

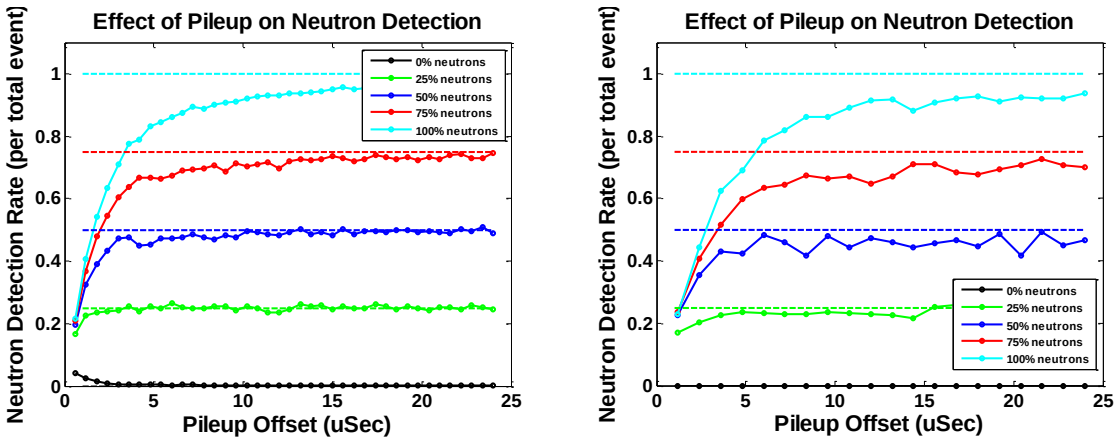

Figure 11.23 (Left) Neutron detection rate for randomly distributed Ni-quenched LiF/ZnS neutron signals. (Right) Neutron detection rate for randomly distributed regular LiF/ZnS neutron signals.

The somewhat faster (around a factor of 2) neutron envelope on the Ni-quenched case allows for a similar increase in allowed pileup before significant neutron undercounting occurred.

11.8 Material Selection Conclusion

Based on analysis results of small and full-scale samples of Ni-quenched and regular LiF/ZnS, as summarized in Table 11.14, the Ni-quenched LiF/ZnS displays superior approximately 13% (or greater) improved neutron count rate, 43-100% improved pulse pileup resistance, while displaying 22% increased gamma-ray sensitivity. In a full-scale system this increased gamma-ray sensitivity could easily be countered with the application of a lead lining. Based on this data and these conclusions, the Ni-quenched material will likely hold greater promise for building a full-scale detector system capable of meeting or exceeding ENMC performance than the regular material.

Measurement results are briefly summarized in Table 11.14.

Table 11.14 Summary of Measurement Results across multiple Metrics.

Metrics	Bare Samples	Full-scale	Notes
Light Emission	Neutron: 9.0% ± 1.3decrease Gamma-Ray: 15% ± 10 increase		Over all Wavelengths 7-14% decrease
Pulse Height	Neutron: 22% ± 1 increase Gamma-Ray: 35% ± 11 increase		
Pulse Shape Neutron Decay Constants (ps^{-1})	NiQ: 8.65, 0.776 Reg: 7.73, 0.659		
Total Count Rate (Hz)	Neutron: 1.8% ± 4.2 decrease Gamma-Ray: 26% ± 2 increase	Neutron: 4% ± 2 increase	
Gamma-Ray Rate	Increase 39% ± 7	Increase 22% ± 2	Ignoring low threshold results
Pulse Pileup Resistance	49% increase	30.1-100% increase	

Table continued on next page

Metrics	Bare Samples	Full-scale	Notes
Gamma-Ray Discrimination		NiQ Gamma-Ray FoM = 1.00 Reg Gamma-Ray FoM = 1.02	

12 Appendix 3: MCNP Model of LiNMC

The following MCNP input was used to model the LiNMC in MCNP. This input contains all of the options required for changing the number of detector stacks and tally options, although changing options will require commenting certain lines in or out. This input in set up for four detector stacks and a neutron capture efficiency tally.

```
c LiF/ZnS-based Neutron Multiplicity Counter - As-Built, Model 2016          *
c ========================================================== #
c Built by:   Edward Siciliano
c             Pacific Northwest National Laboratory, USA
c             <Edward.Siciliano@pnnl.gov>, 509-375-2049
c
c For: The "Alternative Multiplicity Counter" project, continuation of the
c      Neutron Detection Without Helium-3 Tubes" Project sponsored by the
c      US Department of Energy (DOE), National Nuclear Security Administration
c      (NNSA), Office of Nonproliferation Research and Verification.
c ========================================================== #
c Rev.Date:   7/25/2016
c NOTES:
c     The LiNMC16 model is organized into three Cell and Surface parts:
c   The first part controls the construction of the Detection Panels & Corner
c   Moderators.  The second part controls the details of the source. The
c   third part adds the cells and surfaces used to complete the model. Because
c   those components will not be varied for the current studies, they are listed
```

```
c   as separate "READ" files.
c ========================================================== #
c   ############################
c   #  Cell definition cards  #
c   ############################
c ===== Cells for MASTER Panel & MASTER Corner Moderator ============== #
c Tape Wrappings
  21  108  -1.55     (-218: 241:-212: 213)    imp:n=1 u=1 $ DT
  22  106  -2.25     ( 218 -241  212 -213)    &          $ RFT
                 (-219: 240:-215: 216)    imp:n=1 u=1 $
c Inter-Layer-Poly
  23  120  -1.032    ( 219 -220  215 -216)    imp:n=1 u=1 $ WSP
c Layer #1
  24  102  -1.38     ( 220 -221  215 -216)    imp:n=1 u=1 $ Backing
  25  212  -2.14920  ( 221 -222  215 -216)    imp:n=1 u=1 $ Scint
  26  102  -1.38     ( 222 -223  215 -216)    imp:n=1 u=1 $ Backing
c Inter-Layer-Poly
  27  120  -1.032    ( 223 -224  215 -216)    imp:n=1 u=1 $ WSP
c Layer #2
  28  102  -1.38     ( 224 -225  215 -216)    imp:n=1 u=1 $ Backing
  29  212  -2.14920  ( 225 -226  215 -216)    imp:n=1 u=1 $ Scint
  30  102  -1.38     ( 226 -227  215 -216)    imp:n=1 u=1 $ Backing
c Inter-Layer-Poly
  31  120  -1.032    ( 227 -228  215 -216)    imp:n=1 u=1 $ WSP
```

```
c Layer #3
  32  102  -1.38     ( 228 -229  215 -216)    imp:n=1 u=1 $ Backing
  33  212  -2.14920  ( 229 -230  215 -216)    imp:n=1 u=1 $ Scint
  34  102  -1.38     ( 230 -231  215 -216)    imp:n=1 u=1 $ Backing
c Inter-Layer-Poly
  35  120  -1.032    ( 231 -232  215 -216)    imp:n=1 u=1 $ WSP
c Layer #4
  36  102  -1.38     ( 232 -233  215 -216)    imp:n=1 u=1 $ Backing
  37  212  -2.14920  ( 233 -234  215 -216)    imp:n=1 u=1 $ Scint
  38  102  -1.38     ( 234 -235  215 -216)    imp:n=1 u=1 $ Backing
c Inter-Layer-Poly
  39  120  -1.032    ( 235 -236  215 -216)    imp:n=1 u=1 $ WSP
c Layer #5
  40  102  -1.38     ( 236 -237  215 -216)    imp:n=1 u=1 $ Backing
  41  212  -2.14920  ( 237 -238  215 -216)    imp:n=1 u=1 $ Scint
  42  102  -1.38     ( 238 -239  215 -216)    imp:n=1 u=1 $ Backing
c Inter-Layer-Poly
  43  120  -1.032    ( 239 -240  215 -216)    imp:n=1 u=1 $ WSP
c
c   51  0  ( 119 -144  113 -114  109 -110)      imp:n=1 fill=1 u=2 $ Master
  51  0  ( 217 -242  211 -214  281 -282)      imp:n=1 fill=1 u=2 $ Master
c
c *** Clones of Master Stack
c    52 like 51 but trcl=1
```

```
c    53 like 51 but trcl=2
c    54 like 51 but trcl=3
c
c  Add Front Stack Moderator (FSM) Layer
  70  101 -0.96     ( 210 -217  211 -214  281 -282)     imp:n=1 u=2 $ FSM
c
c  Add Master Interstack Moderator(ISM) & Behind Stack Reflector(BSR) Layers
  71  101 -0.96     ( 242 -283  211 -214  281 -282)     imp:n=1 u=2 $ 1st Master ISM
c   72  101 -0.96     ( 52242 -53215  211 -214  281 -282) imp:n=1 u=2 $ 2nd Master ISM
c   73  101 -0.96     ( 53242 -54215  211 -214  281 -282) imp:n=1 u=2 $ 3nd Master ISM
c
c   75  101 -0.96     ( 54242 -251  211 -214  281 -282)   imp:n=1 u=2 $ Master BSR
c   75  101 -0.96     ( 53242 -251  211 -214  281 -282)   imp:n=1 u=2 $ Master BSR
c
c  Add Master Front Stack Moderator (FSM)
c   76  101 -0.96     (  99 -217  211 -214  281 -282)     imp:n=1 u=2 $
c   77  900 -1.205e-3 (  82  -99  211 -214  281 -282)     imp:n=1 u=2 $ Air Fill
c
c   PMTs
c     1st Stack
  81    0          ( -96   282 -100)          imp:n=1 u=2 $ Top PMT
  82    0          ( -96  -281   99)          imp:n=1 u=2 $ Bottom PMT
c     2nd Stack
c   83    0          ( -96   282 -100)          imp:n=1 u=2 $ Top PMT
```

```
c   84    0         ( -96  -281   99)          imp:n=1 u=2 $ Bottom PMT
c     3rd Stack
c   85    0         ( -96   282 -100)          imp:n=1 u=2 $ Top PMT
c   86    0         ( -96  -281   99)          imp:n=1 u=2 $ Bottom PMT
c     4th Stack
c   87    0         ( -96   282 -100)          imp:n=1 u=2 $ Top PMT
c   88    0         ( -96  -281   99)          imp:n=1 u=2 $ Bottom PMT
c
c  Cadmium Liner wrapped with double-thick layer of Duct Tape(DT)
 116  108 -1.55     ( 82 -83  89 -90  281 -282)  imp:n=1 u=2 $ DT
 117   48 -8.65     ( 83 -84  89 -90  281 -282)  imp:n=1 u=2 $ Cd Liner
 118  108 -1.55     ( 84 -85  89 -90  281 -282)  imp:n=1 u=2 $ DT
c
c *** Fill Master Panel
 119  900 -1.205e-3 ( 82 -86  89 -90  93 -94)    &          $ Air Fill
                #70 #81 #82 #116 #117 #118 &          $ Omit DT/Cd/DT & FSM
c             (-217: 251:-211: 214:-281: 282)    imp:n=1 u=2 $
c                ( 251:-211: 214:-281: 282)    imp:n=1 u=2 $
          (-217: 283:-211: 214:-281: 282)    imp:n=1 u=2 $ For Quarter System Test
c
 120   13 -2.70     (-82: 86:-89: 90:-93: 94)    imp:n=1 u=2 $ Al Case
c
 121    0          ( 81 -87  88 -91  92 -95)    imp:n=1 fill=2 $ Master Panel
c
```

```
c ===== Cells for MASTER Corner Component ========================== #
c
c  221 101  -0.96     ( 82 -291  292  281 -282)      imp:n=1 $ Corner Wedge(HDPE)
 221  100 -1.143    ( 82 -294  292 -291  281 -282) &       $ Corner L-Shape
                :( 294 -295  292 -296  281 -282) imp:n=1 $ w/dens for Li-HPDE
 231   13 -2.70     ( 82 -295  292 -291  280 -281) imp:n=1 $ Al Support Plate
c
c ===== Clones of MASTER Panel & Corner Component =================== #
c *** Panels
 122 like 121 but trcl=11
 123 like 121 but trcl=12
 124 like 121 but trcl=13
c
c *** Corners
 222 like 221 but trcl=11
 232 like 231 but trcl=11
 223 like 221 but trcl=12
 233 like 231 but trcl=12
 224 like 221 but trcl=13
 234 like 231 but trcl=13
c
c ===== Cells Source ============================================== #
c  Source Holder - IPL Capsule
 805   202 -8.00     (-805 806)                imp:n=1 $ Steel capsule
```

```
c  Small Finite Sphere for Source Material
 806   900 -1.205e-3 (-806)                imp:n=1 $ Air-Filled for CvT
c  806   901 -1.205e-3 (-806)                imp:n=1 $ Air+Cf252 for DvG
c
c  Three-Layer Source Platform
 701   13 -2.70     ( 325 -701 -706)          imp:n=1 $ 1st Plate
 702   13 -2.70     ( 702 -703 -706  707  708)   imp:n=1 $ 1st Plate
 703   13 -2.70     ( 704 -705 -706)          imp:n=1 $ 1st Plate
 704   13 -2.70     ( 701 -704 -707)          imp:n=1 $ +X Post
 705   13 -2.70     ( 701 -704 -708)          imp:n=1 $ -X Post
c
c ===== Cells All Other Components ================================== #
c     (Include: External Frame, Casters, Corner Moderator Supports,
c      Interior Chamber Supports, and Top and Bottom Plugs with wrapped Cd.)
c === Cells for Exterior Frame & Supports ============================== #
c
c   Bosch Base (BB)Frame, Casters, Al Base (AB)Plate, & Corner Support (CS)Posts
c     BBFrame
 301   13 -2.70     ((-303.2 -303.1 -300.4  303.4 -300.6  303.6)  & $ -Y,-Z
                ( 303.2: 303.1: 301.4:-302.4: 301.6:-302.6)) imp:n=1 $
 302   13 -2.70     ((-303.2 -303.1 -300.3  303.3 -300.6  303.6)  & $ +Y,-Z
                ( 303.2: 303.1: 301.3:-302.3: 301.6:-302.6)) imp:n=1 $
 303   13 -2.70     ((-300.2  303.2 -300.4 -300.3 -300.6  303.6)  & $ -X,-Z
                ( 301.2:-302.2: 300.4: 300.3: 301.6:-302.6)) imp:n=1 $
```

```
304   13 -2.70     (( 303.1 -300.1 -300.4 -300.3 -300.6  303.6)  & $ +X,-Z
                   (-302.1: 301.1: 300.4: 300.3: 301.6:-302.6)) imp:n=1 $
305   13 -2.70     ((-303.2 -303.1 -300.4  303.4 -300.5  303.5)  & $ -Y,+Z
                   ( 303.2: 303.1: 301.4:-302.4: 301.5:-302.5)) imp:n=1 $
306   13 -2.70     ((-303.2 -303.1 -300.3  303.3 -300.5  303.5)  & $ +Y,+Z
                   ( 303.2: 303.1: 301.3:-302.3: 301.5:-302.5)) imp:n=1 $
307   13 -2.70     ((-300.2  303.2 -300.4 -300.3 -300.5  303.5)  & $ -X,+Z
                   ( 301.2:-302.2: 300.4: 300.3: 301.5:-302.5)) imp:n=1 $
308   13 -2.70     (( 303.1 -300.1 -300.4 -300.3 -300.5  303.5)  & $ +X,+Z
                   (-302.1: 301.1: 300.4: 300.3: 301.5:-302.5)) imp:n=1 $
309   13 -2.70     ((-300.2  303.2 -300.4  303.4 -303.6 -303.5)  & $ -X,-Y
                   ( 301.2:-302.2: 301.4:-302.4: 303.6: 303.5)) imp:n=1 $
310   13 -2.70     ((-300.1  303.1 -300.4  303.4 -303.6 -303.5)  & $ +X,-Y
                   ( 301.1:-302.1: 301.4:-302.4: 303.6: 303.5)) imp:n=1 $
311   13 -2.70     ((-300.2  303.2 -300.3  303.3 -303.6 -303.5)  & $ -X,+Y
                   ( 301.2:-302.2: 301.3:-302.3: 303.6: 303.5)) imp:n=1 $
312   13 -2.70     ((-300.1  303.1 -300.3  303.3 -303.6 -303.5)  & $ +X,+Y
                   ( 301.1:-302.1: 301.3:-302.3: 303.6: 303.5)) imp:n=1 $
c    Casters
313   13 -2.70      (-305)                  imp:n=1 $ -X,-Y
314   13 -2.70      (-306)                  imp:n=1 $ -X,-Y
315   13 -2.70      (-307)                  imp:n=1 $ -X,-Y
316   13 -2.70      (-308)                  imp:n=1 $ -X,-Y
c
```

```
c      ABPlate
 317   13 -2.70      (-300.2 -300.1 -300.4 -300.3 -303.6 -304) &       $
                                  #309 #310 #311 #312 imp:n=1 $
c
c     CSPosts
 318   13 -2.70      (-311  304 -318):(-310  318 -280) imp:n=1 $+X,+Y
 319   13 -2.70      (-313  304 -318):(-312  318 -280) imp:n=1 $+X,-Y
 320   13 -2.70      (-315  304 -318):(-314  318 -280) imp:n=1 $-X,-Y
 321   13 -2.70      (-317  304 -318):(-316  318 -280) imp:n=1 $-X,+Y
c
c === Cells for Interior Chamber Support & Plugs ========================== #
c   Bosch Interior (BI)Frame
 329   13 -2.70     (-320.2  321.2 -320.4  323.4 -323.6 -323.5):  & $ -X,-Y
                   (-321.2  323.2 -320.4  321.4 -323.6 -323.5) imp:n=1 $
 330   13 -2.70     ( 321.1 -320.1 -320.4  323.4 -323.6 -323.5):  & $ +X,-Y
                   ( 323.1 -321.1 -320.4  321.4 -323.6 -323.5) imp:n=1 $
 331   13 -2.70     (-320.2  321.2 -320.3  323.3 -323.6 -323.5):  & $ -X,+Y
                   (-321.2  323.2  321.3 -320.3 -323.6 -323.5) imp:n=1 $
 332   13 -2.70     ( 321.1 -320.1 -320.3  323.3 -323.6 -323.5):  & $ +X,+Y
                   ( 323.1 -321.1  321.3 -320.3 -323.6 -323.5) imp:n=1 $
c
c   Chamber Support (CS)Plate
 333   13 -2.70     (-320.2 -320.1 -320.4 -320.3  324 -325)       imp:n=1 $
c
```

```
c   Bottom Plug and Chamber-Side Cd Lining
 334    6 -1.68     (-321.2 -321.1 -321.4 -321.3  326 -327)       imp:n=1 $ Plug
c
c   Cadmium Liner wrapped with double-thick layer of Duct Tape(DT)
 335  108 -1.55     (-321.2 -321.1 -321.4 -321.3  327 -328)       imp:n=1 $ DT
 336   48 -8.65     (-321.2 -321.1 -321.4 -321.3  328 -329)       imp:n=1 $ Cd Liner
 337  108 -1.55     (-321.2 -321.1 -321.4 -321.3  329 -324)       imp:n=1 $ DT
c
c  325   pz 118.8900   $ Zmin of TPSPlate, defines top of 43.18cm[17.0in] Chamber
c  326   pz 119.2075   $ Zmax of TPSPlate, 0.3275cm [1/8th inch] thick
c   Cylindrical Posts for Top Plug Support (TS)Plate
 340   13 -2.70     (-331  325 -335)                    imp:n=1 $ -X,-Y
 341   13 -2.70     (-332  325 -335)                    imp:n=1 $ +X,-Y
 342   13 -2.70     (-333  325 -335)                    imp:n=1 $ -X,+Y
 343   13 -2.70     (-334  325 -335)                    imp:n=1 $ +X,+Y
c
 344   13 -2.70     (-320.2 -320.1 -320.4 -320.3  335 -336)       imp:n=1 $ TPSPlate
c
c   Top Chamber-Side Cd Lining & Top Plug
c   Cadmium Liner wrapped with double-thick layer of Duct Tape(DT)
 345  108 -1.55     (-321.2 -321.1 -321.4 -321.3  336 -337)       imp:n=1 $ DT
 346   48 -8.65     (-321.2 -321.1 -321.4 -321.3  337 -338)       imp:n=1 $ Cd Liner
 347  108 -1.55     (-321.2 -321.1 -321.4 -321.3  338 -339)       imp:n=1 $ DT
 348    6 -1.68     (-321.2 -321.1 -321.4 -321.3  339 -340)       imp:n=1 $ Plug
```

```
c ===== Approximate Laboratory Room in Bldg. 3420 ====================== #
 899  200 -2.30     ( -999  998)                imp:n=1 $ Concrete Fill
c ===== Cells Completing Model World (MW) ============================== #
c Air-Fill Inside of MW, omitting Master & Cloned NDM's, and Source Cell(s)
 900  900 -1.205e-3 -998 #121 #122 #123 #124     &       $ omit Al Panels
        #221 #222 #223 #224 #231 #232 #233 #234 &       $ omit Corner Moderators
        #301 #302 #303 #304 #305 #306 #307 #308 &       $ omit Exterior Frame
    #309 #310 #311 #312 #313 #314 #315 #316 #317 &       $
                        #318 #319 #320 #321 &       $ omit CSPosts
                    #329 #330 #331 #332 #333 &       $ omit Chamber Support & Plate
    ( 321.2: 321.1: 321.4: 321.3:-327: 324) #334 &       $ omit CSPlate,Layers,&Plug
                    #340 #341 #342 #343 #344 &       $ omit TPSPlate Support Posts
    ( 321.2: 321.1: 321.4: 321.3:-336: 339) #348.&       $ omit TPSPlate,Layers,&Plug
                #701 #702 #703 #704 #705 805 &       $ omit Src. Support & Src
                                    imp:n=1 $ World Fill
 901    0      999                          imp:n=0 $ Outer World Void
c
c ### BLANK CARD FOLLOWS #########


c   ###############################
c   #  Surface definition cards  #
c   ###############################
c ========================================================== #
c NOTES on LiNMC16 As-Built Components:
```

```
c

c Exterior Frame & Supporting Components (from floor level up)

c   Bosch Base (BB)Frame, 4.5cm x 4.5cm with 0.8cm thick Al,

c     with o.d.s of 81.28cm x 81.28cm x 161.98cm [32in x 32in x 63.77in].

c   Aluminum Base (AB)Plate, 0.635cm thick, above BBFrame, Zmax= 21cm above
floor.

c   Approximate Version of Casters( for visual completeness)

c

c Sample Chamber:

c     43.18cm [17.0in] high with area defined by

c     2-cm thick Fe Ring with 16.0cm [6.299in] interior diameter. (Same as ENMC).

c ***NOTES STOPPED HERE

c End Plugs & Liners

c  Graphite, 15.24cm [6.0in] high squares with 0.3175cm [0.125in] Al end plates lined
with 25-mil Cd

c ========================================================== #

c === Surfaces for Sample Chamber, End Plugs, PolyShield, & Liners ==== #

c     (Unless otherwise noted, the dimensions are from the ENMC model).

c (Surf#'s 1-27 used. Surf#'s 28-100 reserved for alterations of these parts.)

c

c  Sample Chamber & Liners

c    1   cz     8.0              $ Sample Chamber o.d.

c    2   cz    10.0               $ 2-cm Iron "Scatterer" o.d

c === Surfaces for LiF/ZnS components ================================= #

c  Surfaces for MASTER Stack & Corner Wedge
```

```
c *** Front Stack Moderator ***
 210 5 px  0.0              $ 0.3175cm (1/8th in) from Front Stack DT (surf#217)
c
c --- LiFZnS STACK ---
c   Wrapping Tapes (Products are 3M-ESR for the RFT and Nashua 2280 for the DT.
c   (Thickness from Mfg's specs: 65microns for RFT and 2 x 228 microns for DT.)
 211 5 py -10.2121          $ Ymin for DT
 212 5 py -10.1665          $ Ymin for RFT
 213 5 py  10.1665          $ Ymax for RFT
 214 5 py  10.2121          $ Ymax for DT
c
 215 5 py -10.160           $ Ymin for Master Stack (using 8-inch width)
 216 5 py  10.160           $ Ymax  "     "
c
c *** NOTE ALL X-Values w.r.t. inside Front of 0.3175cm-thick Al Panel
 217 5 px   0.3175          $ Xmin for Front DT (w/ 0.350 OUTER WSP)
 218 5 px   0.3631          $ Xmin for Front RFT (w/ 0.350 OUTER WSP)
c
c  219   px   0.1960         $ Xmin for FRONT 0.7 WSP (formally surf#111)
 219 5 px   0.3696          $ Xmin for FRONT 0.350 WSP
 220 5 px   0.7196          $ Xmin Backing of 1st Scint (formally surf#112)
 221 5 px   0.7446          $ Xmax Backing of Scint in Layer #1
 222 5 px   0.7946          $  Scint to 250 micron Backing
 223 5 px   0.8196          $  Backing of Scint
```

```
224 5 px   1.5196        $  to WSP
225 5 px   1.5446        $ Xmax Backing of Scint in Layer #2
226 5 px   1.5946        $  Scint to 250 micron Backing
227 5 px   1.6196        $  Backing of Scint
228 5 px   2.3196        $  to WLP
229 5 px   2.3446        $ Xmax Backing of Scint in Layer #3
230 5 px   2.3946        $  Scint to 250 micron Backing
231 5 px   2.4196        $  Backing of Scint
232 5 px   3.1196        $  to WSP
233 5 px   3.1446        $ Xmax Backing of Scint in Layer #4
234 5 px   3.1946        $  Scint to 250 micron Backing
235 5 px   3.2196        $  Backing of Scint
236 5 px   3.9196        $  to WSP
237 5 px   3.9446        $ Xmax Backing of Scint in Layer #5
238 5 px   3.9946        $  Scint to 250 micron Backing
239 5 px   4.0196        $  Backing of Scint
240 5 px   4.3696        $  to WSP
c
241 5 px   4.3761        $  Xmax to Back Layer of RFT (w/ 0.350 OUTER WSP)
242 5 px   4.4217        $  Xmax to Back Layer of DT (w/ 0.350 OUTER WSP)
c
c *** Calculate Xmax for Behind Stack Reflector (BSR)
c     Set = Stack Width*No.Stacks + Gap*No.Gaps + Xmin + Thickness of BSR
c     For 5-6, = (surf#242 -surf#215)*4 + 0.3175*3 + surf#215 + 1.0cm = 28.9672cm
```

```
c  251 5 px  18.6868          $ Xmax for BSR using 4 stacks.
 251 5 px  14.5826          $ Xmax for BSR using 3 stacks.
c  251 5 px  10.4784          $ Xmax for BSR using 2 stacks.
c  251 5 px   6.3742          $ Xmax for BSR using 1 stack.
c
c  *** Surfs for Active Height of Stack and used for Corner Moderator
c      (Values take as symmetric about Z=0, with TR=4 to move into Frame.)
 280 4 pz -35.8775          $ Zmin for Corner Moderator Support (CM)Plate
 281 4 pz -35.560           $ Bottom Active Height
 282 4 pz  35.560           $ Top Active Height
c
 283 5 px   4.7392          $ Xmax of 0.3175cm Stack Gap for 5-6, w/ 0.7cm WSP
c
c --- END of Surfaces for Master Stack.---
c
c --- Surfaces for Master Corner Moderator ---
c
c *** Cell# 221 is Corner Moderator MASTER CELL
c     It is listed here for reference to the surfaces it uses.
c     221  1  -0.96   (212 -291  292  281 -282)  imp:n=1 $ Corner
c
c *** Special surfs for Wedge Shape ***
c     Notes on General Plane Defined by Three Points (Four Parameters, A, B, C, D)
c        A*X + B*Y + C*Z = D.
```

```
c       For plane parallel to Z axis, C=0 (and intersecting Z axis, D = 0).
c       Using slope-intercept form, Y = m*X + b, gives A = -m*B and b = D/B,
c       where m = slope and b = X intercept of Y=0 point.
c       Positive sense of this plane is side where X=0, Y = infinity.
c  291   p    1.0  1.0   0.0  40.7975 $ 42.6752 $ 38.92+ 2x1.8775 $  Plane for Wedge
c                        $ (also CW3,CW2=42.75,40.00)
 291   py  31.47             $  Ymax Plane for L-Shaped
 292   py  11.15 $ 10.85      $  Ymin for L-Shaped or Wedge
c  293   px  10.65             $  Xmin for Wedge
c                        $  (needed bec. Wedge is not univ.)
 294 4 px   5.3975           $  2" from surf#82
 295 4 px  20.6375           $  6" from surf#294
 296   py  16.23             $  2" from surf#292
c
c  Surfaces for Al Panel enclosing Stacks (assume 0.3175cm thick)
  81 4 px     0.0000 $                $ Xmin for Left side (FIXED)
  82 4 px     0.3175 $                $ Xmax                "
c
c  Cadmium Liner wrapped with double-thick layer of Nashua 2280 Duct Tape(DT).
c (Thickness from Mfg's specs 2 x 228 microns for DT.)
  83 4 px     0.3631 $ 0.3175 + 0.0456    $ Xmax for DT on -X side of Cd
c  Cadmium Liner 35 mils = 0.0889cm.
  84 4 px     0.4520 $ 0.3631 + 0.0889                $ Xmax for Cd
  85 4 px     0.4976 $ 0.4520 + 0.0456    $ Xmax for DT on +X side of Cd
```

```
 86 4 px    23.1775 $ 9.00" (22.86cm) per 12/28/15 plan $ Xmin for Right
 87 4 px    23.4950 $ 9.00" + 0.3715cm              $ Xmax  "   "
 88 4 py   -10.7975 $ 0.5* 8.25" - 0.3715cm          $ Ymin for Top
 89 4 py   -10.480  $ 0.5* 8.25" (20.96cm)           $ Ymax  "   "
 90 4 py    10.480  $                               $ Ymin for Bottom
 91 4 py    10.7975 $                               $ Ymax  "   "
c
c Ref.Heights from Stack Surfs16
c  281 9 pz -35.560          $ Bottom Active Height
c  282 9 pz  35.560          $ Top Active Height
c
 92 4 pz   -76.2000          $ Zmin of 60in o.d. (per 2015.12.28 Worksheet)
 93 4 pz   -75.8825          $ Zmin for i.d. = o.d. - 0.3175cm
 94 4 pz    75.8825          $ Zmax for i.d.
 95 4 pz    76.2000          $ Zmax for o.d.
c
c   Surfaces for PMT's (using diam=7.76cm and height=15.142cm, per Dec.2015 plans)
 96 4 c/z  4.210 -5.26   3.89 $ X=Radius + surf#82 (thickness of Al Panel)
c   97 4 c/z  4.210 -5.26   3.89 $ X=Radius + surf#82 + position of 2nd Stack
c   98 4 c/z  4.210 -5.26   3.89 $ X=Radius + surf#82 + position of 3rd Stack
 99 4 pz -50.700             $ Bottom of Bottom PMT (15.142cm below surf#281)
100 4 pz  50.700             $ Top of Top PMT (15.142 cm above surf#282)
c === Surfaces for Source & Source Support ============================== #
c Three-Layer Source Platform
```

```
c   Each layer consists of 0.635cm[0.25in] Al.
c   Total Outer H=40.64cm[16.0in] and O.D = 14.22cm[5.6in]
 701   pz    76.3450          $ Zmax of Bottom Plate (0.635cm above surf#325)
 702   pz    95.7125          $ Zmin of 2nd Plate
 703   pz    96.3475          $ Zmax of 2nd Plate
 704   pz   115.7150          $ Zmin of 3rd Plate
 705   pz   116.3500          $ Zmax of 3rd Plate
 706  c/z   0.0  0.0   7.112   $ Outer Diameter of Plates
 707  c/z   6.5  0.0   0.25    $ +X Plate support cyl.
 708  c/z  -6.5  0.0   0.25    $ -X Plate support cyl.
c
c Source Capsule 3014 from IPL (omitting threads)
c   o.d. L=1.25in (3.175cm),D=0.370in (radius=0.47cm), solid w/ Cf sphere hole
 805 10 rcc  0.0  0.0  0.0    0.0  0.0  3.175   0.470  $ steel case o.d.
 806 10  sz  1.5875   0.1                        $ 0.2-cm diameter sphere
c
c ===== Surfaces for All Other Components ============================== #
c     (Include: External Frame, Casters, Corner Moderator Supports,
c      Interior Chamber Supports, and Top and Bottom Plugs with wrapped Cd.)
c
c *** Surfaces for All Other External & Internal Model Components
c === Surfaces for Exterior Frame & Supports ========================== #
c   Bosch Base (BB)Frame, Casters, Al Base (AB)Plate, and Al Corner (AC)Posts
c     BBFrame
```

```
 300  rpp -40.640  40.640   -40.640  40.640    15.865 177.845  $ Outer Surfs
 301  rpp -39.840  39.840   -39.840  39.840    16.665 177.045  $  " Thickness
 302  rpp -37.440  37.440   -37.440  37.440    19.565 174.145  $ Inside "
 303  rpp -36.640  36.640   -36.640  36.640    20.365 173.345  $ Inside Surfs
c
 304   pz  21.000            $ Top of ABPlate
c
c     Casters
 305   s  -32.71  -32.71   7.9325    7.932                $ -X,-Y
 306   s   32.71  -32.71   7.9325    7.932                $ +X,-Y
 307   s  -32.71   32.71   7.9325    7.932                $ -X,+Y
 308   s   32.71   32.71   7.9325    7.932                $ +X,+Y
c
 310  c/z  21.2950  21.3100   1.27                       $ +X,+Y
 311  c/z  21.2950  21.3100   2.27                       $ +X,+Y
 312  c/z  21.2950 -21.3100   1.27                       $ +X,-Y
 313  c/z  21.2950 -21.3100   2.27                       $ +X,-Y
 314  c/z -21.2950 -21.3100   1.27                       $ -X,-Y
 315  c/z -21.2950 -21.3100   2.27                       $ -X,-Y
 316  c/z -21.2950  21.3100   1.27                       $ -X,+Y
 317  c/z -21.2950  21.3100   2.27                       $ -X,+Y
c
 318   pz  23.000            $ Top Post Connector (2.0 cm above surf#304)
c === Surfaces for Interior Chamber Support & Plugs w/ Cd ================== #
```

```
c   Bosch Interior (BI)Frame, Chamber Support (CS)Plate
c     BIFrame
 320  rpp -10.100  10.100   -10.100  10.100    21.000  75.3925  $ Outer Surfs
 321  rpp  -9.500   9.500    -9.500   9.500    21.000  75.3925  $  " Thickness
 322  rpp  -6.600   6.600    -6.600   6.600    21.000  75.3925  $ Inside "
 323  rpp  -6.000   6.000    -6.000   6.000    21.000  75.3925  $ Inside Surfs
c
 324   pz  75.3925     $ Zmin of CSPlate, 0.3175cm [1/8th inch] thick
 325   pz  75.7100     $ Zmax of CSPlate, defines bottom of 43.18cm[17.0in] Chamber
c
c   Bottom Plug & Chamber-Side Cd Lining
 326   pz  59.9978     $ Zmin Bottom Plug, 15.24cm [6.0in] below surf#317
c    Cadmium Liner wrapped with double-thick layer of Nashua 2280 Duct Tape(DT).
c      Thickness from Mfg's specs 2 x 228 microns for DT.
c      Cadmium Liner 25 mils = 0.0635cm.
 327   pz  75.2378     $ 75.3925 -0.0456 -0.0635 -0.0456  $ Zmin for DT -Z side
 328   pz  75.2834     $ 75.3925 -0.0456 -0.0635          $ Zmin for Cd
 329   pz  75.3469     $ 75.3924 -0.0456                  $ Zmin for DT +Z side
c
c   Top Plug Support Posts & Top Support (TS)Plate
 331  c/z  -8.50  -8.50   0.50                        $ -X,-Y Post
 332  c/z   8.50  -8.50   0.50                        $  X,-Y Post
 333  c/z  -8.50   8.50   0.50                        $ -X, Y Post
 334  c/z   8.50   8.50   0.50                        $  X, Y Post
```

```
c
 335   pz 118.8900     $ Zmin of TSPlate, defines top of 43.18cm [17.0in] Chamber
 336   pz 119.2075     $ Zmax of TSPlate, 0.3175cm [1/8th inch] thick
c
c   Top Chamber-Side Cd Lining & Plug
c    Cadmium Liner wrapped with double-thick layer of Nashua 2280 Duct Tape(DT).
c      Thickness from Mfg's specs 2 x 228 microns for DT.
c      Cadmium Liner 25 mils = 0.0635cm.
 337   pz 119.2531     $ 119.2075 +0.0456              $ Zmax for DT -Z side
 338   pz 119.3166     $ 119.2075 +0.0456 +0.0635      $ Zmax for Cd
 339   pz 119.3622     $ 119.2075 +0.0456 +0.0635 +0.0456 $ Zmin for DT +Z side
c
 340   pz 134.6022     $ Zmax Top Plug, 15.24cm [6.0in] above surf#317
c === Surfaces for "Model=World" Boundary ============================== #
c ===== Lab Room (1304) in Bldg 3420
 998  rpp   -484.0  400.0   -422.2  422.2    0.0 271.3  $ Inside ~29'x ~29'x 10'
 999  rpp   -491.62 407.62  -429.82 429.82 -25.4 296.3  $ 10" Floor&Ceiling, 3" Walls
c ===== Boundary of MW ========================================== #
c Use o.d. of Lab Room, surf#999
c ### BLANK CARD FOLLOWS #########

c   ############################
c   ##  Data definition cards  #
c   ############################
```

```
c ===== Transformation Cards ====================================== #

c      x      y      z       xx'  yx'  zx'   xy'  yy'  zy'   xz'  yz'  zz'

c Transformation (TR) Card Notation

c   o1  o2  o3   xx'  yx'  zx'    xy'  yy'  zy'    xz'  yz'  zz'

c where o's are position of new origin, and others are rotation matrix elements

c

c TR1-TR3 position cloned (u=1) stacks within the master Panel.

c *tr1    4.4217 $ 4.3175 $ TR1 = Width_Stck1+Gap1 = Xmax_lastWSP-Xmin_1stWSP
+Gap

c c             $ For 7mm/3.5mm Inside/Outside WSP => 4.0 + 0.3175(gap)

c c             $ Adding Tape Wrappings gives width of wrapped stack = 4.1042 cm

c *tr2    8.8434 $ TR2 = 2*TR1

c *tr3   13.2651 $ TR3 = 3*TR1

*tr1   4.4217 $ 4.3175 $ TR1 = Width_Stck1+Gap1 = Xmax_lastWSP-Xmin_1stWSP
+Gap

*tr2   8.8434 $ TR2 = 2*TR1

*tr3  13.2651 $ TR3 = 3*TR1

c

c TR4 positions the Al Case for Panel enclosing Stacks

*tr4  10.8175  0.0  97.3   $ 10.8175 = 10.4800 (surf#86 for Al o.d.)+0.3375cm Gap

c                       $ Z-value = Same as TR9

c TR5 positions Master Stack inside Al Panel, X-value = TR4 + 0.3175 Gap for FSM

*tr5  12.2676 0.0   0.0 $  Plus "PMT" Gap = 0.9525 [3/8 in] + DT/Cd/DT (0.4976)

c

*tr9   0.0    0.0  97.3    $ Shift in Height for Components in Al Panels.
```

```
c                    $ Value = Zmax ABPlate (21cm) + Zmin Al Panel +1mm gap.
c
*tr10 00.00  00.00 96.3475 $ Source Holder & Sdef
c                    $ 96.3475=midpt(97.3)-1.5875(0.5*surf#801)+0.25inPlate.
c
c TR11-13 position the cloned (u=2) panels around the chamber.
*tr11   0   0   0    90 180  90     0   90  90    90  90  0
*tr12   0   0   0   180  90  90    90  180  90    90  90  0
*tr13   0   0   0    90   0  90   180   90  90    90  90  0
c ===== Material Cards ============================================== #
m6      6000   1.0         $ Graphite,
c                    $ rho = 2.09-2.23 g/cc(Wiki). ENMC uses 1.8, PNNL=1.68
m13    13027   1.0         $ Aluminum, rho = 2.70 g/cc
m26    26000   1.0         $ Iron, rho = 7.874 g/cc, ENMC used 7.86 g/cc
m48    48000   1.0         $ Cadmium, rho = 8.65 g/cc
m100    1001  -0.13294     $ H 7.5% wt. Li Polyethylene,
c                    $ rho = 1.06 g/cc(Shieldwerx), 1.143 g/cc PNNL eval.
       3006  -0.00481     $ Li6 (Natural Composition (7.4% Li6, 95.6% Li7).
       3007  -0.07019     $ Li7
       6000  -0.79206     $ C
m101    1001   0.666662    $ H, Poly Ethylene, C2-H4
       6000   0.333338    $ C, rho = 0.91 (LDPE), >0.941 (HDPE)
m102    1001   0.363632    $ H, Polyethlene Terephthalate (PET), C10-H8-O4
       6000   0.454552    $ C, rho = 1.38 g/cc
```

```
      8016   0.181816    $ O
m106    6000   0.333339    $ C, Teflon (Dupont) aka PTFE=Polytetrafluoroethylene
      9019   0.666661    $ F, rho = 2.25 g/cc
m108    1001  -0.102013    $ H, Duct Tape, assumed rho = 1.55 g/cc
      6000  -0.682382    $ C
      8016  -0.215266    $ O
     11023  -0.000133    $ Na
     17000  -0.000206    $ Cl
m120    1001   0.5245      $ H, PVT scintillator, H/C = 1.103,  rho= 1.032 g/cc
      6000   0.4755      $ C
m200    1001   -0.01       $ H   Concrete (common Portland) , rho = 2.3 g/cc
      8016   -0.532      $ O
     11023   -0.029      $ Na
     13027   -0.034      $ Al
     14000   -0.337      $ Si
     20000   -0.044      $ Ca
     26000   -0.014      $ Fe
m202    6000   -0.00041    $ C, Stainless Steel 316, rho = 8.00 gm/cc
     14000   -0.00507    $ Si
     15031   -0.00023    $ P
     16000   -0.00015    $ S
     24000   -0.17000    $ Cr
     25055   -0.01014    $ Mn
     26000   -0.66900    $ Fe
```

```
      28000   -0.12000    $ Ni
      42000   -0.02500    $ Mo
c  New (2015 NiQ) Scint material
c LiF/ZnS from PNNL (0.50, 1.390e22, 95%6Li) w/ 15%wt LANL Binder, rho = 2.1492 g/cc
m212    3006   -0.13884    $ Li6
       3007   -0.00852    $ Li7
       9019   -0.46159    $ Fluorine
      30000   -0.81726    $ Zn
      16000   -0.40064    $ Sulfur
c LANL Binder
       6000   -0.19338    $ C
       1001   -0.02597    $ H
       8016   -0.10304    $ O
m900    6000   -0.000124   $ C, Air, rho = 1.205e-3 g/cc
       7014   -0.755268   $ N (99.
       8016   -0.231781   $ O
      18000   -0.012827   $ Ar
m901    6000   -0.000124   $ C, Air, rho = 1.205e-3 g/cc
       7014   -0.755268   $ N (99.
       8016   -0.231781   $ O
      18000   -0.012827   $ Ar
c      98252   -1e-20      $ Air with Cf252 for par=sf
c m901   7014 0.7851   8016 0.2103   98252 1e-20  $ Air with Cf252 for par=sf
```

```
c m902   7014 0.7851   8016 0.2103   94240 1e-20  $ Air with Pu240 for par=sf
c  S(alpha, beta)for <~2eV switch from free-gas to molecular compound treatment.
mt101   poly.10t          $ library endf70sab, evaluation 1969, temp=293.6_K
mt102   poly.10t          $
mt6     grph.10t          $
c ===== Physics Cards ========================================== #
MODE N $ A T
c Neutron Transport
phys:n 20 0 0 -1 -1 0 5  $ Emax = 20 MeV, 2nd-6th = defaults, 7th for Recl value.
c                        $ Recl = 3, LIR off, NCIA on, but defaults to xsec data.
c                        $ Recl = 5, LIR off, NCIA on, ignores xsec data.
c Triton Transport
c phys:t 20 3J 1    $ Emax = 20 MeV, 2nd-4th = reserved, 6th=continuous ionization.
c
c Lower Energy Cutoff (MeV) for Alpha and Triton
c cut:a 1j 0.001
c cut:t 1j 0.001
c ===== Source Definition Cards ================================== #
c sdef    x=0 y=0 z=0 par=sf
c sdef cel=1 erg=d1 x=0 y=0 z=0 $ z=d2
sdef  erg=d1 x=0 y=0 z=1.5875 tr=10 $ par=sf
c
c Internal (Watts) Distributions for Cf-252 & Pu-240 Spontaneous Fission Neutrons
c
```

```
sc1  Cf-252 (parameters from MCNPX 2.60 manual, App.H)
sp1  -3   1.180    1.03419  $ 252Cf
c
c sc1  Pu-240 (parameters from MCNPX 2.60 manual, App.H)
c sp1  -3   0.79493  4.68927  $ 240Pu
c
c si1 L  0.00000001          $ Energy
c sp1 D  1.0                 $ Probability
c
c si2   l -23.0 19i 19.0      $ Distributes to 21 z-axis positions
c sp2   1 20r                $ with equal weightings.  Also use following scx
c ft4  scx 2                 $ tally "treatment" for f4 to create (22) bins: one
c                            $ for each (21) source positions in d2, and total.
c ===== Tally Cards ============================================== #
c ### Tallies for Total Capture Efficiency (TCE) Vs. Time -- "CvT."
c
fc4   6Li (n, t) Total Reaction in Layers w/ Time Bins for Die-Away Time Fit
f4:n   (25 29 33 37 41) $ 5 Sheets in MASTER & all Clones
c e4    2.5e-7 20.0
t4       0  49i 5000 1e20
sd4    1         $ Segment Divisor (sd) values sets F4 cells "norm" to Vol.s
fm4  -1 212 105  $ Material 209, Reaction Types 105=(n,t), 106=(n,3He), 107=(n,a)
c
fc14  6Li (n,t) Reactions in Separate Li-Zn-Binder Layers
```

```
f14:n     25 29 33 37 41 T $ &
t14       0  19i 5000 1e20
c sd14   1 19r 1
sd14   1 4r 1
fm14 -1 212 105  $ Material 209, Reaction Types 105=(n,t), 106=(n,3He), 107=(n,a)
tf14   5
c
c fc24  6Li (n,t) Reactions in Separate Layers of 2nd (u=2)Master+Clones
c f24:n  136 140 144 148 152 156 160 164 168 172 176 180 184 188 192 & $ 15 Layers
c                                196 200  204 208 212 T   $  5 Layers
c t24       0  19i 10000 1e20
c sd24   1 19r 1
c fm24 -1 212 105  $ Material 209, Reaction Types 105=(n,t), 106=(n,3He), 107=(n,a)
c tf24   5
c
e0    2.5e-7 20.0
c
c ### Tallies for Multiplicity Moments vs. Gate or Pre-Delay "DvG" or DvPD."
c
c   Special CAP Treatment for F8 Tally for Neutron Capture Moments
c
c fc108  Li6 (n,t) Total Multiplicity Count Rates
c f108:n (25 29 33 37 41) $ 5 Sheets in MASTER & all Clones
c
```

```
c Repeat for new CAP options (FT card)
c fc118  Li6 (n,t) Total Multiplicity Count Rates
c f118:n (25 29 33 37 41) $ 5 Sheets in MASTER & all Clones
c
c ft118  cap 3006 gate  50  400  $ Predelay 0.5us, Gate = 4us
c
c Repeat for new CAP options (FT card)
c fc128  Li6 (n,t) Total Multiplicity Count Rates
c f128:n (25 29 33 37 41) $ 5 Sheets in MASTER & all Clones
c
c Repeat for new CAP options (FT card)
c fc138  Li6 (n,t) Total Multiplicity Count Rates
c f138:n (25 29 33 37 41) $ 5 Sheets in MASTER & all Clones
c
c Repeat for new CAP options (FT card)
c fc148  Li6 (n,t) Total Multiplicity Count Rates
c f148:n (25 29 33 37 41) $ 5 Sheets in MASTER & all Clones
c
c Repeat for new CAP options (FT card)
c fc158  Li6 (n,t) Total Multiplicity Count Rates
c f158:n (25 29 33 37 41) $ 5 Sheets in MASTER & all Clones
c
c Repeat for new CAP options (FT card)
c fc168  Li6 (n,t) Total Multiplicity Count Rates
```

```
c f168:n (25 29 33 37 41) $ 5 Sheets in MASTER & all Clones
c
c Repeat for new CAP options (FT card)
c fc178  Li6 (n,t) Total Multiplicity Count Rates
c f178:n (25 29 33 37 41) $ 5 Sheets in MASTER & all Clones
c
c CAP options
c   Vary Predelay, Fixed Gate
c ft108  cap 3006 gate   25  400  $ Predelay 0.25us, Gate =4us
c ft118  cap 3006 gate   50  400  $ Predelay 0.5us, Gate =4us
c ft128  cap 3006 gate   75  400  $ Predelay 1.0us, Gate =4us
c ft138  cap 3006 gate  100  400  $ Predelay 2.0us, Gate =4us
c ft148  cap 3006 gate  150  400  $ Predelay 3.0us, Gate =4us
c ft158  cap 3006 gate  200  400  $ Predelay 4.0us, Gate =4us
c ft168  cap 3006 gate  250  400  $ Predelay 5.0us, Gate =4us
c ft178  cap 3006 gate  300  400  $ Predelay 6.0us, Gate =4us
c
c   Fixed Predelay, Vary Gate
c ft108  cap 3006              $ ZAID for Li6
c ft118  cap 3006 gate  150  100  $ Predelay 1.5us, Gate =1us
c ft128  cap 3006 gate  150  200  $ Predelay 1.5us, Gate =2us
c ft138  cap 3006 gate  150  400  $ Predelay 1.5us, Gate =4us
c ft148  cap 3006 gate  150  800  $ Predelay 1.5us, Gate =8us
c ft158  cap 3006 gate  150 1600  $ Predelay 1.5us, Gate =16us
```

```
c ft168  cap 3006 gate  150 3200  $ Predelay 1.5us, Gate =32us
c ft178  cap 3006 gate  150 6400  $ Predelay 1.4us, Gate =64us
c
c ### Settings used for either CvT or DvG/DvPD Tallies
c
fq0  s t e  $ Changes Hierarchy of OUT file listing (but not in MCTAL)
c          $ Default: F(cell, surf), D(irect of flagged), U, S, M, C, E, T.
c ===== Peripheral & Problem Cut Off Cards============================== #
c "Print & Dump Cycle" card options 1 - 5
c  1) Tally Prnt Increment, 2) Dump to RUNTPE increment, 3) Create MCTAL file
c  4) Max No. of Dumps on RUNTPE, 5) Controls Rendezvous points.
prdmp 2j 1                  $ MCTAL file only
c prdmp 4j 5e+04            $ Rendezvous points only
c prdmp j 1e+05 1 2 1e+05       $ Example of MCTAL and Rendezvous control
c
c Useful Tables to Add or Omit(-): 10=source params, 38=fission multiplicity,
c 40=material composition, 110=1st 50 histories, -160=TFC analysis,
c print  10 -30 -38 -40 -50 -70 -85 -86 -98 -102 110 -120 -128 -130 -140 &
c       160 161 -162 170
c print 10 110 170
c History Cutoff card
nps 1e+07
c ### BLANK CARD TERMINATOR FOLLOWS ###
```